UNIVERSITAT POLITÈCNICA
DE CATALUNYA
BARCELONATECH

Dynamic large deformation modelling of soils including static liquefaction

Author

Gaia Di Carluccio

Thesis Advisors
Núria M. Pinyol Puigmartí
Eduardo Alonso Pérez de Ágreda

A thesis submitted to the Universitat Politècnica de Catalunya (UPC)
in partial fulfilment of the requirements for the degree of
DOCTOR OF PHILOSOPHY

Ph.D. program on Geotechnical Engineering and Geo-Sciences
Department of Civil and Environmental Engineering
Barcelona, September 2021

Thesis written by Gaia Di Carluccio

This work has been funded by projects Soil in Motion (SiM) (Ref. RTI2018-097365-B-I00) from the Spanish Ministry of Science and Innovation and 2017SGR-1153 from AGAUR-Government of Catalonia.

Alla mia famiglia

ACKNOWLEDGEMENTS

This thesis has been made possible thanks to the support received by the Spanish Ministry of Science and Innovation through the project SiM, coordinated by CIMNE, and by AGAUR-Government of Catalonia and the Centre for Development Cooperation of UPC within the grant 2017SGR-1153.

I want to express my sincere gratitude to my supervisors Núria Pinyol and Eduardo Alonso. Since I first attended your lectures at Master, I breathed your enthusiasm and passion for geotechnics that motivated me to undertake the PhD. Thanks for given me the opportunity to work with you and guiding me along the way with your impressive knowledge and critical vision.

My gratitude is extended to the professors of the Department of Civil and Geotechnical Engineering, in particular to Marcel Hürlimann who helped me in the field investigation and Antoni Lloret who dedicated part of his time to assist me in the laboratory activities. Both contributions have been fundamental for my research.

Thanks are addressed to the members of the Anura3D developers team for their collaboration and friendly support.

I also would like to acknowledge the friends and colleagues that I met during the PhD journey, it was nice to enjoy our mutual satisfactions and less hard to face the difficulties.

Thank you to Riccardo who, like a brother, was my safety net since the early years of this experience we shared.

Lastly, thank you to those who are at my side by encouraging me in the most difficult times: my family, whose love accompanies me anytime and reminds me where I come from and Salvo with whom it is exciting to look at the future.

ABSTRACT

Modelling geotechnical problems involving large deformation is a research field that arouses growing interest since it is fundamental for evaluating the risk and quantifying the magnitude of consequences. However, it is still challenging and requires to develop solution schemes able to reproduce failure initiation as well as post-failure dynamics.

This thesis focuses on studying large deformations geotechnical problems subjected to static and dynamic loadings including static liquefaction in saturated and partially saturated soils that induces flow-like landslides.

Accounting for the difficulties to treat large deformations with the traditional lagrangian approaches, due to the excessive distortion of the mesh elements, the Material Point Method (MPM) is adopted. MPM discretises the continuum media into a set of material points that can move attached to the material and carry all the information. The governing equations are solved at the nodes of the computational mesh that remains fixed in space. This double discretization provides to MPM the capabilities of handling problems involving large displacements and deformations. The numerical developments and simulations are carried out in the open-source MPM Anura3D code.

The method is applied for the simulation of geotechnical cases dealing with soil excavation. First, the stability of strutted excavations in clay is studied and MPM results, which provides a realistic interpretation of failure, are compared with analytical solutions based on simplified assumption. An interesting discussion of the discrepancies found between the methods is also included. In the second example, the well-documented Cortes de Pallás landslide due to toe excavation is simulated. Consistently with field observation, the excavation produces significant displacements after which a new stable configuration is reached.

Later on, the thesis presents the study of a complex real landslide occurred during a dam construction project, including its seismic assessment. This is a case of creeping slide motion and it is characterized by two superimposed sliding surfaces. Different scenarios of geometry and groundwater conditions, representing the landslide history and futures stabilizing measures and rainfall regimes, are considered for the stability analysis with FEM. MPM is used instead to carry-out a motion back-analysis on an unstable scenario. The creeping behaviour observed is also discussed through an analytical calculation in which the case is simplified to a planar landslide. Finally, the seismic assessment is performed with a focus on the effect of the superimposed slip surfaces. Results of MPM are compared with Newmark's approach in its classical form and by introducing the strain-rate dependence on the residual friction angle.

The last part of the thesis focusses on modelling a liquefaction-induced flow landslide from the failure triggering to the subsequent slide-to-flow transition. With this aim, an advanced constitutive model able to simulate static and cyclic soil response such as accumulation of permanent strains, excess pore pressure and degradation of soil stiffness modulus, is implemented in the open-source MPM Anura3D code. For the validation and calibration of the code and the constitutive model, laboratory tests published in the literature are reproduced. After validation, the model is applied to a real case of flow landslide recently occurred in Catalonia (Spain) Its parameters are calibrated based on data of undrained triaxial tests that show the liquefaction potential of the material involved. MPM simulation is able to reproduce the failure initiation caused by a water inflow and the large deformations in the post-failure stage. The final run-out calculated is found to be significantly affected by the model parameter accounting for liquefaction susceptibility.

RESUMEN

La modelización de problemas geotécnicos que involucran grandes deformaciones es un campo de investigación que despierta un interés creciente ya que es fundamental para evaluar el riesgo y cuantificar la magnitud de las consecuencias. Sin embargo, sigue siendo un desafío y requiere desarrollar soluciones capaces de reproducir el inicio de la rotura, así como la propagación del movimiento.

Esta tesis se centra en el estudio de problemas geotécnicos de grandes deformaciones, incluida la licuefacción estática en suelos saturados y parcialmente saturados que inducen flujos de tierra.

Teniendo en cuenta las dificultades en tratar grandes deformaciones con los enfoques tradicionales lagrangianos, debido a la excesiva distorsión de los elementos de la malla, se ha adoptado el Método del Punto Material (MPM). MPM discretica los medios continuos en un conjunto de puntos materiales que pueden moverse unidos al material y llevan toda la información. Las ecuaciones de gobierno se resuelven en los nodos de la malla computacional que permanece fija en el espacio. Esta doble desratización proporciona a MPM la capacidad de manejar problemas que involucran grandes desplazamientos y deformaciones. Los desarrollos numéricos y las simulaciones se llevan a cabo en el código abierto Anura3D.

El método se ha aplicado para la simulación de casos geotécnicos relacionados con excavación de suelo. Primero, se ha estudiado la estabilidad de excavaciones sostenidas en arcilla y se han comparado los resultados del MPM, que proporcionan una interpretación realista de la rotura, con soluciones analíticas basadas en hipótesis simplificadas. También se ha incluido una discusión interesante de las discrepancias encontradas entre los métodos. En el segundo ejemplo, se ha simulado el bien documentado deslizamiento de tierra de Cortes de Pallás debido a la excavación del pie. Consistentemente con las observaciones de campo, la excavación produce desplazamientos significativos después de los cuales se alcanza una nueva configuración estable.

Luego, la tesis presenta el estudio de un complejo deslizamiento real ocurrido durante el proyecto de construcción de una presa, incluyendo su evaluación sísmica. Este es un caso de movimiento deslizante lento y se caracteriza por dos superficies de deslizamiento superpuestas. Para el análisis de estabilidad con FEM se han considerado diferentes escenarios de geometría y condiciones de aguas subterráneas, que representan el historial de deslizamientos y futuras medidas de estabilización y regímenes de lluvia. En cambio, MPM se ha utilizado para llevar a cabo un análisis inverso de movimiento en un escenario inestable. El comportamiento observado de movimiento lento también se ha analizado a través de un cálculo analítico en el cual el caso se ha simplificado a un deslizamiento de tierra plano. Finalmente, se ha realizado la evaluación sísmica con un enfoque en el efecto de las superficies de deslizamiento superpuestas. Los resultados del MPM se han comparado con el método de Newmark en su forma clásica e introduciendo la dependencia de la velocidad de deformación en el ángulo de fricción residual.

La última parte de la tesis se centra en la modelización de un flujo de tierra inducido por licuefacción, desde el desencadenamiento de la rotura hasta la posterior transición de deslizamiento a flujo. Con este objetivo, se ha implementado en el código abierto Anura3D un modelo constitutivo avanzado capaz de simular la respuesta estática y cíclica del suelo, como la acumulación de deformaciones permanentes, el exceso de presión de poros y la degradación del módulo de rigidez del suelo. Para la validación y calibración del código y del modelo constitutivo se han reproducidos ensayos de laboratorio descritos en la literatura. Después de la validación, el modelo se ha aplicado a un caso real de flujo de tierra ocurrido recientemente en Cataluña (España). Sus parámetros se han calibrado basándose en datos de ensayos triaxiales no drenados que muestran el potencial de licuefacción del material involucrado. La simulación MPM es capaz de reproducir la iniciación de la rotura causada por afluencia de agua y las grandes deformaciones en la etapa post-rotura. El alcance final del deslizamiento calculado se ve significativamente afectado por el parámetro del modelo que tiene en cuenta la susceptibilidad a la licuefacción.

CONTENTS

CHAPTER 1 - INTRODUCTION

In the first chapter of the thesis, the motivation of the work is briefly described. Then, the main objectives and the adopted methodology are highlighted and finally, the organisation of the document is outlined.

1.1 MOTIVATION

Modelling geotechnical problems involving soil large deformation, such as landslide dam failure and ground excavation, is fundamental for evaluating the risk and quantifying the magnitude of consequences. Despite the growing interest in this research field, the simulation of this kind of phenomena is still challenging since it requires numerical tools able to capture the failure triggering and the subsequent post-failure behaviour.

One of the phenomena that may induce large deformations in saturated and partially saturated granular soils is the liquefaction. The damage resulting can occur in different forms: displacements of buildings; lifting of buried structures; earth dams collapse; flow-like landslides.

In the literature, there are many documented cases of liquefaction produced by seismic events. One of the most surprising examples due to its severity is the one of Kobe (1995) that caused damages to civil structures in the city harbour and in the coastal zone mainly due to liquefaction of foundation soil.

However, liquefaction can also occur in areas not subjected to seismic events. In the field of landslides, once the instability is triggered, the movement may induces the effective stress to drop due to the increase of pore water pressure and static liquefaction occurs.

This is the case of the Oso landslide (March 22nd, 2014, Washington), one of the most catastrophic landslides in the US (Wartman *et al.*, 2016) that caused 43 human losses and economic losses of 120 million dollars (Department of Natural Resources [DNR], 2015) due to 8 million cubic meters of glacial and fluvial deposits that travelled more than 1 km. One of the causes of the catastrophic consequences is attributed to the liquefaction of fluvial deposits (Keaton *et al.*, 2014; Iverson *et al.*, 2015; Iverson and George, 2016).

The phenomenon is widely known experimentally and theoretically, however, its numerical modelling is challenging mainly because it involves large deformations, dynamic factors and requires a proper constitutive model. It should be able to capture all aspects of static and cyclic soil response like the accumulation of permanent deformations and excess pore pressure, and also the soil moduli degradation and the concurrent hysteretic damping increase as a function of the imposed cyclic shear strains.

Furthermore, the most widely used calculation methods based on lagrangian approaches such as Finite Element Methods (FEM), or the Finite Differences Methods (FDM), in its standard version, do not allow to adequately simulating large deformations due to the problems associated with the distortion of mesh elements that deform with the material. On the other hand, methods based on Eulerian approaches, in which the computational mesh remains fixed, present limitations in the monitoring of dynamic boundaries.

To overcome such difficulties, modern numerical approaches are being developed. This is the case of the Material Point Method (MPM). It was developed to represent fluid dynamic by Harlow *et al.* (1964) and extended to soil mechanics problems by Sulsky *et al.* (1994, 1995). This method combines a discrete system of material points representing the continuum media, which can move attached to the material and carry all the information. The governing equations are solved in the nodes of the computational mesh, which remains fixed in space. This double discretization can simulate large deformations without the problems associated with mesh elements distortion.

The lack of proper tools able to simulate the liquefaction together with the outstanding potential of the MPM in geotechnical problems involving large deformations stimulated the interest of undertaking this line of research.

1.2 OBJECTIVES AND METHODOLOGY

This thesis aims to investigate geotechnical problems involving large deformations within the framework of the Material Point Method (MPM). A focus is directed on modelling static liquefaction phenomena in saturated and partially saturated soils inducing flow-like landslides.

The following specific objectives are formulated:

- Development, within MPM, of initial and boundary conditions dealing with geotechnical problems treated in the thesis: (1) cyclic loading; (2) initial hydraulic boundary conditions in saturated and partially saturated soils; (3) soil excavation;
- Implementation and validation, in the MPM code used in this thesis, of an advanced constitutive model able to reproduce static and cyclic liquefaction in order to simulate landslide transition to flow type landslide during itself motion.
- Numerical developments application on real cases.

The methodology followed to achieve these objectives can be summarized in:

- Collect in a state of the art constitutive models and numerical methods used in geotechnics, focusing on their performance in simulating liquefaction phenomenon, and select a suitable one to be implemented;
- Acquire the necessary knowledge related to the MPM code used and its programming language (FORTRAN). This is the open-source Anura3D software (http://www.anura3d.com), developed by the MPM research community
- Validate the numerical developments, listed above, through benchmarks and analytical solutions;
- As a member of Anura3D developers team, adapt the pre-processor interface to the numerical developments carried out and make it available to the community as user-friendly;
- Model real cases of landslides: Cortes de Pallás, Yesa, Valarties.

1.3 THESIS LAYOUT

The Thesis is organised in 8 chapters.

After an introduction on liquefaction phenomenon, Chapter 2 includes a state of the art of the constitutive models for liquefaction available in the literature and the numerical methods used to simulate this phenomenon. MPM is described and the advanced constitutive model for liquefaction selected to be implemented (Ta-Ger model, Tasiopoulou and Gerolymos 2016a, b) is introduced.

Chapter 3 presents the MPM Anura3D software and provides a general view of MPM formulations for multi-phase materials. Further numerical features are discussed and finally, the main contributions of the thesis to the code numerical development are outlined.

In Chapter 4, MPM is applied to simulate geotechnical problems dealing with soil excavation. First, the stability of supported vertical excavation in elasto-plastic material is analysed. Results are compared and discussed concerning solutions reported in the literature. Then, a well-documented real case of landslide in Cortes de Pallás, reactivated by quarry excavations, is simulated (Alonso *et al.*, 1993).

In Chapter 5, a large landslide located in the Spanish Southern Pyrenees (Yesa) during a dam construction project is investigated. In addition to a stability analysis, the seismic response of the landslide is analysed with different methods. Results from Newmark's approach and MPM are compared and discussed.

Chapter 6 is dedicated to describe Ta-Ger model including details on its implementation in Anura3D. The model is verified and validated by simulating the results of monotonic and cyclic laboratory tests and liquefaction phenomenon is analysed at laboratory scale.

Chapter 7 focuses on the MPM modelling of a real case of liquefaction-induced flow-like landslide. The liquefiable soil is described with the Ta-Ger model after calibrating its parameters with data from in situ and laboratory tests. The development of the initial failure surface and the dynamics of the motion in the post-failure stage are discussed together with the evolution of effective stresses and pore water pressures. An emphasis is directed towards identifying the model parameters accountings for liquefaction susceptibility.

A summary of the conclusions and future developments can be found in Chapter 8.

Finally, the Appendix includes the Ta-Ger constitutive model algorithm implemented in the MPM code.

CHAPTER 2 - STATE OF THE ART

The numerical simulation of large deformations in soils, involving liquefaction, is challenging from several points of view. It requires a proper numerical method combined with a constitutive model able to capture the soil dynamic behaviour. After a brief description of the liquefaction phenomenon, the purpose of chapter 2 is to collect in a state of the art the available numerical methods and constitutive models for liquefaction with the aim of assessing the potential of each one to the objectives of the thesis.

2.1 INTRODUCTION

The term "liquefaction" is commonly referred to a phenomenon whereby a saturated or partially saturated soil loses strength and stiffness, changing from a solid to a nearly liquid state (shear strength is almost equal to zero) due to the effective stress drop produced by an increase of pore water pressure. Liquefaction by dynamic loads can be observed in saturated sands due to earthquakes or wave action and liquefaction by static load in slides due to pore water pressure generation during the landslide mass movement itself.

In order to fully understand this phenomenon is necessary to know granular soils behaviour for different loading (monotonic or cyclic) and drainage conditions.

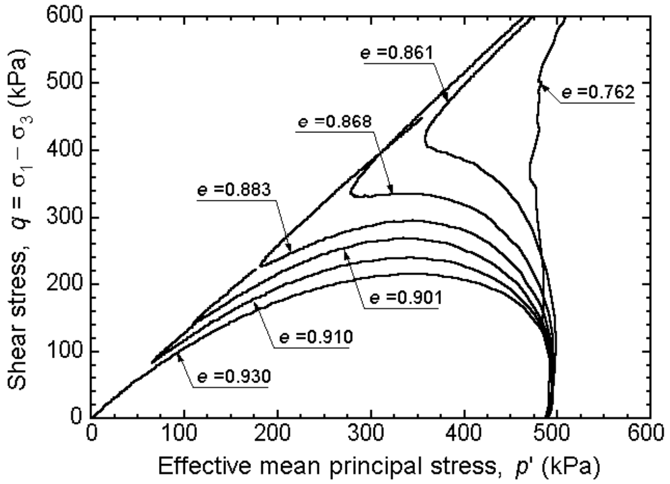

Figure 2.1. Results from monotonic undrained triaxial tests on loose sand (Verdugo, 1992).

Castro and Poulos (1977) discussed on the monotonic and cyclic response of loose and dense saturated soil. Loose saturated soils subjected to monotonic or cyclic shear loading tend to have a contractive behaviour so, under undrained conditions, pore water pressure progressively increases and effective stress reduces with the shear load straining. Under monotonic shearing, a contractive soil reaches a peak shear strength and then softens, eventually achieving a residual shear resistance. If this value becomes less than the shear stress required to ensure static equilibrium conditions, the soil can undergo large deformations and can occur the so-called "liquefaction" failure (Fig. 2.1, see curve corresponding to void index e = 0.930). If the same soil is subjected to cyclic shear loading, excess pore pressures are generated at each cycle of load with a progressive decrease of effective stress. When the shear strength falls below the static shear stress, deformations continue after cyclic loading stops and a flow failure results (Fig. 2.2).

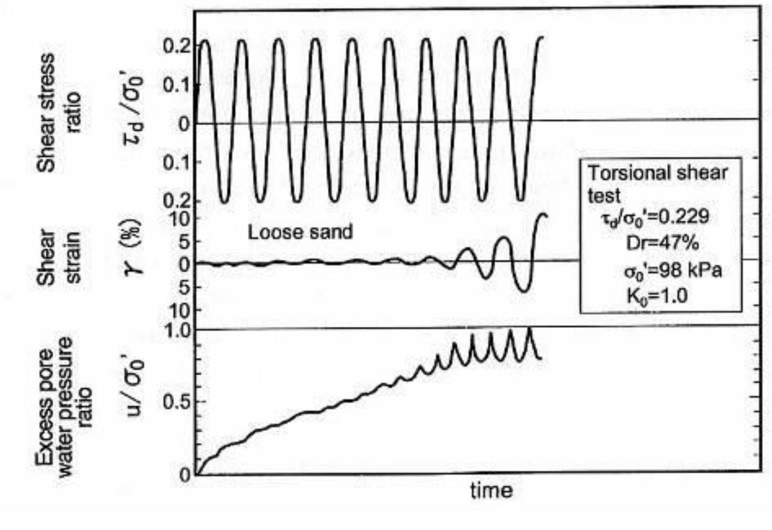

Figure 2.2. Results from cyclic torsional shear test on loose sand (Ishihara, 1985).

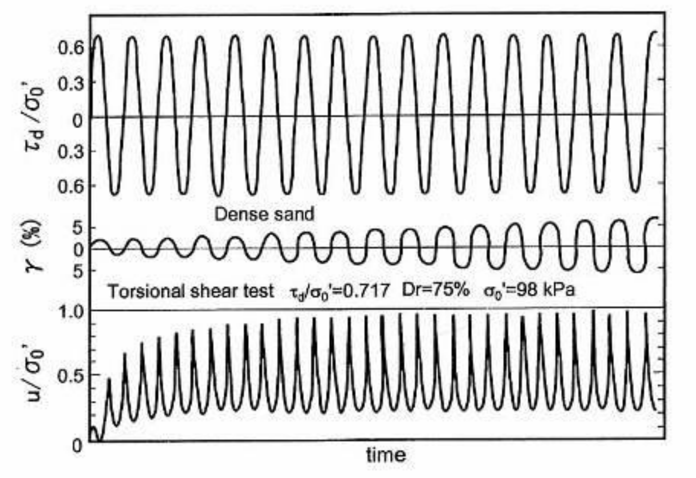

Figure 2.3. Results from cyclic torsional shear test on dense sand (Ishihara, 1985).

Dense sands under monotonic shear loading, initially exhibit contractive response, then dilative. In undrained conditions, the dilative behaviour results in a decrease in pore water pressure and an increase in effective stress and shear strength (Fig. 2.1, see curve corresponding to void index $e = 0.861$). Under small shear strains cycles, pore pressure may be generated at each load cycle leading to softening and deformations accumulate. At larger shear strains, the tendency to dilate leads to reduce the excess pore pressure resulting in an increase of shear resistance. After the cyclic loading stops, deformations developed during the shearing stop and the soil exhibits the full strength that would be observed in a monotonic shear test. Hence, cyclic shear on dilative soils does not induce liquefaction failures because both cyclic and post-cyclic shear strength are greater than the static shear stress. This case is commonly known as “cyclic mobility” (Fig. 2.3).

Robertson and Fear (1995) did a complete classification system for describing liquefaction:

- Flow liquefaction can occur only in strain softening soils with contractive behaviour, under monotonic or cyclic shear loading, when the residual strength of the soil becomes smaller than the static shear stress.
- Cyclic softening can occur in soils that tend to dilate in undrained monotonic shear and undergo large deformations during cyclic shear due to pore pressure build-up.

When deformations do not continue after cyclic loading stops, it can be distinguished into:

- Cyclic liquefaction, when cyclic shear stresses exceed the initial static shear stress to produce a condition of zero effective stress, during which large deformations can occur.
- Cyclic mobility, when deformation accumulates in each cycle of shear stress but cyclic loads do not induce a condition of zero effective stress.

Hence, the liquefaction numerical modelling presents some difficulties due mainly to the complex behaviour of sands, above described. It renders particularly complicated to develop a constitutive model able to capture all aspects of static and especially cyclic soil response like the accumulation of permanent deformations and excess pore pressure, and also the soil moduli degradation and the concurrent hysteretic damping increase as a function of the imposed cyclic shear strains.

Furthermore, the computational methods implemented in commercial software, now available, cannot model the evolution of liquefaction from the conditions that determine its activation to the interpretation of the effects resulting from its propagation.

2.2 CONSTITUTIVE MODELS FOR LIQUEFACTION

Constitutive models are mathematical idealisations of the material behaviour, which characterise the stress-strain relationship and define the stiffness of the material. In the past decades, many constitutive models for sands have been proposed aiming to reproduce liquefaction, each with varying degree of accuracy and applicability. They include extended hardening concepts, bounding surface or multi-surface plasticity. Therefore, it was considered appropriate to direct the efforts in selecting the most suitable model to the objective of the thesis rather than to develop a new one. From the Generalized Plasticity model (Pastor *et al.*, 1990) and its latest developments, the following models have been investigated with a focus on their capabilities in capturing sand behaviour under monotonic and cyclic loading: Multi-yield surface plasticity (Prevost, 1977, 1978), NorSand (Jefferies, 1993); Hypoplastic models (Bardet, 1990; Bauer, 1996; Gudehus, 1996); NTUA-SAND (Andrianopoulos *et al.*, 2010); SANISAND (Taiebat and Dafalias, 2008); UBCSAND (Beaty and Byrne, 1998); Ta-Ger (Tasiopoulou and Gerolymos, 2016a, b).

Among the various models, the Ta-Ger has been chosen in this thesis to study liquefaction in saturated and partially saturated soils.

2.2.1 Generalized Plasticity

The Generalized Plasticity model was developed by Pastor *et al.* (1990) to model clay and sand behaviour, in drained and undrained conditions under monotonic and cyclic loading. This theory avoids some complexities associated with classical plasticity since it assumes that plastic deformations can be determined without explicitly defining yield surface and plastic potential and, furthermore, it does not require consistency laws to obtain plastic modulus.

To take into account more accurately cyclic loading phenomena, the model introduced a discrete memory factor multiplying the plastic modulus. This factor is equal to 1 during virgin loading; larger than 1 during reloading where higher deformations take place, in agreement with experiments results of Castro (1969).

Pastor *et al.* (1999) implemented the model in the Finite Element Program GeHoMadrid in order to validate it through the liquefaction simulation of a sand column subjected to dynamic acceleration and by recording time history of pore water pressure. Furthermore, results of a centrifuge test on San Fernando dam liquefaction failure, described by Zienkiewicz *et al.* (1999), were reproduced in a numerical model. Numerical and experimental results of vertical displacement were compared showing a quite good agreement.

However, it is well known that sand behaviour depends on its density and confining pressure. For a determinate density, a sand shows its loose behaviour at sufficiently high confining pressures and dense behaviour at sufficiently low confining pressures. The major limitation of the model was that for samples of given sand characterized by different values of density and confining pressures were needed different sets of parameters to reproduce the behaviour observed experimentally. Hence, Manzanal *et al.* (2011) introduced in the model the state parameter $\psi = e - e_{cs}$ (Been and Jefferies, 1985), where e_{cs} is the void ratio at the critical state. It describes the relative position on the plane $e - p'$ of the current state and the projection of the CSL (critical state line) in order to reproduce the sand behaviour for a wide range of confining pressures and densities (Fig. 2.4).

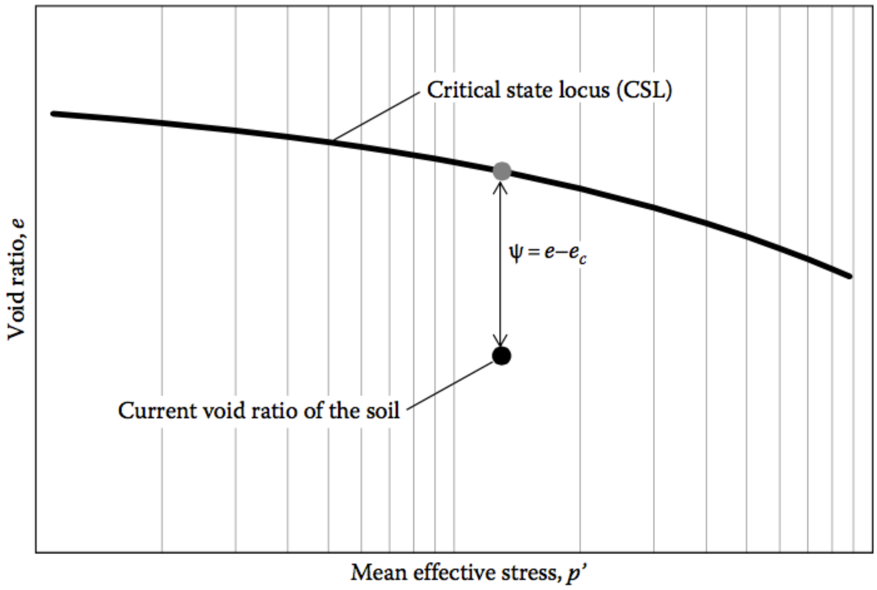

Figure 2.4. Definition of state parameter ψ in $e - p'$ plane (Jefferies and Been, 2006).

In spite of a relatively simple fitting of experimental data, the fact that yield surfaces are not clearly defined in the model can lead to the phenomenon called "Ratcheting" (Alonso-Marroquín and Herrmann, 2004; McNamara, Garcia Rojo and Herrmann, 2008; O'Sullivan and Cui, 2009; Calvetti and di Prisco, 2010) under small stress cycles: plastic deformations grow indefinitely when the material is subjects to many stress-controlled loading cycles.

2.2.2 NorSand

The NorSand constitutive model for sand was developed within the generalized critical state framework by Jefferies (1993) in order to overcome some limitations of Cam-Clay model. It was the first elastoplastic Cambridge-type model based on the state parameter ψ (Been and Jefferies, 1985) that permits to define a unique set of parameters for a given material, regardless of the initial conditions.

The model assumes a Cam-clay type yield surface (Fig. 2.5), which is a function of the "image pressure" p_i, and two material parameters, N and M:

$$F = \eta' - \frac{M}{N}[1 + (N-1)(\frac{p'}{p_i})^{N/(1-N)}] \quad \text{for } N > 0 \tag{2.1}$$

$$F = \eta' - \frac{M}{N}[1 + (N-1)(\frac{p'}{p_i})^{N/(1-N)}] \quad \text{for } N = 0 \tag{2.2}$$

N can be viewed as a volumetric coupling; M is the stress ratio at image state.

The model is based on the hypothesis of isotropy and it neglects the change in sand behaviour caused by the so-called change in fabric.

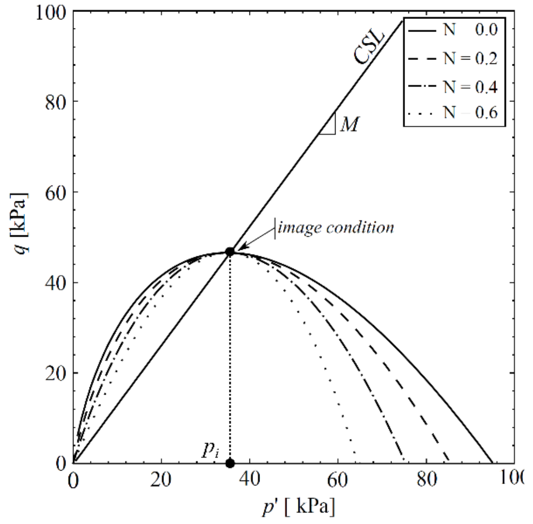

Figure 2.5. NorSand yield surface (Fern *et al.*, 2016).

NorSand performance at stress point level is presented first by Jefferies and Shuttle (2005). They report numerical simulations of static and cyclic liquefaction compared to experimental data of undrained triaxial compression tests on Erksak sand and undrained cyclic simple shear tests of Nevada sand. Results of NorSand predictions show a good match between the model and the sand behaviour. Unlike previous plasticity models for soil NorSand includes the effect of principal stress rotation.

In the book "Soil Liquefaction" (Jefferies and Been, 2006) the authors try to better understand the liquefaction phenomenon by analysing laboratory data and full-scale case histories. NorSand model is presented as a simple computable model able to capture the salient aspect of liquefaction.

More recently Sternik (2014) showed NorSand performance in simulating static liquefaction on saturated sand under undrained monotonic loading and Li and Leao (2018) discussed the results of undrained and drained monotonic triaxial tests simulation to study a case of highway fill embankment failure induced by liquefaction of foundation soils.

2.2.3 SANISAND and NTUA-SAND

The SANISAND (Taiebat and Dafalias, 2008) and NTUA-SAND (Andrianopoulos *et al.*, 2010) models were built on the formulation of bounding surface models proposed by Manzari and Dafalias (1997) and Papadimitriou and Bouckovalas (2002). They were developed within the critical state framework with the aim to reproducing the cyclic response of sands under small as well as large cyclic strains, by using a unique set of parameters independent from initial conditions, density or loading direction. They directly associate the shear behaviour of the sand to the state parameter ψ (Been and Jefferies, 1985).

The NTUA-SAND model uses a narrow open cone-type yield surface in $p - q$ space with the apex at the origin obeying rotational hardening. It implies that only changes in the stress ratio $\eta = q/p$ can cause plastic deformations, while constant stress-ratio loading induces an only elastic response.

On the contrary, SANISAND model introduces a modified equation representative of a narrow but closed cone-type yield surface that obeys rotational and isotropic hardening. For constant η stress path, the closed shape of the yield surface can capture the elasto-plastic behaviour.

For both models, the non-linear soil response under small to medium cyclic strain amplitudes is simulated by introducing a Ramberg-Osgood-type hysteretic formulation.

The accuracy of the NTUA-SAND model has been evaluated against several soil-foundation centrifuge tests by Andrianopoulos *et al.* (2010).

SANISAND model has been validated by Cheng *et al.* (2013) through the comparison of the results of triaxial compression tests and cyclic simple shear tests simulations with experimental data on Toyoura sand. With a focus on the sand cyclic behaviour, numerical simulations of cyclic triaxial tests at various mean pressures were conducted to back-calculate the relation between the damping ratio ξ and the shear modulus degradation ratio G/G_{max}, with shear strain. G is the current shear modulus and G_{max} is the the maximum value at minimal level of shearing for linear elastic soil behaviour. The authors compared the results with the curves based on Seed and Idriss (1970), Idriss (1990) and EPRI (1993), showing that the damping ratios are underestimated at low strains and overestimated at the high strain levels.

2.2.4 UBCSAND

The UBCSAND model has been developed by Beaty and Byrne (1998) and implemented in the finite difference software FLAC mainly for study granular soils liquefaction under seismic loading.

Tsegaye (2010) presents the validation of the 3D version of the model, implemented in the software PLAXIS. It is based on the classical plasticity theory, containing a Mohr-Coulomb yield surface and a non-associated flow rule based on the Drucker-Prager plastic potential function. In order to ensure a smooth transition into the liquefied state of the soil a secondary yield surface is introduced in the model and the plastic shear modulus during the secondary loading is formulated as a function of the number of cycles.

Due to the non-associated flow rule, once the stress path has reached the yield surface defined by the peak friction angle, the volumetric strain becomes constant. This issue makes not possible to model the stiffness degradation of the soil which is observed in the experimental data. The model tries to overcome this limitation by implementing an equation, which gradually decreases the plastic shear modulus as a function of the plastic deviatoric strain generated during dilation of the soil element.

In the report of Petalas and Galavi (2013) an improved version of the model together with its validation is presented by simulating cyclic simple shear test on loose Fraser sand. The numerical predictions were compared with experimental data from Sriskandakumar (2004) in terms of the evolution of excess pore pressures for different shear stress ratios ($CSR = \tau/\sigma'_0$) by using the same set of parameters.

The comparison is quite satisfactory, however, the evolution of the excess pore pressures obtained by the model during the first cycle is higher than the experimental results. Another limitation of the model is related to the use of a linear elastic unloading rule, with constant shear modulus equals to G_{max}, that induces an overestimation of the damping in the system.

2.2.5 Hypoplasticity

Hypoplastic models for sand have been developed by authors like Bardet (1990), Bauer (1996) and Gudehus (1996). It is an alternative model to simulate the nonlinear and irreversible behaviour of loose and dense sand.

In contrast with the classic elasto-plastic concept, the plastic strain rate is defined without reference to any plastic potential surface or yield surface. The model does not distinguish explicitly the elastic from the plastic deformations and the material behaviour is described by a unique constitutive equation able to consider loading and unloading.

Vanden Berghe (2011) presented results of undrained triaxial tests simulations under cyclic strain control by using the hypoplastic constitutive equation. They fit only part of experimental results showing some limitation:

- After a few numbers of cycles, no more strength degradation is observed and the hysteresis loops reach an equilibrium. The author attributes this equilibrium, in contrast with experimental results, to a kind of compensation between the dilation and contraction phases.

- The model cannot simulate the backbone curve and the behaviour under small deformations cyclic tests; furthermore, it overestimates the contractive behaviour of the soil because does not consider the grain reorganization consecutive to the transition from the consolidation to the shearing phase.

Although the Hypoplastic model provides a unique set of parameters for a particular soil type at a chosen stress range, its parameters are relatively difficult to be obtained from real test data.

2.2.6 Multi-yield surface plasticity

The Multi-yield surface plasticity model has been first applied by Prevost (1977, 1978) to soil mechanics, then modified and implemented in the Finite Element software Open Sees by Yang (2000) and Elgamal *et al.* (2003).

This model employs the concept of plastic moduli field to achieve a piecewise linear elastoplastic behaviour under cyclic loading conditions. This field is defined by a collection of nested yield surfaces of constant size in the stress space, which define the regions of constant plastic shear moduli (Fig. 2.6). An associative flow rule is used to compute the plastic strain increments and a pure deviatoric kinematic hardening rule is employed to capture the Masing-type hysteretic cyclic.

Elgamal *et al.* (2003) show the performance of the model to simulate the cyclic mobility response observed in saturated cohesionless soils. After the calibration conducted on monotonic and cyclic laboratory tests data on Nevada sand, the authors report the results of a strain-controlled undrained cyclic shear loading simulation showing the following aspects:

- The cyclic shearing process leads to a gradual build-up of pore pressure with a corresponding decrease in effective confinement.

- As the excess pore pressure increases, the soil gradually loses all shear stiffness and strength and is unable to resist any appreciable shear loading.

As observed by the authors, one of the limitations of this model is that it does not take into account the Lode angle effect. Thus, it could not reproduce satisfactorily load paths that depend on this effect. This limitation has been overcome in a later version by Yang and Elgamal (2008).

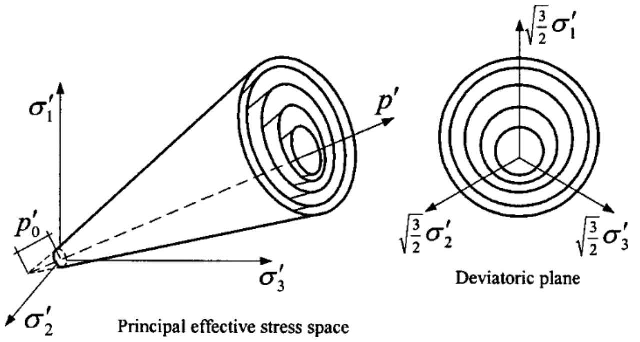

Figure 2.6. Conical yield surface in principal stress space and deviatoric plane (after Prevost, 1985; Parra, 1996 and Yang, 2000).

2.2.7 Ta-Ger model

Ta-Ger sand model was developed by Tasiopoulou and Gerolymos (2016a, b) at the National Technical University of Athens (Greece) with the aim to capture complex aspects of soil behaviour under monotonic and cyclic loading. It is based on critical state theory and it is formulated as a single-surface model with a vanished elastic region. The main features of the model are:

- A new plastic flow rule based on Rowe's dilatancy theory (Rowe, 1962) that accounts for the anisotropic distribution of dilatancy to the normal plastic strain increments, depending on the loading direction. It also includes the densification phenomenon due to cyclic loading;
- An elasto-plastic matrix that provides a gradual transition from the elastic to perfectly plastic response and an appropriate loading/unloading/reloading mapping rule;
- A new formulation for the critical state concept that introduces two "state" parameters. The first is the cumulative deviatoric strain increment $\sum d\varepsilon_q$, which controls the stress ratios evolution from the initial to the critical state value; the second one is the relative dilatancy index I_r (Bolton, 1986).
- A failure surface described as an open-end cone type surface that works similarly to a bounding surface, which cannot be surpassed.

Ta-Ger showed advantages in the numerical implementation, compared with other models, since the formulation of the elasto-plastic matrix that does not require the explicit definition of the plastic modulus and the loading index. Furthermore, the number of model parameters is reduced to a minimum by incorporating the initial state of the soil through the relative dilatancy index I_r and just three parameters need to be calibrated from data of conventional laboratory tests. Its validation was carried out by the authors at point level through comparisons with experimental data.

Fig. 2.7 and Fig. 2.8 show the comparison between the experimental data of monotonic undrained triaxial tests and cyclic undrained torsional shear test on Toyoura sand with model predictions. It can be seen that the model is able to capture the soil behaviour under static and cyclic loading conditions leading eventually to liquefaction.

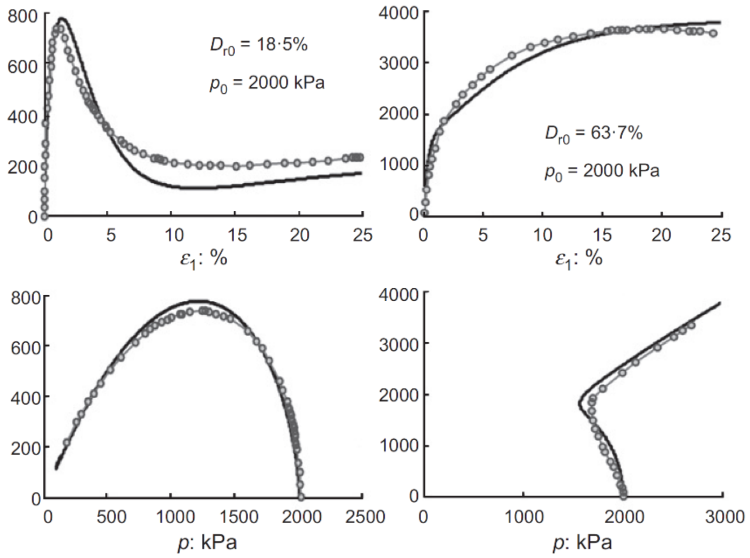

Figure 2.7. Comparison between experimental data from monotonic undrained triaxial tests on Toyoura sand by (Verdugo and Ishihara, 1996) and model predictions (Tasiopoulou and Gerolymos, 2016b).

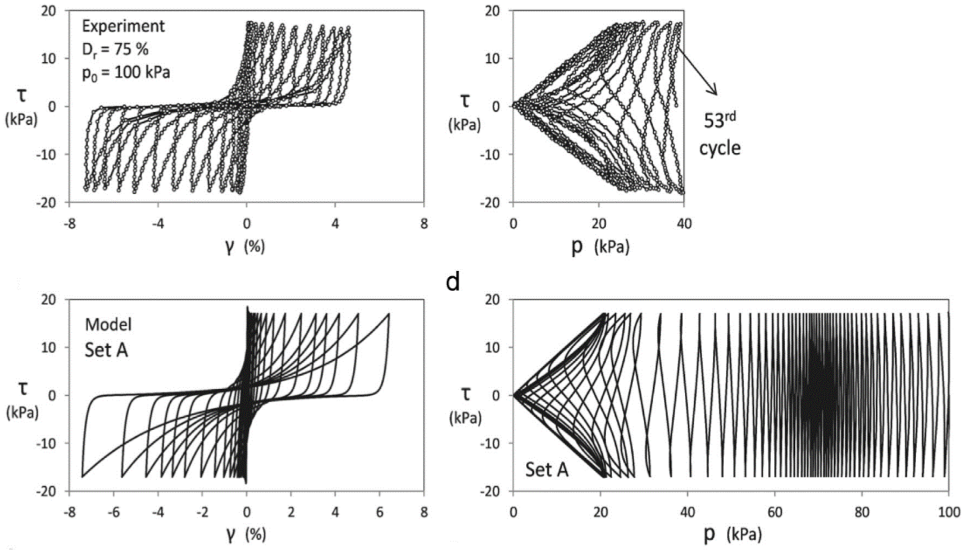

Figure 2.8. Comparison between experimental data from cyclic undrained torsional shear tests on Toyoura sand and model predictions (Tasiopoulou and Gerolymos, 2016a).

2.3 NUMERICAL METHODS AND SOFTWARE

Currently, several examples of numerical modelling of large deformation problems including liquefaction can be found in literature by using some of the constitutive models previously mentioned with different numerical methods (FDM, FEM, ALE, SPH, PFEM, MPM) and commercial software (Plaxis, Flac, OpenSees). Some simulations are conducted on reduced scale models like centrifuge tests and shaking table tests, others on real scale models; in some cases, the effects of liquefaction are analysed, in others the causes. The aim of this review of the literature is to evaluate the ability of these methods, in the simulation of large deformations with a focus on soil liquefaction under static and dynamic loading. These are divided into Mesh-based and Particle-based methods, depending on the discretisation approach. Within the framework of the Particle-based methods the Discrete Element Method (DEM) is also mentioned despite the numerical contribution to the liquefaction modelling is limited to laboratory tests simulations.

2.3.1 Mesh-based methods

Mesh-based methods divide the analysis domain into a collection of subdomains, so-called elements, thus forming a mesh. Each element has several nodes in which governing equation are solved, with a fixed number of predefined neighbours, with whom they are related by shape functions. The response of each node depends on the response of the nodes to which it is related. They can be based on a lagrangian approach, in which the computational mesh deforms during the deformation process of the continuum. It facilitates the treatment of materials with history-dependent constitutive relations. However, they are unable to follow large distortions of the computational domain. On the contrary, in the methods that are based on a eulerian approach, the computational mesh is fixed and the continuum moves with respect to the grid. Here, large distortions can be handled with relative ease but serious limitations can be found in following deforming material interfaces and mobile boundaries (Fig. 2.9). Finite Difference Method (FDM) and Finite Element Method (FEM) are two classical mesh-based methods.

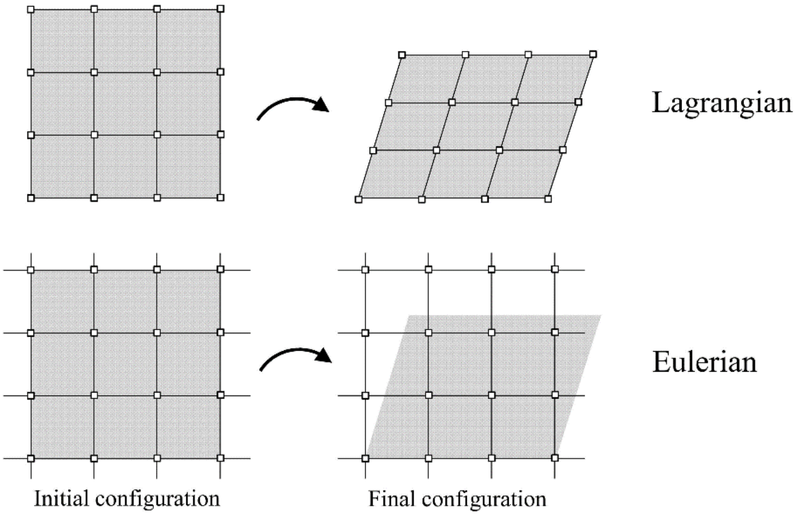

Figure 2.9. Spatial discretisation scheme of lagrangian and eulerian mesh-based methods (Yerro, 2015).

2.3.1.1 Finite Difference Method (FDM)

The Finite Difference Method (FDM) is a numerical discretization method for solving differential equations by replacing continuous functions, of continuous variables, with discrete variables defined only in a discrete number of point of the integration domain. These points constitute the computational grid. Derivatives in the differential equations are directly approximated with finite difference equations. This method is able to simulate large deformation problems by updating the coordinates of the grid.

An explicit finite difference formulation is used in the software for advanced geotechnical analysis FLAC (Fast Lagrangian Analysis of Continua) (Itasca Consulting Group, Inc.).

Qiao *et al.* (2008) compared data of shaking-table tests on ground slope and pipe buried models with numerical results by describing the soil behaviour with the Mohr-Coulomb constitutive model. The evolution of excess pore water pressure ratios and soil/pipe displacements are analysed in order to investigate ground deformations and pipe deflection due to the mechanism of liquefaction underneath the slope.

Andrianopoulos *et al.* (2011) reported the comparison between data of centrifuge test conducted on Nevada sand and numerical results obtained by using the NTUA-SAND model. The authors studied the dynamic response of: (a) a liquefiable horizontal sand layer; (b) the same sand layer improved with vertical drains; (b) a laterally spreading mildly sloping sand layer; (c) a shallow foundation lying on a liquefiable sand layer. The rates of excess pore pressure build-up and dissipation are quite well simulated, with some exceptions. The model predicts, during the first two loading cycles, a larger rate of build-up than the experimental data, in cases (a) and (c). In case (b) numerical results underestimate the excess pore water pressure ratio ($r_u = \Delta u/\sigma_{v0}$) at large depths. In this case, as observed by authors, the improvement with vertical drains only delays the initial liquefaction appearance and enables faster dissipation of excess pore pressures after the end of shaking.

In the paper presented at the GeoCongress in 2012, Giannakou *et al.* (2012) presented the calibration procedure of UBCSAND by focusing on liquefaction triggering and post-liquefaction deformations. The model is validated by simulating a centrifuge test of an earth embankment on liquefiable foundation. The calibrated constitutive model was used to evaluate liquefaction-induced slope movement by modelling the assessment of an existing immersed tunnel, the Offshore Transbay Tube (TBT) of the Bay Area Rapid Transit in San Francisco Bay Area (California).

In the same study, the authors investigated the slope movement occurred at the foundation of a suspension bridge crossing of Izmit Bay, (Turkey). In order to model the behaviour of the liquefiable sand layer of the bridge foundation, coupled dynamic-groundwater flow analyses were performed.

In Barrero and Taiebat (2015) a tailings dam numerical analysis is reported, accounting for the mechanical response of solid and hydro-mechanical response of pore fluid. SANISAND constitutive model is used to describe the behaviour of the potentially liquefiable sand layer; the remaining layers of dam soil foundation are modelled with the Mohr-Coulomb model.

In the 1st International Conference on the Material Point Method, organized by the Anura3D MPM Research Community, Antoinet *et al.* (2017) reported the numerical modelling of an earth dam in Guadeloupe under earthquake solicitations by using FLAC software. The dynamic input was applied at the base of the dam model as a stress history. Pore pressure before and after the earthquake and horizontal displacements of the dam were recorded. The authors recognize the difficulty to carry on dynamic computations due to the huge number of parameters that are involved.

More recently, Tasiopoulou *et al.* (2019) simulated with Ta-Ger model the liquefaction-induced settlements of shallow foundations in centrifuge experiments (Tasiopoulou *et al.*, 2019) using FLAC code (Itasca, 2012, 2016). With the same software, Tasiopoulou *et al.* (2021) analysed with Ta-Ger the lateral response of bucket foundations subjected to wave loading by reformulating the model to reproduce the cyclic response of sand for undrained, fully drained and partially drained conditions.

2.3.1.2 Finite Element Method (FEM)

The Finite Element Method (FEM) is the most used technique in geotechnics for finding approximate solutions to boundary value problems. It allows determining the stress and strain state of a continuous body, with infinite degrees of freedom, by discretizing it in a set of finite dimension elements, interconnected in points called nodes. In this way, the space is divided by a lagrangian mesh type and at each time step, variables and displacement are calculated in the nodes. Once calculated variables and displacement, the mesh remains deformed and the next time step can start.

If compared with the implicit finite difference schemes, the finite element method has the advantage that mesh elements can be chosen with more flexibility and it allows to represent complex geometries. However, in large deformation FEM can have problems due to excessive grid deformation and distortion.

The software PLAXIS, created by the research team led by prof. P.A. Vermeer from Delft University of Technology (TU Delft), is based on the finite element method.

Galavi *et al.* (2013) presented a numerical simulation of the caisson type quay wall liquefaction failure occurred in the region of Kobe (Japan) after the Hyogoken-Nambu earthquake in 1995. The behaviour of the soil is modelled by using UBC3D-PLM which is an extension of the UBCSAND model. Numerical results in terms of horizontal and vertical displacements, for a point selected at the upper sea-side corner of the wall, and evolution of the excess pore water pressures are compared with field measurements. The results are quite satisfactory but the authors recognize the need to improve the implementation of proper boundary conditions. In particular, free field boundaries are very sensitive to liquefaction and get liquefied very soon, leading to some difficulties in numerical convergence.

Even the software OPENSEES (Open System for Earthquake Engineering Simulation) is based on the finite element method. It was created at the NSF-sponsored Pacific Earthquake Engineering (PEER) Centre, for simulating the response of structural and geotechnical systems subjected to earthquakes.

Elgamal *et al.* (2008) simulated the Humboldt Bay bridge-foundation ground model to study the influence of the soil-structure interaction on the seismic response of a bridge structure. The soil behaviour is modelled by using the Multi-yield Surface Plasticity constitutive model. Numerical results in terms of acceleration time history of ground surface and displacement time histories at bridge pier tops and bases are reported.

Wobbes *et al.* (2016) presented a numerical simulation of soil column liquefaction in order to model the state transition from saturated soil to liquid sand-water mixture and the post-liquefaction phenomenon. The simulation is conducted with the velocity-based two-phase finite element method and the saturated soil behaviour is described by the UBC3D-PLM model. In this study, the dynamic boundary condition at the bottom of the column is applied as an inertial force according to d'Alembert principle.

Recently, a FEM analysis has been performed by Kato and Nagao (2020) to simulate shaking table test that aimed to evaluate the effectiveness of soil desaturation procedure on liquefaction mitigation.

2.3.1.3 The Arbitrary Lagrangian-Eulerian Method (ALE)

In order to prevent the inaccuracy generated by large mesh distortion typical of mesh-based methods, the Arbitrary Lagrangian-Eulerian Method (ALE) has been developed by Donea *et al.* (1977, 2004). In ALE formulation the nodes of the computational mesh can be moved with the continuum (lagrangian approach) or be kept fixed (eulerian approach) with an increase of the computational time.

The method has been recently applied by Liu *et al.* (2021) to carry out liquefaction analyses on saturated sand subjected to seismic excitation. Common geotechnical problems caused by liquefaction such as embankment settlement, caisson wharf inclination and slope lateral spreading has been simulate to test the capabilities of this approach.

2.3.2 Particle-based methods

The coupled solid-fluid response of saturated granular soils is commonly modelled using continuum formulations; the alternative to continuum methods is to use particle-based techniques such as the Smoothed Particle Hydrodynamics (SPH) (Gingold and

Monaghan, 1977; Lucy, 1977) Discrete Element Method (DEM) (Cundall and Strack, 1979), the Particle Finite Element Method (PFEM) (Aubry *et al.*, 2005) and the Material Point Method (Sulsky *et al.*, 1994, 1995).

This section provides a short overview of the most popular particle-based methods which have also been applied in geomechanics. These methods are based on the generation of free particles, without any relationships, that move attached with the domain and store all the physical properties of the material. Within this framework, continuum and also discrete domains, such as granular materials, can be modelled (Fig. 2.10).

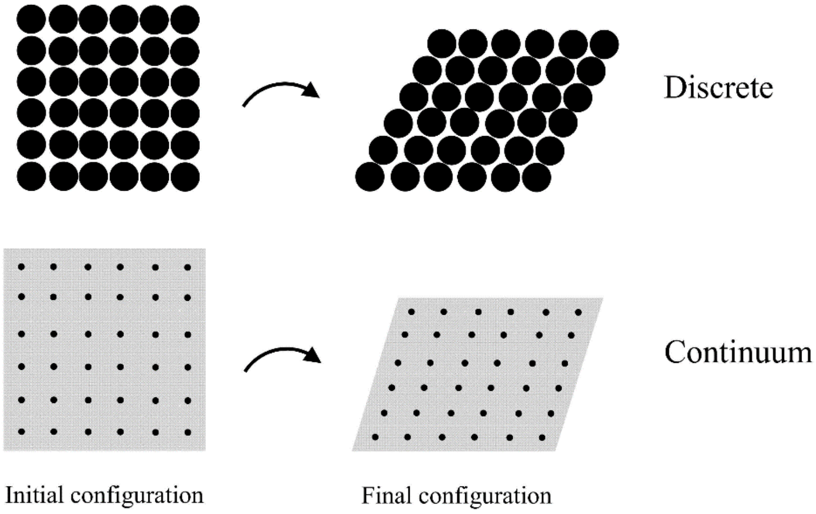

Figure 2.10. Spatial discretisation scheme of particle-based methods, representing discrete or continuum media (Yerro, 2015).

Their main advantage is the possibility to deal with large deformations overcoming the drawbacks associated with mesh distortion encountered in mesh-based methods. The complexity and computational cost are highly dependent on the specific method; in general, they are higher than FEM and FDM.

2.3.2.1 Smoothed Particle Hydrodynamics (SPH)

The Smoothed Particle Hydrodynamics (SPH) method is the oldest particle-based method. It was first developed by Lucy (1977) and Gingold and Monaghan (1977) and it is widely used for modelling in fluid dynamics. The considered domain is divided into a set of particles that move attached to the material and contain the information corresponding to the portion of material surrounding it. Each particle has a spatial distance over which the properties are smoothed by a kernel function.

The method has been applied in several works to simulate large deformation problems (Bui and Nguyen, 2021) including liquefaction phenomenon.

Huang *et al.* (2011) analysed with SPH the flow processes of liquefied soils modelled as viscous fluids, then (Huang *et al.,* 2013) the interactions between pore water and the soil skeleton has been introduced and applied to a real flowing case of liquefied soils.

In Hiraoka *et al.* (2013) the method has been applied to simulate the response of a slope subjected to an earthquake loading. An elasto-plastic constitutive model with Drucker-Prager yield criterion is used to model soil behaviour. Experimental tests on a small-scale slope model were also conducted to verify numerical results in terms of failure surface, horizontal and vertical displacement of the sliding mass.

The role played by static liquefaction for the evolution of a real case of flow-like landslides, occurred in Southern Italy, has been investigated with SPH first by Pastor *et al.* (2009) through a depth-integrated coupled model and then by Cascini *et al.* (2014) that performed a coupled stress-strain analyses with Mohr-Coulomb model extended to unsaturated conditions.

The method has been also used to study the lateral response of pipe in liquefied sand after failure (Wang *et al.*, 2019).

Recently, Mahardim *et al.* (2021) analysed with SPH the interaction between soil and water particles during liquefaction of a soil control volume. Particles movement and arrangement were investigated through a sensitivity analysis on initial viscosity, particles volume, surface tension, shear strain rate and control volume size. However, factors like effective stress reduction and excess pore water pressure development were not quantify.

2.3.2.2 Discrete Element Method (DEM)

In DEM, a soil sample consists of discrete particles, which only interact at particle contacts. During the deformation process, the nonlinear behaviour of soils results from particle sliding, rotation and breakage of inter-particle contacts. Thus, DEM is particularly suitable for modelling granular material behaviour or structures with discontinuous features and can simulate the liquefaction mechanism at the microscopic level. The macroscopic response can be obtained by keeping track of particles microscopic behaviour and by calculating the average coordination number, as the total number of contacts divided by the number of particles. One of the major limitations of the application of DEM to soil mechanics is the number of particles that can be used in the simulation.

In the literature, there are several examples of laboratory tests numerical simulations with DEM, in order to study the development of liquefaction in loose granular materials.

In the paper presented at the 4th International Conference on Recent Advances Geotechnical Earthquake Engineering and Soil Dynamics, Ravichandran *et al.* (2001) investigated the behaviour of saturated granular soil by simulating the hollow cylindrical torsion test with a three-dimensional DEM. They analysed the time histories of pore water pressure and void ratio measured during the packing process and at the base of the sample.

In the next edition of the same conference, Shamy *et al.* (2010) presented the results of shaking table test simulations on a saturated granular deposit subjected to dynamic excitations. They were conducted to investigate the liquefaction-induced lateral spreading process by using a fully coupled fluid-particle model. Numerical results seem to reproduce quite well the mechanisms observed in shaking table experiments such as the liquefaction propagation inside the deposit, the associated large strain localization and the redistribution of the sand void.

In Shi *et al.* (2010), based on undrained cyclic triaxial test data on Fujian sand, a two-dimensional DEM code PFC2D was used to investigate the liquefaction behaviour of an assembly of 4061 discs subjected to undrained cyclic loading. The model could simulate quite well the sand cyclic behaviour such as gradual hysteresis loops decrease with number of cycles; shear modulus degradation and excess pore water pressure build up. Results in terms of average coordination number versus cycles number show that the coordination number progressively decreases after liquefaction onset, which means that the number of contacts between particles reduces. In a macro scale, this leads to effective stresses decrease.

Later on, further authors simulated liquefaction phenomenon with DEM at laboratory scale by performing numerical simulations of monotonic (Gong *et al.*, 2012) and cyclic undrained tests (Manne and Satyam, 2015; Martin *et al.*, 2020) to evaluate static and seismic-induced liquefaction potential of granular soil.

2.3.2.3 Particle Finite Element Method (PFEM)

The PFEM was introduced by Aubry *et al.* (2005) and extended to solve fluid-structure interaction problems by Oñate *et al.* (2011). This method discretises the media by means a cloud of nodes. After recognising the distribution of these points, the boundaries are detected and a computational mesh is constructed by connecting the nodes belonging to the same material domain. The governing equations are solved at the nodes of the computational grid and the nodes transport their momentum together with all their physical properties, thus behaving as particles. At the end of each time step, the mesh is regenerated based on the Delaunay Tessellation algorithm.

Among its many applications (Cremonesi *et al.*, 2020), the method has been used to simulate large deformation and granular flow problems (Zhang *et al.*, 2013, 2015; Zhang *et al.*, 2014; Zhang *et al.*, 2018), landslide-generated impulse waves (Cremonesi *et al.*, 2011; Salazar *et al.*, 2015) and submarine landslides (Zhang *et al.*, 2019).

Liquefied sands behaviour has been, finally, investigated by Della Vecchia *et al.* (2019) through simulation of dam-breaking tests in which the material is modelled as non-Newtonian Bingham fluids.

2.3.2.4 Material Point Method (MPM)

The Material Point method was developed to represent fluid dynamic by Harlow *et al.* (1964) and extended to soil mechanics problems by Sulsky *et al.* (1994, 1995). The method is intermediate between the particles method and finite element method. The continuum media is described by a set of lagrangian materials points that can move with the material and a computational mesh that remains fixed through the calculation and covers the whole domain. Each point represents a portion of the domain and carry all the information of the material like mass, speed, strain and stress. This double discretization can simulate large deformations without the problems associated with the distortion of the mesh elements, moreover, contact between different bodies is automatically solved.

Fig. 2.11 show the MPM discretization scheme and computational cycle: (1-2) all the physical properties of the continuum are transferred from MPs to the mesh nodes where governing equations are solved (lagrangian phase); (3-4) solutions are mapped back from nodes of the deformed mesh to MPs and their positions are updated (convective phase); (5) nodal values are discarded and the computational mesh is reset to the initial configuration.

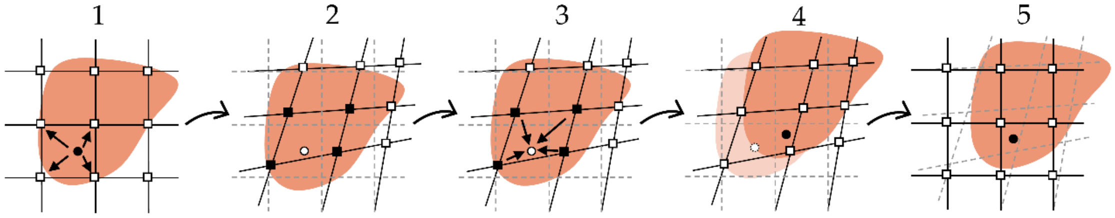

Figure 2.11. MPM discretization scheme and computational cycle.

MPM was selected in the last decades to simulate progressive slope failures (Zabala and Alonso, 2011; Yerro *et al.*, 2016a, b) retrogressive slope failures induced by excavation (Wang *et al.*, 2016), landslide propagation (Ceccato and Simonini, 2016; Calvello *et al.*, 2018; Conte *et al.*, 2019) and granular flows interaction with structures (Mast *et al.*, 2014; Ceccato and Simonini, 2016; Ceccato *et al.*, 2018; Ng *et al.*, 2020; Cuomo *et al.*, 2021). The method was extended for unsaturated soils by Yerro *et al.* (2015) with a "3 phases-1 point" formulation, then Bandara *et al.* (2016), Wang *et al.* (2018) and Ceccato *et al.* (2019, 2021) proposed simplified approaches. Thermal effects in the landslide mobility were introduced by Pinyol *et al.* (2018) and combined with strain rate effects by Alvarado *et al.* (2019). Recent developments included implementation of boundary conditions to simulate hydraulic head, seepage face and infiltration process (Ceccato *et al.*, 2021; Martinelli *et al.*, 2021).

The method was used by Bhandari *et al.* (2016), He *et al.* (2019), Ering and Sivakumar Babu (2020) and more recently by Alsardi and Yerro (2021) and Alsardi *et al.* (2021) to reproduce earthquake-induced slope failures and landslides.

MPM simulations of soil liquefaction are also available in the literature.

The widely investigated Oso Landslide (Keaton *et al.*, 2014; Iverson *et al.*, 2015; Iverson and George, 2016) has been modelled by (Yerro *et al.*, 2019). The static liquefaction of the debris deposits at the toe of the slope, after an abnormal period of wet weather, has been identified as one of the causes of the long runout distance reached. However, liquefaction has been simulated in a simplified way by instantaneously reducing the Mohr-Coulomb strength parameters of the material.

Cuomo *et al.* (2019) simulated a retrogressive slope failure in reduced scale involving static liquefaction. They explored more in detail the phenomenon by using a hypoplastic constitutive model (Von Wolffersdorff, 1996) whose parameters were calibrated through an inverse analysis procedure.

CHAPTER 3 - THE MATERIAL POINT METHOD FOR MULTI-PHASE MATERIALS

In this chapter, an overview of the MPM Anura3D software is presented and the different formulations implemented for multi-phase materials are described. Further numerical aspects are discussed and finally the main implementations, included in the thesis, which contributed to the code numerical development are outlined.

3.1 ANURA3D SOFTWARE

The numerical developments and the MPM simulations presented in this thesis have been carried out within the Anura3D software.

This is an open source code programmed using FORTRAN, developed by the MPM research community (http://www.anura3D.com), constituted by international universities and research centres that collaborate with the common objective to carry on the research on numerical modelling of large deformation and soil-water-structure interaction within MPM.

Anura3D includes different computational methods (MPM-MP, MPM-MIXED, UL-FEM, and FEM) and integration schemes (Explicit, Implicit) with 2D and 3D implementation.

Performing a numerical simulation requires the creation of input data (pre-processing) with GiD software (https://www.gidhome.com/), the calculation with Anura3D compiled executable and the visualization of results (post-processing) with ParaView open source software (https://www.paraview.org/).

Two input files are generated by GiD:

- The GOM file stores information about the geometry of the problem, the material data, initial and boundary conditions, loading conditions, excavation phases, contact properties, number of material points, and computational mesh.
- The CPS file includes the calculation data such as the computational method, calculation time step data, gravity data, load multipliers, damping, output data, etc. CPS file is required for each calculations phase. GiD is used to define the initial CPS file, whilst the subsequent CPS files are generated at the end of each calculation phase.

The calculation process is carried out by copying in the same folder the Anura3D executable with the input files (GOM and CPS) and the .dll library containing the constitutive models. Then, the Anura3D software can be executed from the Windows command line. The output information are stored in a set of files with VTK extension that can be visualized through ParaView.

3.2 MULTI-PHASE MATERIAL FORMULATIONS

Soil is a multi-phase porous material, characterised by a solid skeleton filled with liquids or gases.

The numerical modelling of multi-phase materials with MPM is possible through different approaches as shown in Fig 3.1. Focusing on saturated soils, the interaction between solid and liquid phases can be studied with the 2-phase 1-point formulation that assumes that each MP carries the properties of both phases and the 2-phase 2-point formulation that assigns to each phase a set of MPs that can move and interact with each other. The first formulation is the one used in this thesis.

In saturated soil, depending on the soil permeability and the rate of load, drained, partially drained and undrained conditions can be considered. In numerical analyses dealing with drained conditions and undrained conditions the presence of the water can be considered in a simplified way in which only the solid velocity field is considered and the 1-phase 1-point formulation can be applied.

However, the excess pore pressure generation and dissipation are no longer negligible in partially drained conditions for which the fully-coupled 2-phase formulation is necessary. Finally, partially saturated materials can be modelled with two approaches: the fully coupled 3-phase 1-point formulation (Yerro *et al.*, 2015) in which each MP is representative of the three phases and a simplified formulation (2-phase 1-point with suction effect), recently implemented in Anura3D by Ceccato *et al.* (2021), which is the one used in this thesis.

In the following, are listed and briefly described the different ways to model saturated materials in Anura3D and the unsaturated materials with the simplified approach, distinguishing between 1- and 2-phase 1-point formulations.

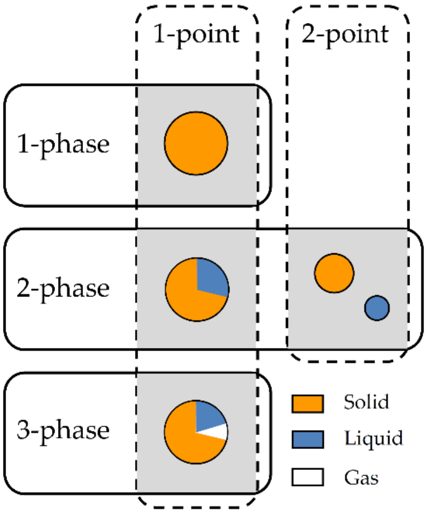

Figure 3.1 - Scheme of the different MPM numerical existing approaches depending on the number of phases and the number of material point sets (modified from Yerro, 2015).

3.2.1 1-phase 1-point MPM formulation

Drained

When drained conditions are hypothesized in the analysis, the development of excess pore water pressures can be neglected because it is assumed that the deformation is slow enough that the excess pore water pressures is rapidly dissipated. The soil can be regarded as dry with a weight equal to the submerged unit weight γ' (Eq. 3.1).

$$\gamma' = \gamma_{sat} - \gamma_w \tag{3.1}$$

$$\gamma_{sat} = \rho_{sat} g \tag{3.2}$$

Where γ_{sat} and γ_w are the saturated and the water unit weight respectively, ρ_{sat} is the saturated density and g is the gravity.

Undrained effective stresses

In undrained conditions, the loading rate is considered so fast or the permeability so low that there is a significant generation of excess pore pressures inducing an effective stress decrease. The relative movement between solid and liquid phase is negligible, thus, pore pressure dissipation can be neglected in the analysis. In this case the equilibrium of the soil-water mixture can be considered rather than the equilibrium of soil and water as separate phases.

One way to model a material in undrained conditions is through the effective stress analysis, which is based on the assumption of strain compatibility between the soil skeleton and the pore water (Veermer, 1993).

If soil grains are assumed incompressible, strain compatibility imply that the change of volume of the soil-water mixture, due to total load, corresponds to the change of volume of the soil skeleton, due to effective stress that is equal to the change of volume of the water-filled pores, due to pore water pressure. For an elastic soil skeleton:

$$\Delta\varepsilon_v = \frac{\Delta p}{K_u} = \frac{\Delta p'}{K'} = \frac{\Delta p_w}{K_w/n} \tag{3.3}$$

Where p and p' are the total and effective mean stresses, p_w is the pore water pressure, n is the porosity, K_u is the undrained bulk modulus and represent the stiffness of the soil mixture in undrained conditions, K_w and K' are the bulk modulus of the water and the solid skeleton respectively. Considering the effective stress principle, Eq. 3.3, leads to:

$$K_u = K' + \frac{K_w}{n} \tag{3.4}$$

The bulk moduli can be written as a function of the Poisson ratio ν and the shear modulus G.

$$K' = \frac{2G(1+\nu')}{3(1-2\nu')} \tag{3.5}$$

$$K_u = \frac{2G(1+\nu_u)}{3(1-2\nu_u)} \tag{3.6}$$

Where ν_u indicates the Poisson's ratio of the mixture in undrained conditions (equal to 0.5 for incompressible pore water), while the shear modulus G is the same for the mixture and the soil skeleton. Inserting Eqs. 3.5 and 3.6 in Eq. 3.4 and solving for the bulk modulus of water, it leads to:

$$\frac{K_w}{n} = \frac{3(\nu_u - \nu')}{(1-2\nu_u)(1+\nu')}K' \tag{3.7}$$

In order to prevent numerical problems due to the assumption of incompressible pore water, the undrained Poisson ratio is set to a slightly lower value of $\nu_u = 0.495$.

The incremental pore water pressure at each calculation step can be obtained by Eq. 3.8.

$$\Delta p_w = \frac{K_w}{n}\Delta\varepsilon_v \tag{3.8}$$

This type of analysis is used in this thesis to simulate the undrained laboratory tests necessary to reproduce liquefaction phenomenon. The typical decreasing curve in effective stress path can be reproduce together with the development of increasing pore water pressures.

Undrained total stresses

Stress state of saturated soils in undrained conditions can be furthermore described in terms of total stresses. This type of analysis does not provide a prediction of pore water pressures and can be applied to describe geotechnical problems in which the soil undrained shear strength c_u (with $\varphi = \varphi_u = 0$) is known or to no-porous materials.

In Ch. 4 the undrained total stress analysis is applied to model strutted-excavation in clay.

3.2.2 2-phase 1-point MPM formulation

Fully coupled

The fully coupled hydro-mechanical formulation is adapt to model saturated soils in partially drained conditions. The interaction between solid and liquid phases can be reproduced, including the dissipation of excess pore water pressure with time allowing transitioning from undrained conditions to drained conditions.

Fully coupled with suction effect

Within the 2-phase 1-point formulation framework has been recently implemented in Anura3D, by Ceccato *et al.* (2021), a simplified approach to model unsaturated soils.

The gas phase is not explicitly included: the mass balance equation of gas is neglected and the gas pressure is assumed to remain constant. This formulation is applied in Ch. 7 to model a real case of liquefaction induced flow-like landslide. It allows to simulate the saturation process during the post-failure stage concurring to the liquefaction development.

3.3 OTHER NUMERICAL ASPECTS

This section briefly describes some numerical features implemented in Anura3D and used in the thesis. More details can be found in Fern *et al.* (2019).

3.3.1 Mixed integration scheme

The simulation presented in this thesis have been performed with the MPM-MIXED integration scheme. It consist on the combination of the classical MPM and the Gauss integration schemes as proposed (Beuth *et al.*, 2007) in order to mitigate the cell-crossing instability. In fact, in the MPM integration the internal forces are computed by summing the values of the MPs belonging to a given element, thus if a MP cross the element boundary, the internal forces suffer an unphysical instability. The Gauss integration, used in FEM, is based on a fixed number of integration points in an optimal location that can move according to the deformation of the element, but never leave the element. Based on it, in the mixed integration scheme a constant stress is considered for each element, σ_{const}. Then, using the Gauss integration, the internal forces can be computed considering a single point in each element with $\sigma = \sigma_{const}$. Notice that the calculation of the internal forces by means of the Gauss integration scheme is only considered for fully filled elements (degree of filling ≥ 90%), otherwise the classical MPM is adopted.

3.3.2 Strain smoothing

MPM can suffers of kinematic locking that consists in the build-up of fictitious stiffness due to the inability of an element to reproduce the correct deformation. This happens when an element wants to deform but cannot because it is constrained by neighbouring elements, making this element nearly incompressible and leading to a large error in the solution. The technique that is implemented in Anura3D to overcome this issue is the Nodal Mixed Discretisation (NMD) technique proposed by (Detournay and Dzik, 2006). This technique consists of modifying the element volumetric strain component through an averaging procedure over the elements sharing its nodes leading to an increase of degrees of freedom per element.

3.3.3 Local damping

For a dynamic analysis, the damping in the numerical simulation should reproduce the energy losses in the natural system when subjected to a dynamic loading. Furthermore, some problems in the geotechnical field involve very slow processes for which the steady state solution is searched. In order to introduce the system energy dissipation and to accelerate convergence in quasi-static problems, an artificial damping should be included in the formulation of the dynamic momentum conservation. In Anura3D, a so-called local non-viscous damping (Cundall, 1987) is implemented. It assumes that the damping force on a node is proportional to the magnitude of the unbalanced force $(\boldsymbol{F_{ext}} - \boldsymbol{F_{int}})$ and acts opposite to the direction of the velocity. The direction of the damping force is taken in such a way that energy is always dissipating (opposite to the velocity).

$$\boldsymbol{M} \cdot \boldsymbol{a} = (\boldsymbol{F}_{ext} - \boldsymbol{F}_{int}) + \boldsymbol{F}_{damp} \tag{3.9}$$

Because the damping force can be understood as a frictional force, it is written as follows:

$$\boldsymbol{F}_{damp} = -sign(\mathbf{v})|\boldsymbol{F}_{ext} - \boldsymbol{F}_{int}|\alpha \tag{3.10}$$

in which $sign(\mathbf{v}) = \frac{\mathbf{v}}{|\mathbf{v}|}$ and α is a dimensionless parameter that ranges between 0 and 1.

3.3.4 Absorbing boundaries

In dynamics calculations, the use of finite boundaries produces wave reflections that do not characterise a naturally unbounded domain and lead to incorrect computed results. Among the different strategies proposed in the literature, the one used in this thesis and implemented in Anura3D is the absorbing boundaries approach. It was originally presented by Lysmer and Kuhlemeyer (1969) and consisted in applying viscous damping forces (dashpots) along boundaries and then implemented with some modification for MPM by Al-Kafaji (2013). The dashpots are replaced by Kelvin-Voigt elements that consider a viscous part (dashpot) and an elastic part (spring), working in parallel (Fig. 3.2).

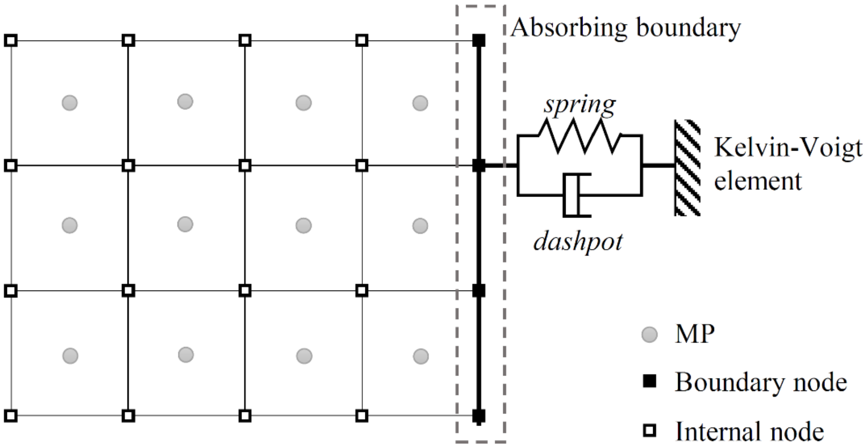

Figure 3.2. Absorbing boundary with Kelvin-Voigt element (Fern *et al.*, 2019).

The normal and the two tangential components of the traction vector corresponding to the absorbing boundary are:

$$\tau_n^{ab} = -a\rho V_p \dot{u}_n - k_p u_n \tag{3.11}$$

$$\tau_{t1}^{ab} = -b\rho V_s \dot{u}_{t1} - k_s u_{t1} \tag{3.12}$$

$$\tau_{t2}^{ab} = -b\rho V_s \dot{u}_{t2} - k_s u_{t2} \tag{3.13}$$

where a and b are dimensionless parameters, $\dot{u}_n$, $\dot{u}_{t1}$ and $\dot{u}_{t2}$ the velocities, u_n, u_{t1} and u_{t1} the displacements, ρ is the density, V_p and V_s the compression and shear waves velocities, respectively. k_p and k_s represent the stiffness per unit area associated to the elastic component and can be expressed as function of the elastic moduli (E_c and G) and a thickness δ of a virtual layer which extends outside the boundary (Eqs. 3.14 and 3.15).

$$k_p = \frac{E_c}{\delta} \tag{3.14}$$

$$k_s = \frac{G}{\delta} \tag{3.15}$$

The first term in the right side of Eqs. 3.11 to 3.13 represents the traction given by the dashpot, which is proportional to the velocity. The second term represents the traction given by the spring, which is proportional to the displacement.

For the two-phase formulation, a further set of Kelvin-Voigt element is defined. For the liquid phase, the normal traction of the absorbing is given by Eq. 3.16.

$$p_L^{ab} = -a_L \rho_L V_L \dot{u}_{L,n} - k_L u_{L,n} \tag{3.16}$$

where $\dot{u}_{L,n}$and $u_{L,n}$ are the liquid velocity and displacement, respectively. The velocity of the compression wave in the liquid is given by Eq. 3.17.

$$V_L = \sqrt{\frac{K_L}{\rho_L}} \tag{3.17}$$

The stiffness coefficient k_L can be expressed as a function of the bulk modulus of the liquid K_L and the virtual thickness δ_L as in Eq. 3.18.

$$k_L = \frac{K_L}{\delta_L} \tag{3.18}$$

3.3.5 Stress initialization

Initial stresses in soil are influenced by the weight of the material and the history of its formation. In Anura3D, initial stresses may be generated by using quasi-static gravity loading or the K_0 procedure.

In the first case stresses and pore water pressures can be initialized by applying during the first calculation phase the gravity loading until reaching convergence in a quasi-static equilibrium condition. Convergence criteria depend on the chosen tolerated error of the out-of-balance force, the tolerated error of the kinetic energy or the maximum number of time steps.

The initial stress and pore water pressure distribution can be also obtained with the K_0 procedure. It assumes that the vertical effective stress at MP increases linearly with depth and can be computed with Eqs. 3.19 and 3.20.

$$\sigma'_{v,0} = \rho g z - \rho_p g z_w \tag{3.19}$$

$$\sigma'_{h,0} = K_0 \sigma'_{v,0} \tag{3.20}$$

where z is the depth of the considered MP below the soil surface, ρ_w the density of water z_w the depth of the considered MP below the groundwater table, and K_0 the earth pressure coefficient at rest. K_0 procedure does not ensure an equilibrium condition for the stress field, since it does not generate shear stresses. Full equilibrium can be only obtained for horizontal soil surfaces and a horizontal phreatic level.

3.4 NUMERICAL DEVELOPMENTS

The main contribution of this work to Anura3D can be summarized in the numerical developments following described.

3.4.1 Constitutive model for liquefaction

The advanced constitutive model Ta-Ger (Tasiopoulou and Gerolymos 2016a, b), able to reproduce complex aspects of sand behaviour under static and cyclic loading including liquefaction phenomenon, has been implemented. Model description and its numerical implementation is presented in detail in Ch. 6.

3.4.2 Dynamic boundary conditions

With the aim to simulate the dynamic behaviour of soils and validate Ta-Ger model implementation under dynamic loadings, dynamic boundary conditions were needed.

Similarly to Alsardi and Yerro (2021) and Alsardi *et al.* (2021), they consist on apply a prescribed velocity variable with time on nodes or MPs during the convective phase of the computational cycle. When the condition is applied on MPs, velocity of the MPs are overwritten, the momentum balance is recalculated and the nodal velocity is updated according to it. When velocity is applied on nodes, the value at the MPs is recalculated according to the assigned nodal velocities to properly update their position.

The velocity-time function has to be defined in a text file with format shown in Fig. 3.3 The first number coincides with the total number of data rows, in the left column the incremental time are listed while in the right one the velocity values.

This feature has been applied in Ch. 5, for the seismic assessment of a real landslide. Furthermore, results of strain controlled cyclic tests with Ta-Ger model are presented in Ch. 6.

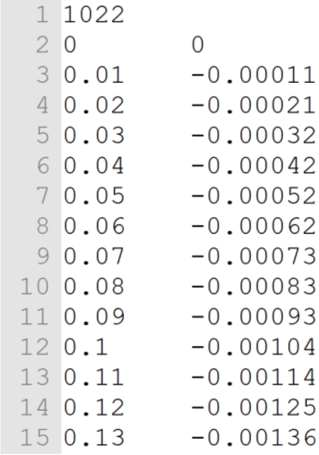

```
1022
0       0
0.01    -0.00011
0.02    -0.00021
0.03    -0.00032
0.04    -0.00042
0.05    -0.00052
0.06    -0.00062
0.07    -0.00073
0.08    -0.00083
0.09    -0.00093
0.1     -0.00104
0.11    -0.00114
0.12    -0.00125
0.13    -0.00136
```

Figure 3.3. Velocity-time history text file format.

3.4.3 Initial hydraulic conditions

One of the latest contributions, carried out in collaboration with Anura3D developers team, allow to assign in the numerical model one or more initial water levels with pressure equal to zero to different materials. The code is able to read the water levels coordinates included in external text files.

The main motivation behind its implementation can be found in the interest of simulating confined aquifers independent from the general groundwater table that affect just specific soil layers. The feature has to be used in combination with K_0 procedure. The water levels are assigned at the very beginning allowing the calculation of the initial distribution of pore water pressures. Based on it, effective stresses can be obtained from total stresses by using the K_0 procedure.

Since K_0 procedure does not ensure that the stress field is in equilibrium, a quasi-static calculation phase should be performed afterwards. However, an advantage of starting from a given distribution of stresses and pore water pressures lies in reaching faster an equilibrium condition for a desired scenario. Applications of this feature on landslide models can be found in Ch. 5 and Ch. 7.

CHAPTER 4 - EXCAVATION-INDUCED SOIL DEFORMATIONS

This chapter aims to show the capabilities of MPM to simulate geotechnical problems dealing with soil excavation. The stability of supported vertical excavation in elasto-plastic material is analysed. Results are compared and discussed with respect to solutions reported in the literature. Furthermore, a well-documented real case of a large landslide reactivated by quarry excavations is simulated. The MPM is able to predict satisfactorily the main aspects of soil behaviour when subject to an excavation process. The results of these simulations contribute to the validation of the excavation feature implemented in the Anura3D software. This chapter is part of the published book "The Material Point Method for Geotechnical Engineering: a Practical Guide (2019)" (See list of publication).

3.1 INTRODUCTION

A proper numerical analysis of geotechnical problems dealing with soil excavation is a useful tool for monitoring and design of civil engineering projects. It allows the prediction of the variation of stress and strain fields induced by excavation and its impact on surrounding environment. A specific feature to simulate soil excavation is implemented in the MPM Anura3D software. In the pre-processing phase, once the geometry and the computational mesh are created, it is possible to define the range of calculation steps in which the material points (MPs) belonging to a certain volume have to be removed. In order to contribute to the validation of this feature, numerical analyses of two excavation problems are carried out. In the first example the bottom heave stability of a supported excavation in clay is analysed. This stability problem has been widely investigated theoretically and numerically by using different approaches. In this chapter a series of undrained total stress analyses with decreasing value of soil strength are performed until failure conditions are reached. The aim is to discuss capabilities and limitations of MPM in simulating this kind of problem and to compare its results with solutions reported in the literature. The second application is a well-documented case of large landslide reactivated by quarry excavation (Alonso, Gens and Lloret, 1993).

3.2 STRUTTED EXCAVATIONS IN CLAY

There are typically three methods to evaluate the stability conditions for strutted excavations: limit equilibrium methods (LEM), limit analysis methods (LAM) and finite-element methods (FEM). Terzaghi (1943) used the conventional limit equilibrium method in order to analyse the stability of the bottom of an excavation, on the basis of bearing capacity theory. The clayey soil was supposed to be homogeneous and isotropic under undrained conditions. The shearing resistance of soil was equal to its undrained strength value c_u Fig. 4.1 shows the failure mechanism assumed. The weight of the clay located on both side of the excavation produce a uniformly distributed load on the horizontal section passing through the bottom.

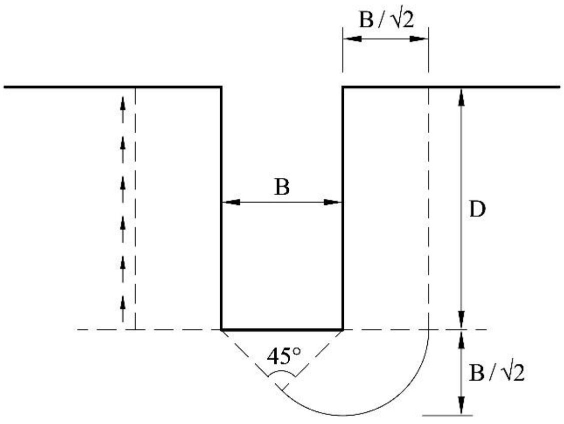

Figure 4.1. Failure mechanism of a 2D excavation in a clayey soil, according to Terzaghi (1943).

When this load exceeds the bearing capacity of the soil located below the bottom of the excavation, the surrounding soil moves downward and induces the heave of the base. According to Terzaghi (1943), the critical depth D_{crit} for an excavation under plain strain conditions is given by:

$$D_{crit} = \frac{5.7c_u}{\gamma_{sat} - \frac{c_u\sqrt{2}}{B}} \tag{4.1}$$

Where γ_{sat} is the saturated unit weight of soil; B is the excavation width; c_u is the undrained shear strength.

Bjerrum and Eide (1956), after field studies, showed that, in case of deep excavations or in presence of non-homogeneous clay, the bottom heave occurs at smaller depths than indicated by Eq. 4.1 without fully mobilizing the shear strength of the upper clay layers. They suggested a more localized failure mechanism that is approximated by the bearing capacity factor N_c for deep foundations, proposed by Skempton (1951). This stability factor depends on the shape and the depth of the foundation and is expressed as:

$$N_c = \frac{\gamma_{sat} D_{crit}}{c_u} \tag{4.2}$$

These solutions are widely used in the initial phases of the excavation design for its relative simplicity but they strongly depend on some assumptions regarding the shape and the location of the failure surface or the values of the bearing capacity factor.

Limit analysis theory provides another method to evaluate this stability problem. It allows the calculation of an upper and lower bound for the bearing capacity factor in order to restrict the range of solutions for the basal stability calculations.

Finite element methods, whose results depends on the constitutive model and the input parameters chosen, are usually used in advanced stages of the excavation design. In this case, the influence of the support system on ground movements is taken into account. Strutted excavation stability can be evaluated by using a strength reduction procedure consisting in reducing gradually the strength parameters of the soil until lack of convergence occurs in non-linear finite element analysis (Brinkgreve and Bakker, 1991; Faheem *et al.*, 2003). Alternatively, the finite element method can be combined with the upper and lower bound limit analyses (Ukritchon *et al.*, 2003).

In order to investigate the strutted excavation stability in clay with MPM, a numerical analysis in undrained total stresses is conducted with Anura3D software. In the following sections, the numerical model will be described and the simulations results will be discussed with respect to the data published in the literature. The support system of the excavation will not be modelled and the main reference for the comparison of results will be the limit equilibrium approaches which remain the fundamental methods for evaluating basal heave stability in braced excavations.

4.2.1 MPM model

4.2.1.1 Model description

The geometry of the problem after the excavation process is given in Fig. 4.2. The values of the dimensions of the model analysed are indicated in Tab. 4.1. This is a plane strain case analysed by a 3D model having a 0.1 m thickness. Plane strain conditions are imposed by means of the boundary conditions restricting the horizontal displacement along the vertical contours. According to the hypothesis assumed by (Terzaghi, 1943), the thickness of the soil below the excavation base is chosen greater than $B/\sqrt{2}$ in order to neglect the effect of an underlying stiff layer.

The defined mesh is generated by using a thin 3D mesh of tetrahedral elements. The thickness of the model is considered to be the same as the element size of the computational mesh. Fig. 4.3 shows the discretized domain and the boundary conditions for the case of $D/B = 2$. At the left and right boundaries the horizontal displacements are prevented, at the top of the model the displacements are constrained in vertical direction, while at the bottom no displacements are allowed. The hypothesis of strutted excavation is ensured by constraining horizontal displacements at the vertical contours of the excavation.

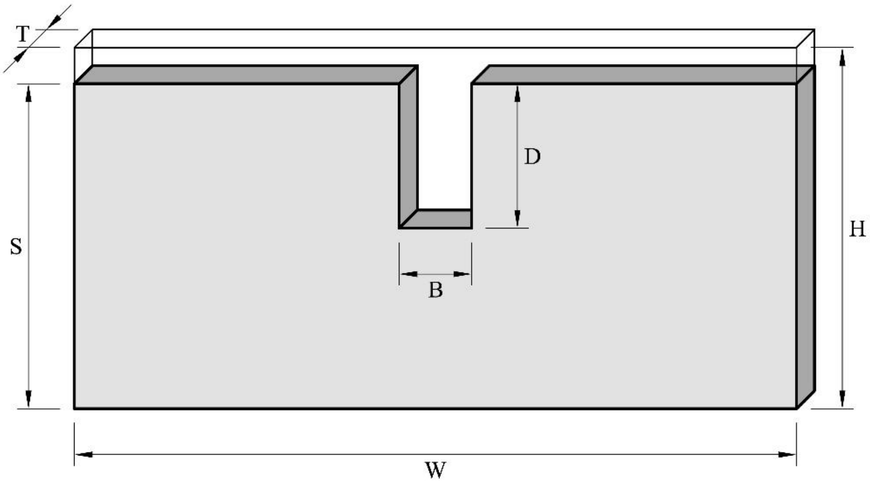

Figure 4.2. Geometry of strutted excavation.

Table 4.1. Dimensions of strutted excavation for different ratios of depth to width.

D/B ratio	Box height H $[m]$	Box width W $[m]$	Soil height $S[m]$	Model thickness T $[m]$	Excavation width B $[m]$	Excavation depth D $[m]$
1	3.5	9	3	0.1	1	1
2	4.5	9	4	0.1	1	2
4	6.5	9	6	0.1	1	4

Soil is assumed to be a purely cohesive material ($\varphi = 0º$), obeying the elasto-plastic Mohr-Coulomb failure criterion. The stability against failure of the excavation base is evaluated by using a shear strength reduction procedure. Several simulations with decreasing value of the undrained shear strength c_u are performed until a sudden increase of upward vertical displacements at the excavation bottom is computed. The 1-phase 1-point MPM formulation is used to perform this set of undrained analyses in total stresses (§3.2.1). The input parameters for the material are summarized in Tab. 4.2. Soil is assumed to be a purely cohesive material ($\varphi = 0º$), obeying the elasto-plastic Mohr-Coulomb failure criterion. The stability against failure of the excavation base is evaluated by using a shear strength reduction procedure. Several simulations with decreasing value of the undrained shear strength c_u are performed until a sudden increase of upward vertical displacements at the excavation bottom is computed. The 1-phase 1-point MPM formulation is used to perform this set of undrained analyses in total stresses (§3.2.1). The input parameters for the material are summarized in Tab. 4.2.

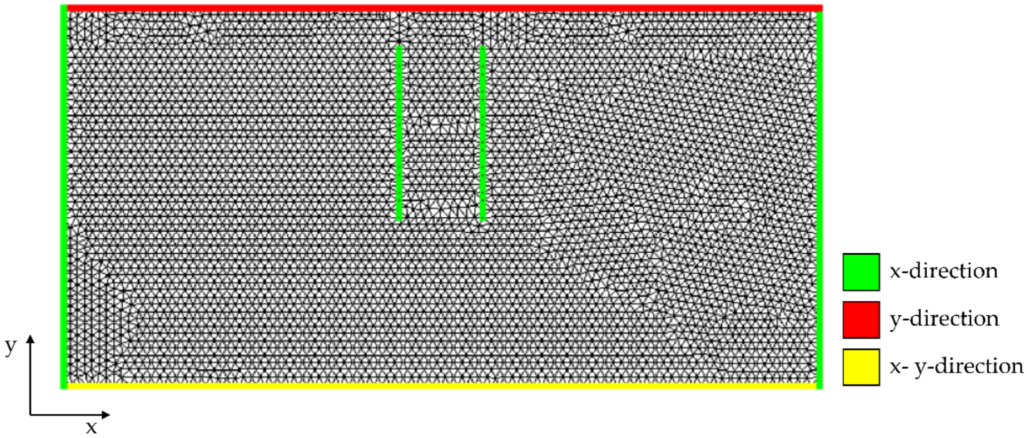

Figure 4.3. Computational mesh and boundary fixities in y and x direction.

Table 4.2. Material properties.

Constitutive model		Mohr-Coulomb
Initial porosity	$\phi\ [-]$	0.2
Density solid	$\rho_s\ [kg/m^3]$	2650
Density liquid	$\rho_l\ [kg/m^3]$	1000
Saturated unit weight	$\gamma_{sat}\ [kPa]$	22.8
Undrained Young modulus	$E_u[kPa]$	10000
Undrained Poisson ratio	$\nu_u[-]$	0.49
Undrained friction angle	$\varphi_u\ [º]$	0

4.2.1.2 Stages of analysis

The simulations are performed in two phases: 1) the initialization of stresses by quasi-static gravity loading; and 2) the excavation process by consecutively removing soil volumes.

Stresses are initialized by applying a gravity loading at the first calculation step. A local damping factor of 0.75 is applied to reach a quasi-static equilibrium state in a faster way allowing a considerable reduction in the computational time.

In the second phase, the excavation process is simulated in more stages by removing the material points belonging to volumes of 1 m height. They are removed immediately at the beginning of each excavation stage and then enough time is left in order to reach the equilibrium. In this case, the full dynamic behaviour of the soil is analysed. Intermediate excavations are performed in five calculation steps of 0.2 seconds while, for the last one, additional calculation steps are performed until the maximum upward vertical displacement at the excavation bottom is reached for a given value of undrained shear strength. Fig. 4.4 shows the calculation stages for the case $D/B = 2$.

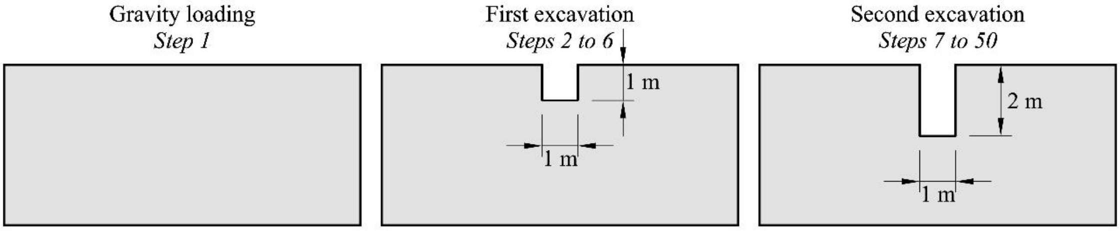

Figure 4.4. Calculation stages for $D/B = 2$.

4.2.2 Numerical results

Fig. 4.5 shows, for the case $D/B = 2$, the final maximum values of soil heaving movement for each simulation in terms of the undrained shear strength c_u. They refer to the material point located at the middle of the excavation. Two different ways to simulate the failure mechanism are considered. In the first case (Case 1), soil is allowed to accumulate into the braced excavation during the failure mechanism development. The second approach (Case 2) respects an implicit hypothesis of classical solutions that consists in continuously removing soil as it rises inside the excavation. For both cases, when using the undrained strength value of 8 kPa, upward vertical displacements are very small and the soil behaviour can be considered still elastic. As the cohesion is reduced, at first, a gradual increase in vertical displacements is expected. Then a lower bound of c_u should be reached when displacements increase considerably. This trend is not observed in the Case 1, in which the material is allowed to accumulate into the excavation, and maximum vertical displacements are significantly lower compared with Case 2. This behaviour can be explained considering that the accumulation of soil leads to a new stable configuration. Geometric conditions change and a sudden increase of soil heaving movement cannot be observed. In this case it is difficult to detect an undrained strength at which failure occurs.

On the contrary, by removing the material points as they rise into the excavation, a more evident lower bound value of undrained cohesion is reached. This result is very close to Terzaghi's solution obtained by Eq. 4.1 for a critical depth of 2 m. Actually, as commented in § 4.2, when $D/B > 1$ the reference solution is the one proposed by (Bjerrum and Eide, 1956), based on the bearing capacity factors calculated by Skempton (1951). Accepting the N_c value for strip foundations and $D/B = 2$ ($N_c = 7$), Eq. 4.2 gives a critical undrained strength of 6.5 kPa, significantly higher than the value obtained by MPM. However, the accumulated deviatoric strains are localized at the excavation base, as expected for deep foundations (Fig. 4.6).

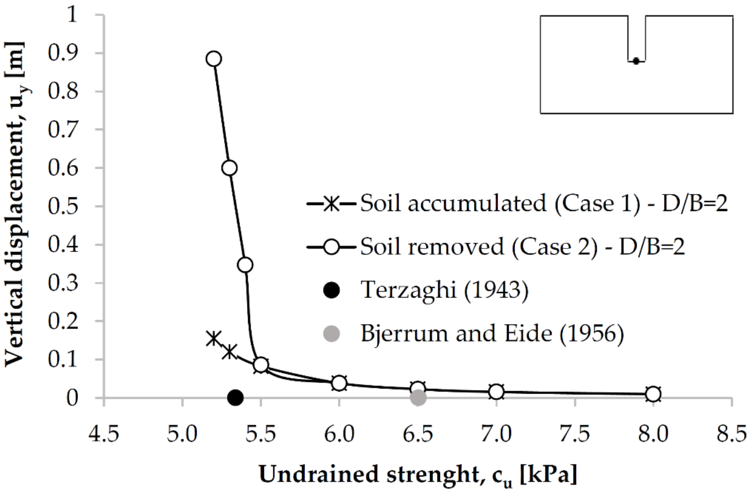

Figure 4.5. Maximum soil heaving movement for different values of undrained cohesion when $D/B = 2$.

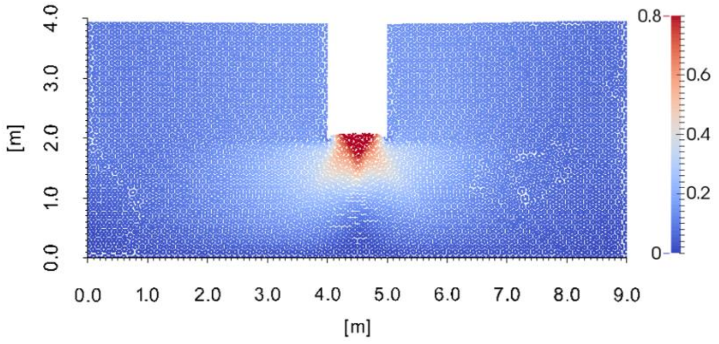

(a)

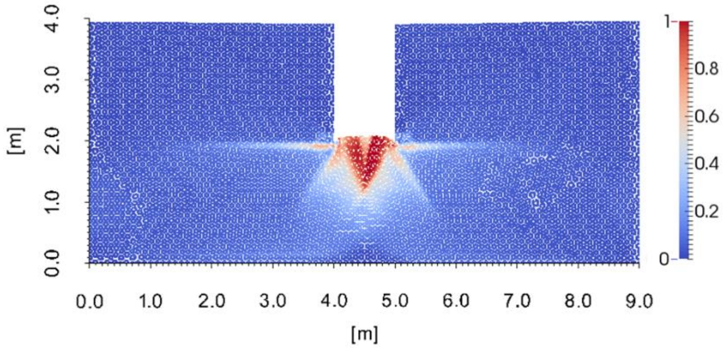

(b)

Figure 4.6. Results after about 10 seconds from last excavation for $c_u = 5.2kPa$ and $D/B = 2$ (Case 2). (a) Total displacements [m]; (b) deviatoric strain [-].

The results for $D/B = 1$ are shown in Fig.4.7. In this case the theoretical solutions by Terzaghi and Skempton are very close and for critical c_u values slightly lower, the displacement computed in MPM increases significantly. Fig. 4.8 shows the failure mechanism.

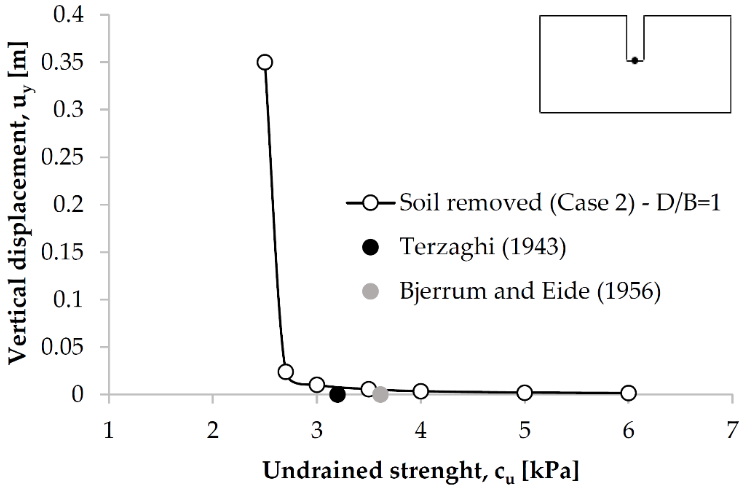

Figure 4.7. Maximum soil heaving movement for different values of undrained cohesion when $D/B = 1$.

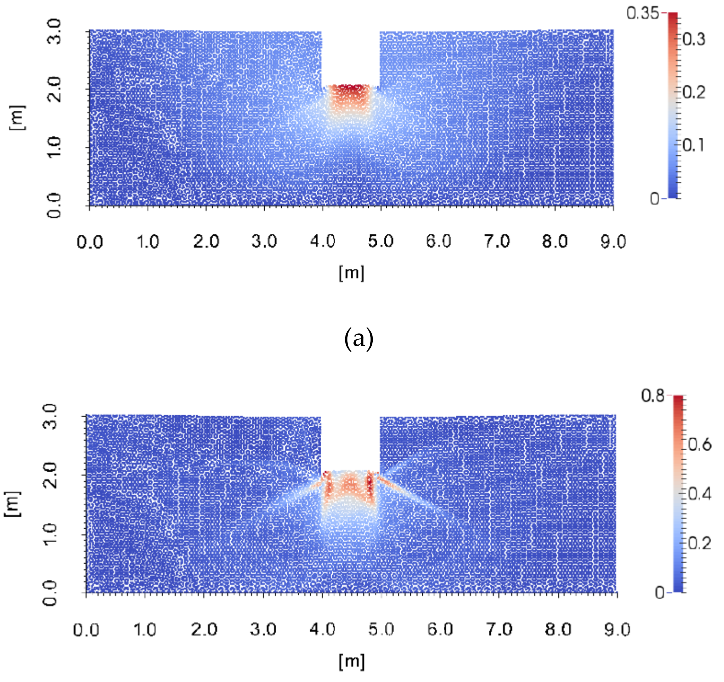

(a)

(b)

Figure 4.8. Results after about 2 seconds from the excavation for $c_u = 2.5kPa$ and $D/B = 1$ (Case 2). (a) Total displacements [m]; (b) deviatoric strain [-].

For a deep excavation ($D/B = 4$), Terzaghi's method provides unreliable results. The sudden increase of displacements is observed, when using Anura3D, for values of strength slightly lower than the critical undrained strength calculated with Eq. 4.2 (Fig. 4.9). According to Bjerrum and Eide observations in the case of deep excavation, the accumulated deviatoric strains are localized at the excavation base (Fig. 4.10).

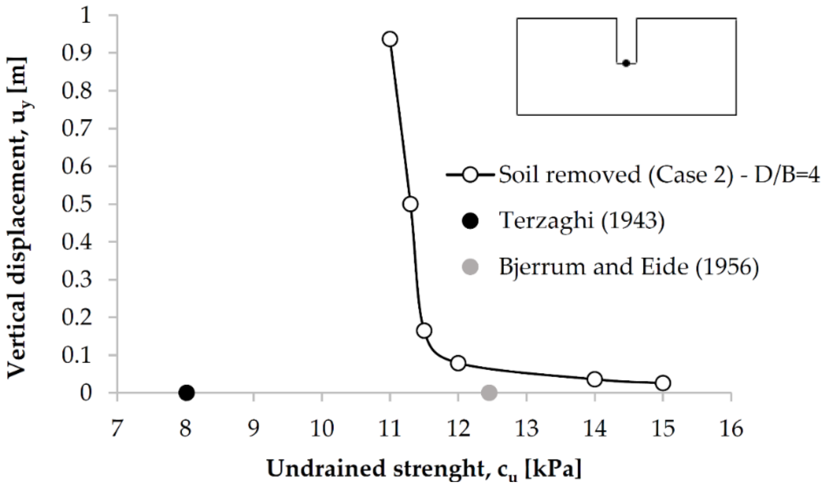

Figure 4.9. Maximum soil heaving movement for different values of undrained cohesion when $D/B = 4$.

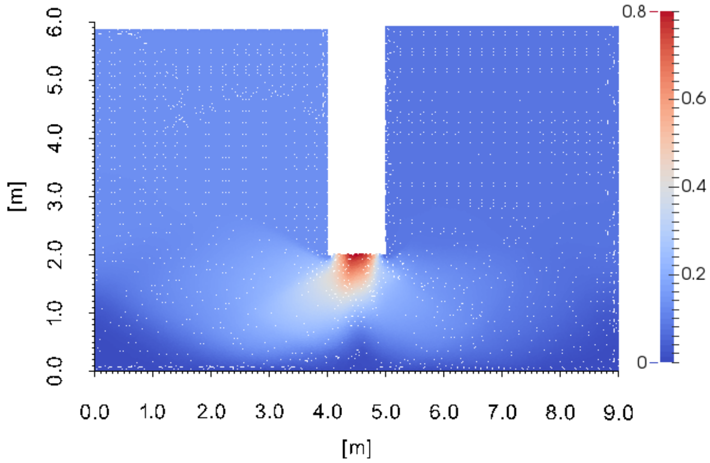

(a)

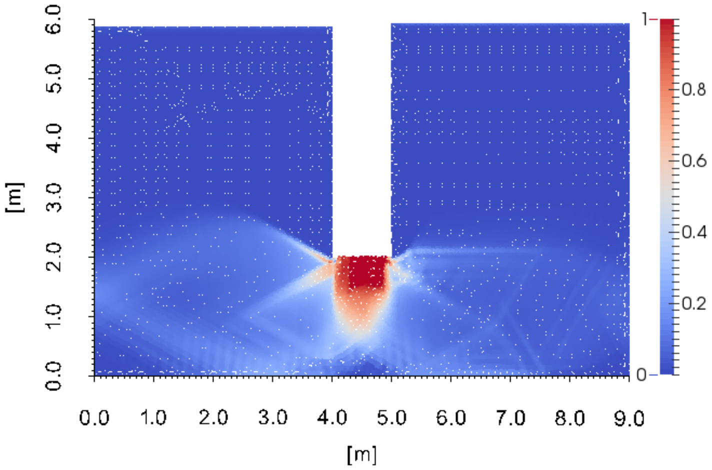

(b)

Figure 4.10. Results after about 15 seconds from last excavation for $c_u = 11kPa$ and $D/B = 4$ (Case 2). (a) Total displacements [m]; (b) deviatoric strain [-].

4.3 THE LANDSLIDE OF CORTES DE PALLAS

4.3.1 Geological context and case description

A large reactivated landslide was identified in 1985 in the East of Spain (Valencia) affecting the left bank of a river upstream of the Cortes arch-gravity dam. The case is described in Alonso *et al.* (1993). The bank, constituted by massive layer and a thin marl level, was part of a large isocline into which the river canyon is cut. The instability was observed in some silos and retaining walls founded on the upper part of the slope used in the construction of the dam.

The works carried out to identify and characterize the landslide included boreholes, inclinometers, and topographic measurements. The geological works described noted the existence of an ancient landslide affecting the upper limestone layers, which were severely broken at the surface. The failure surface was located in a 2 m thick "marl" stratum dominated by illite and dolomite crystal. No indication of water levels was found in any of the borings. The topographic marks, installed after the identification of the failure, indicated a large area moving downwards in a direction approximately parallel to the average dip direction of the strata. The inclinometers readings (Fig. 4.11) indicated clearly that the mobilized mass was sliding on the thin marl stratum. The total volume of the landslide was estimated as $5 \cdot 10^6$ m^3.

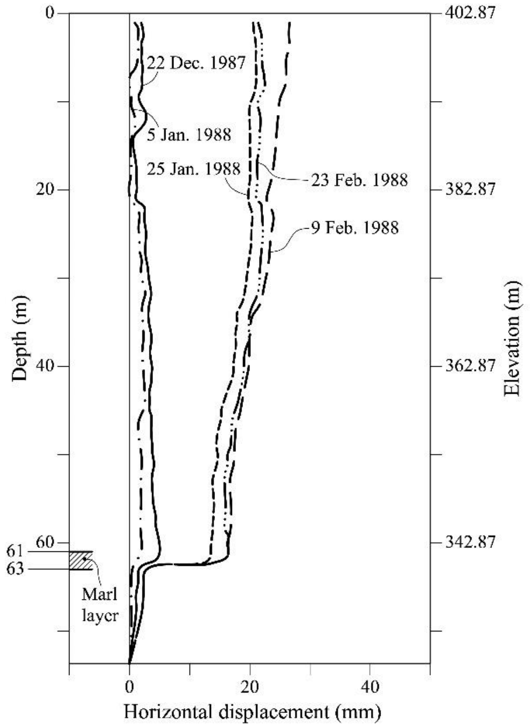

Figure 4.11. Inclinometer measurements in Cortes landslides (Alonso, Gens and Lloret, 1993).

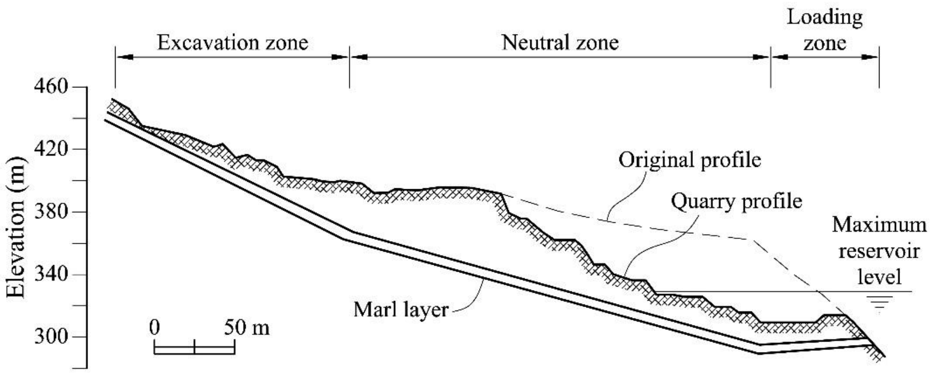

Figure 4.12. Representative cross-section of Cortes landslide (Alonso, Gens and Lloret, 1993).

Fig. 4.12 shows a representative cross-section of the slide. A quarry, which provided the granular aggregate for the concrete used in the dam construction, was excavated in the lower part of the old landslide at the position indicated in Fig. 4.13. This excavation of the toe was identified as the reason for the reactivation of the ancient landslide.

Laboratory shear tests were carried out on samples from the marl layer, as well as from block samples taken in places where the marl layer outcropped. The marl material was characterized as a low plasticity clay ($w_L = 20\% - 28\%$, $w_P = 13\% - 14\%$) with high consistency ($w = 10\% - 13.6\%$) and low porosity ($\phi = 0.25$). A peak and residual frictional angles of 23° and 22° were obtained from direct shear tests. Similar values ranging between 20° and 21° were obtained in consolidated undrained triaxial test with pore water pressure measurements under relatively large effective confining stress (0.2, 0.45 and 0.7 MPa).

Since it was a reactivation of an ancient landslide, it was considered appropriate to assume that the residual strength of the marl layer was mobilized in this case. It turn out that the value of the marl residual frictional angle reported in the experimental program (around 21°) was significantly higher than the frictional angle (17.7°) obtained by the back-analysis reported by (Alonso *et al.*, 1993). This discrepancy was explained later on when the stabilization works were carried out and undisturbed samples from the sliding surface were analysed.

To guarantee security conditions during the reservoir operation which will partially submerged the unstable slope, it was decided to stabilize the hillside by reducing the weight of the upper part and to increase the weight of the lower part by filling in part the quarry excavation. This excavation uncovered the failure surface and the clayey soil located in the shear band of the landslide could be identified. Mineralogical differences were observed between closely located samples taken from the shear band and in the marl stratum itself. A block sample including the sliding surface was taken and tested in the laboratory in direct shear testing. The actual sliding surface was aligned carefully with the middle plan of the shear box. It was observed that the softening behaviour from a peak value to a residual one observed in the previously tested sample was absent. A moderately nonlinear strength-strain curve was observed. The average frictional angle for the range of stresses considered was 18°. For higher values of normal stress, corresponding to the average normal stress on the sliding surface in the central part of the landslide (around 0.8 MPa), the representative frictional angle was lower (17°). The obtained values in the shear box testing agree very well with the value derived from the back-analysis.

4.3.2 MPM model

4.3.2.1 Model description and material parameters

A one-phase analysis MPM mixed calculation is carried out with Anura3D to simulate the observed failure of Cortes landslide due to the excavation of part of the bank toe. No groundwater is included in the modelling taking into account that, according to (Alonso *et al.*, 1993), no water table above the sliding surface is observed.

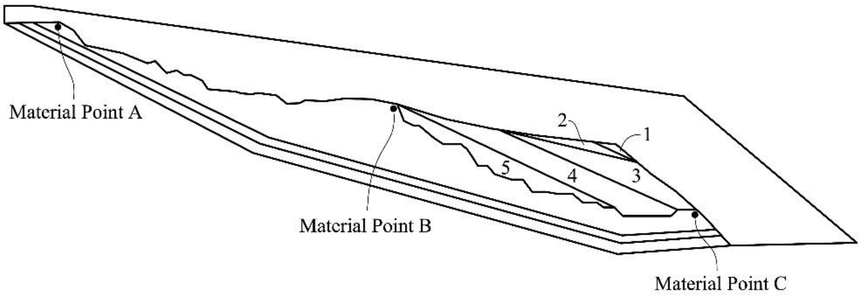

Figure 4.13. Cross section defined for MPM calculation.

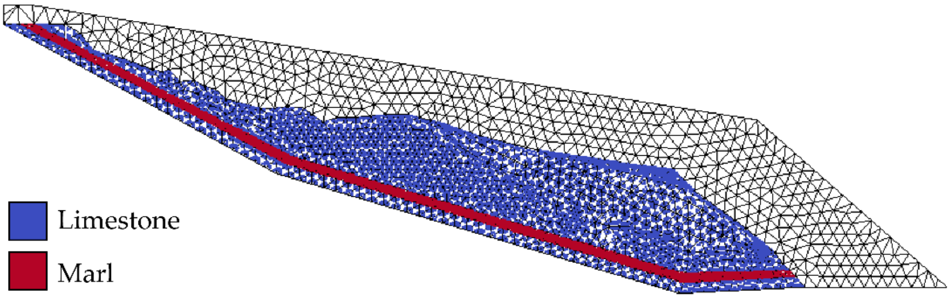

Figure 4.14. Materials and Computational mesh of 8,264 tetrahedral elements and 16,409 nodes.

The representative section presented by (Alonso *et al.*, 1993) (Fig. 4.12) is indicated in Fig. 13a distinguishing two materials (Fig. 4.13b) and different volumes to simulate the excavation process. The materials (marl layer and limestone below and above the marl layer) were characterized by means the Mohr-Coulomb model with the parameters indicated in Tab. 4.3. The limestone was defined by a brittle material by means a strain-softening Mohr-Coulomb model in which the effective cohesion and effective friction angle defining the linear relationship between stress and strength drop from a peak to residual values as a function of the deviatoric plastic strain invariant following an exponential law controlled by a "shape factor" parameter η:

$$c' = c'_r + (c'_p - c'_r)e^{-\eta\varepsilon_d^p} \tag{4.3}$$

$$\varphi' = \varphi'_r + (\varphi'_p - \varphi'_r)e^{-\eta\varepsilon_d^p} \tag{4.4}$$

where:

$$\varepsilon_d^p = \sqrt{\frac{2}{3}e_{ij}^p e_{ij}^p} \tag{4.5}$$

where e_{ij}^p is the deviatoric component of the plastic strain tensor. Peak and residual values are indicated by the subindex p and r, respectively.

Residual strength conditions were assigned to the marl layer where the sliding surface was located. According to the test carried out on block samples taken from the sliding surface described above (§ 4.3.1), the residual friction angle introduced in the calculation was 17.5°. The rest of parameters (stiffness, Poisson's coefficient) and the initial porosity were estimated.

Table 4.3. Model parameters and properties of materials involved in Cortes Landslide modelling.

		Limestone	Marl layer
Constitutive model		Mohr-Coulomb	Mohr-Coulomb
Initial porosity	ϕ $[-]$	0.3	0.3
Young's Modulus (MPa)	E $[MPa]$	1000	200
Poisson's coefficient (-)	ν $[-]$	0.33	0.33
Peak effective cohesion (kPa)	c'_p $[kPa]$	100	-
Residual effective cohesion (kPa)	c'_r $[kPa]$	20	-
Peak effective friction angle (º)	φ'_p [º]	30	-
Residual effective friction angle (º)	φ'_r [º]	35	17.5

As boundary conditions, displacements were restricted in the three directions along the lower boundary surface. The motion in z-direction (Fig. 4.14) was also prevented in x-y plane to simulate two dimensional (2D) plane strain conditions.

The excavation volumes and the time interval for their excavation are indicated as input data. The material points included in the specified volumes are instantaneously removed at the beginning of the step. The excavation process of a given volume actually carried out in the field is significantly different from being an instantaneous unload. In order to simulate the excavation process in a more realistic way, the total volume excavated was divided into five subvolumes that were excavated subsequently. Since no pore water pressure is included and the constitutive model for the involved materials are not time dependent, the duration of the steps is not relevant. However, it is ensured that the slope is at rest prior to any excavation.

4.3.2.2 Stages of analysis

The calculation is divided into 7 stages. In the first stage, the initial stress distribution was calculated by the definition of a quasi-static stage in which the gravity loading is applied gradually and a local damping of 0.75 is applied. The initial stress distribution of the slope was not easy to estimate and there are no measurements available. It was assumed that the stress distribution resulting by imposing the weight of the materials is a good approximation. Afterward, five stages of different loading steps of 0.5 seconds each one were defined to simulate the excavation of the volumes (1 to 5) indicated in Fig. 4.13. For theses stages, the local damping is reduced to a low value of 0.05. Finally, the last stage of seventy five load steps, 0.5 seconds each, is defined to evaluate the response of the slope without applying any change in the model.

4.3.3 Numerical results

The initial distribution of mean effective stresses, caused by the gravity loading prior to any excavation, is shown in Fig. 4.15

Fig. 4.16 shows the accumulated deviatoric strain and accumulated displacement at the end of calculation. The excavation process induces displacements of around 20 cm at the slope surface and the slope reaches a new equilibrium. Fig. 4.17 shows the displacement curve versus the time step calculation for three materials points of the slope (also indicated in the figure). Notice that for each stage of excavation, the accumulated displacement increases abruptly and the motion is interrupted quickly, after a few centimetres when a new equilibrium is reached. The displacement observed is not homogeneous along the slope. Maximum accumulated displacement of 24 cm is computed in the upper part of the landslides, probably favoured by a local failure of the upper part due to the geometry of the slide cross section. The minimum accumulated displacement calculated is located in the more stable part of the toe of the slope due to the shape of the marl layer.

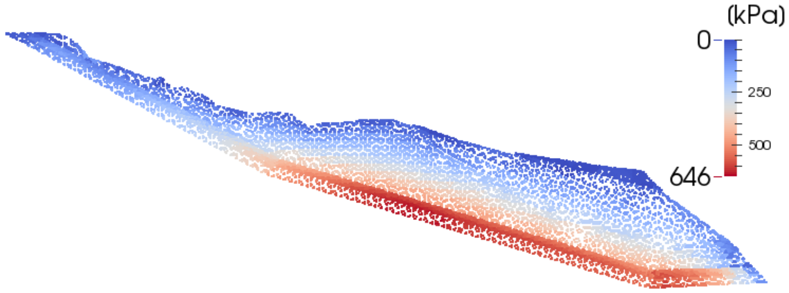

Figure 4.15. Initial distribution of mean effective stresses after gravity loading stage.

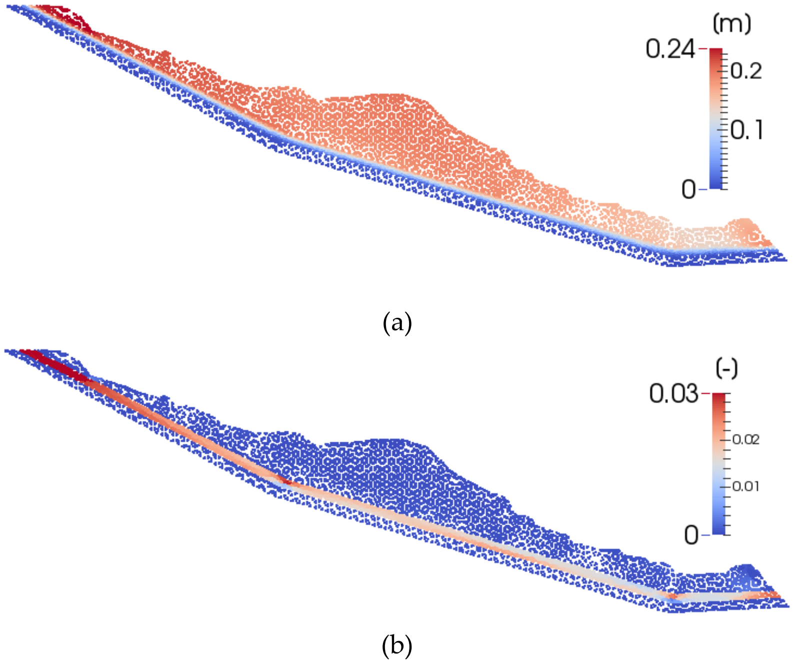

Figure 4.16. (a) Total displacements [m] and (b) accumulated deviatoric strains at the end of calculation, after excavation.

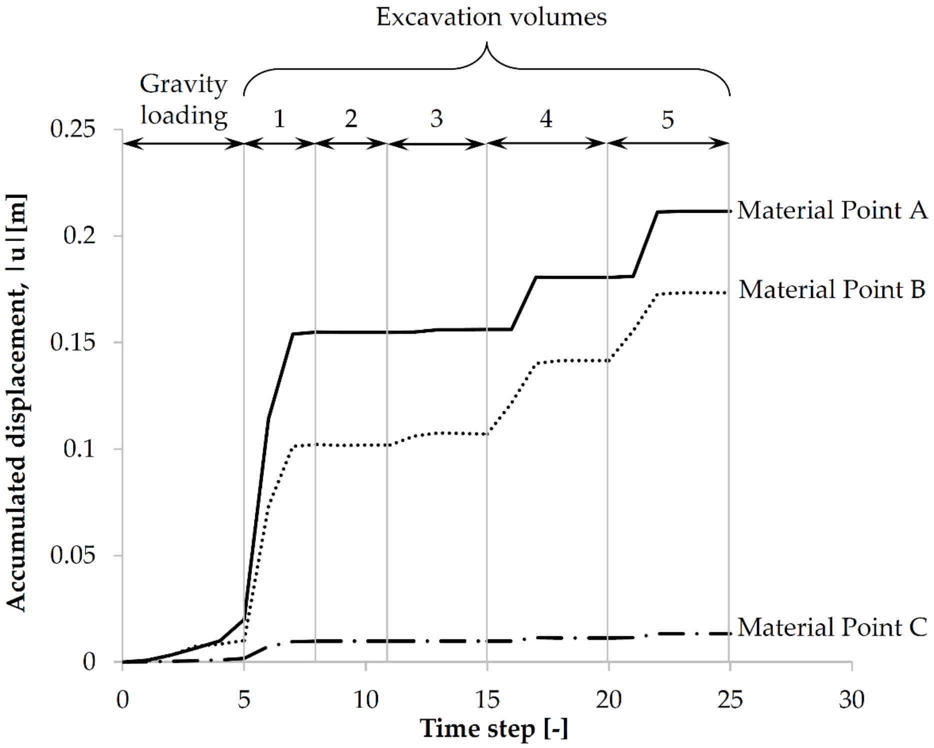

Figure 4.17. Displacement versus time step of the two materials points indicated in the figure.

4.4 DISCUSSION

The capabilities of MPM to model large displacement in a natural way provides a more realistic interpretation of excavation problems. The analysis of deep excavations protected by lateral walls is a good example. Failure is understood as an increasing soils displacement rate. However, the resulting accumulation of soil mass on the excavation bottom has the positive effect of retarding the motion. The realistic interpretation of failure offered by MPM was compared with classical solutions based on simplified assumptions. This cross check of established procedures and a discussion of some discrepancies is also an interesting contribution.

The second example solved refers to a well-documented case history: Cortes Landslide. Again, the concept of failure closely related with the accumulation of landslide displacements provides an insight no available in Limit Analysis. In the case of Cortes, the excavation resulted in significant displacements but it did not result in a catastrophic accelerated motion. This information is outside the formulation of Limit Analysis. The MPM analysis was consistent with field observation: the landslide displaced downward response to the excavation but it reached a new stable configuration at the expense of severe straining of the sliding surface and the rock cover.

CHAPTER 5 – SEISMIC ASSESSMENT OF A COMPLEX LANDSLIDE

In this chapter, a large landslide located in the Spanish Southern Pyrenees during a dam construction project is investigated. It is characterized by two distinct sliding surfaces, which threatens a recently heightened dam located at the landslide toe. The stability analysis of the slope focuses on the discussion of safety factors and their implication not only in terms of static limit equilibrium, but also on creeping velocity. The seismic response of the landslide is also analysed with different methods. Results from Newmark's approach and MPM are compared and discussed with emphasis on the effect of the superimposed slip surfaces on the dynamic landslide response.

5.1 INTRODUCTION

First-time instabilities of river banks and reactivation of ancient landslides are one of the most important concerns in the design and construction of dams and complementary structures, as well as during reservoir operation. Schuster (2006) presented a compilation of case histories of different types of landslides interacting with dams in different countries and Yin *et al.* (2016) described induced landslides in the Three Gorges Project (China). Most of dams and reservoir sites are located in fluvial or glacial valleys. Geological features commonly found in valleys are synclinal structures involving stratified layers parallel or subparallel to the direction of the topographic valley slopes. This situation favours translational landslides kinematically compatible with failure surfaces which follow sedimentation planes or weak layers. A consequence is that river banks in reservoirs are potentially unstable. In fact, excavations and applied loads during dam construction and the subsequent changes in reservoir water level, which partially or totally submerge the banks, favour the activation or reactivation of landslides.

This is the case of Yesa landslide, located in the north of Spain (Navarra region). The deep seated landslide, located in a syncline of a Flysch formation, applies a thrust against the right abutment of the dam(s). Instability problems, manifested since the beginning of the dam construction in 1928 (Gómez, 2018), led to interruptions of construction in the years to follow. In 1959 the construction of a gravity dam, 78 m high, was completed. The slope instability of the right margin became especially relevant when a project of heightening the dam, up to 108 m, was carried out to supply drinking water, land irrigation and flood control (Fig. 5.1).

Figure 5.1. The old and new Yesa dams and the landslide in the background.

The heightening project was resolved by building a new rockfill structure partially supported by the ancient concrete gravity dam. The new dam required additional excavations which triggered a large landslide, called Marmayor (11.9 Mm^3). Comprehensive geological and geomorphological investigation were carried out at various times on Yesa reservoir site (Fig. 5.2).

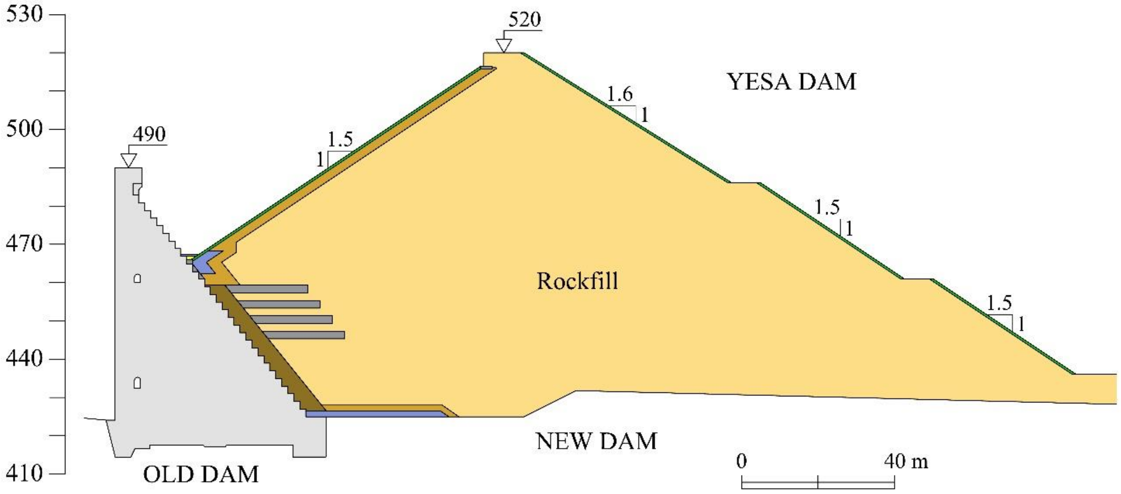

Figure 5.2. Cross section of old and new Yesa dams.

Gutiérrez *et al.* (2010) describe the site and analyse five smaller landslides located around the reservoir. Corominas (2013) carried out a thorough study, focussing on Marmayor landslide, based on previous works, field surveys, interpretation of deep borehole cores, inclinometer and topographic data. They provided a comprehensive geological model of the Marmayor landslide, and identified the geometry of a translational landslide in which shear strains localize in two well-defined superimposed sliding surface(s).

The aim is to provide a further insight into the Marmayor landslide behaviour, to evaluate the stability conditions, and to assess the evolution of landslide motion. The known landslide history is a creeping motion with periods of acceleration that can be related with rainfall periods. First the main characteristics of the landslide are described. The complexity of the material involved in the motion and the uncertainties on hydrogeological conditions introduced difficulties. Strength parameters of the sliding surfaces were first estimated by a back analysis of the active landslide, which required the development of a hydrogeologic model of the valley slope. Understanding the landslide goes beyond analysing limiting conditions, in terms of mobilized strength, because it requires also the prediction of slide motions. Post failure response may involve large displacements in a relatively short time, or else, small accumulated displacement in long periods of time. Being able to model landslide motion and how it will evolve is not an easy task, even if the geometry of the landslide and the materials involved are well characterized. An example in this regard is the case of Canelles landslide (Pinyol *et al.*, 2012).

Current available numerical methods find difficulties to provide reliable predictions of the creeping stage. Due to computational cost, the methods are not able to provide realistic accumulated displacement of few millimetres or centimetres in realistic long periods of time, especially when landslide modelling includes the solving of the governing coupled hydromechanical equations combined with advanced constitutive models. Alvarado *et al.* (2019) describe the alternative of simplifying the problem to a planar landslide, which may be approached analytically.

Different numerical approaches and models are adopted to analyse Yesa landslide and to predict the future response under different actions. In particular, the earthquake action, defined by current regulations will be discussed in some detail.

5.2 CASE DESCRIPTION

5.2.1 Geology and geomorphology of the landslide

The geological structure of the right margin of Yesa dam can be described as a folded flysch formation of Eocene age overlying a marl stratum (Pamplona Marl), equally folded, of low porosity and low permeability. Both strata, Yesa Flysch and Pamplona Marl, describe an anticline at high elevations and a syncline at a lower elevation, near the Aragón River. The axes of these folds have a westward direction and dip 10º in the downstream direction. This configuration, has a relevant effect on the water flow direction in the hill, because the direction of maximum dip of flysch strata are not perpendicular to the river. Fig. 5.3 shows a plan view of the slope and the heightened dam. The profiles indicated in the figure (P8-P11) follow the maximum dip direction of the strata. The section following these profiles are plotted in Fig. 5.4. The flysch stratum is divided in three levels depending on the relative content of sandstone and claystone (Corominas, 2013):

- Lower level (F1), around 30 m thick, is constituted by layers of a few centimetres or decimetres thick of claystone (also called marl in what follows) and sandstone. The sandstone levels exhibit a maximum thickness of 2 m and the thickness of claystone strata vary between 1 and 2 m. The proportion of sandstone with respect to the total thickness of this unit is around 65%.

- Intermediate level (F2), 15-20 m thick, with a predominance of shale strata with intercalation of sandstone's layers, 30 cm thick. The proportion of claystone with respect to sandstone is higher than 80%.

- Upper level (F3), up to 50 m thick, with a predominance of sandstone strata. The proportion of sandstones is variable with depth. It is around 40-60% in the upper part and increases with depth to 70%.

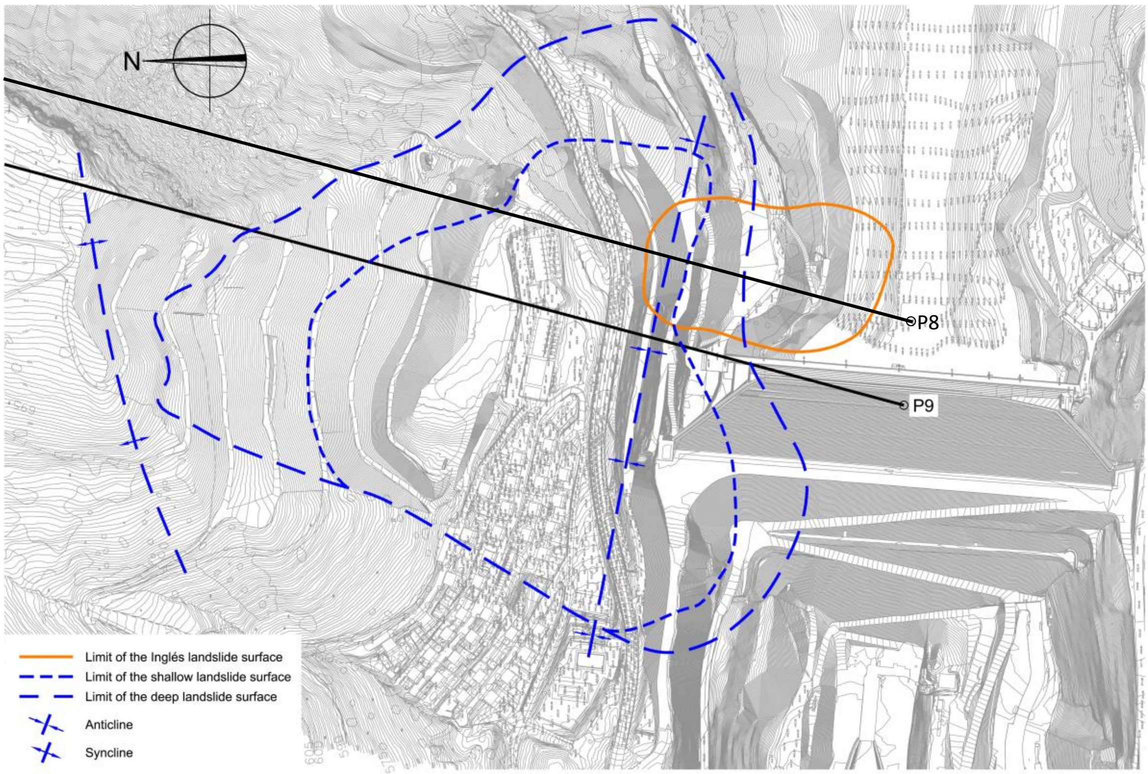

Figure 5.3. Plane view right margin slope of Yesa dam including contours of landslides and profiles.

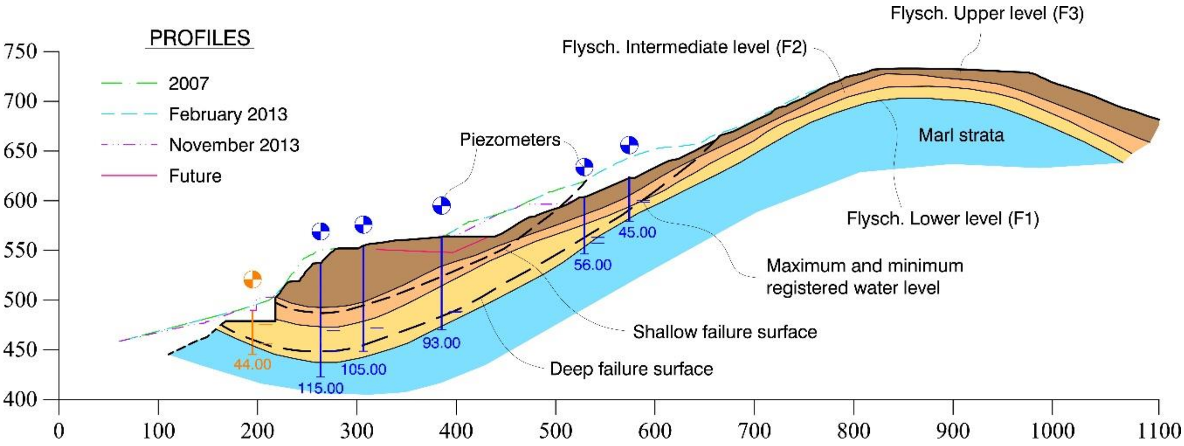

Figure 5.4. Cross-section P9 (see Fig. 5.3) of Marmayor landslide. The geometry corresponds to Scenario 3.

Following the procedure described in Pinyol *et al.* (2018) and Corominas (2013), the sliding inclinometers measurements and a careful interpretation of borehole cores, led to describe Marmayor landslide as two overlapping landslides favoured by the geological structure and limited by two sliding surfaces located in weak layers or contacts between flysch strata. Fig. 5.3 indicates the limits of the identified continuous sliding surfaces and Fig. 5.4 their position in vertical profiles. The shallow sliding surface, where the largest displacements are registered, develops along the contact between the upper (F3) and intermediate (F2) level of flysch. The deeper sliding surface is located at the contact of the lower level of flysch (F1) and the marl strata. Additional signs of motion of this deeper sliding surface were identified by the lifting of concrete blocks, on the right abutment of the old concrete dam.

The so-called "Inglés Landslide" was detected during the construction of the original dam. It affects part of the Marmayor landslide toe.

5.2.2 Mechanical properties

Mechanical properties derive from tests carried out at the time of dam design and construction. The apparent density of clayey layers in Flysch varies between 2.24 and 2.66 g/cm^3 and it is higher in Pamplona marl substratum (2.5-2.7 g/cm^3). Sandstone density ranges from 2.41 g/cm^3 to 2.68 g/cm^3. These values remain almost constant with depth except in the first meters where the rock is weathered. The mineralogy of marls, similar in all of units, is characterized by 20-51% of phyllosilicates, illite being the most dominant clayey mineral. The rest of the minerals are carbonates (31-65%), quartz (2-22%), and gypsum (6-10%). The fine fraction is of low plasticity (CL) and tested samples exhibit a liquid limit, $\boldsymbol{w_L}$ = 30-35%, plastic limit, $\boldsymbol{w_P}$ = 8-19% and plasticity index, IP = 14.5%. According to these properties, a relatively high residual effective friction angle, larger than 15º is expected (Lupini *et al.* , 1981; Mesri and Cepeda-Diaz, 1986).

The sandstone mineralogy is dominated by quartz (55%) and carbonates (45%). Compression tests on rock samples indicate a representative value of unconfined compression strength of Yesa marls of 9 MPa - 15 MPa and 65MPa for the sandstone. The Young's modulus measured in these tests ranges from 6.8 GPa to 8.6 GPa in Yesa Flysch marl samples, it is larger in samples of Pamplona Marl substratum (16.5 GPa) and it reaches 32.2 GPa - 69.9 GPa in sandstones. Poisson's ratio of marls and sandstones are 0.16 and 0.23, respectively.

The residual strength of marls taken from the opposite margin of the river, belonging to the same formation, was evaluated in residual shear tests. They exhibited a high dispersion with an average value of residual friction angle of 16º. Corominas (2013) reported values of friction angles varying between 16º and 18º in drained direct shear tests carried out on samples from the upper sliding surface.

Field geophysical tests indicated that a characteristic value of P-wave velocity of flysch marls is around 2000 m/s. The p-wave velocity measured in Pamplona marls range between 998 and 3060 m/s. In sandstone strata the P-wave velocity increases to about 4000 m/s.

Table 5.1. Material properties.

Lithology	Specific weight γ $[kN/m^3]$	Young's modulus E $[kN/m^2]$	p-wave velocity V_p $[m/s]$	Poisson's coefficient ν $[-]$	Effective cohesion c' $[kN/m^2]$	Effective friction angle φ' [º]
Flysch Sandstone (F3)	26.4 [24.1-26.8]	$3.2\cdot10^7$ $[3.2\text{-}69.9\cdot10^7]$	4000	0.23	2200.0	23
Flysch Marl (F1-F2)	25.4 [22.4-26.6]	$6.8\cdot10^7$ $[6.8\text{-}8.6\cdot10^7]$	2000	0.16	250.0	17 [>15; 16-18]
Pamplona Marl	26.2 [25-27]	$16.5\cdot10^7$	998-3060	0.20	400.0	20
Shallow sliding surface	25.4	$6.8\cdot10^6$	-	0.20	0.1	Calibration
Deep sliding surface	26.2	$6.8\cdot10^6$	-	0.20	0.1	Calibration

According to the available information described above, the parameters selected to characterize the materials involved in the landslide are collected in Tab. 5.1. These parameters are selected for modelling purposes. Brackets indicate the range of values of parameters estimated from available data. The two identified sliding surfaces (shallow and deep sliding surface) are at residual conditions and exhibit weaker stiffness and strength properties than the values given for the Flysch units.

5.2.3 History of Marmayor landslide motion

The excavations carried out during old Yesa dam construction (1928-1959) led to the first signals of instabilities of the right margin and the triggering of Inglés Landslide whose motion, which is controlled by Yesa reservoir level changes, persists nowadays. The Marmayor landslide was first identified in 2011 during excavation works for the foundation of the new and higher rockfill dam. In September/October 2012, the landslide registered displacement rates of 10 mm/month that could be correlated with an intense rainfall period. In January-February of 2013, the landslide, already characterized by the two main continuous sliding surfaces described above, accelerated, coinciding again with an intense rainfall period. Displacement rates of up 40 mm/week were registered. Fig. 5.5 shows the inclinometer measurements located in the upper part of the landslide along Profile 8 (Fig. 5.3).

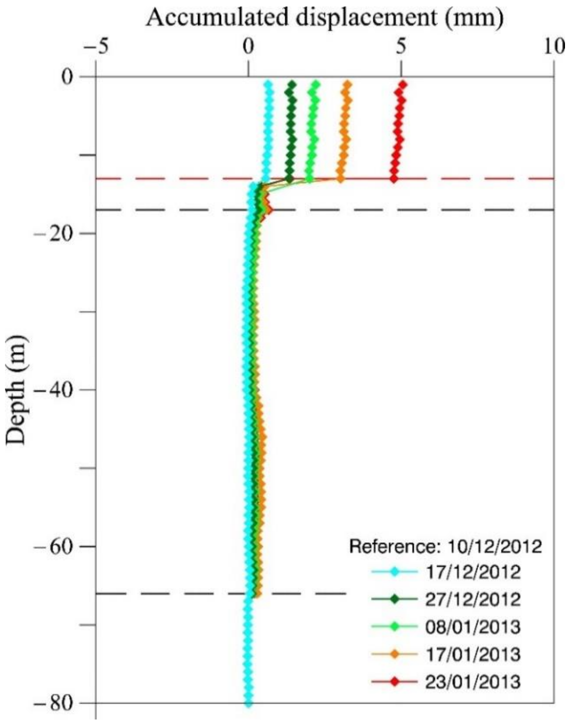

Figure 5.5. Inclinometer measurements located in Profile 8 (see Fig. 5.3) at a distance of 25 m from the crack of the upper sliding surface.

Figure 5.6. Displacement rate (a) and accumulated displacement (b) from topographic landmarks located around Profile 9 and accumulated daily rainfall (c).

5.2.4 Hydrogeology

Several deep open standpipe piezometers were installed in the landslide area (Fig. 5.7). All of them were longer than the depth of the lower sliding surface. Slug and pumping tests were carried out. The individual response observed in the piezometers indicated a complex hydrogeological system driven by geological heterogeneities and the influence of discontinuities. The groundwater regime of the slope is defined by a deep aquifer that mainly reacts to the reservoir levels, the discharge to the river, and the recharge from the hill (Fig. 5.7). Fig. 5.4 includes the range of water level variation during 2014-2018 in some piezometers installed along Profile 9. It was concluded that, near the reservoir, the piezometer head is controlled by the reservoir level and it decreases from the front toe of the slope, partially submerged, towards the inner part of the hill due to the natural discharge drainage path that follows the direction of the axis of the syncline axis, subparallel to the river. The piezometer head increases uphill due to the flow coming from the upper heights of the valley. Piezometers located in the middle and upper elevations respond to rainfall with a certain delay.

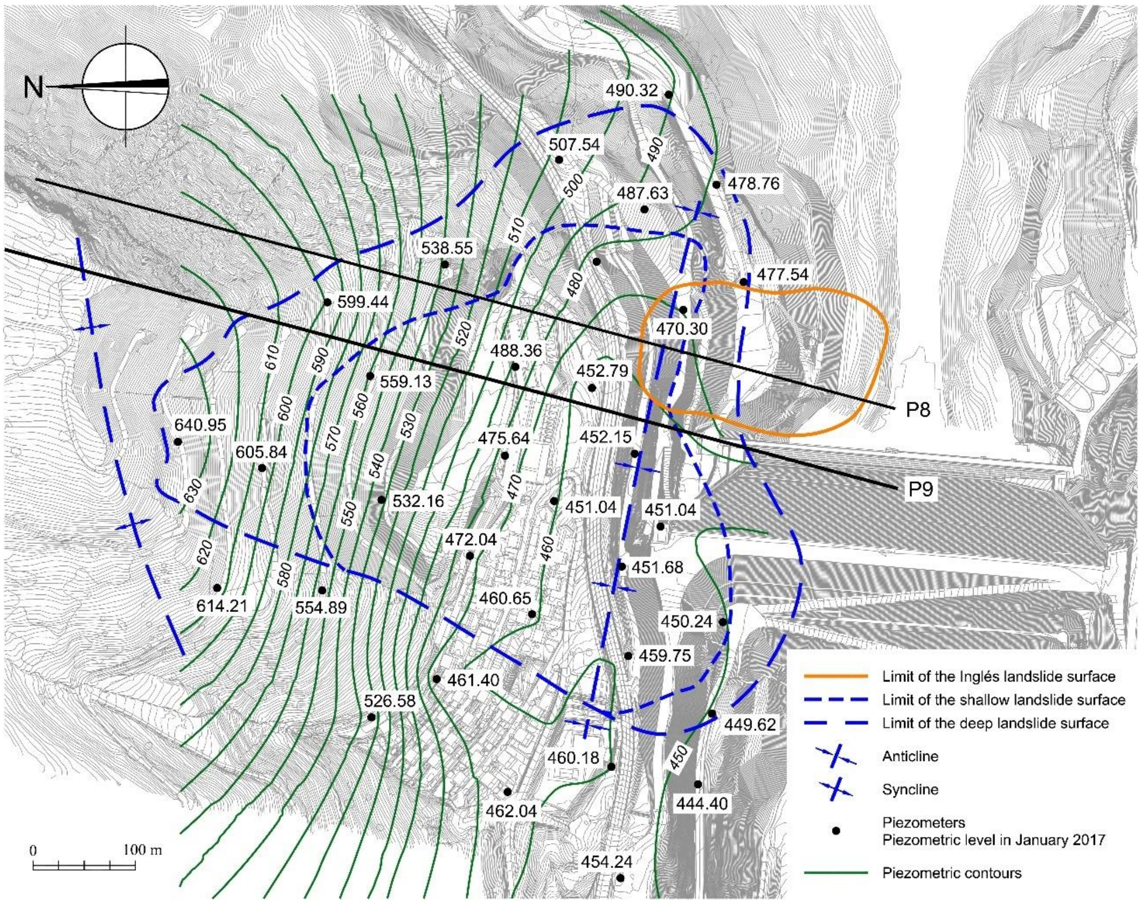

Figure 5.7. Plant map of Marmayor Yesa landslide indicating the hydrogeological model domain limits, position of piezometers and piezometer head measured in January 2017.

There is no precise data to estimate the pore water pressure distribution at shallow depth and in particular along the upper sliding surface. There are no indications of a persistent shallow aquifer. However, the correlation between periods of rainfall and snow thaw and displacement rates observed in the upper landslide, indicates that transient positive pore pressures may build up. Under high infiltrations from rainfalls an ephemeral perched water table, bounded by the contact between the upper level of pervious sandstone-dominated Flysch and the lower clay-rich level, probably develops. To estimate the hydrogeological conditions of the landslide and to provide a consistent and comprehensive hypothesis in terms of pore water pressure distribution for the stability analysis, a depth-averaged 3D hydrogeological numerical analysis was developed. Based on field available data, the model aims at characterizing the anisotropic permeability of the domain, simulating the flow and determining the response of the system to rainfall periods.

The numerical analysis was carried out by means of Modflow, a software developed by the Geological Service of United States, and the graphic interface ModelMuse. Modflow solves the water mass balance and Darcy flow equations assuming rigid porous media (Harbaugh, 2005) by means of finite difference and finite element methods. The model assumes that two overlying hydrogeological units exist at the slope scale in order to provide the estimated perched phreatic level. The contact between the two modelled layers follows the contact between the upper (F3) and intermediate (F2) level of Yesa Flysch.

The model was first calibrated for stationary regime based on the piezometer levels measured in January 2017, when the accumulated precipitation in a month was of 82 mm. Concerning the identification of permeability, because of the layered structure of the Flysch, two horizontal principal directions are adopted: the maximum one ($\boldsymbol{K_x}$) in the direction towards the river (N212N) and the minimum one ($\boldsymbol{K_y}$ in direction N97E); $\boldsymbol{K_x/K_y = 3}$. The low permeability in vertical direction, $\boldsymbol{K_z}$, was taken as $\boldsymbol{K_x/K_y = 1000}$. The domain was also divided in different domains in order to reproduce the measured piezometric head levels.

Once the stationary model was calibrated, transitory scenarios were simulated in order to reproduce the response of the system affected by different intensity of rainfall periods. In particular, the situation from mid-January to mid-February 2013, which coincides with a significant increase of the landslide displacement rate (Fig. 5.6), was analysed. The rainfall registered in that period was 350 mm. No rainfall short event of significant high intensity was registered during that period, but the 30-days accumulated rainfall corresponds to a return period of 50 yr. With the aim of assessing the future landslide response, an extreme rainfall period of 500 yr return period was also modelled. It corresponds to a 446 mm of 30-days accumulated rainfall.

The obtained results in terms of permeability were consistent with the results estimated from slug and pumping tests from wells. The hydrogeological model also provided the pore water distribution inside the hill. The water level of the deep aquifer does not show significant variations due to rainfall and the position of the deep phreatic level is consistent with range of the maximum and minimum values registered (Fig. 5.4). The level varies significantly near to the toe following the reservoir level.

The results of pore water pressure distribution corresponding to the perched water table can be interpreted in terms of $\boldsymbol{r_u}$:

$$r_u = \frac{\gamma_w h_w}{\gamma_s D} \tag{5.1}$$

where $\boldsymbol{\gamma_s}$ and $\boldsymbol{\gamma_w}$ are the unit weight of soil (20 kN/m^3) and water (10 kN/m^3) respectively, $\boldsymbol{h_w}$ is the water column above the sliding surface and $\boldsymbol{D}$ the depth of the sliding surface. For the stationary case, which corresponds to a scenario of average/moderate intensity, the value of $\boldsymbol{r_u}$ is equal to 0.12 and it increases to 0.15 for high intensity rainfall.

Table 5.2. Combinations of intensity rainfall periods and deep phreatic levels.

	Accumulated rainfall per month	Value of r_u for shallow sliding surface	Deep phreatic level
Low intensity	< 80 mm/month	0	Interpolation with lowest measured values
Moderate (average) intensity	≈ 80 mm/month	0.12	Interpolation with mean measured values
High intensity	≈ 350 mm/month	0.15	Interpolation with maximum measured values
Extremely high intensity	≈ 446 mm/month	0.20	Interpolation with maximum measured values

Based on this hydrogeological analysis, correlations between situations for different intensity rainfall periods and pore water pressure distribution, shown in Tab. 5.2, are used in the landslide model. Parameter r_u refers to the shallow sliding surface and defines the position of the perched phreatic level. The deep phreatic level is defined in terms of the pore pressure values measured in piezometers in 2014-2018 period and an average for a reservoir elevation of 490 m.a.s.l., indicated in Fig. 5.4.

5.3 CONCEPTUAL MODEL BASED ON STABILITY ANALYSIS BY FEM

A 2D stability analysis of the Marmayor landslide is carried out by using the FEM software Plaxis 2D (Version 2021, Plaxis bv) in a representative section based on Profile 9. The interaction between landslide toe and dam is out of the scope of this work and the dam blocks is not included in the representative section in order to consider a critical section.

5.3.1 Model description

The geometry is discretized by quadratic triangle elements with an average side length of 20 m. Since the analysis focuses on the landslide stability instead of the stress-strain response, the materials are characterized by a linear elastic perfectly plastic Mohr-Coulomb model. The required parameters, specific weight, Young modulus, Poisson's ratio, effective cohesion (c') and effective frictional angle (φ') of the materials are estimated from the available data (Tab. 5.3). The representative section for stability analysis only distinguishes between two layers for the flysch formation: an upper layer corresponding to flysch unit F3 and a deeper level that includes unit F1 and F2 (Fig. 5.8). The continuous sliding surfaces defined according to the geological and geomorphological analysis of the landslide are included explicitly in the model (Fig. 5.8) with their own properties, different from the rest of the materials involved in the model. They are defined as a preferential sliding surface by means "joint elements" available in Plaxis. The proper values of elastic stiffness of the joint elements are assigned in such a way that the program is numerically stable and elastic deformations are negligible.

Five scenarios are defined to evaluate the model by back-analysis and to assess the future response. The corresponding geometries are described in Tab. 5.3 in accordance with the landslide history and the defined correlations between different intensity rainfall periods and pore water pressure distribution (Tab. 5.2).

The water levels are imposed fixed at each stage and the pressure calculated at each point corresponds to the stationary situation defined by the water levels. The position of the deep phreatic level is defined by considering the range of values measured in piezometers. Water levels affecting only the Upper Flysch Level and the shallow sliding surface are defined to simulate the pore water pressure distribution induced by the different intensity of rainfall periods (Tab. 5.2). In all scenarios, the reservoir level is assumed to be at 490 m.a.s.l, as indicated in Fig. 5.9 that shows the particular case of the water levels assigned for Scenario 1.

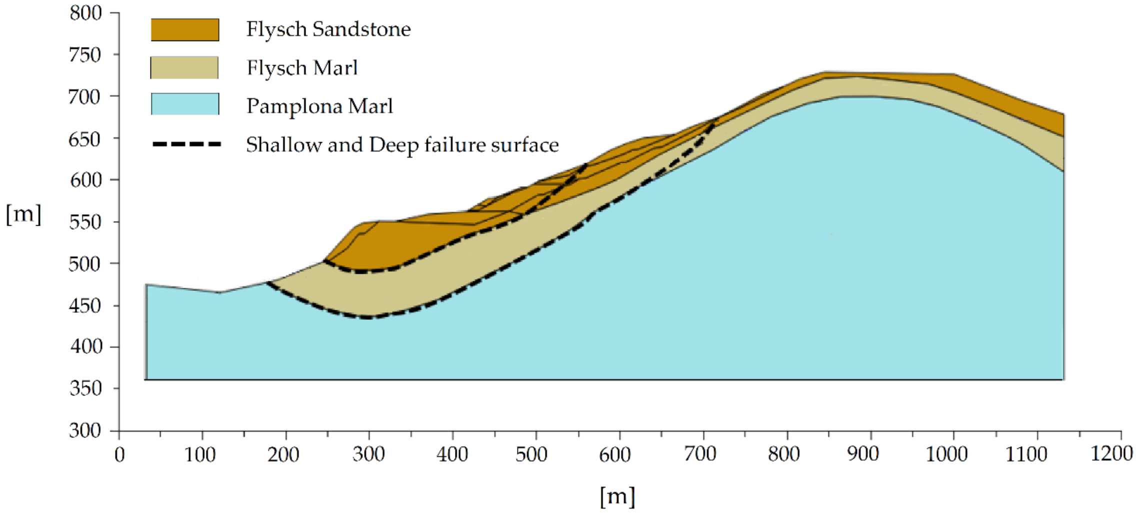

Figure 5.8. Representative section in Plaxis of Scenario 1.

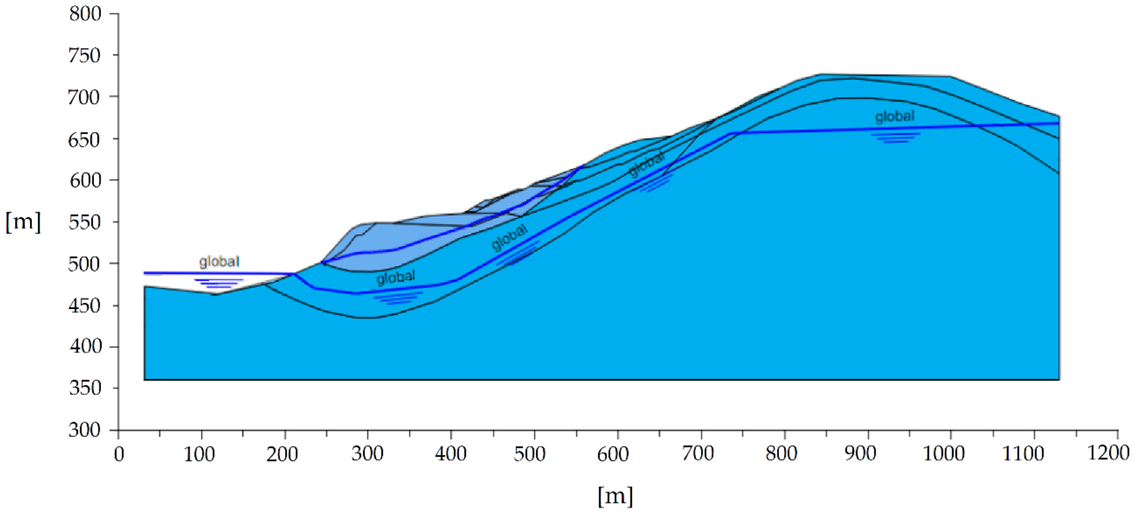

Figure 5.9. Water levels defined in Plaxis for Scenario 1. The deep level corresponds to the maximum values measured in the field during 2014-2018, the upper level is calculated for a value of r_u = 0.15.

5.3.2 Stages of analysis

In the first calculation stage, the initial stress distribution is calculated by applying the gravity loading. Then, the stability analysis is carried out in terms of safety factor (SF) defined as a ratio of the mobilized strength and the available strength at failure:

$$c'_{mob} = c'/SF \tag{5.2}$$

$$\varphi'_{mob} = tan^{-1}(tan\varphi'/SF) \tag{5.3}$$

The "c-phi reduction method" (Griffiths and Lane, 1999) is used to calculate the SF. In this procedure, the position of the critical surfaces is automatically determined and it is not necessary to define their position ad-hoc. However, in Marmayor landslide model, the position of the sliding surfaces is favoured by the definition of the joint elements and no new rupture surfaces are developed.

5.3.3 Numerical results

In a back analysis of landslides, it is common to calibrate the strength parameters knowing the scenario in which the landslide became unstable. In case of Yesa landslide, the definition of the scenario corresponding to a safety factor equal to 1 is not straight forward. Prior to the accelerated motion observed in January-February 2013, signals of instability, induced by an intense period of rainfall, were observed. According to this, the critical scenario (Scenario 1) is defined for the existing geometry from 2007 until 2013 and for water pressure distribution corresponding to an intense rainfall period (Tab. 5.3). Under this assumption, calculations for SF = 1 indicate residual friction angles of 18º and 15º for the deep and shallow sliding surface, respectively. These angles are consistent with the friction measured in direct shear tests on samples of the sliding surface (upper landslide) recovered in boreholes. Fig. 5.10 shows the calculated final displacement, in a coloured scale, at the end of the c-phi reduction calculation. It provides information on the limits of the mobilized mass which define the critical, kinematically admissible mechanism. The precise magnitude of displacements (not indicated in Fig. 5.10 to 5.13) have a numerical bias because of the proximity of instability. The critical failure affects the upper landslide while the lower one has a limited activity.

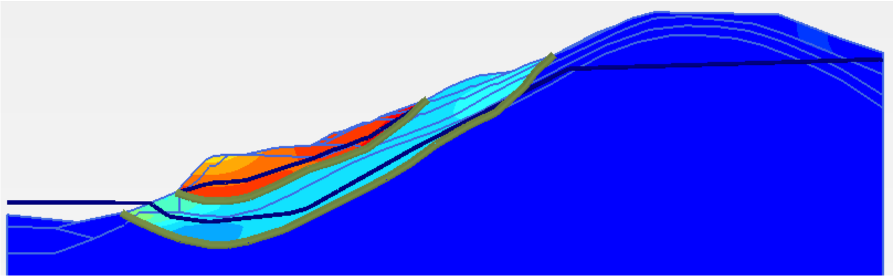

Figure 5.10. Failure surface obtained by c-phi reduction procedure for Scenario 1 and SF = 1.

The next scenario (Scenario 2, Tab. 5.3) corresponds to the acceleration of the landslide after the toe excavation carried out to build a road around the reservoir (geometry for year 2013 in Fig. 5.4) and after an intense rainfall period (Tab. 5.2). Although limit equilibrium is not an appropriate analysis to provide an estimation of landslide velocity, we can expect that higher sliding velocities are associated with lower safety factors (Leroueil, 2001). A safety factor, lower than one, is then calculated for the new geometry after excavation assuming the same pore water distribution defined in Scenario 1. A safety factor lower than one cannot be obtained by means of the c-phi reduction method since the calculations should start from an equilibrium condition. To overcome such limitation and to calculate the SF associated to Scenario 2, the input strength parameters of all the materials involved in the model are increased in the same ratio in order to reach an equilibrium condition ($SF_{Scenario2} > 1$). Therefore, the "real" safety factor (lower than 1) corresponding to Scenario 2 can be calculated from the increment of the strength parameters imposed to reach $SF_{Scenario2} = 1$. In particular, in the calculation carried out, the safety factor equal to one for Scenario 2 is obtained for an increment ratio of strength parameters of 20% (Fig. 5.11). Therefore, the estimated safety factor of Scenario 2 is equal to 0.82. In case of instability, the upper landslide is the critical one while the lower one remains non-active.

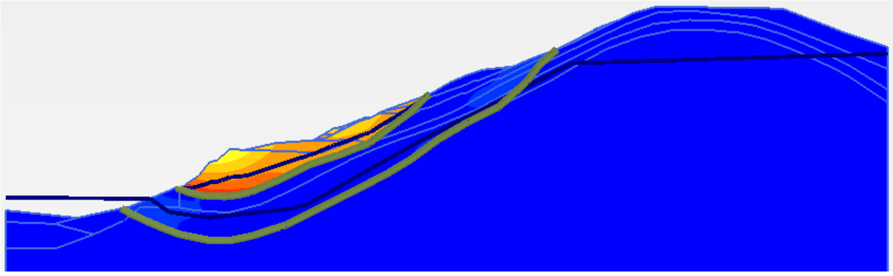

Figure 5.11. Failure surface obtained by c-phi reduction procedure for Scenario 2 and SF = 0.82.

The next scenario, Scenario 3, corresponds to a more stable geometry after the excavation in the upper part of the landslide. During a period of time in which no intense rainfall period occurred the measured average velocity of the landslide is 1 mm/month. This scenario is modelled assuming a water phreatic level for the upper sliding surface corresponding to moderate rainfall period ($r_u = 0.12$). The lower phreatic level for this scenario is defined following the minimum level of piezometer head measured in the field during 2014-2018 (Tab. 5.2). Under these hypotheses, the safety factor is equal to 1.18 (Fig. 5.12). Again, in this case the upper slide is the critical one.

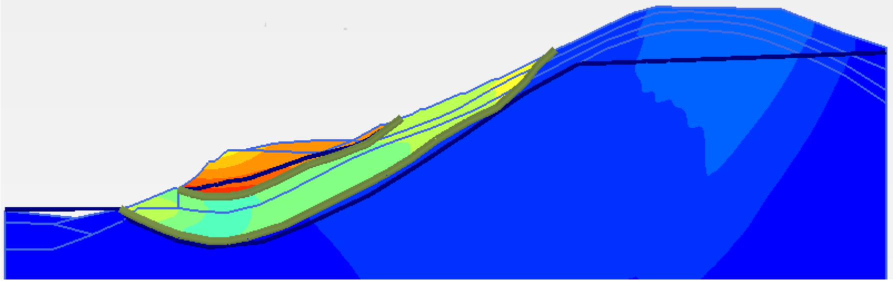

Figure 5.12. Failure surface obtained by c-phi reduction procedure for Scenario 3.

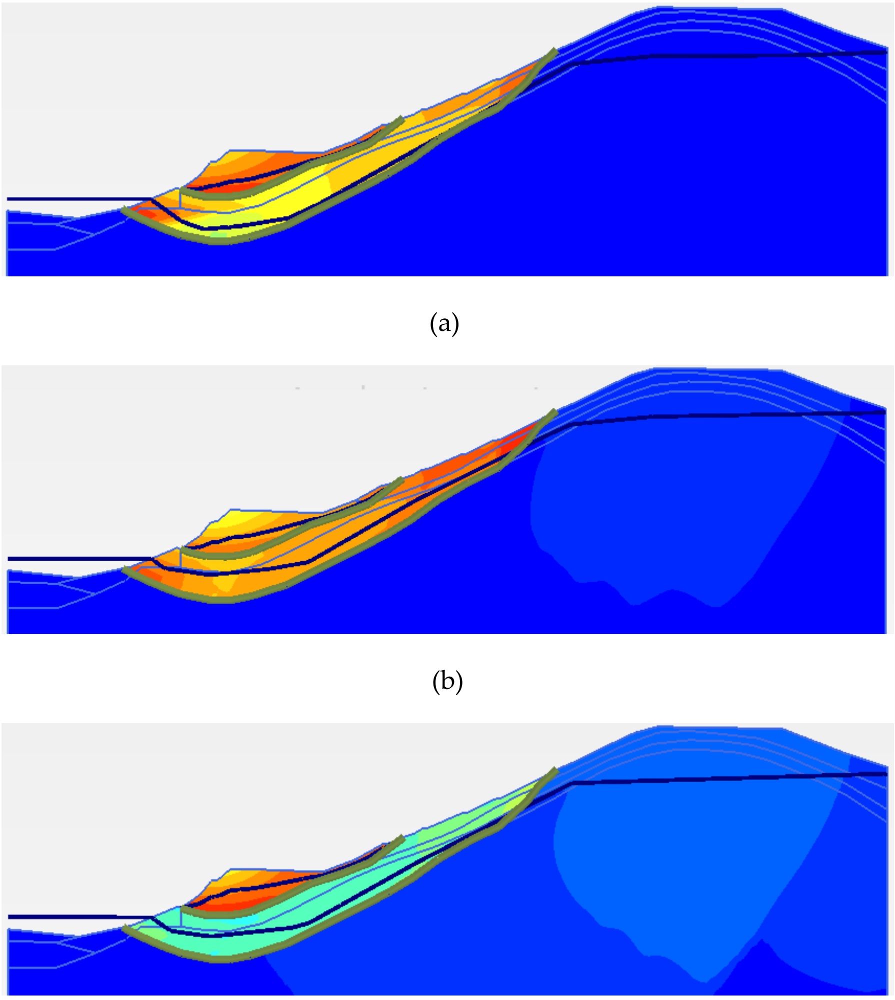

(a)

(b)

(c)

Figure 5.13. Failure surface obtained by c-phi reduction procedure for Scenario 4: (a) $r_u = 0.12$; (b) $r_u = 0.15$; (c) $r_u = 0.2$.

A future scenario including the foreseen total excavation to increase the slope stability is analysed under the assumption of moderate ($r_u = 0.12$), intense ($r_u = 0.15$) and extreme rainfall period ($r_u = 0.20$). Tab. 5.3 collects the obtained safety factors and Fig. 5.13 shows the failure surfaces obtained by c-phi reduction procedure. The safety factor reduces from 1.13 to 1.08 for the case of moderate and intense rainfall period (Fig. 5.13a, b), due to the increase in phreatic level.

This is the most interesting case to examine the interaction between the external actions and the expected mobilization of the two sliding surfaces. Under a moderate rainfall the upper landslide is the critical one but the deeper slide, especially the toe, is also mobilized. For an intense rainfall the two landslides are jointly mobilized. An extreme rainfall ($r_u = 0.2$) reduces significantly the stability of the upper landslide, which becomes critical.

The calculated safety factors for each Scenario are indicated in Tab. 5.3.

Table 5.3. Overview of each scenario and Safety Factor calculated by c-phi reduction method.

Scenario	Date	Geometry (see Fig. 5.4)	Comments	Safety Factor
Scenario 1	Before 2013	Geometry of 2007	- First signs of movements - Heavy rainfall period: Upper piezometric level induced by high intensity rains ($r_u = 0.15$). Deep piezometric level corresponding to maximum values measured. - Calculation by back analysis to obtain the friction angles ($\varphi_{shallow\_surface} = 15º$, $\varphi_{deep\_surface} = 18º$)	$SF = 1$
Scenario 2	February 2013	Geometry after excavation under road berms	- Heavy rainfall period: Upper piezometric level induced by high intensity rains ($r_u = 0.15$). Deep piezometric level corresponding to maximum values measured. - Velocities (in module) of almost 40 mm/month - Safety factor assessment	$SF = 0.82$
Scenario 3	November 2013	Geometry after 2nd stage of excavation (current)	- Upper piezometric level induced by moderate rains ($r_u = 0.12$). - Deep piezometric level corresponding to minimum values measured. - Velocities (in module) of almost 1 mm/month. - Safety assessment	$SF = 1.18$
Scenario 4	Future	New stabilizing excavation designed	- Safety assessment under different hypothesis of rainfall periods	$SF_{low} = 1.3$ $SF_{moderate} = 1.13$ $SF_{high} = 1.08$ $SF_{extreme} = 1.01$

5.4 MOTION BACK-ANALYSIS

5.4.1 MPM analysis

For a more complete understanding of the case, an MPM analysis is performed on Scenarios 1 and 2. The aim is to ascertain the stability conditions of Scenario 1, assuming the friction angles for the deep and shallow sliding surface obtained by back-analysis ($\varphi_{shallow\_surface} = 15^{\circ}$ and $\varphi_{deep\_surface} = 18^{\circ}$), and to calculate displacements and deformations occurred after toe excavation at Scenario 2 that cannot be estimated by FEM.

5.4.1.1 Model description

The MPM model consists of a plane-strain analysis. Fig. 5.14 shows the geometry of the problem, the materials and the computational mesh. The computational mesh is made of triangular elements with a minimum size of 10 m in the flysch materials. Initially, three material points are distributed within each element in the position of Gauss points. Boundary conditions for solid and liquid phases are applied on the left and right sides of the model, to constrain the horizontal displacement, at the top of the mesh to constrain the vertical displacement and at the bottom where both vertical and horizontal displacements are prevented. The materials are modelled with 2-phase fully coupled formulation and Mohr-Coulomb constitutive model, whom parameters are the same used in FEM analysis and indicated in Tab. 5.1. The intrinsic permeability of soil is assumed constant and equal to 10^{-10}m^2, corresponding to a hydraulic conductivity of 10^{-3} m/s.

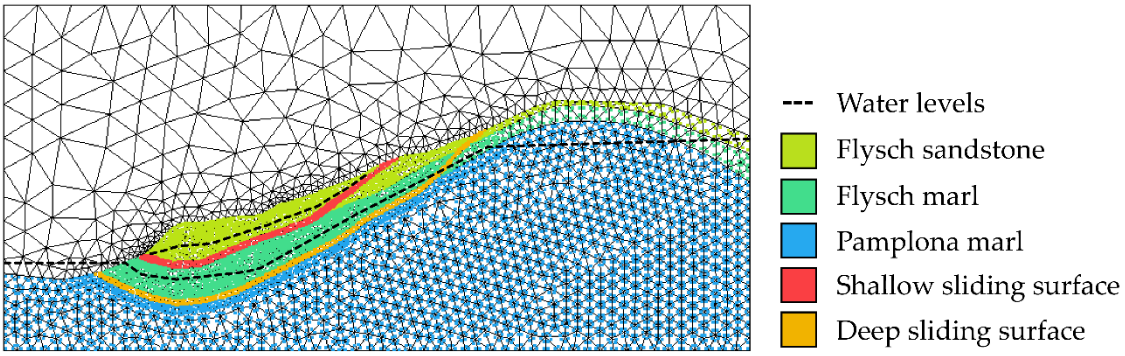

Figure 5.14. Geometry, materials, computational mesh and water surfaces with pressure equal to 0 assigned in MPM model.

Two water surfaces with pressure equal to zero are assigned to the model (Fig. 5.15) by using the numerical feature explained in §3.4.3. Accounting for the pore water pressure distribution of Scenario 1 and 2, as indicated in Tab. 5.3, the first surface is general and corresponds to the deep piezometric level obtained from the maximum values measured, the second is assigned to the material located above the shallow sliding surface and reproduce the piezometric level induced by high intensity rains ($r_u = 0.15$).

5.4.1.2 Stages of analysis

The initial distribution of pore water pressure is set as hydrostatic, below the water levels assigned to the model, and equal to 0 above. These pressure values are maintained constants along the calculation (Fig. 5.15).

Based on this distribution, the effective stresses are obtained by a K_0 procedure followed by a quasi-static calculation phase (see §3.4.3). A local damping factor of 0.75 is imposed in this stage and a value of 0.5 is assumed for the coefficient of earth pressure at rest.

In the next stage the slope toe is excavated, according to geometry of Scenario 2. The dynamic calculation is performed reducing the local damping factor to 0.05 and applying the strains smoothing technique (see §3.3.2)

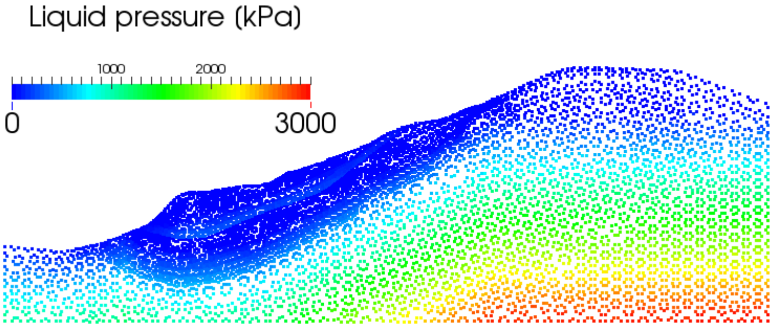

Figure 5.15. Hydrostatic distribution of pore water pressures in MPM model for high intensity rainfall period ($r_u = 0.15$).

5.4.1.3 Numerical results

Fig. 5.16 shows the results in terms of accumulated displacements at the end of the quasi-static calculation phase for Scenario 1. The displacement obtained, due to gravity, albeit low confirms that the slope is at critical condition ($SF_{Scenario1} = 1$) as it emerged from FEM back-analysis.

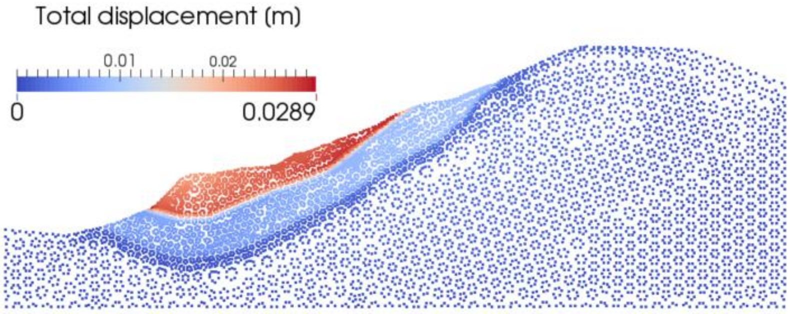

Figure 5.16. Accumulated displacements at Scenario 1 at the end of quasi-static calculation phase.

The computed accumulated displacements and deviatoric strains after toe excavation (Scenario 2) are shown in Fig. 5.17. The safety factor calculated by c-phi reduction method for this geometry is < 1 ($SF_{Scenario2} = 0.82$) showing an instability condition. Consistently with FEM analysis, MPM results show that the shallow landslide is the critical one, however, the deep sliding surface is not fully stable.

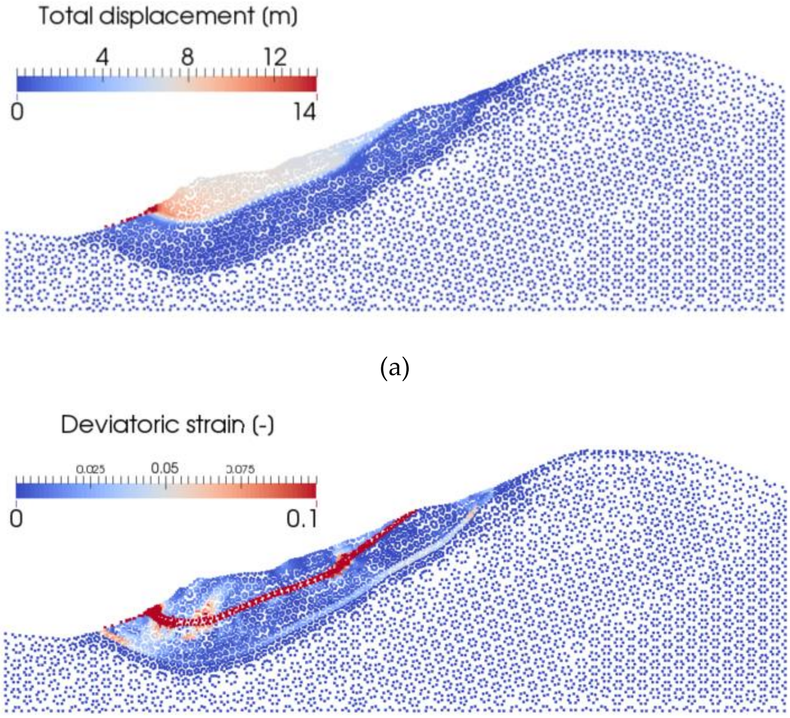

(a)

(b)

Figure 5.17. Accumulated displacements (a) and deviatoric strains (b) after toe excavation at Scenario 2 with $r_u = 0.15$.

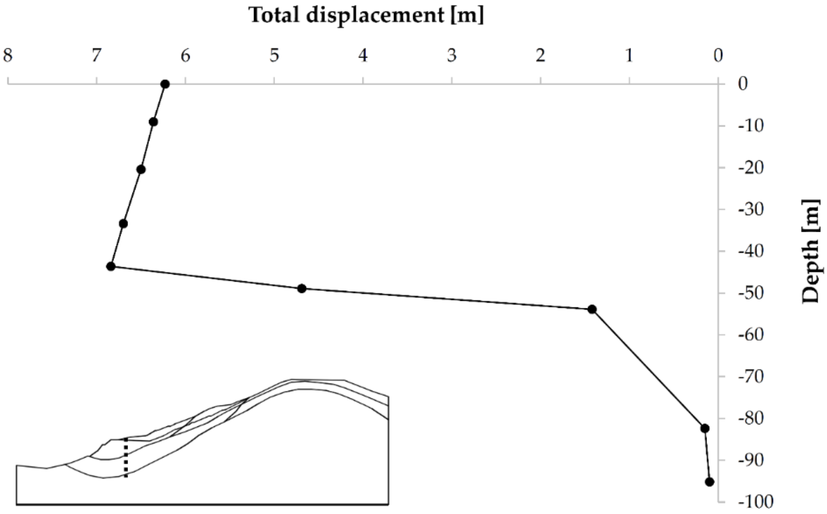

Figure 5.18. Accumulated displacements profile after toe excavation at Scenario 2.

For a better understanding of the slope motion, Fig. 5.18 shows the accumulated displacements profile along a vertical passing through the involved soil formations. At a depth of about 50 m from the ground surface is evident the displacement discontinuity between the shallow sliding surface that moves about 6 - 7 m and the underlying Flysch Marl formation whose displacements are lower than 1m.

Furthermore, control MPs in the positions indicated in Fig. 5.19 are selected to estimate the evolution with time of their displacement and velocity.

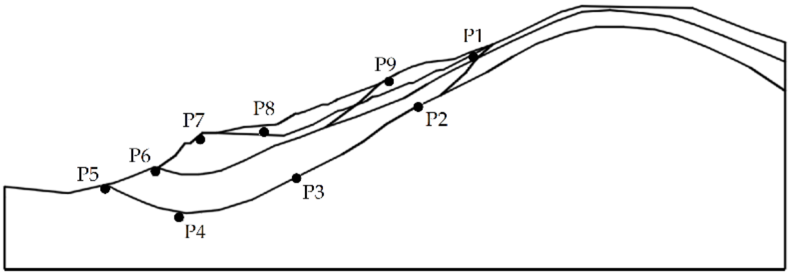

Figure 5.19. Position of material points selected to examine in detail their velocity and displacement.

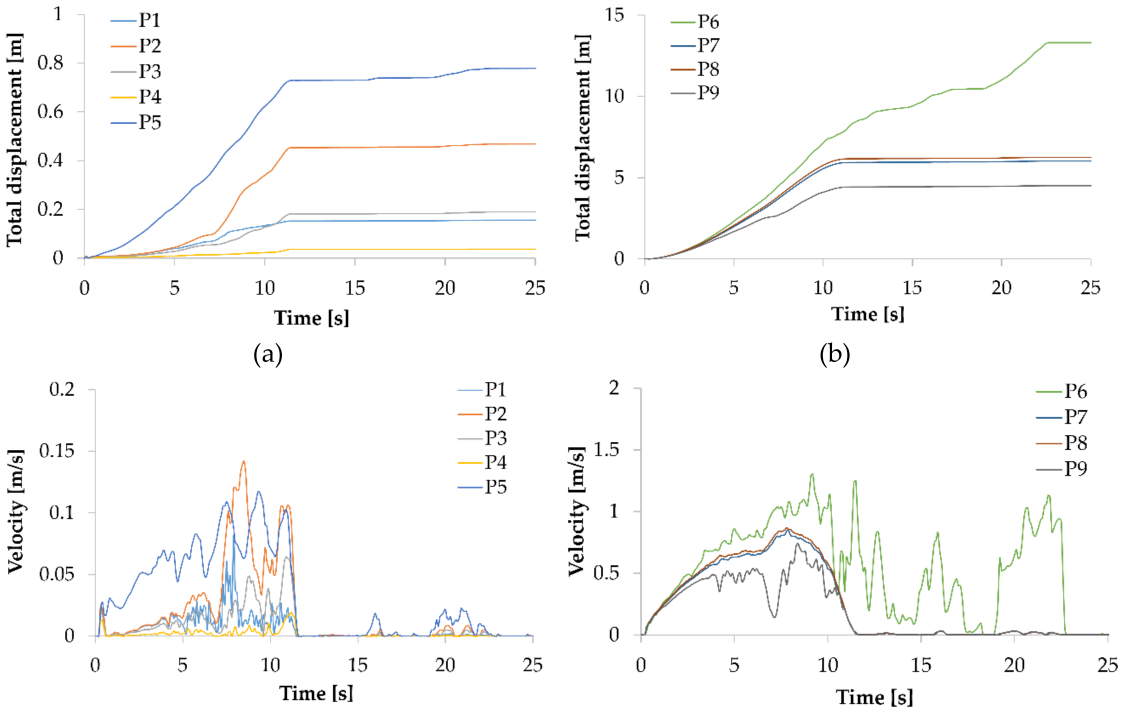

(a) (b)

(c) (d)

Figure 5.20. Histories of displacement (a-b) and velocity (c-d) of selected points.

As expected, Fig. 5.20 shows that displacement and velocity reached by the MPs located along the deep sliding surface are much lower than the ones exhibited by the MPs at the ground surface. However, the values resulted from the MPM analysis are larger than the observed ones. It can be explained considering that strain-rate effects on sliding surfaces shear strength are not included in the analysis despite Yesa is a case of creeping slide motion. This aspect is discussed in the following section §5.4.2 through an analytical calculation in which Yesa is simplified to a planar landslide as presented in Pinyol *et al.* (2021).

5.4.2 Creeping motion

Since the safety factor is a measure of the unbalance between driving and resisting forces, it can be correlated with the acceleration of the landslide, even if the SF is calculated statically. It could be expected that the smaller (and lower than one) the safety factor, the greater the acceleration. Field data in Tab. 5.3 supports this relationship: The lowest safety factor calculated is associated with the maximum registered velocity (100 mm/month).

In order to evaluate the landslide velocity and to correlate it with the safety factor, Yesa upper landslide was simplified to a planar slide defined by a sliding surface at a depth $D = 30\,m$, a slope inclination equal to $\beta = 14º$, and a level of water parallel to the sliding surface at a distance h_w. Although the parameters are inspired by the profile analysed previously, the results are not expected to be accurate because of the simplified geometry. However, the model may provide a good understanding of the creeping phase.

Applying Newton's second law and assuming a constant friction angle of 15º, $h_w = 4.2m$ ($r_u = 0.07$ leads a slope in strict equilibrium ($SF = 1$):

$$SF = (1 - r_u)\frac{tan\varphi'}{tan\beta} \tag{5.4}$$

Assuming a constant frictional strength and $r_u = 0.15$ (Scenario 2), which corresponds to SF = 0.91, it is simple to calculate from the motion equation (Eq. 5.5), an acceleration of the landslide equal to 0.2 m/s^2 (the slide will reach 1 m in 5 seconds).

$$a = gcos\beta[tan\beta - (1 - r_u)tan\varphi'] \tag{5.5}$$

where g is the gravity acceleration. Even considering the simplification assumed in the landslide geometry, this acceleration is completely unrealistic. This inconsistency can be resolved when a positive effect of the strain rate on the frictional strength is invoked (following the approach discussed in Alvarado *et al.*, 2019).

Fig. 5.21 shows the strain-rate-dependent strength defined for the discussion presented here. The following equation defines this curve:

$$tan\varphi'_v = tan\varphi'_{min} + (tan\varphi'_{max} - tan\varphi'_{min})(1 - e^{-\chi v}) \tag{5.6}$$

where the friction angle φ'_v is expressed in terms of the sliding velocity, v, and varies from a minimum value φ'_{min} (15º) to maximum one, φ'_{max} (18º) at a rate controlled by parameter χ.

Under this assumption, the increment of strength with sliding velocity is able to compensate the driving forces and to prevent the landslide acceleration when the water level remains lower than $h_{w\_max} = 14m$ $(r_u = 0.23)$. For this range of water levels $(h_{w\_min} < h_w < h_{w\_max})$ the landslide remains in motion at constant velocity:

$$v_{const} = -\frac{1}{\chi}\ln[\frac{tan\varphi'_{max} - tan\varphi'_{v_{const}}}{tan\varphi'_{max} - tan\varphi'_{min}}] \tag{5.7}$$

where

$$tan\varphi'_{v_{const}} = tan\beta/(1 - r_u) \tag{5.8}$$

Parameter χ should be calibrated. Notice that according to Eq. (5.7), this parameter controls the constant velocity reached in the field. For the case of Yesa, in which, maximum velocities around 40 mm/week were reached, the parameter χ is found to be close to 0.1 month/mm. The resulting frictional law is plotted in Fig. 5.21. The velocity-induced increment of the frictional strength (3º) is in accordance with available experimental studies (Tika *et al.* 1996; Kenney 1967; Wang *et al.* 2010; Schulz and Wang 2014; Scaringi *et al.* 2018 for references). However, the experimental data available indicates that the effect of the displacement rate on the strength in shear tests is relevant when displacement rate is larger than 0.01 mm/min (432 mm/month) which is much larger than the landslide velocity observed in Yesa landslide. This discrepancy may be attributed to the curved, self-stabilizing geometry of the sliding surface. Nevertheless, the analysis made remains useful to explain the relationship between SF and creeping rates. Parameter χ is accepted in this case as a model parameter to be estimated by a validation against field monitoring data.

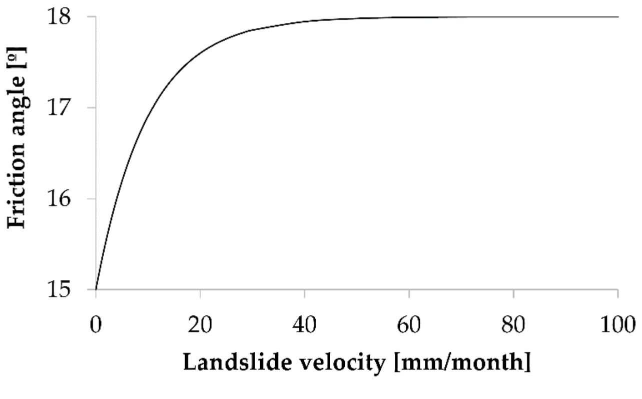

Figure 5.21. Strain-rate-dependent friction law.

Maintaining the definition of the SF (Eq. 5.4) associated with the friction angle at rest (φ'_{min}), the constant velocity reached can be expressed in terms of SF (Fig. 5.22). This result indicates that, for the values assumed, the safety factor can reduce to 0.83 without involving an accelerated motion of the landslide.

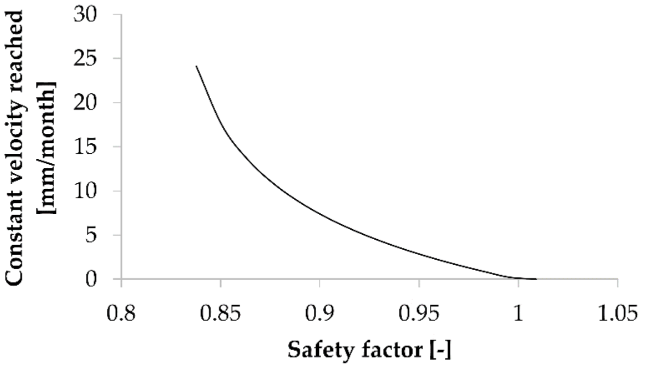

Figure 5.22. Relationship between creeping constant velocity and safety factor for of planar landslide representing the upper Yesa landslide.

Accounting for the geometry of Yesa sliding surface(s) requires more general calculation procedures capable of representing large displacement and dynamic effects. Alvarado *et al.* (2019) describe the analysis of Canelles landslide under the combined effect of strain rate effects on friction (to account for creeping behaviour) and thermal interaction. The shape of Canelles sliding surface can also be described as a self-stabilizing geometry which is a consequence of the folded geological structure of the involved strata. With the purpose of extending the capabilities of MPM modelling, a strain rate dependent Mohr-Coulomb model was formulated and included in the GEOPART code (Zabala and Alonso, 2011; Pinyol *et al.*, 2018). The constitutive model follows the procedure described in Wedage *et al.* (1998). The expected reaction of Yesa upper landslide against a large increase of pore pressure quantified by a change in $\boldsymbol{r_u}$ from 0.15 to 0.20 was analysed in Alonso *et al.* (2021). This increase corresponds to a 500 yr return period extremely, which corresponds to high rainfall intensity (446 mm/month) (see §5.2.4). A moderate strain rate effect on residual friction, similar to Eq. (5.6), was included in the calculation. The geometry analysed reproduced the current geometry of the landslide after a more recent excavation stage (Scenario 3). The calculated maximum displacement (20 cm of the toe of the upper landslide) was an indication of the positive effect of the syncline geometry. In view of this result and the reduced effect of safety factor on creeping velocities (Fig. 5.22) for the simplified planar geometry, it is concluded that extreme rainfall events in Yesa are unlikely to result in a catastrophic event.

5.5 MOTION ANALYSIS UNDER EXPECTED SEISMIC ACTION

5.5.1 Definition of seismic actions

The response of the slope under the dynamic action of future earthquakes concerned the authorities and owners of the dam because of the recent substantial increase of the basic acceleration assigned to Yesa dam site in the new regulatory seismic hazard maps of Spain. The Instruction defines the hazard spectrum to consider in designing reservoir slopes on the basis of basic acceleration, return period, amplification and risk coefficients. A deterministic risk analysis was carried out to provide an estimation of the accumulated displacement of Yesa landslide under imposed seismic action. The accelerograms, required for the analysis as input data, are obtained following the procedure described in Vargas et al. (2013). This methodology provides hybrid accelerograms obtained from the manipulation of real accelerograms with the aim of fitting them to the design uniform hazard spectrum specified by the Instruction. The real accelerograms were taken from the extensive European data base of strong seismic movements (Ambraseys *et al.*, 2002, 2004) and 1000 additional events registered in Spain. Fig. 5.23 shows four of the accelerograms (horizontal acceleration) considered in the seismic analysis of Yesa landslide for a horizontal peak acceleration (PGA) of 0.38g m/s^2, which corresponds to a return period of 5000 yr.

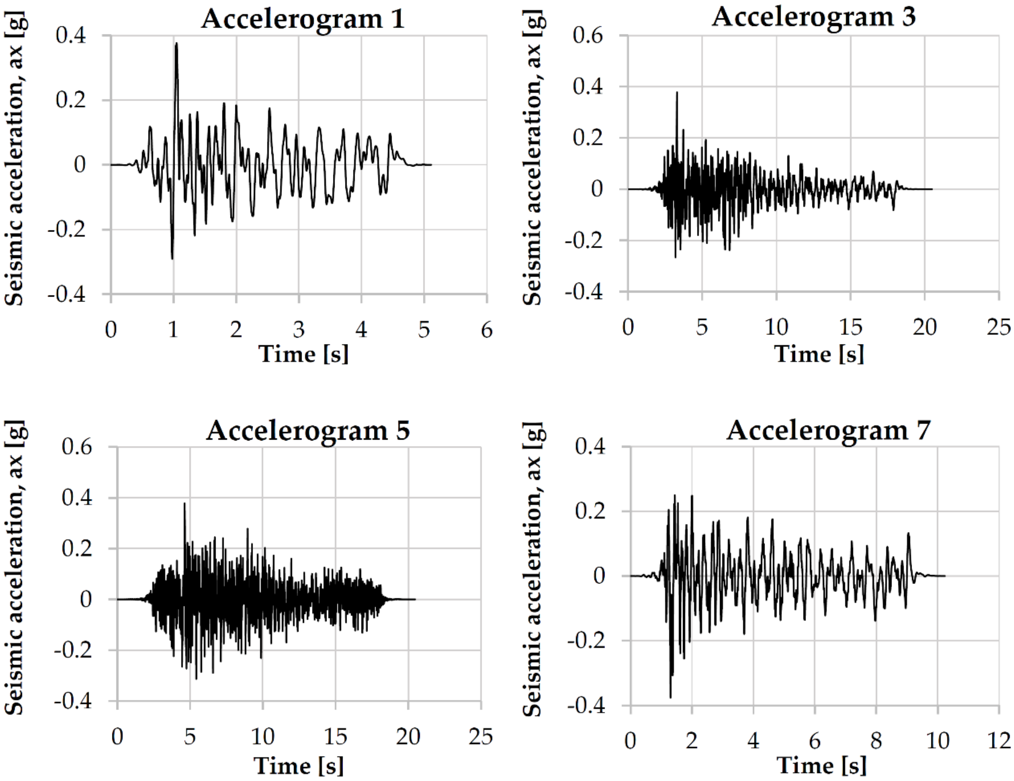

Figure 5.23. Four of the ten earthquake accelerograms used in the seismic analysis. Horizontal acceleration.

5.5.2 Dynamic stress-strain analysis by MPM

The MPM dynamic calculations are performed for the seismic event characterized by horizontal accelerogram No. 7 with a return period of 5000 yr. Scenario 4 is analysed under the hypothesis of low and extremely high intensity rainfall period (Tab. 5.3).

This is a simplified analysis to assess the slope stability under seismic loading since it does not account for dynamic aspects like damping increase and stiffness degradation with shear strains.

For a better understanding of the effect of the two preferential sliding surfaces, the safety factor at the moment of earthquake application associated with each sliding surface is evaluated. To do that the safety factor is re-calculated with Plaxis c-phi reduction method considering separately the shallow and the deep sliding surfaces. When only one preferential sliding surface is considered, the other one is deactivated which means that the corresponding "joint elements" are not assigned in the Plaxis model. Tab. 5.4 summarizes the results of the computed safety factors. The joint "global" SF coincides in this case with the calculated minimum of the sliding surfaces, when considered independently from the companion one.

Table 5.4. Safety factor for the two sliding surfaces under two rainfall intensities.

Rainfall period	Safety factor at the moment of earthquake application		
	Only shallow sliding surface activated	Only deep sliding surface activated	Both sliding surfaces activated
Low intensity	1.30	1.22	1.22
Extreme intensity	1.01	1.09	1.01

5.5.2.1 Model description

The geometry of the problem, the materials and the computational mesh are shown in Fig. 5.24.

Using the numerical feature explained in §3.4.2, the seismic action is introduced in the MPM analysis by defining at the model base an elastic material ("Shaking base") on whose MPs a velocity-time function is applied. Fig. 5.25 shows the prescribed velocity-time function obtained by integrating with the trapezium rule the horizontal accelerogram No. 7 with a return period of 5000 yr. Unlike others materials, one MP per element is considered sufficient to discretize the shaking base.

In order to reduce waves reflection at the lateral sides of the slope model, which may lead to distortions in the computed results, absorbing boundary conditions are defined (see §3.3.4). Since, in the current implementation, the absorbing boundaries do not prevent MPs from leaving the mesh and are not effective if displacement constrains are applied, very stiff elastic walls are defined at the lateral sides of the model and absorbing boundaries for solid phase is applied at the position indicated in Fig. 5.24. Moreover, since one reference material can be assigned for the calculation of the traction vectors corresponding to the absorbing boundaries, the same material properties ("Pamplona marl") are assigned to the soil volumes located below the deep sliding surface. The dashpot coefficients and the virtual thickness (Eqs. 3.12-3.17 and 3.19 of §3.3.4) have the same values for the solid and the liquid phase. The dashpot coefficients a and b are assumed equal to 1.0. As showed by Lysmer and Kuhlemeyer (1969) these values can give the maximum absorption for both compression and shear waves for a wide range of incidence angles. The virtual thickness δ is assumed equal to $500m$ that is about half model width.

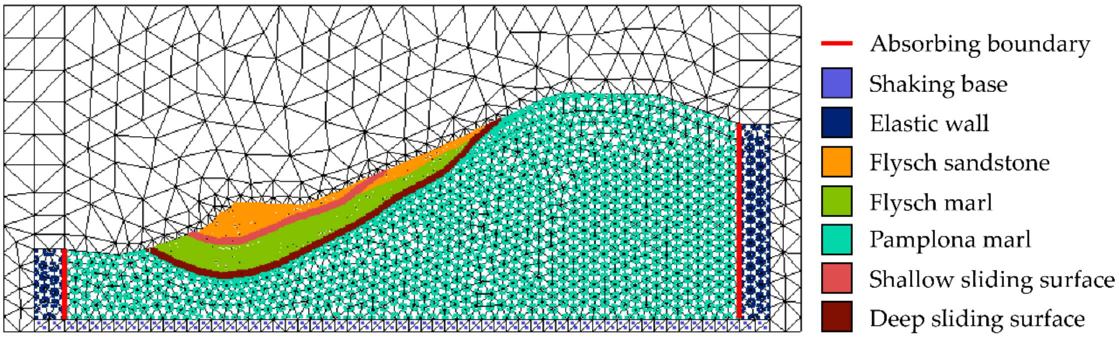

Figure 5.24. MPM geometry, materials and computational mesh.

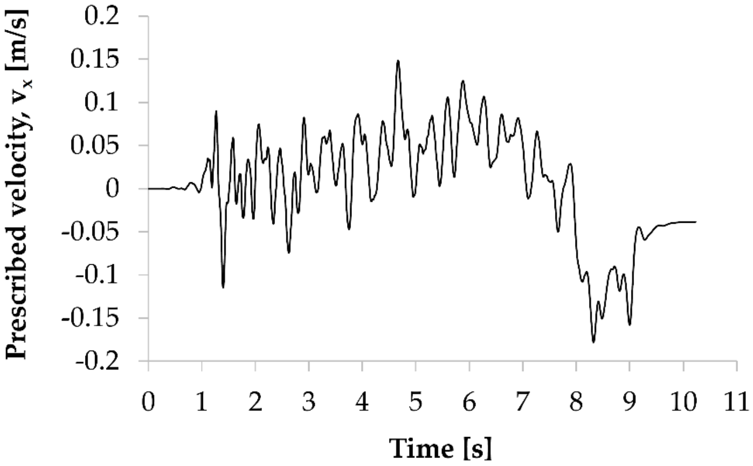

Figure 5.25. Horizontal prescribed velocity applied at the shaking base material.

The horizontal displacement are constrained at the lateral boundaries of the mesh, while the bottom is initially assumed fully fixed. The slope materials are modelled with 2-phase fully coupled formulation and the Mohr-Coulomb parameters are the ones used in the motion back-analysis. When the effect of just one of the imposed sliding surfaces is considered in the calculation, the properties of the overlying material are assigned to the deactivated one. The intrinsic permeability of soil is assumed constant and equal to 10^{-10}m^2, corresponding to a hydraulic conductivity of 10^{-3} m/s.

Finally, the water surfaces corresponding to the deep piezometric level and the two hypothesis of low and extremely high intensity rainfall period (Tab. 5.2) are assigned to the model as explained in §3.4.3.

5.5.2.2 Stages of analysis

Starting from the two assigned pore water pressure distributions (Fig. 5.26) corresponding to the two hypothesis of rainfall intensity considered, stresses are initialized in the first calculation phase with the procedure described in §5.4.1.1 for the motion back-analysis. Pore water pressures are maintained constants along the calculation

In the next stage, the horizontal fixities are removed at the mesh bottom and the prescribed velocity-time function (Fig. 5.25) is assigned to the MPs of the shaking base material. A homogeneous local damping factor of 0.05 is applied to the system and the strains smoothing technique (see §3.3.2) is also activated. The dynamic calculation is carried out beyond the velocity-time function duration until the accumulated displacements remain constants.

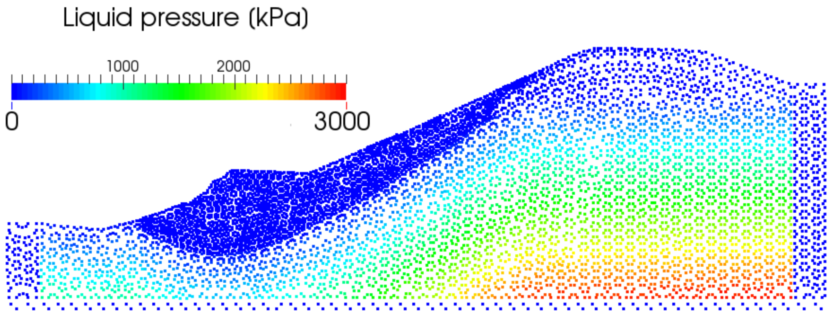

(a)

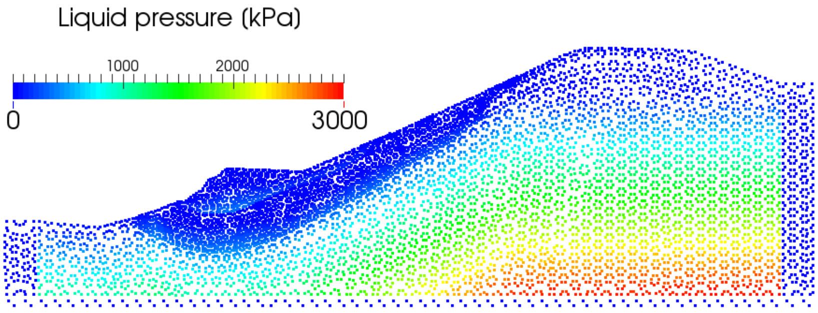

(b)

Figure 5.26. Initial distribution of pore water pressures in MPM model for two hypotheses of rainfall intensities: (a) Low intensity; (b) Extremely high intensity.

5.5.2.3 Numerical results

Tab. 5.5 indicates the maximum accumulated displacements for accelerogram 7 for 0.38 m/s^2 of PGA, corresponding to a return period of 5000 yr, and the two hypothesis of rainfall period intensity (Tab. 5.4). Three cases are solved for each of the two rainfall intensities regarding the selected sliding surface activated: shallow, deep or both of them. Obviously, in the field the two landslide surfaces are activated.

Consider first the situation of extremely high rainfall intensity. For this situation, a similar safety factor is associated to both sliding surfaces. The calculation provides a smaller displacement of the deeper landslide than the shallow if they are considered separately (Tab. 5.5 and Fig. 5.28a, b). The geometry of the sliding surface provides an explanation for this result because the shallow sliding surface is more planar than the deeper surface. This geometry facilitates the downward motion of the upper landslide. In the situation of low intensity rainfall period, the deeper sliding surface exhibit a lower safety factor. However, the seismic-induced accumulate displacements are slightly larger in the shallow landslide due to the sliding surface geometry (Tab. 5.5 and Fig. 5.27a, b).

Table 5.5. Maximum displacements reached for Scenario 4 and Accelerogram No. 7 with T = 5000 yr.

Rainfall period	Activated sliding surface	Maximum displacement (m)	Comments
Low intensity	Shallow	0.34	The shallow sliding surfaces is mobilized. The maximum displacement is calculated at the toe of the shallow sliding surface.
	Deep	0.30	The deep sliding surfaces is mobilized. The maximum displacement is calculated at the deep sliding surface toe.
	Shallow and Deep	0.37	The two sliding surfaces are mobilized. The maximum displacement is calculated at the toe of the shallow sliding surface.
Extreme intensity	Shallow	0.55	The shallow sliding surfaces is mobilized. The maximum displacement is calculated at the toe of the shallow sliding surface.
	Deep	0.45	The deep sliding surfaces is mobilized. The maximum displacement is calculated at the toe of the deep sliding surface.
	Shallow and Deep	0.68	The two sliding surfaces are mobilized. The maximum displacement is calculated at the toe of the shallow sliding surface.

In both cases, when both sliding surface are activated, the maximum displacement occurs at the toe of the shallow landslide which accumulates the relative displacements between the deep and shallow sliding surfaces.

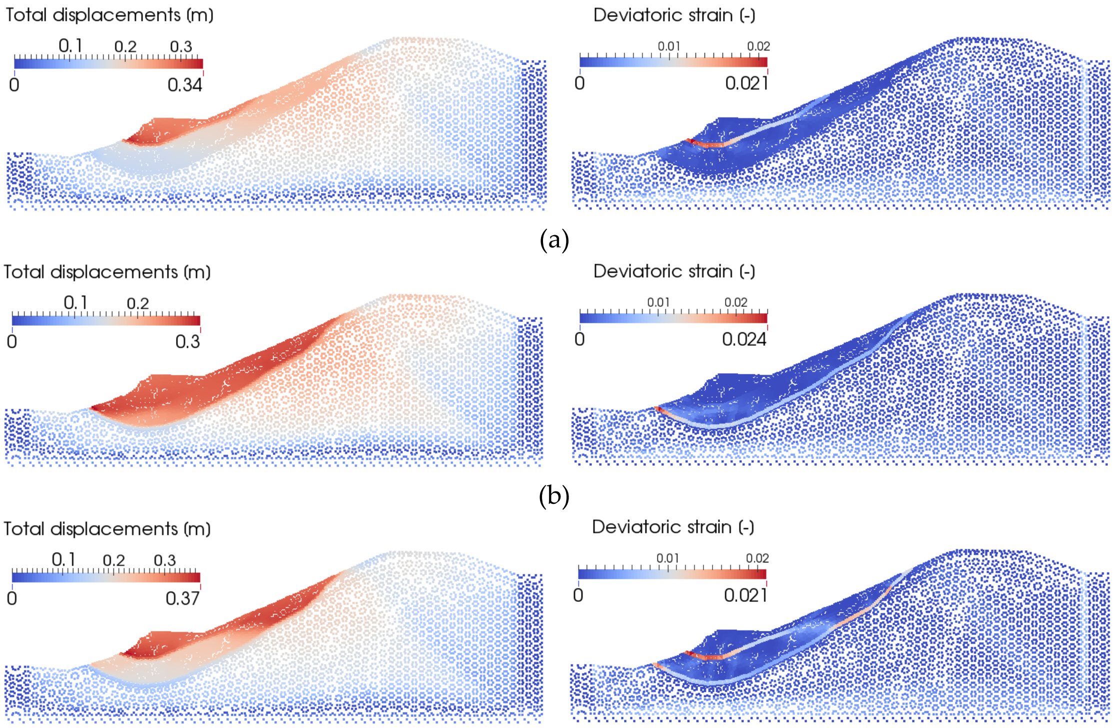

(a)

(b)

(c)

Figure 5.27. Computed accumulated displacement and deviatoric strain induced by accelerogram 7 ($T = 5000yr$) for low intensity rainfall. (a) Shallow sliding surface activated; (b) Deep sliding surface activated; (c) Both sliding surfaces activated.

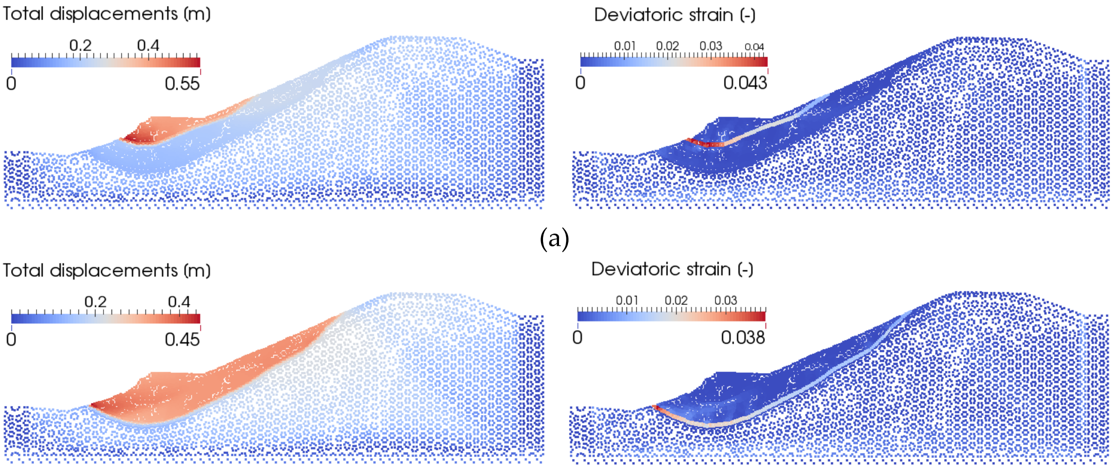

(a)

(b)

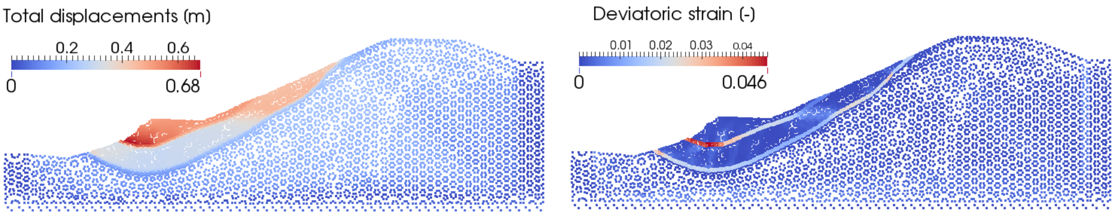

(c)

Figure 5.28. Computed accumulated displacement and deviatoric strain induced by accelerogram 7 ($T = 5000yr$) for extreme intensity rainfall. (a) Shallow sliding surface activated; (b) Deep sliding surface activated; (c) Both sliding surfaces activated.

5.5.3 Seism-induced permanent displacements: Newmark-type analysis

In this section the seismic permanent displacements are computed by means of Newmark's method (Newmark, 1965; Jibson, 1993). The effect of two preferential sliding surfaces on the results in terms of seismic-induced accumulated displacements is not discussed in the following analysis in which a unique well-defined slip surface is considered. Newmark's method simplifies the landslide as a rigid block that can move over a previously defined sliding surface. It is subjected to the earthquake ground motion defined by a force expressed in terms of $k \cdot m \cdot g$, where m is the unstable mass, g the gravity acceleration and k the coefficient defined by the earthquake accelerogram. Assuming a frictional strength (nil cohesion), the motion equation which provides the landslide acceleration (a) simplifies to:

$$tan\beta + (r_u - 1)tan\varphi' + k\frac{sin\alpha}{cos\beta}tan\varphi' + k\frac{cos\alpha}{cos\beta} = \frac{\alpha}{g\,cos\beta} \tag{5.9}$$

Angle α indicates the direction of the earthquake acceleration with respect to the slope of the sliding surface computed from the horizontal and vertical earthquake acceleration. For a proper discussion with MPM results, only the horizontal component of acceleration is considered.

The downslope sliding occurs when the seismic acceleration exceeds the yield acceleration. This is defined as the critical earthquake acceleration below which the slope remains stable. Obviously, this value depends on the stability condition of the slope at the moment of earthquake application:

$$k^{critical} = \frac{(SF - 1)sin\beta}{(sin\alpha\ tan\varphi' + cos\alpha)} \tag{5.10}$$

Considering Eq. (5.10) in Eq. (5.9), the landslide acceleration becomes:

$$a(t) = g(sin\alpha\ tan\varphi'(t) + cos\alpha)[k(t) - k^{critical}(t)] \tag{5.11}$$

which allows the calculation of the accumulated displacement following Newmark's procedure. A constant value of friction angle $\varphi' = 15º$ and a slope inclination $\beta = 12º$, are assumed in the analysis.

After calculating the 10 accelerograms, the maximum displacements are computed for the No. 7. Fig. 5.29 shows the results for accelerogram No. 7 with a return period of 5000 yr under three different slope stability safety factors. The order of magnitude of the displacements obtained are consistent with the results of the MPM analysis.

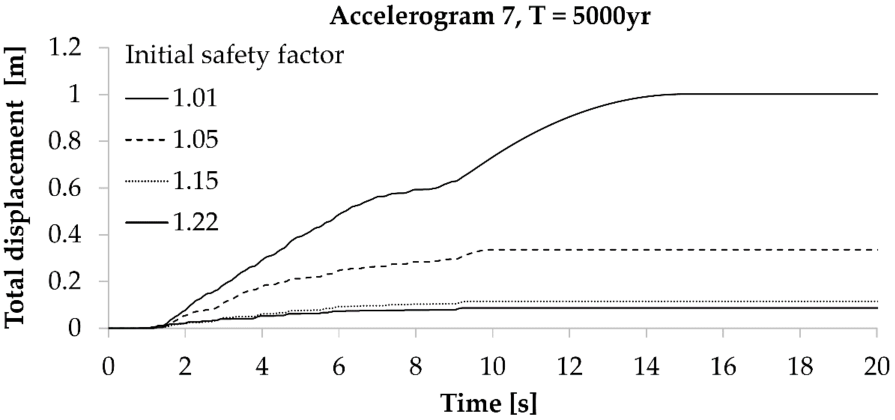

Figure 5.29. Newmark's accumulated displacement of Marmayor (planar) landslide for different safety factor of slope when earthquake is applied (Accelerogram 7, T = 5000 yr).

The strain-rate effect on the residual friction angle can be evaluated by including Eq. 5.6 in the calculation of the critical acceleration (Eq. 5.10). Similarly to the analysis presented in §5.4.2, the friction angle varies from a minimum value $\varphi'_{min} = 15º$ to a maximum one $\varphi'_{max} = 18º$ at a rate controlled by the parameter χ assumed equal to 0.1 month/mm. As expected, the accumulated displacements computed are significantly lower (Fig. 5.30).

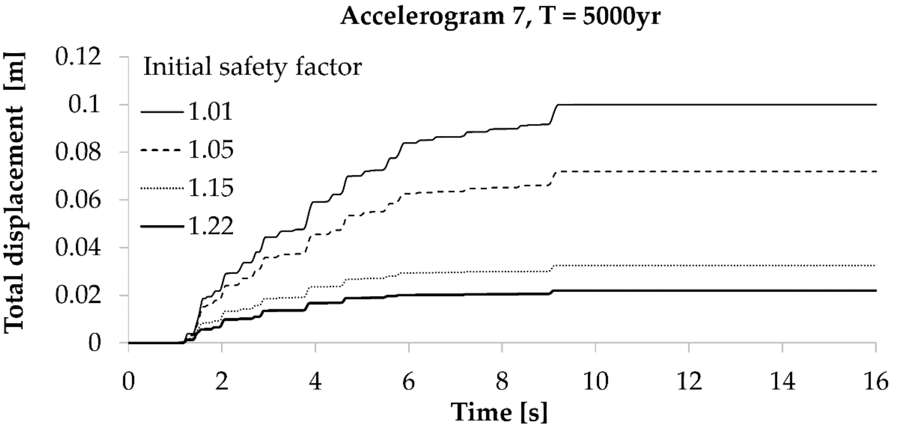

Figure 5.30. Newmark's accumulated displacement of Marmayor (planar) landslide for different initial safety factor of slope when earthquake is applied (Accelerogram 7, T = 5000 yr) accounting for strain-rate-dependent strength.

5.5.4 Results comparison

Fig. 5.31 shows a comparison of maximum displacements, in terms of safety factor, calculated by Newmark's method and MPM. The methods are widely different, not only because of the geometry of the landslide but also because of the constitutive model of the materials involved.

When the SF is very small (SF = 1.01) the larger maximum displacement is computed by Newmark's approach while for larger values of SF, the trend is reversed. When close to a critical situation (SF = 1) the Newmark's analysis predicts larger displacements after the end of the earthquake because there is no available additional strength to stop the motion induced by the earthquake. This behaviour is significantly mitigated when the strain-rate dependence on the residual friction angle is introduced. In this case, as indicated in Fig. 5.31, the lowest values of displacements are obtained. However, this simplified analysis it is not realistic when the actual geometry of the landslide is a very determinant feature.

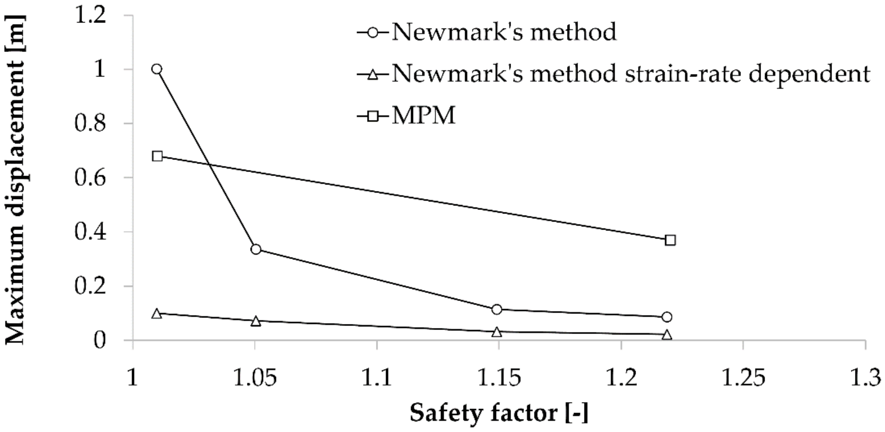

Figure 5.31. Maximum displacements calculated by the Newmark's method and the MPM analysis with the corresponding safety factor.

5.6 DISCUSSION

The large Yesa landslide (11.9 Mm^3), located in a flysch faces of Eocene-Oligocene age, is an interesting case because of the double sliding surface, the anticline-syncline structure folding of claystone-sandstone thin layers and the threat it poses to two existing dams at the landslide toe.

The landslide is in a situation of slow creeping motion except for the periods of intense rainfall which result in transient accelerations. Two aspects require definite answers: a) the general question of safety and b) the definition of acceptable creeping threshold limits for the landslide mobility. In fact, both aspects are directly related. It is not clear if the landslide is a reactivation of an ancient slide or a “first time” motion triggered by the excavations associated with dam construction. However, the synclinal folding the flysch strata probably led to a significant reduction of the original shear strength of the sandstone-claystone interfaces. Therefore, in any case, the residual shear strength of the interfaces is a reference value for the two sliding surfaces. Direct shear tests on sheared surfaces recovered in cores and the back analysis of unstable mass lead to residual friction angles in the range 16º-18º which is compatible with the low plasticity of claystone layers.

The estimation of excess pore pressures, operating on the more active and smaller upper landslide (4.35 Mm^3), required the development of a hydrogeological model, which accounted for the anisotropic permeability of flysch and the natural drainage of the flysch in a sub-parallel direction to the river valley. Transient pore water pressure increments acting on the upper sliding surface were characterized by r_u values directly related with return periods for rainfall intensity. In contrast, the lower sliding surface was controlled by reservoir level in lower elevations, by (slow) infiltration from rainfall and by seepage from distant areas uphill.

The chapter discussed first the relevance of safety factors determined by a FE-based c-phi reduction method applied to a number of “scenarios” which synthesized the known history of landslide behaviour and its relationship with dam construction and rainfall intensity. Future scenarios, aimed at stabilizing the landslide, are also defined. Calculated safety factors remain uncertain because the failure condition (SF = 1) is indeterminate. In fact, Yesa landslide has been always in a creeping state of varying velocity. Strictly speaking, all the known scenarios are at the limit of stability (SF = 1). Selecting (arbitrarily) a given scenario for the condition SF =1 allows the computation of safety factors, in the classical sense, for other scenarios. This exercise resulted in safety factors below or above 1 for the known history and future actions to improve stability. In addition, it was possible to investigate which one of the two sliding surfaces would reactivate in a critical (unstable) situation of defined scenarios.

A slope motion back analysis has been then performed by MPM to estimate displacements and deformations associated with an unstable scenario that FEM calculation could not provide. A further step in the analysis performed is to explore, by means of a planar landslide, the relationship between SF and creeping velocity. By considering a strain rate dependence of residual friction in the motion equation of the landslide, a closed-form equation relating SF and creeping velocity could be derived. For a planar slide inspired by the geometry, residual friction and expected range of r_u values of the upper Yesa landslide, the calculated creeping velocities for SF in the range 0.85-1, varies between 15 mm/month and 0.

The last part of the chapter analysed the response of the double sliding Yesa landslide under earthquake accelerograms defined by the recent regulation of seismic hazard in the Pyrenees regions. There was an interest in comparing two calculation methods: MPM and Newmark's approach. A common scenario, which includes a future stabilizing excavation and rainfall regimes, varying from low to extreme intensity, was calculated in both procedures for the worst accelerogram out of ten generated earthquakes for a return period of 5000 yr. The comparison was made in terms of the maximum landslide displacement, which was made dependent of the safety factor through varying values of r_u.

It was found that, for a critical situation (SF close to 1), Newmark's method, which relies on a single frictional contact, predicts substantially larger displacement when compared with the more accurate dynamic MPM analysis. However, this behaviour cannot be observed if the strain-rate dependence on the residual friction angle is introduced. The MPM analysis provided also information for the interaction between the two sliding surfaces. The more "planar" surface of the upper landslide, if compared with the curved syncline geometry of the deep surface, explains that the critical landslide in terms of earthquake-induced permanent displacements is the upper one.

The results obtained provide a deeper understanding of Yesa complex landslide. The results obtained may help to adopt stabilizing measures and to provide rational explanations. The discussion made concerns mainly the Yesa landslide but some results, especially those concerning the creeping and seismic response of planar slides and its relationship with the practical concept of safety factor are of general applicability.

CHAPTER 6 - CONSTITUTIVE MODELLING FOR LIQUEFACTION: TA-GER MODEL. IMPLEMENTATION AND VALIDATION

This chapter describes the main features of the constitutive model selected to be implemented in Anura3D to model sand behaviour under monotonic and cyclic loading. Once explained the procedure adopted for its numerical implementation, the model is verified and validated against data of drained and undrained triaxial tests under monotonic loading. The effects of model parameters on the results are highlighted through simulating further stress paths of conventional tests. Afterwards, the model is adapted for unsaturated conditions with the aim of simulating static liquefaction occurrence in partially saturated soils. Finally, the model implementation is verified for cyclic loading conditions through simulation of strain- and stress-controlled conventional tests with an emphasis on the model parameters affecting the cyclic behaviour.

6.1 INTRODUCTION

Elasto-plastic models based on critical state theory managed to describe the main aspects of the mechanical behaviour of soils (Gens and Potts, 1988). Critical state theory states that granular materials if continuously sheared will reach a state called the critical state. It will deform without any changes in volume and sustain a constant stress state, although there is a dependency to the mean effective stress. Among the constitutive models available in literature within the critical state framework, the Ta-Ger model was selected to be implemented in the MPM code Anura3D (www.anura3d.com) because of its flexibility in predict the mechanical behaviour of saturated soils under both static and cyclic loading. It is characterized by the formulation of an explicit elasto-plastic matrix that not requires the definition of the plastic modulus and the loading index. This fact renders the numerical implementation simpler and more efficient, compared with other constitutive model. Furthermore, the number of model parameters is reduced to a minimum by incorporating the initial state of the soil and just three need to be calibrated from data of conventional laboratory tests.

6.2 MODEL DESCRIPTION

The Ta-Ger constitutive model was developed by Tasiopoulou and Gerolymos (2016a, b) with the aim of reproducing the behaviour of soil under different types of loading (monotonous, cyclical), drainage conditions and initial stresses, without the need to recalibrate its parameters. It is an elastoplastic model that combines the perfect plasticity with the smooth hysteretic model of Bouc-Wen type (Bouc, 1971; Wen, 1976; Gerolymos and Gazetas, 2005).

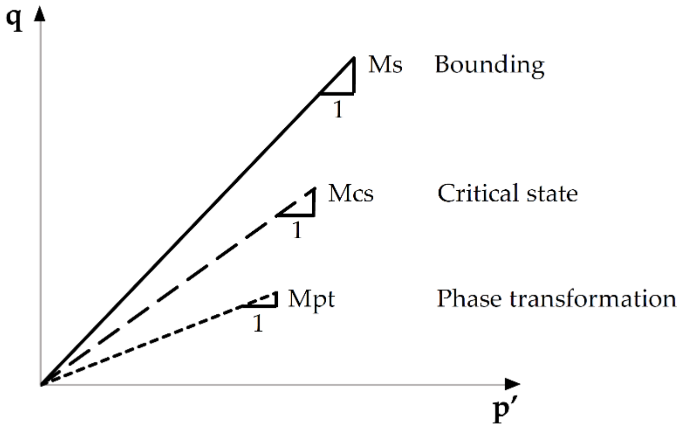

Figure 6.1. Bounding, phase transformation and critical state lines in $p' - q$ space.

The model does not include a yield surface to define the elastic region, which is trivialized to a single point at the beginning of loading, unloading and reloading, where elastic behaviour is expected. Ta-Ger model is defined by an open-end cone type failure surface that works similarly to a bounding surface that cannot be surpassed. In the triaxial space it is expressed by Eq. 6.1.

$$q - p'M_s = 0 \tag{6.1}$$

The ratio between deviatoric stress and mean effective stress is limited by the bounding stress ratio M_s that represents the ultimate strength (plotted in Fig 6.1).

This is ensured by controlling a dimensionless parameter ζ that ranges between [0, 1] and tracks the distance of the current state from the ultimate state. When the stress point reaches the ultimate failure state, ζ is equal to unity while all its values from zero to unity correspond to intermediate stress states. In this sense, there is always an "image" stress state lying on the failure surface that acts as a boundary surface and so that the ratio, ζ, between the actual and "image" stress states can be computed.

In the multiaxial stress-strain space, it is defined as in Eq. 6.2.

$$f = \left[(\boldsymbol{s} - \boldsymbol{r_p} p):(\boldsymbol{s} - \boldsymbol{r_p} p)\right]^{1/2} - \left(\sqrt{\frac{2}{3}} M_{s,\theta} - n_p\right) p = 0 \qquad (6.2)$$

$$\boldsymbol{s} = \boldsymbol{\sigma} - p\boldsymbol{I} \qquad \boldsymbol{r_p} = \frac{\boldsymbol{\sigma_p} - p_p \boldsymbol{I}}{p_p} \qquad n_p = \boldsymbol{n}:\boldsymbol{r_p} \qquad (6.3)$$

This is a function of the current stress state ($\boldsymbol{s}$, p) as well as the stress state at the last reversal of loading ($\boldsymbol{r_p}$, n_p). $\boldsymbol{n}$ is a normalized stress ratio tensor, normal to f. In case of cyclic loading the stress ratio tensor at pivot points, $\boldsymbol{r_p}$, need to be updated when the first order work changes sign (Eq. 6.4). The first order work is equal to the inner product of the strain rate tensor and the difference of the current stress ratio tensor from the stress ratio tensor obtained by the last pivot point:

$$dW = (\boldsymbol{r} - \boldsymbol{r_p}):\boldsymbol{\varepsilon} \qquad (6.4)$$

The term $M_{s,\theta}$ is the bounding stress ratio depending on the lode angle θ (Eq. 6.5).

$$M_{s,\theta} = \left(\frac{M_c + M_e}{2} - M_{ss}\right) cos^2(3\theta) + \left(\frac{M_c - M_e}{2}\right) cos(3\theta) + M_{ss} \qquad (6.5)$$

where $M_c = \frac{6sin\phi}{3-sin\phi}$, $M_e = \frac{6sin\phi}{3+sin\phi}$ and $M_{ss} = 2sin\phi$ are the bounding stress ratio in triaxial compression, extension and in simple shear.

The plastic flow rule is based on Rowe's dilatancy theory (Rowe, 1962) and takes into account the anisotropic distribution of dilatancy respect to the three normal plastic strain increments, depending on the loading direction. In the conventional $p' - q$ space, the dilatancy, d, can be expressed as the difference between the current stress ratio $\frac{q}{p'}$ and the phase transformation line M_{pt} (Eq. 6.6). This line corresponds to the stress state at which the soil response passes from contractive to dilative behaviour (Fig. 6.1) (Ishihara *et al.*, 1975).

$$d = M_{pt} - \frac{q}{p'} \tag{6.6}$$

In loose materials generally occurs that $\frac{q}{p} < M_{pt}$ and $d > 0$ which correspond to contraction, whereas dense materials have a contractive behaviour for stress ratio states below the phase transformation ($\frac{q}{p'} < M_{pt}$ and $d > 0$) and dilative for stress ratio states above ($\frac{q}{p'} > M_{pt}$ and $d < 0$). At very low confining stress, loose materials may behave as dense materials and may be dilative at large strains.

In the multiaxial stress-strain space the dilatancy is defined as in Eq. 6.7, where R_d is a parameter that accounts for densification effects due to cyclic drained loading and $M_{pt,\theta}$ is the phase transformation stress ratio depending on the lode angle θ. The current stress state and the loading direction are included through the inner product of tensors $\mathbf{r}:\mathbf{n}$.

$$d = R_d\left(\sqrt{\frac{2}{3}}M_{pt,\theta} - \boldsymbol{r}:\boldsymbol{n}\right) \tag{6.7}$$

Both the bounding stress ratio (M_s) and the phase transformation (M_{pt}) stress ratio tend to converge to the critical state stress ratio, M_{cs}, which is function of the critical friction angle, when the current stress state reaches the critical state and no change in volume occurs despite the continuous increase of shear strain. In Ta-Ger formulation, the bounding and the phase transformation stress ratios are expressed as a function of the cumulative deviatoric strain increments $\sum d\varepsilon_q$ (Eq. 6.8 and 6.9).

$$M_s = M_{cs} + \left[M_{sp} + \left(M_{s0} - M_{sp}\right)e^{-c\sum d\varepsilon_q} - M_{cs}\right]e^{-c\sum d\varepsilon_q} \tag{6.8}$$

$$M_{pt} = M_{cs} + \left(M_{pt0} - M_{cs}\right)e^{-0.5c\sum d\varepsilon_q} \tag{6.9}$$

$$M_{sp} = 2M_{speak} - M_{cs} + 0.5\sqrt{\left(2M_{cs} - 4M_{speak}\right)^2 - 16M_{s0}\left(M_{speak} - M_{cs}\right) - 4{M_{cs}}^2} \tag{6.10}$$

In previous equations M_{s0} and M_{pt0} are the initial values of M_s and M_{pt}, M_{sp} is the maximum values that can be potentially reached depending on parameter c (Eq. 6.10). For typical values of c in the range of 3 – 10, the bounding stress ratio reaches a lower value called M_{speak}.

The model includes a reformulation of perfect elastoplasticity with the aim of attributing hardening/softening characteristics to its capabilities. The elasto-plastic matrix is given by Eq. 6.11.

$$\{E_h^{ep}\} = \{E^e\}\left[\{I\} - \frac{\{\Phi_g\}\{\Phi_f\}^T\{E^e\}\{H\}}{\{\Phi_f\}^T\{E^e\}\{\Phi_g\}}\right]\{\eta\} \tag{6.11}$$

$\{E^e\}$ is the elastic matrix, $\{\Phi_f\}$ and $\{\Phi_g\}$ are the gradients of failure surface and plastic potential. An appropriate plastic matrix $\{H\} = \zeta^n\{I\}$ controls the rate of transition from elastic state to the perfectly plastic response through the hardening exponent parameter n; and provides an appropriate loading/unloading/reloading mapping rule through the dimensionless parameter ζ.

The hysteretic behaviour is then introduces trough matrix $\{\eta\} = \eta\{I\}$ (Gerolymos and Gazetas, 2005) that accounts for stiffness degradation by modifying the shape and size of the hysteretic loops depending on deviatoric strain.

The shear modulus G is defined as a function of the mean effective stress p' (Eq. 6.12).

$$G = G_0 \cdot p'^m \tag{6.12}$$

Where G_0 and m are dimensionless material parameter. G_0 can be expressed as $1000k_{2max}$ where $k_{2max} = 0.13D_{r0} + 3.6$ is a coefficient adapted from Seed and Idriss (1970), dependent on initial relative density. The bulk modulus K is derived from it by assuming a constant value of the Poisson ratio ν.

As a summary, the implemented version of the Ta-Ger model has nine model parameters included in Tab. 6.1.

Table 6.1. Ta-Ger model parameters.

Parameter	Symbol	Unit
Shear modulus parameter	G_0	-
Shear modulus exponent	m	-
Poisson's ratio	ν	-
Critical state stress ratio	M_{cs}	-
Initial value of phase transformation stress ratio	M_{pt0}	-
Initial value of bounding stress ratio	M_{s0}	-
Maximum value of bounding stress ratio	M_{speak}	-
Hardening exponent	n	-
Bounding and Phase transformation coefficient	c	-

In order to provide physical meaning of the model parameters, critical stress ratio and maximum and initial values for the phase transformation and bounding stress ratio are defined in terms of critical (φ_{cs}), peak (φ_{peak}) and initial (φ_{s0}) frictional angle.

For triaxial compression, the critical stress ratio (M_{cs}), as well as the initial (M_{s0}) and maximum (M_{speak}) value of the bounding stress ratio can be calculated from:

$$M_{cs} = \frac{6sin\varphi_{cs}}{3 - sin\varphi_{cs}} \tag{6.13}$$

$$M_{s0} = \frac{6sin\varphi_{s0}}{3 - sin\varphi_{s0}} \tag{6.14}$$

$$M_{speak} = \frac{6sin\varphi_{peak}}{3 - sin\varphi_{peak}} \tag{6.15}$$

Peak and initial friction angles can be correlated with the called relative dilatancy index $I_r$presented by Bolton (1986) and defined as:

$$I_r = D_r(Q - \ln(p')) - R \tag{6.16}$$

where D_r is the relative density,

$$D_r = \frac{e_{max} - e}{e_{max} - e_{min}} \tag{6.17}$$

that defines the density of the packing by comparing the current void ratio state with the loosest and densest states possible, which are characterised by the maximum void ratio e_{max} and the minimum void ratio e_{min}, respectively. Q is an empirical parameter which is influenced by grain characteristics, such as mineralogy, grain shape and grain size distribution and R is a fitting parameter. These constants assume values close to 10 and 1 respectively. When the relative dilatancy index is positive ($I_r > 0$), the sand is dense and it will dilate in order to reach the critical state. When the index is negative ($I_r < 0$), the sand is loose and it will contract to reach the critical state. Thus, when the index is nil ($I_r = 0$), the sand is at critical state and the critical state line (CSL) in terms of critical void index e_c versus $ln(p')$ can be derived from it (Eq. .6.18).

$$e_c = e_{max} - \frac{R}{Q - \ln(p')}(e_{max} - e_{min}) \tag{6.18}$$

According to Bolton (1986), maximum and initial friction angles are expressed as:

$$\varphi_{peak} = \varphi_{cs} + \alpha I_r \geq \varphi_{cs} \qquad \text{for } 0 < I_r < 4 \tag{6.19}$$

$$\varphi_{s0} = \kappa\varphi_{cs} + 5I_{r0} \leq \varphi_{cs} \tag{6.20}$$

where α has values in the range of 3 to 5 for triaxial and plane strain conditions (Bolton 1986; Tasiopoulou and Gerolymos 2016b) and coefficient κ can be determined through a calibration procedure to fit experimental data resulting from drained and undrained triaxial compression tests. The limitation $\varphi_{s0} \leq \varphi_{cs}$ is imposed to avoid numerical instability issues from Eq. 6.10.

The initial phase transformation stress ratio is also expressed in terms of relative dilatancy index, I_r, maximum friction angle φ_{peak}, (taking into account Eq.6.8), hardening parameter n, and dimensionless parameter ζ:

$$M_{pt0} = M_{speak}\zeta^n - \frac{3(0.3I_r)}{3+3(0.3I_r)}\frac{1}{\chi} \qquad I_{r0} > 0 \tag{6.21}$$

$$M_{pt0} = M_{speak}\zeta^n \qquad I_{r0} < 0 \tag{6.22}$$

Finally, parameter c that controls the evolution of bounding and phase transformation stress ratios is expressed as a function of the relative dilatancy index through a coefficient δ that needs a calibration procedure to be obtained, $c = 6 + \delta I_{r0}$, and the hardening exponent n is expressed as a function of the initial relative density, $n = 0.4D_{r0} + 0.14$.

6.3 NUMERICAL IMPLEMENTATION

6.3.1 Implementation in Anura3D

The Ta-Ger constitutive model has been included in Anura3D code as an external soil model (ESM). This feature enables users to implement a constitutive models in the software without having access to its source code.

Two main subroutines, written in FORTRAN programming language, are needed to let the code reading the model. One is the external soil model (ESM) interface that allows

Anura3D to provide information about the previous stress and state variables to the constitutive model in which the current ones are calculated.

Table 6.2. Parameters defined as "PROPS".

Parameter	Symbol	Unit
Shear modulus parameter	G_0	-
Shear modulus exponent	m	-
Poisson's ratio	ν	-
First parameter determining I_r	Q	-
First parameter determining I_r	R	-
Initial void ratio	e_0	-
Minimum void ratio	e_{min}	-
Maximum void ratio	e_{max}	-
Critical friction angle	φ_{cs}	°
Parameter determining c	κ	-
Coefficient determining φ_{s0}	δ	-

Table 6.3. State variables defined as "STATEV".

Variable	Symbol	Unit
Void ratio	e	-
First order work	dW	-
Stress tensor at pivot point	$\boldsymbol{r_p}$	-
Accumulated deviatoric strain	$\sum \varepsilon_d$	-
Bulk modulus of water	K_w	kPa

The other is the ABAQUS user material subroutine (UMAT) (Bienen *et al.*, 2014) in which the constitutive model is implemented. It is characterized by a standardized format. In fact, material parameters and state variables have to be included in specific arrays called "PROPS" and "STATEV" respectively. Ta-Ger model parameters and state variables as defined in UMAT subroutine are summarized in Tab. 6.2 and 6.3. Finally, the FORTRAN project including both subroutines have to be compiled as Dynamic Link Library (DLL) in order to run a simulation with Anura3D.

6.3.2 Stress point algorithm

The methods for integrating constitutive relations, in order to obtain the unknown stress increment for a given current stress and a given strain increment, are known as stress-point algorithms and can be classified into explicit and implicit. In the both algorithms, the objective is to integrate the constitutive equations along an incremental strain path.

Implicit integration schemes use a step-by-step calculation method in which an appropriate convergence criterion allows to continue or not the analysis, eventually reducing the increment of time, depending on the accuracy of the results at the end of each step. Into the implicit algorithms the solution at the time step $n + 1$ is obtained by the knowledge of the solution at time step n and the conditions imposed at step $n + 1$. They can provide an unconditionally stable integration solution. Implicit methods are usually used for simple constitutive laws. For complex highly non-linear constitutive laws the iterative process may not converge and hence the efficiency of these codes may deteriorate.

Explicit integration schemes are not conditioned by a convergence criterion, the time increment is defined at the beginning of the analysis and remains constant during the calculation. The method is called "explicit" because each new variable increment requires only the knowledge of the parameters related to the previous increment without the need of iterative procedure. This fact is particularly beneficial when highly non-linear models are considered. This method is conditionally stable, namely its stability depends on the time increment of integration. The advantage of the explicit methods is due to the fact that, despite smaller time increments, computational time analysis is much less if compared with implicit methods.

In this thesis, an explicit sub-stepping algorithm with automatic error control (Sloan *et al.*, 2001) is adopted. It allows to better track the strong non-linearity of the constitutive model and get a more accurate solution.

This algorithm automatically divides the applied strain increment into sub-increments (sub-steps) small enough to ensure that the desired integration accuracy is enforced. The integration error is controlled by automatically modifying the number of sub-steps. Using an estimate of the local error, the size and the number of sub-steps is function of the specified error tolerance, the magnitude of the imposed strain increment, and the non-linearity of the constitutive relations.

More in detail, the scheme involves splitting the elasto-plastic strain step $\Delta\boldsymbol{\varepsilon}$ into a series of smaller sub steps, $\Delta\boldsymbol{\varepsilon}^s = \Delta T_n \Delta\boldsymbol{\varepsilon}$ (where $0 < \Delta T_n \leq 1$), and using a modified Euler approximation for each sub step. The size of each sub step is determined by estimating the error in the stress changes and comparing this with a user-defined tolerance, $STOL$. At the beginning it is assumed that only one sub step is necessary. Consequently ΔT_n is set to unity and the pseudo time T_n is set to zero.

A first estimative of the changes in stresses and hardening parameters at the end of the pseudo time step ΔT_n are evaluated using a first order Euler approximation (Eq. 6.23).

$$\Delta\boldsymbol{\sigma}'_1 = \boldsymbol{D}^{ep}(\boldsymbol{\sigma}', \chi)\Delta\boldsymbol{\varepsilon}^s \tag{6.23}$$

Where $\boldsymbol{D}^{ep}$ is the elastoplastic matrix. Then, a second estimative for the changes in stress over the sub step can be calculated as function of the stress $\boldsymbol{\sigma}' + \Delta\boldsymbol{\sigma}'$ (Eq. 6.24).

$$\Delta\boldsymbol{\sigma}'_2 = \boldsymbol{D}^{ep}(\boldsymbol{\sigma}' + \Delta\boldsymbol{\sigma}'_1)\Delta\boldsymbol{\varepsilon}^s \tag{6.24}$$

A more accurate estimate at the end of interval ΔT_n is computed using the modified Euler procedure (Eq. 6.25).

$$\Delta\boldsymbol{\sigma}' = \frac{1}{2}(\Delta\boldsymbol{\sigma}'_1 + \Delta\boldsymbol{\sigma}'_2) \tag{6.25}$$

The accumulated stresses are now updated (Eq. 6.26).

$$\boldsymbol{\sigma}' = \boldsymbol{\sigma}' + \Delta\boldsymbol{\sigma}' \tag{6.26}$$

The local error in the Euler and modified Euler solutions is $O(\Delta T^2)$ and $O(\Delta T^3)$ respectively. For each sub increment, the local error measure is found by taking the difference between a second order accurate modified Euler solution and a first order accurate Euler solution. A relative error measure is computed from Eq. 6.27.

$$R_n = \frac{1}{2} max\left\{\frac{||\Delta\boldsymbol{\sigma}'_2 - \Delta\boldsymbol{\sigma}'_1||}{||\boldsymbol{\sigma}'||}\right\} \tag{6.27}$$

The current strain sub increment is accepted if R_n is not greater than the prescribed tolerance, $STOL$. If $R_n > STOL$ then the solution is rejected and a smaller step size is computed.

A drift correction scheme (Boulanger and Ziotopoulou, 2015) is applied at this point as well as at the beginning of the algorithm to ensure that stress state lies inside the bounding surface. In Ta-Ger model the dimensionless variable ζ tracks the distance of the current state from that surface. Then, if $\zeta > 1$, stresses are projected back to the bounding surface by scaling the stress tensor by ζ at constant p'.

After accepting or rejecting the current sub step, the size of the next sub step is calculated based on the estimated error and the set tolerance. The next pseudo-time step is found from the relation, $\Delta T_{n+1} = \beta \Delta T_n$ where β is chosen so that, $R_n \leq STOL$. Since the local truncation error in the Euler method is $O(\Delta T^2)$, then, $R_{n+1} \approx \beta^2 R_n$ and, $\beta \leq \sqrt{STOL/R_n}$. A conservative choice for β is, $\beta = 0.9\sqrt{STOL/R_n}$ and also constrain it to lie within the limits, $0.1 \leq \beta \leq 1.1$, so that, $0.1\,\Delta T_{n-1} \leq \Delta T_n \leq 1.1\Delta T_{n-1}$. The end of the integration procedure is reached when the entire increment of strain is applied so that $\sum \Delta T_n = T_n = 1$. This type of error control permits the size of each sub increment to vary throughout the integration process, depending on the non-linearity of the constitutive relations. A flowchart of the sub stepping algorithm for Ta-Ger implementation is following presented (Fig. 6.2) and the meaning of the used symbols are listed in Tab. 6.4.

Elastoplastic Stress integration scheme with Sub stepping

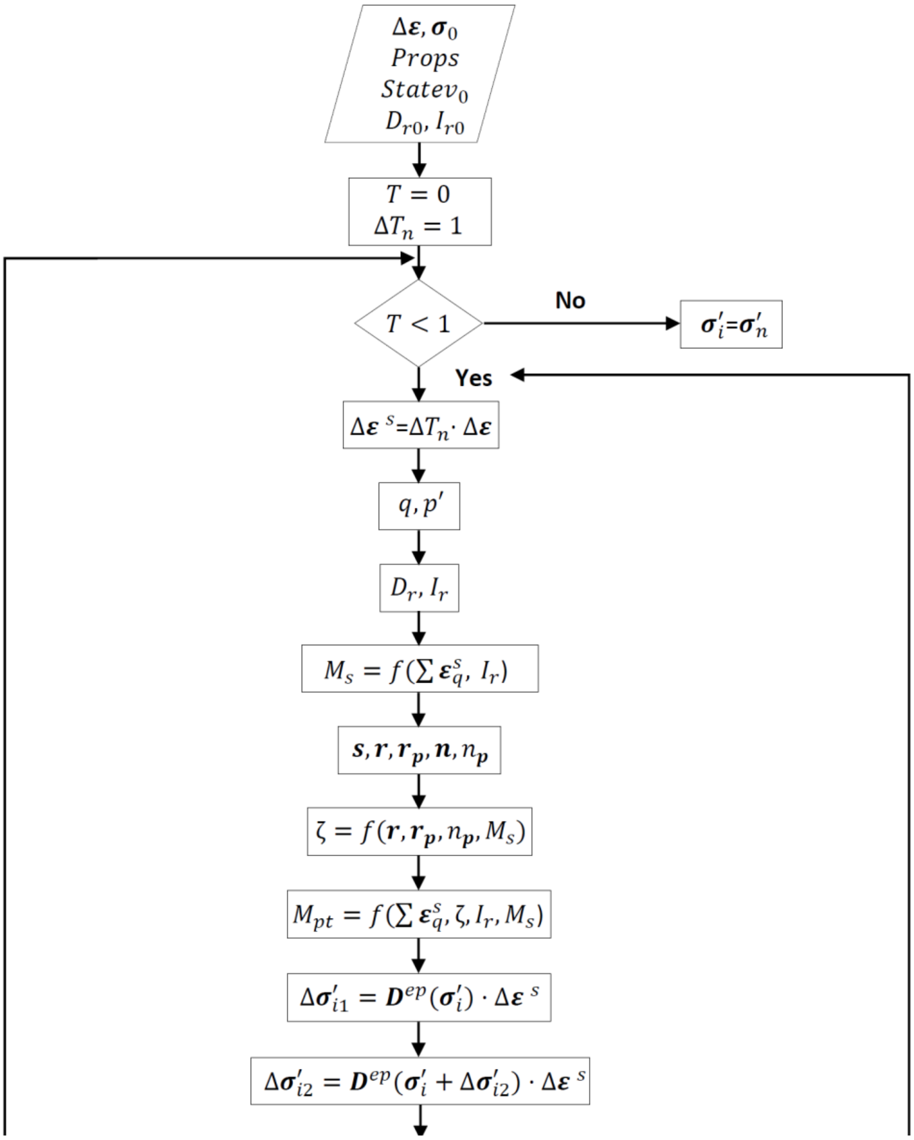

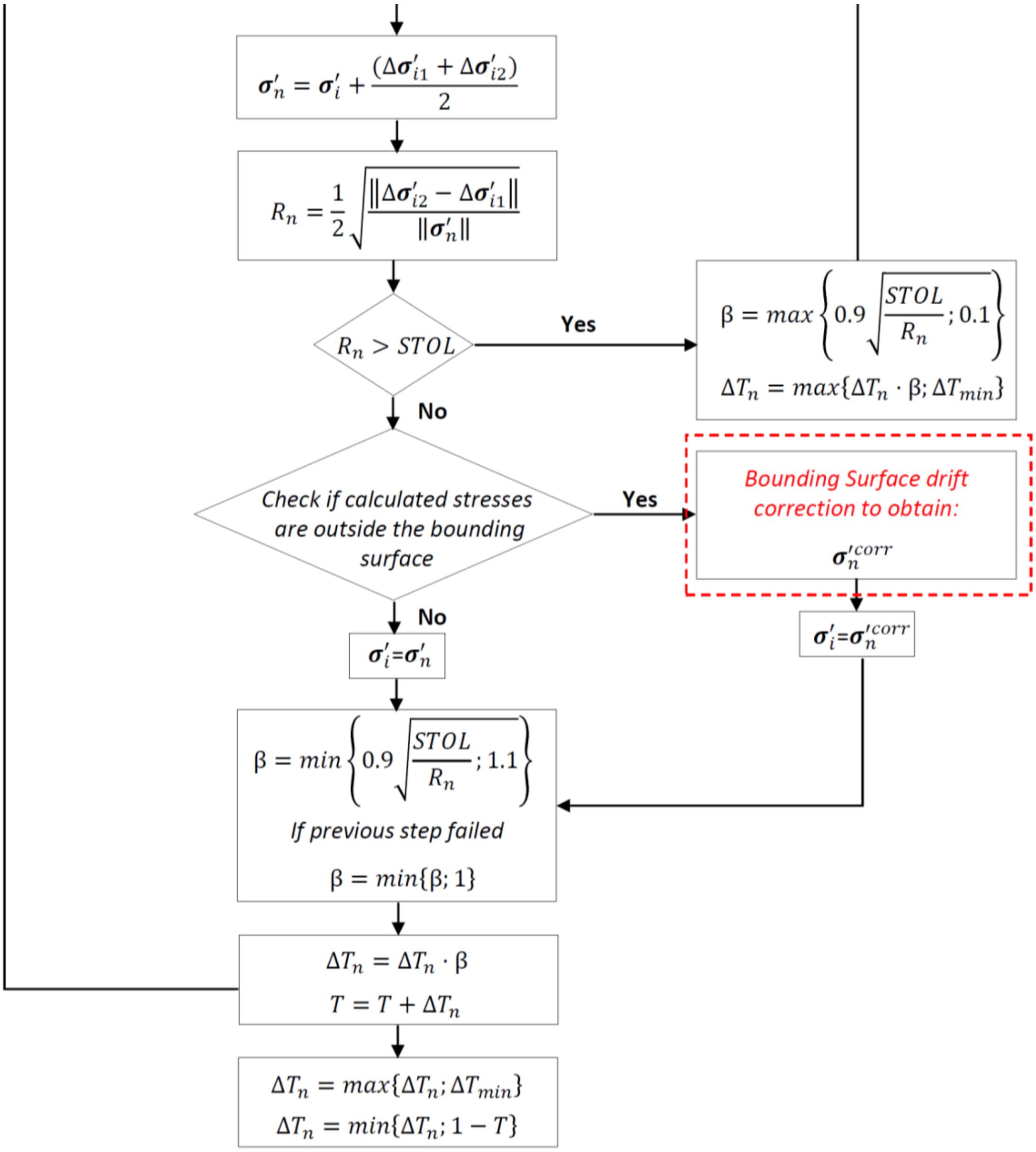
$\boldsymbol{\sigma}'_n = \boldsymbol{\sigma}'_i + \frac{(\Delta\boldsymbol{\sigma}'_{i1} + \Delta\boldsymbol{\sigma}'_{i2})}{2}$
$R_n = \frac{1}{2}\sqrt{\frac{\|\Delta\boldsymbol{\sigma}'_{i2} - \Delta\boldsymbol{\sigma}'_{i1}\|}{\|\boldsymbol{\sigma}'_n\|}}$
$R_n > STOL$
Yes
$\beta = max\left\{0.9\sqrt{\frac{STOL}{R_n}}; 0.1\right\}$
$\Delta T_n = max\{\Delta T_n \cdot \beta; \Delta T_{min}\}$
No
Check if calculated stresses are outside the bounding surface
Yes
Bounding Surface drift correction to obtain:
$\boldsymbol{\sigma}'^{corr}_n$
No
$\boldsymbol{\sigma}'_i = \boldsymbol{\sigma}'_n$
$\boldsymbol{\sigma}'_i = \boldsymbol{\sigma}'^{corr}_n$
$\beta = min\left\{0.9\sqrt{\frac{STOL}{R_n}}; 1.1\right\}$
If previous step failed
$\beta = min\{\beta; 1\}$
$\Delta T_n = \Delta T_n \cdot \beta$
$T = T + \Delta T_n$
$\Delta T_n = max\{\Delta T_n; \Delta T_{min}\}$
$\Delta T_n = min\{\Delta T_n; 1 - T\}$

(a)

Bounding surface drift correction scheme (Boulanger and Ziotopoulou, 2015)

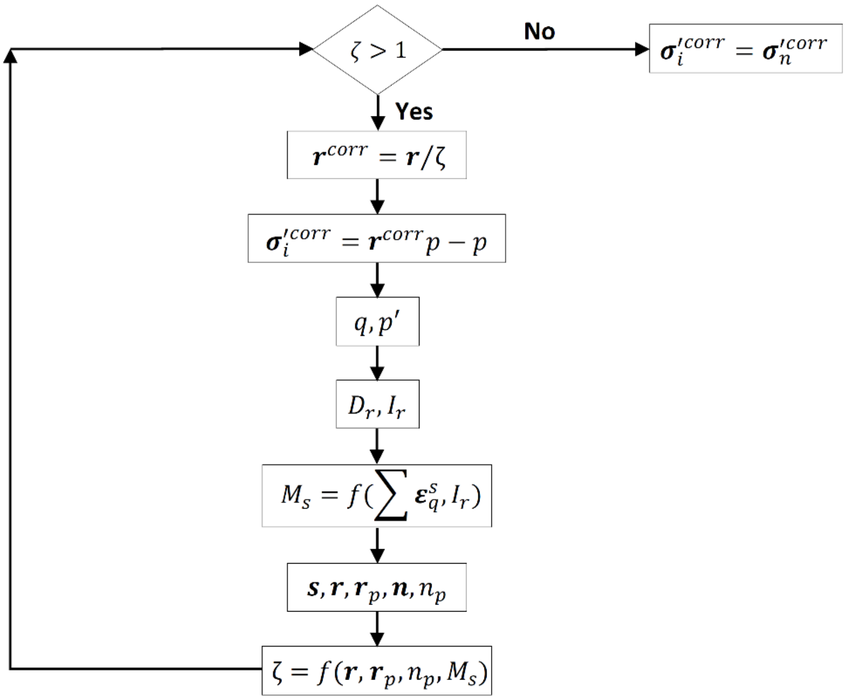

(b)

Figure 6.2. Flowchart for the implementation of Ta-Ger model. Elasto-plastic stress integration scheme with sub-stepping (a); Bounding surface drift correction scheme (b).

Table 6.4. List of symbols used in the flowchart

$\Delta\boldsymbol{\varepsilon}$	Strain increment vector
$\boldsymbol{\sigma_0}$	Historic stress vector
$Props$	Model parameters
$Statev$	State variables
Dr_0	Initial relative density
Ir_0	Initial relative dilatancy index
T	Pseudo time in the range between 0-1 used in the stress integration
ΔT_n	Pseudo time sub increment
$\Delta\boldsymbol{\varepsilon}^s$	Strain sub increment vector
$\Delta\varepsilon^s{}_q$	Deviatoric strain sub increment
$\Delta\varepsilon^s{}_v$	Volumetric strain sub increment
p'	Mean effective stress
q	Deviatoric stress
D_r	Current relative density
I_r	Current relative dilatancy index
M_s	Bounding phase ratio

$\sum \varepsilon_q^s$	Accumulated deviatoric strains
$\boldsymbol{s}$	Second order deviatoric stress tensor
$\boldsymbol{r}$	Stress ratio tensor
$\boldsymbol{r_p}$	Stress ratio tensor at pivot point
$\boldsymbol{n}$	Normalized stress ratio tensor normal to the bounding surface
n_p	Scalar valued stress ratio
ζ	Hardening parameter
M_{pt}	Phase transformation stress ratio
$\boldsymbol{D}^{ep}$	Elasto-plastic matrix
$\Delta\sigma'_{i1}$	First order stress increment
$\Delta\sigma'_{i2}$	Second order stress increment
$\boldsymbol{\sigma'_i}$	Trial stress vector
$\boldsymbol{\sigma'_n}$	Computed stress vector
R_n	Relative error of the stresses for the current time sub increment
$STOL$	Relative tolerance
β	Scalar to calculate the size of the next pseudo time sub increment
ΔT_{min}	Minimum pseudo time sub increment
$\boldsymbol{\sigma}'^{corr}_{i}$	Corrected trial stress vector
$\boldsymbol{\sigma}'^{corr}_{n}$	Computed corrected stress vector
$\boldsymbol{r}^{corr}$	Corrected stress ratio tensor

6.4 VALIDATION AND PARAMETRIC ANALYSIS

The verification and validation of Ta-Ger model implementation is carried out by simulating laboratory tests stress-strain paths. The aim is to check the performance of the model algorithm to predict the measured sand behaviour under different loading and drainage conditions. Experimental data of monotonic triaxial compression tests obtained by (Verdugo and Ishihara, 1996) on Toyoura sand are reproduced. The results are compared with the ones from Ta-Ger authors (Tasiopoulou and Gerolymos, 2016b) by assuming the same values for the model parameters. Furthermore, a parametric analysis is performed to show the effect of model parameters on the results. The model is, then, adapted for unsaturated conditions with the aim to simulate static liquefaction occurrence in partially saturated soils. Finally, the cyclic response is studied by reproducing strain- and stress controlled cyclic loading paths.

6.4.1 Monotonic triaxial compression tests

The validation of the algorithm has been carried out by simulating triaxial compression stress–strain path with the finite element (FE) package implemented in Anura3D code.

The triaxial compression test is carried out as strain-driven, for which the top face of a soil cube is compressed with a constant velocity of 0.001 m/s. The gravity is neglected as its contribution towards the effective stress state is very small and, therefore, the dimensions of the cube do not influence the results; a 1 m wide cube is used. Fig. 6.3 describes the geometry of the problem. The boundary conditions are such that the bottom surface is constrained in normal direction while the lateral surfaces have a compressive load in the normal direction equal to the considered confining stress value. The specimen is assumed to be isotropically consolidated and the initial stress can be initialised using the K_0-procedure with $K_0 = 1.0$.

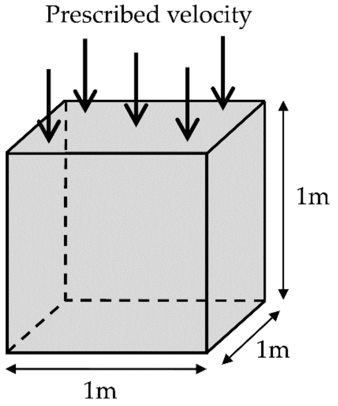

Figure 6.3. Schematic description of triaxial compression test simulation.

The model parameters are listed in Tab. 6.5. They result from a calibration procedure carried out by Tasiopoulou and Gerolymos (2016b) on Toyoura sand.

Fig. 6.4 and. 6.5 show results of drained and undrained simulations, respectively, at various density and initial consolidation stress levels and their comparison with the ones obtained by Tasiopoulou and Gerolymos (2016b) and the experimental data of Verdugo and Ishihara (1996).

Table 6.5. Ta-Ger model parameters calibrated for Toyoura sand.

Symbol	Unit	Value
G_0	-	$1000k_{2max}$
m	-	0.4
ν	-	0.15
ϕ_{cs}	°	33
n	-	$0.4D_{r0} + 0.14$
κ	°	0.8
δ	-	1
Q	-	9.1
R	-	0.77

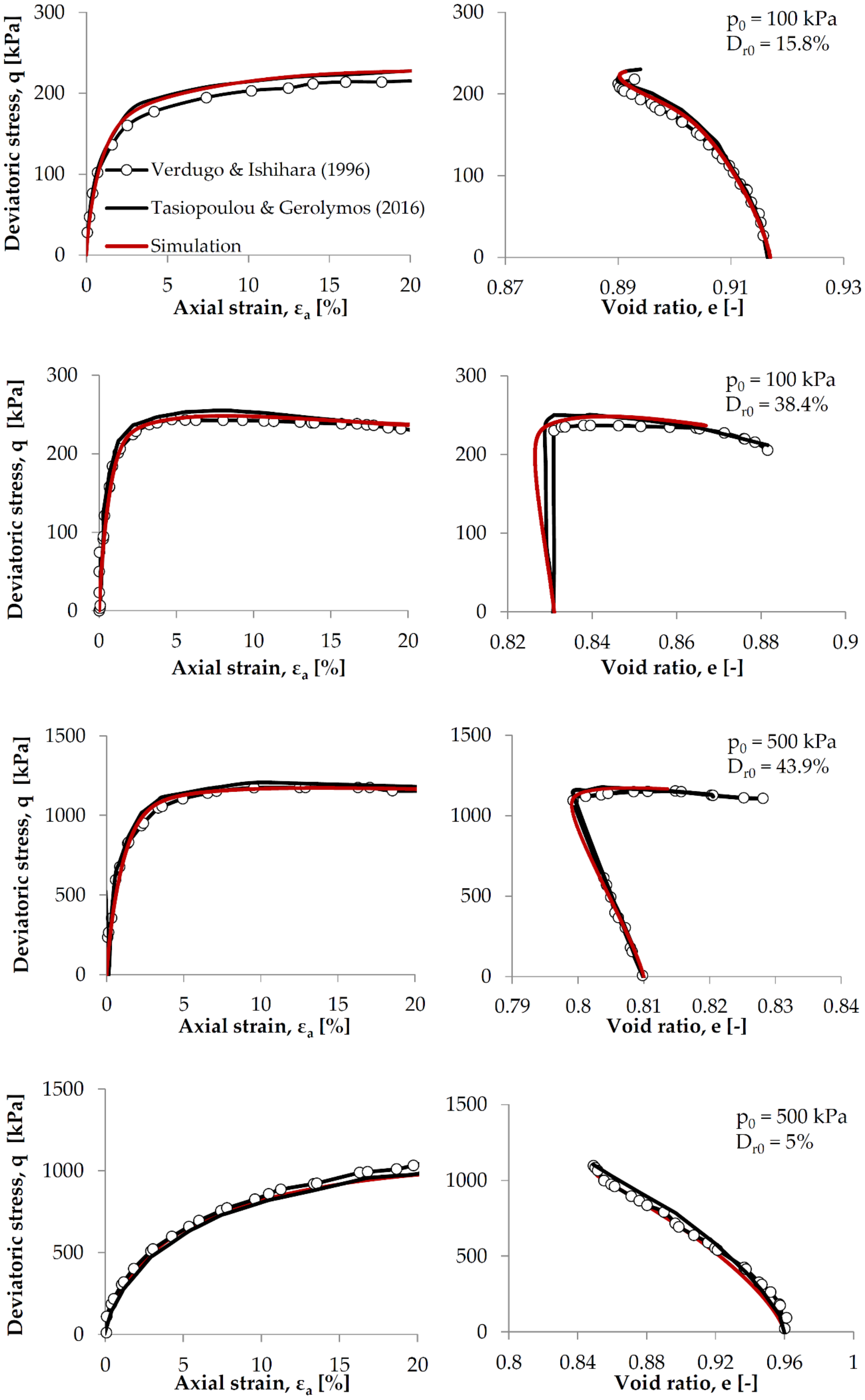

Figure 6.4. Comparison between simulated results and experimental data of drained triaxial tests at various density and initial consolidation stress. (a) Deviatoric stress-axial strain relationship; (b) Deviatoric stress-void ratio relationship.

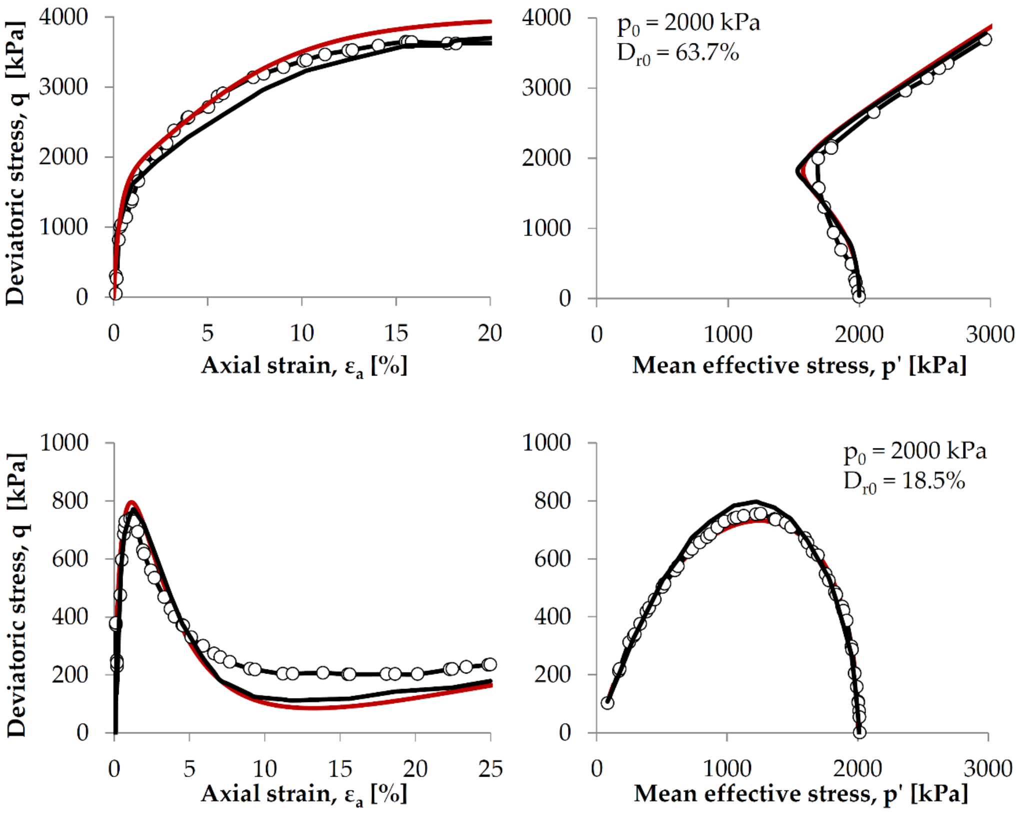

Figure 6.5. Comparison between simulated results and experimental data of undrained triaxial tests at various density and initial consolidation stress. (a) Deviatoric stress-axial strain relationship; (b) stress path in the triaxial plane.

6.4.1.1 Parametric analysis

The aim of this section is not to model a particular set of results but to demonstrate the capability of the formulation to reproduce characteristic features of loose and dense sand behaviour. For a given value of confining stress, the influence of the model parameters n, φ_{s0} and c are investigated since they are the ones that need to be calibrated.

Consider a sandy soil characterized by $e_{max} = 0.977$ and $e_{min} = 0.597$ at two initial relative density, $D_{r0} = 73\%$ and 15%. Constants Q and R have values of 9 and 1 respectively. Parameters n, φ_{s0} and c are obtained from correlations previous described in § 6.2, assuming $\kappa = 0.95$ and $\delta = 3$. The model parameters are indicated in Tab. 6.6. The saturated drained and undrained triaxial paths are simulated assuming a confining pressure of 300 kPa which correspond to different values of initial relative dilatancy index I_{r0} of 1.4 and -0.51.

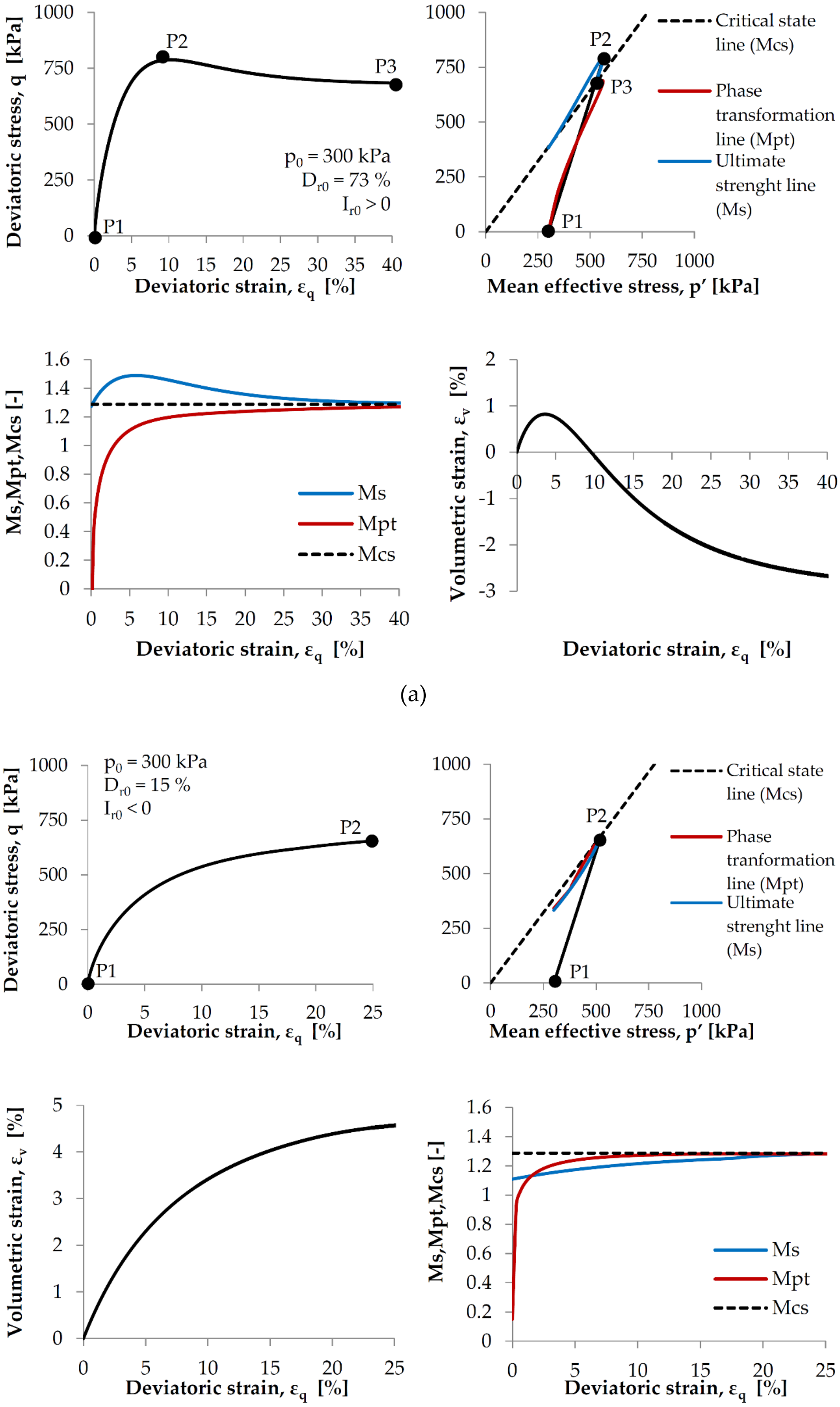

(a)

(b)

Figure 6.6. Simulation results of drained triaxial tests at two initial relative density. (a) D_{r0} = 73%; (b) D_{r0} = 15%.

Table 6.6. Ta-Ger model parameters for dense and loose sand used in monotonic triaxial tests simulations.

Symbol	Unit	Value
G_0	-	2000
m	-	0.4
ν	-	0.15
φ_{cs}	°	32
φ_{s0}	°	$37-28$
n	-	$0.43-0.2$
c	-	$10-4.5$

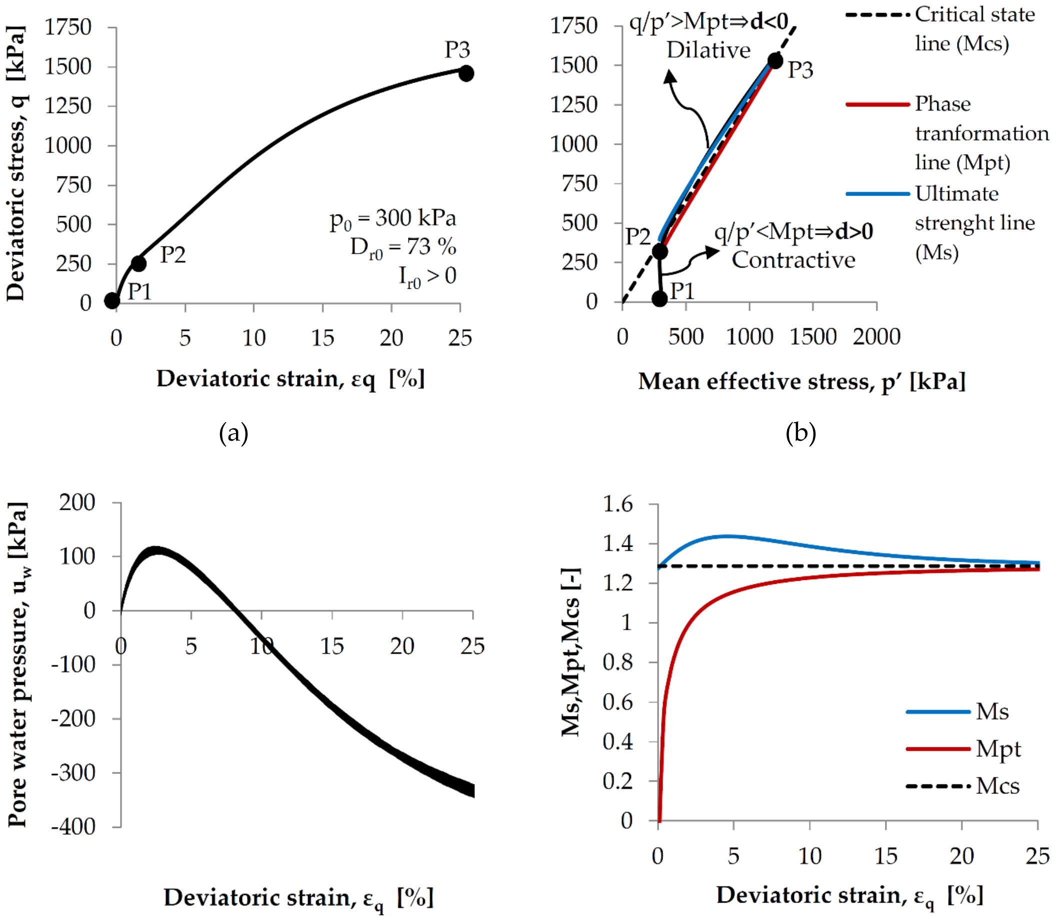

(a) (b)

(c) (d)

Figure 6.7. Simulation results of undrained triaxial tests for $D_{r0}=73\%$.

Fig. 6.6 shows the results of the simulation in drained conditions for dense and loose sand. The dense sample initially contracts from point P1 until the stress ratio reaches the critical state stress state. However, the sample is not at critical state. The behaviour becomes dilative and the shear resistance increases until reaching the peak state at point P2. At this point the sample starts softening from point P2 to point P3 where the stress ratio and the void ratio are at critical state and no more changes in volume occur. The loose sample hardens in a non-linear way from point P1 to P2 and contracts. Once at point P2, the stress ratio is equal to the ultimate strength one ($q/p' = M_{cs}$), and hence the sample is at the critical state. The bounding stress ratio evolves gradually from the initial value $M_{s0} = \frac{6sin\phi_{s0}}{3-sin\phi_{s0}} = 1.11$ to the critical state one $M_{cs} = \frac{6sin\phi_{cs}}{3-sin\phi_{cs}} = 1.29$.

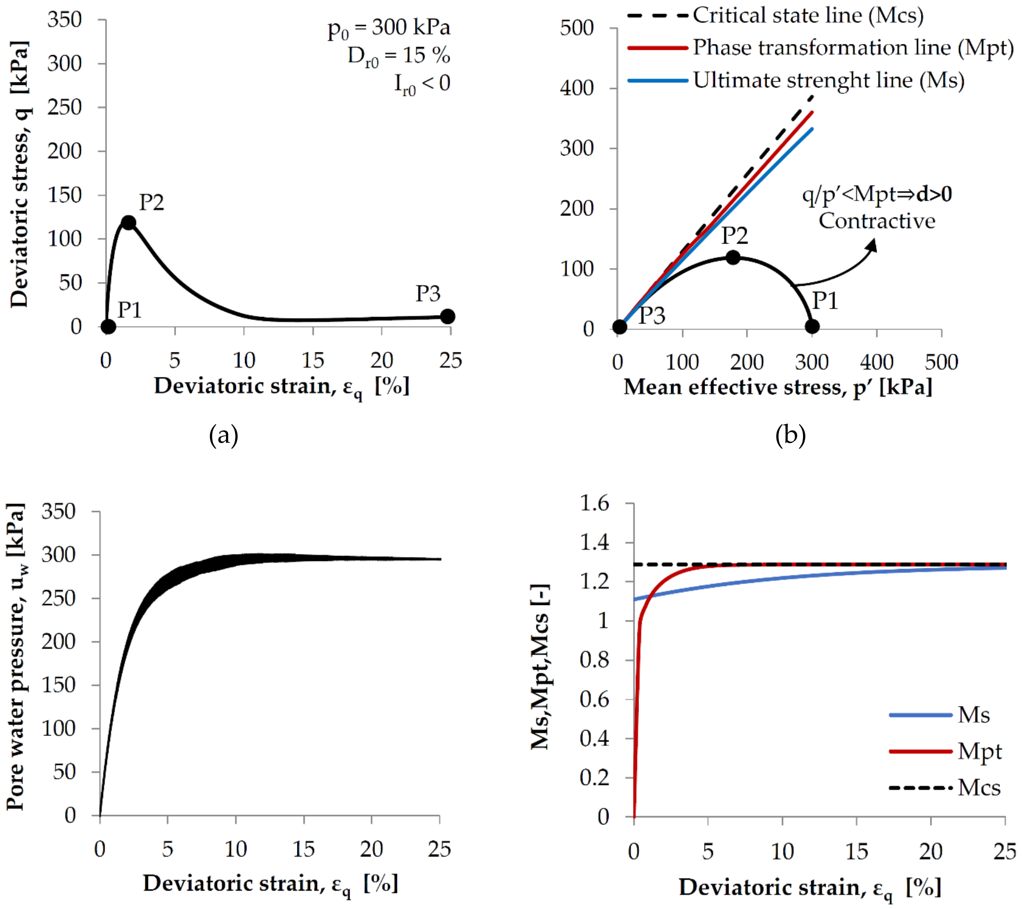

(a) (b)

(c) (d)

Figure 6.8. Simulation results of undrained triaxial tests for $D_{r0} = 15\%$.

Fig. 6.7a show the deviatoric stress-strain relationship and the saturated undrained triaxial path for the case of $D_{r0} = 73\%$. The stress state is initially on the contractive side ($\frac{q}{p'} < M_{pt}$) and hence positive excess pore pressure develops from point P1 to P2. At point P2 the stress path crosses the phase transformation line an after that it passes on the dilative ($\frac{q}{p'} > M_{pt}$) side and hence negative excess pore pressure are generated. The excess pore pressure decreases and the mean effective stress increases together with the deviatoric stress. The stress path continue to rise and lies on the ultimate strength line until reaching the critical state at P3. The evolution of phase transformation M_{pt} and bounding stress M_s ratios are illustrated in Fig. 6.7d as a function of deviatoric strain. As shown in Fig. 6.7b, if the density is hug, a slight drop in mean effective stress can be seen and the behaviour is considerably stiff. When the sand is looser, a point of minimum mean effective stress appear where the dilatancy behaviour changes from contractive to dilative which corresponds to the phase transformation stress ratio.

For the case of $D_{r0} = 15\%$ (Fig. 6.8b) the stress ratio is always smaller than the phase transformation line exhibiting a contractive behaviour. From point P1 to P2 the mean effective stress decreases because of growing of positive excess pore water pressure. The reduction in mean effective stress is accompanied by the reduction in deviatoric stress and hence the path softens from point P2 to point P3 until reaching the critical state. The evolution of phase transformation M_{pt} and bounding stress M_s ratios for the looser sand case are illustrated in Fig. 6.8d as a function of deviatoric strain.

Drained triaxial tests

$D_{r0} = 73\%$

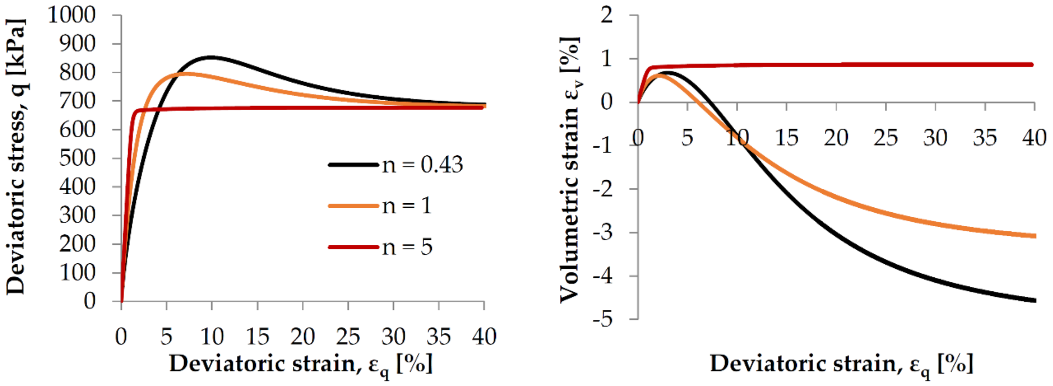

(a)

$\boldsymbol{D_{r0} = 15\%}$

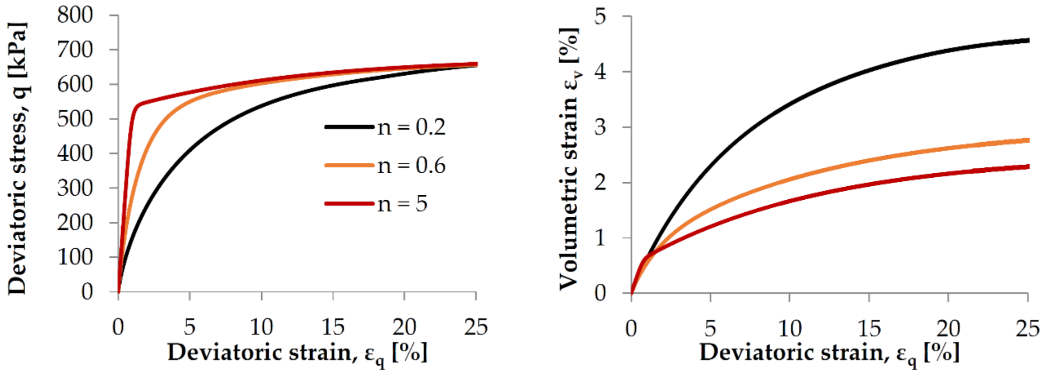

(b)

Figure 6.9. Effect on drained behaviour of dense ($D_{r0} = 73\%$) (a) and loose soil ($D_{r0} = 15\%$) (b) of different values of hardening parameter n.

In the following, a sensitivity analysis is finally presented to examine the effect of parameters n, φ_{s0} and c on drained and undrained soil response. The hardening exponent n controls the degree of coupling between the elastic and the perfectly plastic behaviour. As shown in Fig. 6.9 and 6.10 when the value of n increases the response tends to be elastic/perfectly-plastic while, when it decreases, the coupling between the elastic and plastic components of total strain increment increases until ultimate failure is reached, resulting in a smoother transition to failure. Moreover, by decreasing the value of exponent n, the failure state is faster reached.

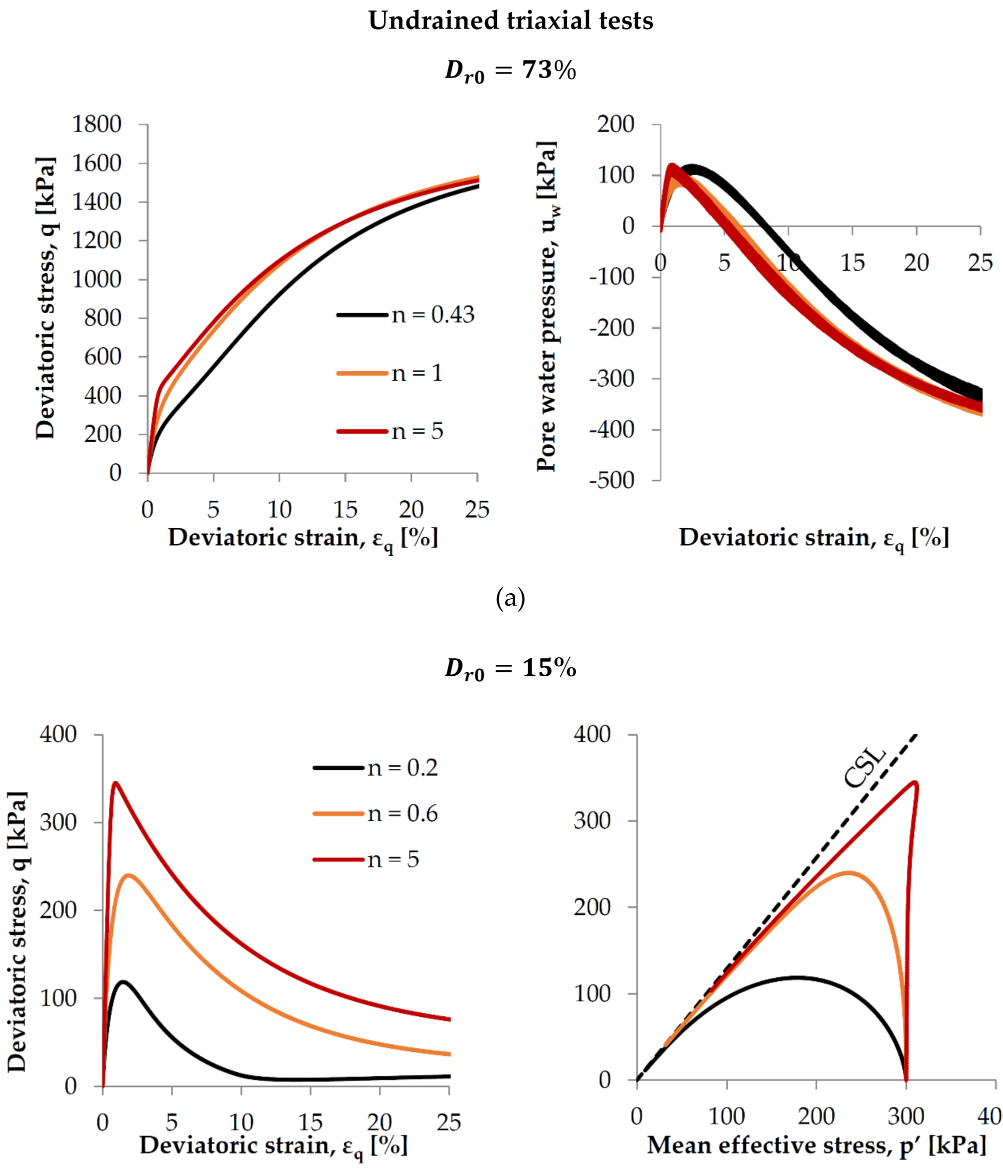

(a)

(b)

Figure 6.10. Effect on undrained behaviour of dense (D_{r0} = 73%) (a) and loose soil (D_{r0} = 15%) (b) of different values of hardening parameter n.

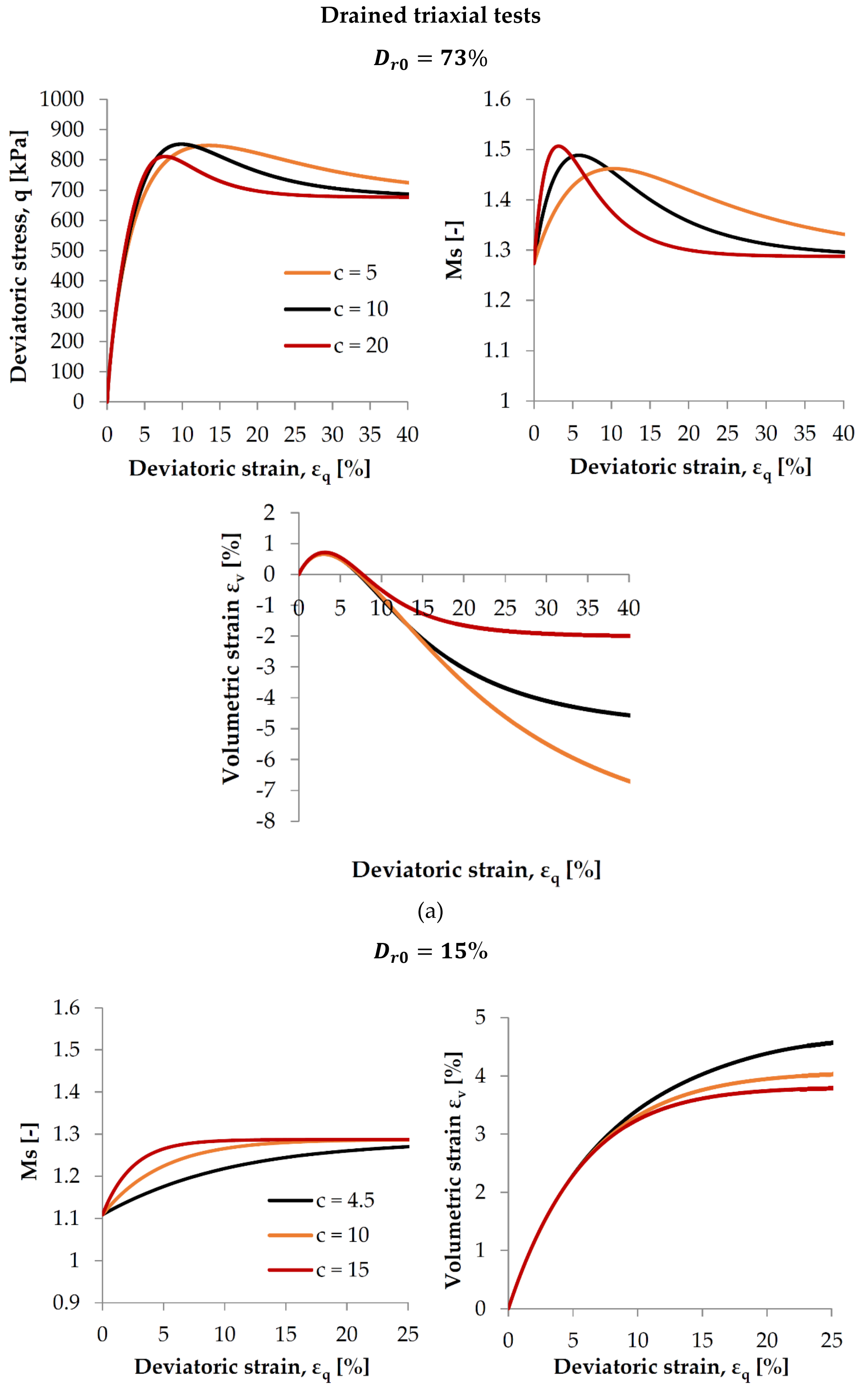

(a)

(b)

Figure 6.11. Effect on drained behaviour of dense (D_{r0} = 73%) (a) and loose soil (D_{r0} = 15%) (b) of different values of hardening parameter c.

Undrained triaxial tests

D_{r0} = 73%

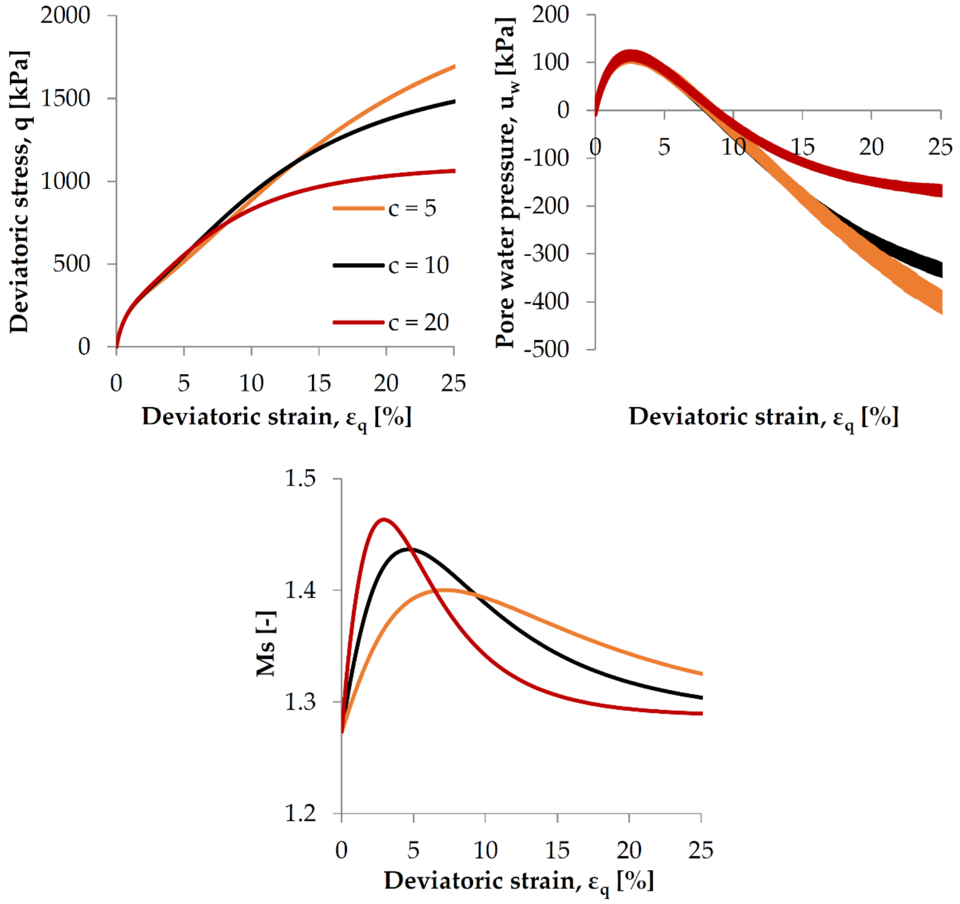

(a)

D_{r0} = 15%

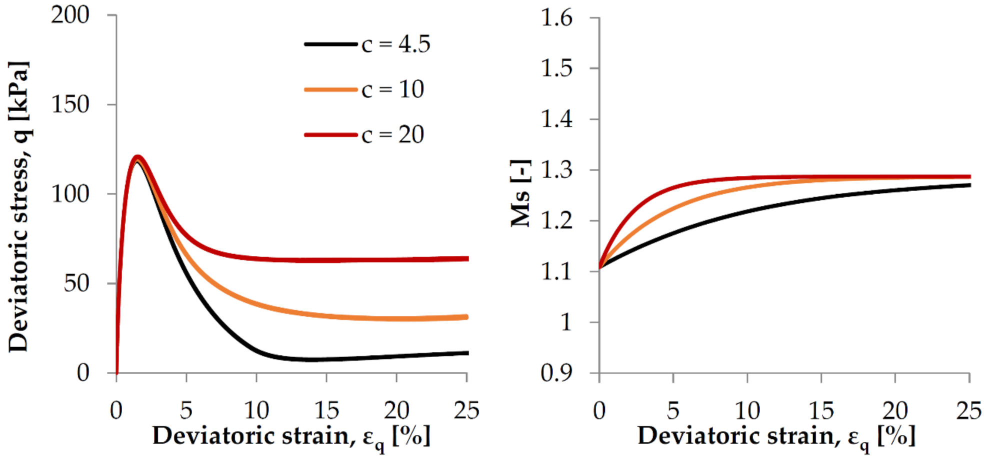

(b)

Figure 6.12. Effect on undrained behaviour of dense (D_{r0} = 73%) (a) and loose soil (D_{r0} = 15%) (b) of different values of hardening parameter c.

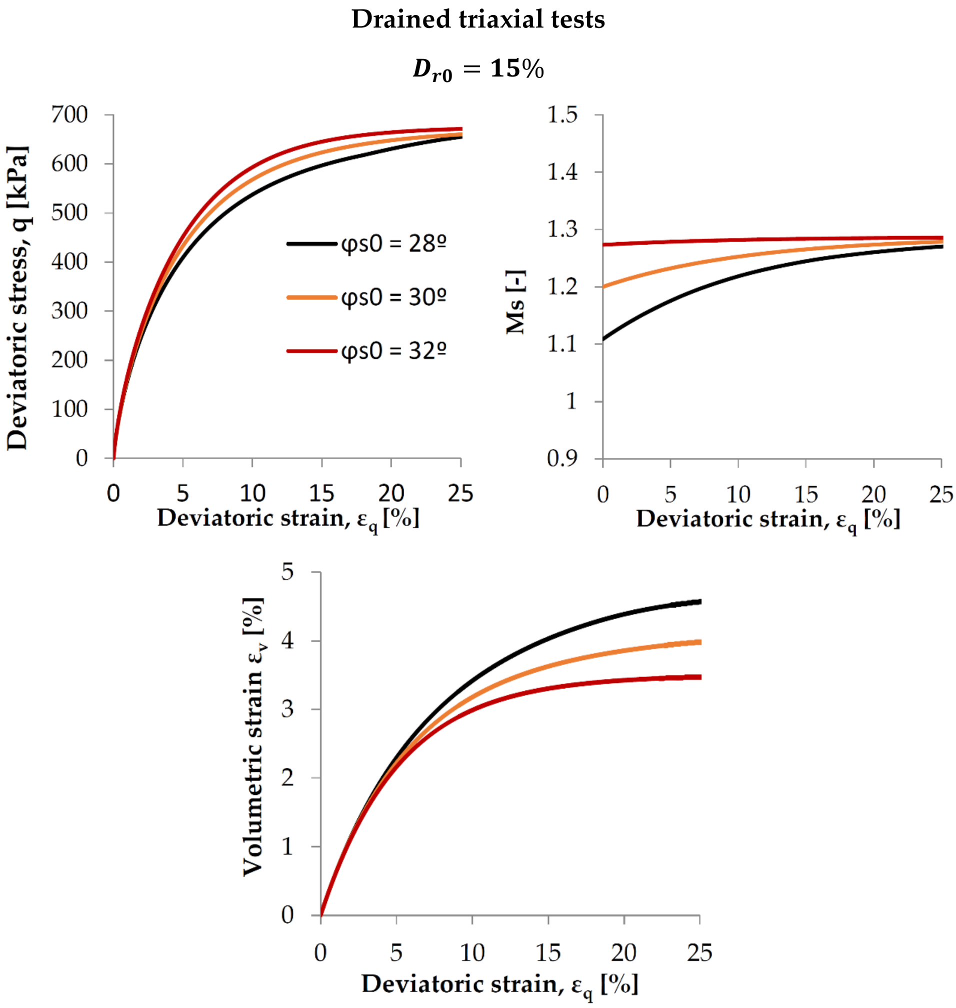

Figure 6.13. Effect on drained behaviour of loose soil (D_{r0} = 15%) different values of initial friction angle φ_{s0}.

The coefficient c controls the rate of evolution of the bounding, M_s, and the phase transformation, M_{pt}, stress ratio. For large values of c, the critical state ($M_{cs} = 1.29$) is reached fast as shown in the evolution of the bounding stress ratio with accumulated deviatoric strains (Fig. 6.11 and 6.12). This tendency results in a less contractive behaviour of the loose soil and a less dilative behaviour for the dense soil in the deviatoric stress-strain plane ($q - \varepsilon_q$). Fig. 6.13 and 6.14 show that decreasing values of φ_{s0} leads to an enhanced contractive behaviour of the soil.

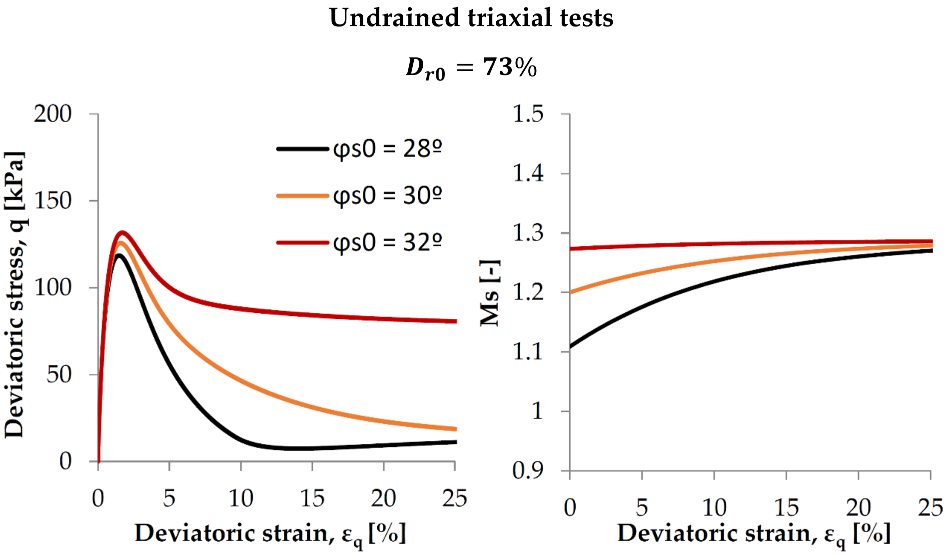

Figure 6.14. Effect on undrained behaviour of loose soil (D_{r0} = 15%) of different values of initial friction angle φ_{s0}.

6.4.2 Unsaturated monotonic triaxial compression tests

Ta-Ger model implementation was generalized for unsaturated conditions in Anura3D code. To do that, the model has been formulated in terms of Bishop's stress σ'' (Bishop, 1959):

$$\sigma'' = \bar{\sigma} + \chi \cdot s \tag{6.28}$$

where, $\bar{\sigma}$ is the net stress defined as the difference between the total stress and gas pressure and s is the suction defined as the difference between gas and water pressure. Parameter χ is assumed to be equal to the degree of saturation. The Terzaghi's effective stress is recovered when pore water pressure becomes positive. The degree of saturation is correlated with the suction in a simple way by means of a constant water retention curve. With the definition of the constitutive equations in terms of Bishop's stress, suction induces increments of the elastic stiffness and strength. The generalization of the equation to unsaturated states does not intend to reproduce the whole behaviour of the unsaturated soils. The model is not able to reproduce, for instance, the swelling and collapse response during wetting.

The previous examples of undrained triaxial stress paths of a loose sand is repeated for different initial values of saturation degree. The Van Genuchten model (Van Genuchten, 1980) has been selected for the water retention curve whose parameters are listed in Tab. 6.7. The predicted response of the loose sand in terms of stress-strain relationship, stress path, volumetric strains, suction and degree of saturation is plotted in Fig. 6.15.

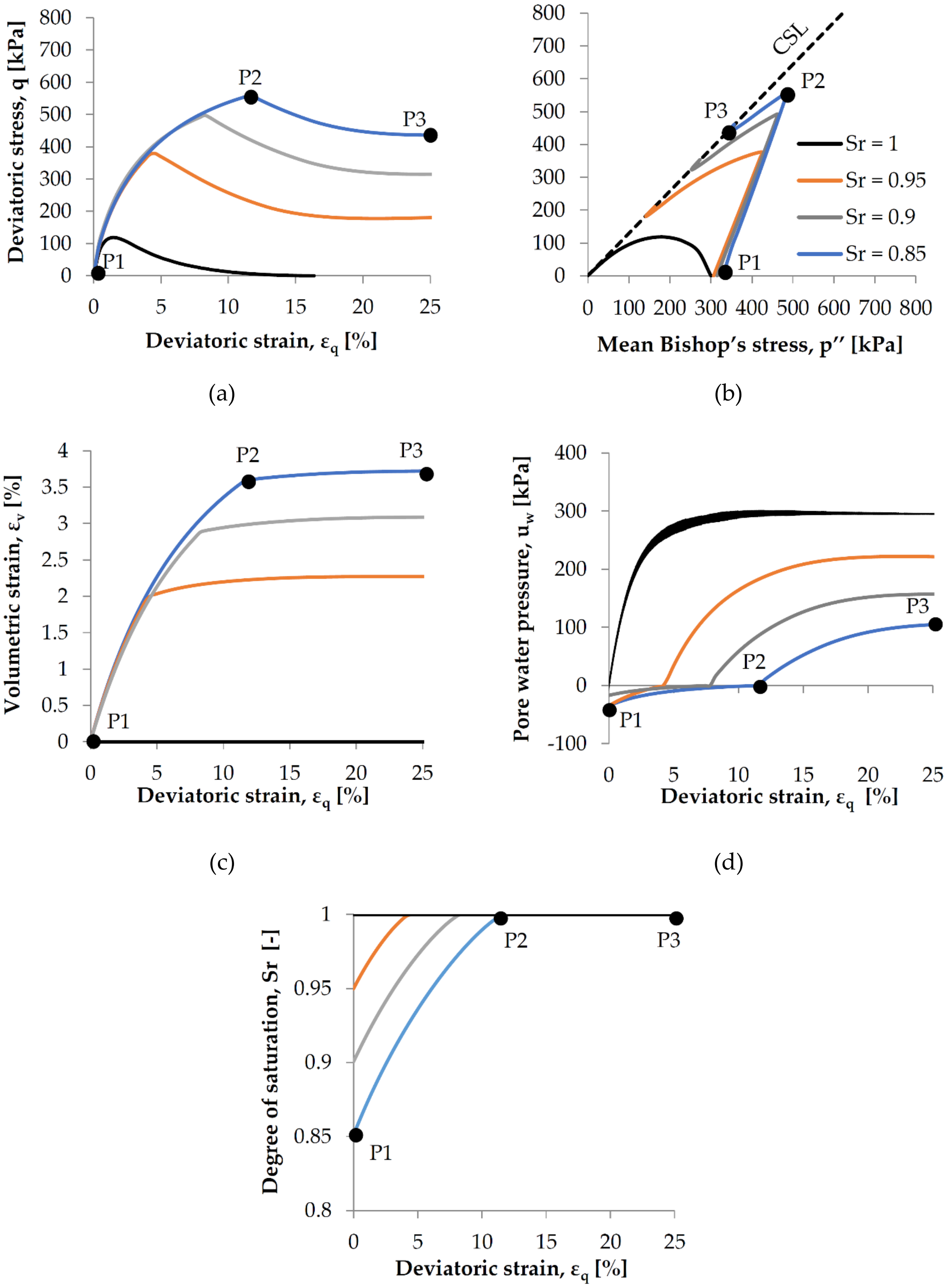

(a)

(b)

(c)

(d)

(e)

Figure 6.15. Results of simulation of monotonic triaxial loading on unsaturated loose sand ($D_{r0} = 15\%$): (a) deviatoric stress-strain relationship; (b) stress path in the triaxial plane; (c) Volumetric strain-deviatoric strain relationship; (d) suction-deviatoric strain relationship; (e) degree of saturation-deviatoric strain relationship.

In the first stage, as a result of progressive volumetric contraction during shearing, the sample becomes saturated and suction reduces until zero (from P1 to P2). The subsequent compressive volumetric strains result in an increasing of pore water pressure that leads to reduce effective stress and strength (from P2 to P3).

Table 6.7. Van Genuchten water retention curve parameters.

Symbol	Unit	Value
S_{rmin}	-	0
S_{rmax}	-	1
p_0	kPa	10
λ	-	0.1

6.4.3 Cyclic triaxial tests

Aiming to assess the capabilities of Ta-Ger model in reproducing the dynamic behaviour of soils and to verify the model implementation under cyclic loading conditions, numerical simulations of strain- and stress- controlled conventional tests have been carried out.

6.4.3.1 Strain-controlled undrained tests

Strain controlled cyclic triaxial tests have been performed with Anura3D code following a similar procedure indicated in § 6.4.1. Unlike the simulation of a monotonic test, a sinusoidal velocity is applied on the top face nodes of the soil cube (Fig. 6.16).

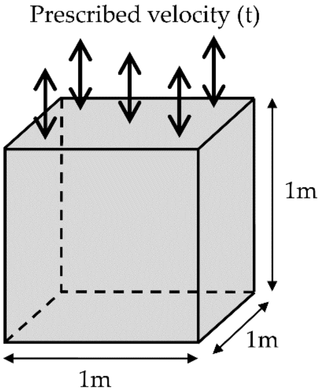

Figure 6.16. Schematic description of cyclic triaxial compression test simulation.

The velocity-time function shown in Fig. 6.17 is assigned to the code based on the numerical implementation explained in § 3.4.3. The same Ta-Ger model parameters used to simulate the monotonic tests in § 6.4.2 (Tab. 6.6) are assigned. Sandy soil samples at two initial relative density, D_{r0} = 73% and 15% are considered in the simulations.

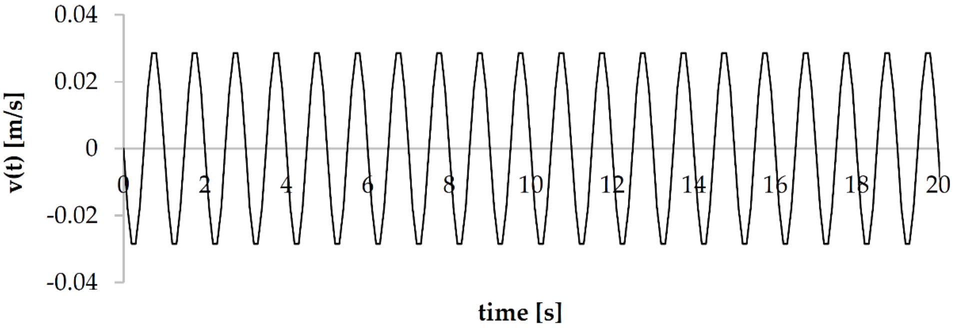

Figure 6.17. Input prescribed velocity ($N_{cycles} = 20; A = 0.03m/s, T = 1s$)

As shown in Figs 6.18 and 6.19, cyclic paths are characterized by an excessive pore pressure build up, followed by a decrease of both the mean effective stress and the shear stiffness until reaching a complete loss of shear resistance. The number of axial strain cycles necessary to liquefaction is equal to 3 for the loose sample while it increases to 8 for the denser.

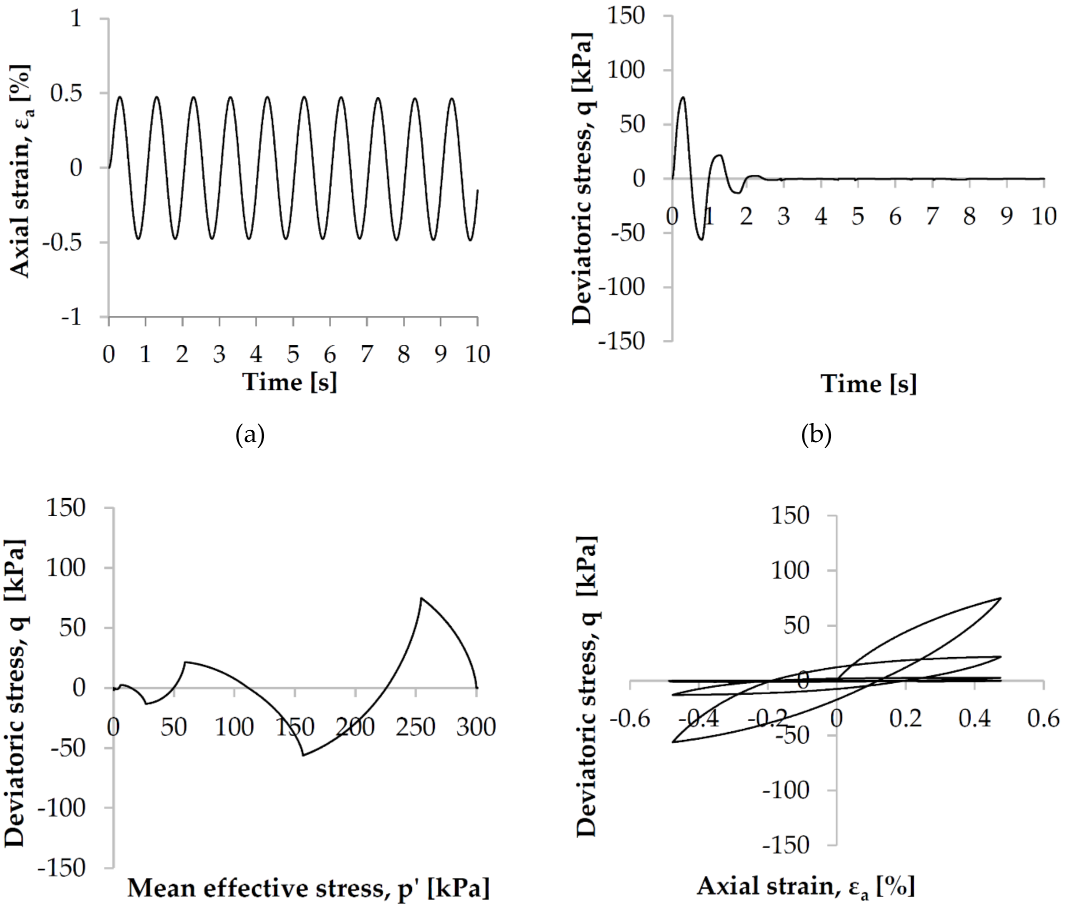

(a) (b)

(c) (d)

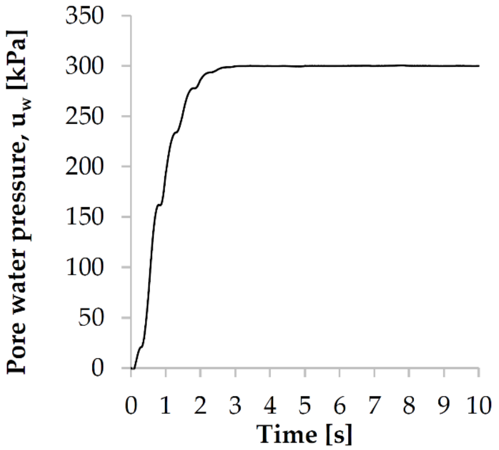

(e)

Figure 6.18. Simulation results of strain-controlled cyclic undrained triaxial test for $D_{r0} = 15\%$ in terms of: (a) applied axial strain; (b) deviatoric stress with time; (c) $p' - q$ curve; (d) $q - \varepsilon_a$ curve; (e) pore pressure evolution with time.

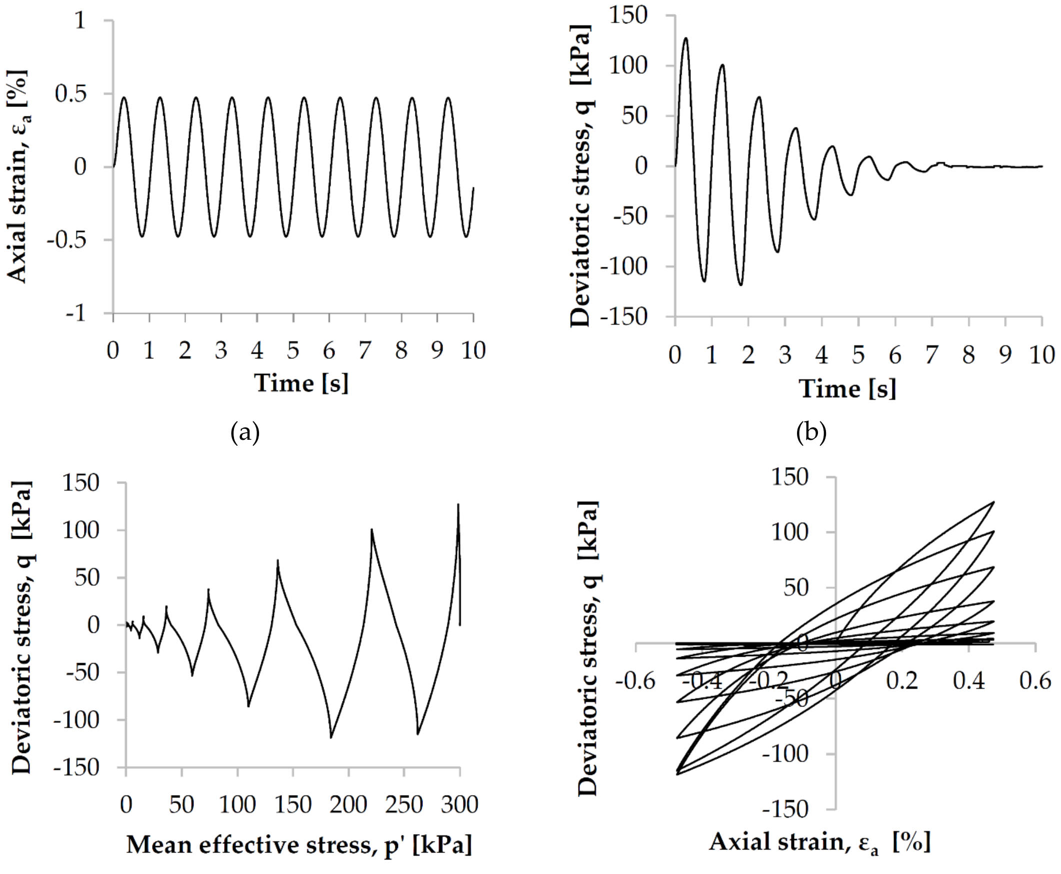

(a) (b)

(c) (d)

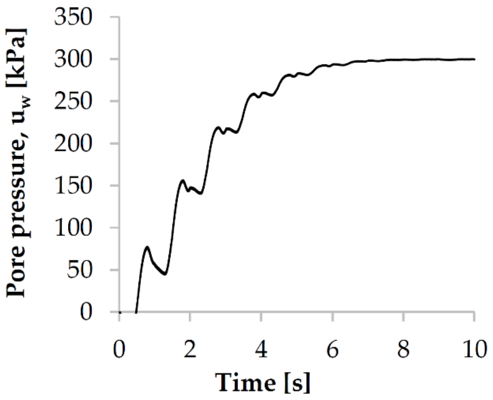

(e)

Figure 6.19. Simulation results of strain-controlled cyclic undrained triaxial test for D_{r0} = 73% in terms of: (a) applied axial strain; (b) deviatoric stress with time; (c) $p' - q$ curve; (d) $q - \varepsilon_a$ curve; (e) pore pressure evolution with time.

Effect of parameter η

As mentioned in § 6.2 matrix $\{\eta\} = \eta\{I\}$ (Gerolymos and Gazetas, 2005) accounts for stiffness degradation affecting the shape and size of the hysteretic loops. With the aim of observe the effect of this parameters, further simulation are performed for the case of $D_{r0} = 73\%$ and three different values of η. Results shown in Fig. 6.20 indicate that greater is η, greater is the shear stiffness and the area of the loop, thus the hysteretic damping.

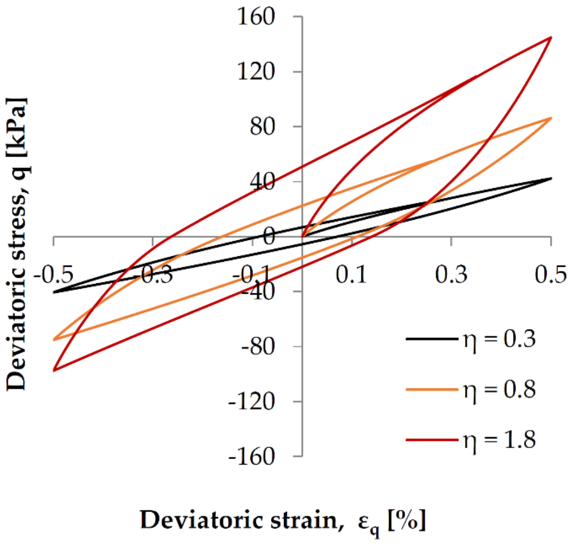

Figure 6.20. Effect on cyclic undrained behaviour of parameter η.

6.4.3.2 Stress-controlled undrained tests

Since the current version of Anura3D code does not allow to simulate cyclic loading conditions, the algorithm has been verified externally in order to simulate stress-controlled cyclic tests.

The model parameters are indicated in Tab. 6.8. A sandy soil characterized by $e_{max} = 0.977$ and $e_{min} = 0.597$ at an initial relative density of $D_{r0} = 73\%$, is considered. Constants Q and R have values of 9 and 1 respectively. Parameters n, φ_{s0} and c are obtained from correlations described in § 6.2, assuming $\kappa = 0.95$ and $\delta = 3$. The cyclic undrained triaxial paths are simulated assuming an initial confining pressure of 150 kPa, which correspond to an initial relative dilatancy index of $I_{r0} = 1.91$. A value of 20 kPa for the cyclic deviatoric stress applied is considered.

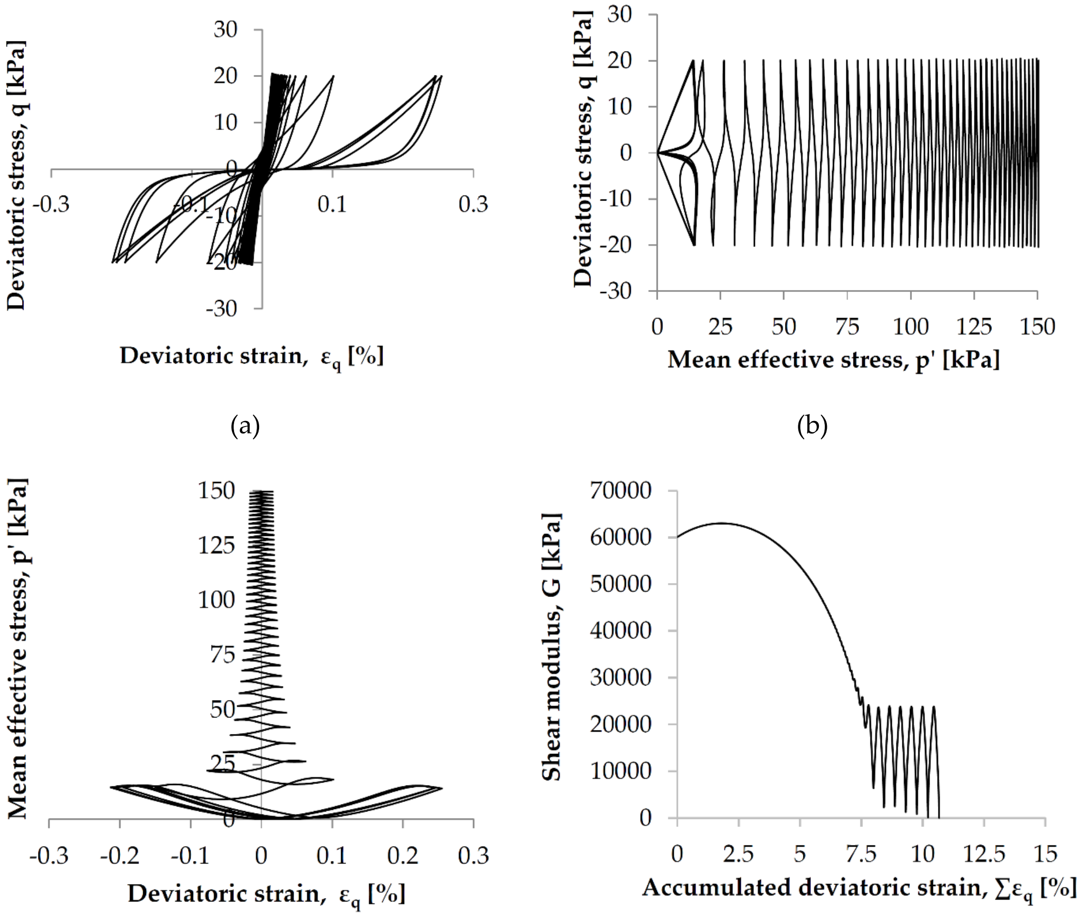

(a)

(b)

(c)

(d)

Figure 6.21. Simulation results of stress-controlled cyclic undrained triaxial test for $D_{r0} = 73\%$ in terms of: (a) $q - \varepsilon_q$ curve; (b) $p' - q$ curve; (c) $p' - \varepsilon_q$ curve; (d) Shear modulus curve.

Table 6.8. Ta-Ger model parameters for dense sand used in cyclic stress-controlled simulations.

Symbol	Unit	Value
G_0	-	8000
m	-	0.4
ν	-	0.15
φ_{cs}	°	31
φ_{s0}	°	39
n	-	0.43
c	-	11.7

Fig. 6.21 shows the typical undrained behaviour of dense sand under cyclic loading with the charactistic "butterfly" shape.

Effect of hardening parameter $\boldsymbol{n}$

As presented in Tasiopoulou and Gerolymos (2016b), the response under cyclic undrained loading is greatly affected by the hardening parameter n in terms of number of cycles required to cause liquefaction ($p' = 0$).

The previous simulation is repeated for two extreme values of $n = 0.2$ and 0.8. As shown in Fig. 6.22, in case of $n = 0.2$, 14 cycles of loading are required for liquefaction occurrence. On the contrary, the higher value of hardening parameter of $n = 0.8$ leds to reproduce cyclic mobility phenomenon for which liquefaction cannot be achieved.

It worth to mention that, since exponent n is crucial in the determination of the number of cycles necessary to cause liquefaction, Ta-Ger authors propose to express it as function of the cumulative deviatoric strain increment, for more realistic results:

$$n = n_f + \left[n_{peak} + \left(n_0 - n_{peak}\right)e^{-\beta \sum d\varepsilon_q} - n_f\right]e^{-\gamma(1-sign(\sum d\varepsilon_p))\sum d\varepsilon_q} \tag{6.29}$$

where, n_f is the final value when p tends to zero, n_0 is the initial value, n_{peak} is the potentially reached maximum value dependent on constants β and γ.

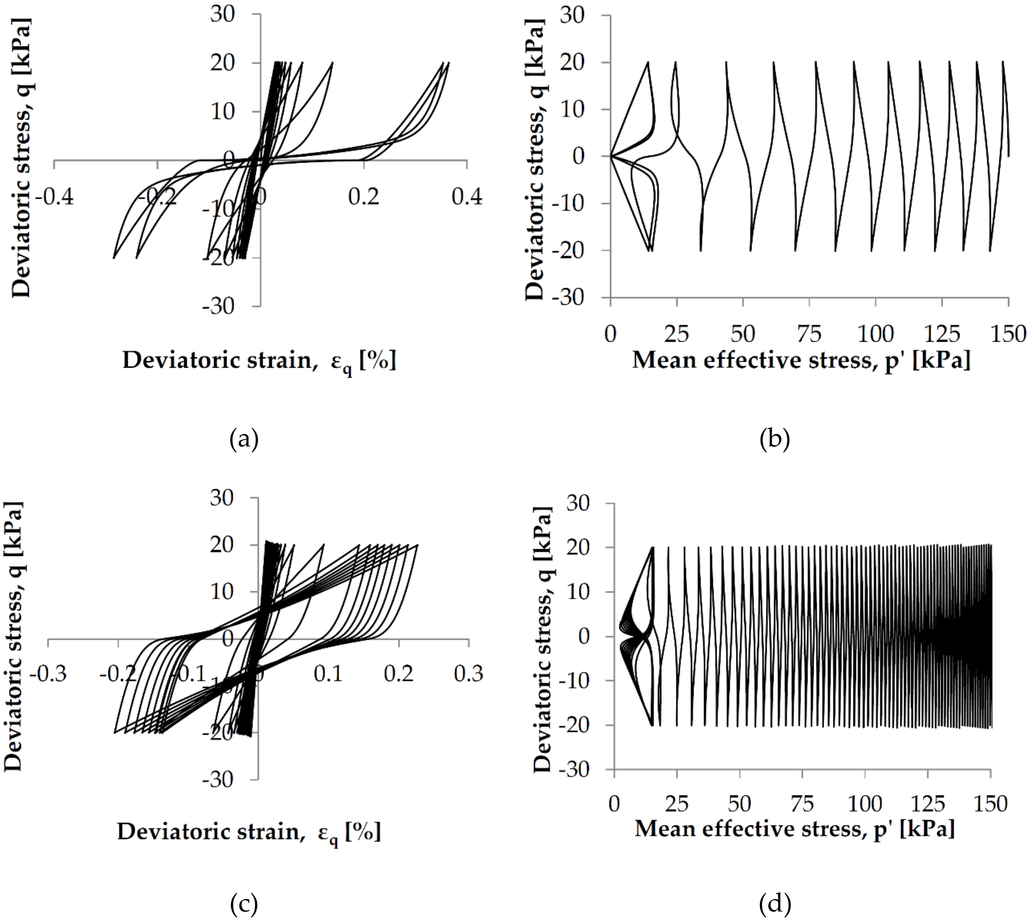

(a) (b)

(c) (d)

Figure 6.22. Effect on cyclic undrained behaviour of parameter n: (a) $n = 0.2$; (b) $n = 0.8$.

CHAPTER 7 - LIQUEFACTION-INDUCED FLOW-LIKE LANDSLIDE

A real case of flow-like landslide induced by static liquefaction, occurred in Val d'Arán (Catalonia, Spain), is investigated in this chapter. In situ and laboratory tests are carried out to characterize the material involved in the failure. Data from undrained triaxial tests showed the liquefaction susceptibility of the mobilized soil and allowed to calibrate the Ta-Ger model parameters. In the last part, plane strain analyses on a representative cross-section are performed with MPM in order to simulate triggering and post-failure stage. As expected, it was found that liquefaction susceptibility, accounted for in the model through the relative dilatancy index I_r plays a key role for the slide-to-flow transition to occur.

7.1 INTRODUCTION

Valarties flow-like landslide occurred on 11 May 2018 in Val d'Arán (Catalonia, Spain) after a period of significant rainfall. Fig. 1a shows a front view of the landslide 10 days after the event. The upper scarp is located 1380m.a.s.l, 150m high from the riverbed. The landslide involved an estimated volume of 50.000 m3 of glacial and colluvial material, travelled 280m down to the valley floor and climbed about 100m on the opposite hillside up to 1249m.a.s.l. (Fig. 7.1b). Although being difficult to guarantee, it is accepted that the most probable triggering reason was an increase in pore water pressure induced by an inflow from karstic spring in the upper part of the slope. After failure, a significant amount of water flowed out from the head scarp. Field surveys and laboratory tests in combination with information gathered by the "Cartographic and Geological Institute of Catalonia" provided a basic geological understanding and offered details of the main characteristics of the landslide and materials involved in the failure.


(a) (b)

Figure 7.1. View of the landslide 10 days after the event (courtesy of Conselh Generau d'Aran) (a) Landslide scar; (b) Mobilized material accumulated on the opposite slope.

Flow-like landslides can begin with a mechanism of general shear failure but are characterized by a subsequent spreading, outside the failure area, of the slide material that adapts itself to any morphological slope change. Johnson and Rodine (1984) and Ellen and Fleming (1987) described the potential for a transformation from sliding into flowing and a first general approach of the mechanisms involved. Both contributions resulted in a mobility index based on geotechnical material properties and, in particular, the liquid limit and the water content.

Iverson (1997), in a comprehensive review, provided a detailed analysis of theoretical aspects and described data gathered by the U.S. Geological Survey in large-scale flume experiments. The authors proposed three main mechanisms responsible for the mobilization of debris flows. The development of positive excess pore pressures in the post-failure stage, due to static or dynamic effects, and the associated decrease of effective stresses are considered to be fundamental in the triggering of flow-like landslides. This hypothesis is also supported by more recent studies that includes geotechnical laboratory tests and some field observations (Gabet and Mudd, 2006) and centrifuge tests (Milne *et al.*, 2012). The role played by static liquefaction in the evolution of slope instabilities in flow-like landslides has been extensively investigated in the literature (Cascini *et al.*, 2010). (Buscarnera and Prisco, 2013) identified, in the saturation process caused by volumetric instability, a relevant explanation of this phenomenon in unsaturated slopes.

The lack of data in real cases of flow-like landslides led several authors to carry out flume laboratory tests. The aim was to capture the fundamental aspects of rainfall-induced landslides and to assess the role played by single factors such as geometry, soil properties and stress conditions on the development of the failure mechanism including static liquefaction (Wang and Sassa, 2001; Okura *et al.*, 2002; Olivares *et al.*, 2009; De Groot *et al.*, 2018).

In this section, the site of the landslide is investigated and the soils involved in the failure is characterized. Undrained triaxial tests demonstrated the liquefaction potential of the mobilized soil and allowed the calibration of the Ta-Ger model parameters. The case was first analysed without accounting for the potential liquefaction of the involved materials. Under such assumption, it was not possible to reproduce the observed run-out even in the case of including a realistic material strain softening. The MPM-modelling of the landslide including a sensitivity analysis with respect to the initial porosity, a relevant parameter controlling the liquefaction susceptibility. Calculated stress paths, velocity and displacements in different locations along the landslide help to understand the phenomena taking place in a flowslide.

7.2 Geological context and case description

The Valarties landslide is located in the Val d'Aran, a region in the Spanish side of the Central Pyrenees. It took place just before midnight of May 11th, 2018 at the lower part of a west-facing slope in a tributary valley that drains the Valarties River (Fig. 7.2a). The original slope was covered with dense forest and had an average slope angle of about 33 degrees.

The mass movement involved an estimated volume of about 50,000 m3, which makes the event the largest reported slope failure in the southern Pyrenees of the last decades. The landslide did not cause important damage, but covered a secondary road with sediments and affected the water supply of downstream villages. Fortunately, the landslide sediment was not able to create an uncontrolled dam, which might have provoked a catastrophic dam-breach flooding of the downstream area.

The climate of the Val d'Aran region is influenced by the westerly winds from the Atlantic Ocean and the orographic effects of the Pyrenees. It can be defined as alpine Atlantic climate. In the valley floor, the annual precipitation is about 1000 mm and the mean temperature is 9° (CAC, 2004).

From a geological point of view, the region is located in the axial zone of the Pyrenees, where the bedrock mainly consists of metamorphic Paleozoic rocks and intrusions of late hercinian plutonic rocks (Fontboté, 1911). In addition, quaternary superficial formations comprising colluvium and glacial deposits cover the bedrock with variable thicknesses. In particular, the glaciations have strongly shaped the present morphology of the region creating steep-sided and U-shaped valleys (Pallàs *et al.*, 2006).

The lithological description of the failed slope can be divided into two main units: 1) the karstic bedrock made of massive marbles of Carboniferous-Permian age, and 2) superficial formations including a glacial deposit at the bottom and a colluvium at the top. The soil-rock contact is highly irregular since the marbles were strongly reshaped by the glacier erosion. Therefore, the thickness of the superficial formations varies between less than 1 m and more than 15-20 m. The glacial deposit can be described as a matrix-supported sandy soil with a thickness varying between 1 and 10 meters, while the colluvium has generally a smaller thickness of 0.5 to 5 meters. The head scarp of the failure was located at the bedrock-soil contact, which outcropped with a slope angle of about 56 degrees at an altitude of 1375 m.a.s.l (Fig 7.2b). Field observations showed that the initial failure was affected by the bedrock-soil contact, which finally formed an approximate circular sliding surface.

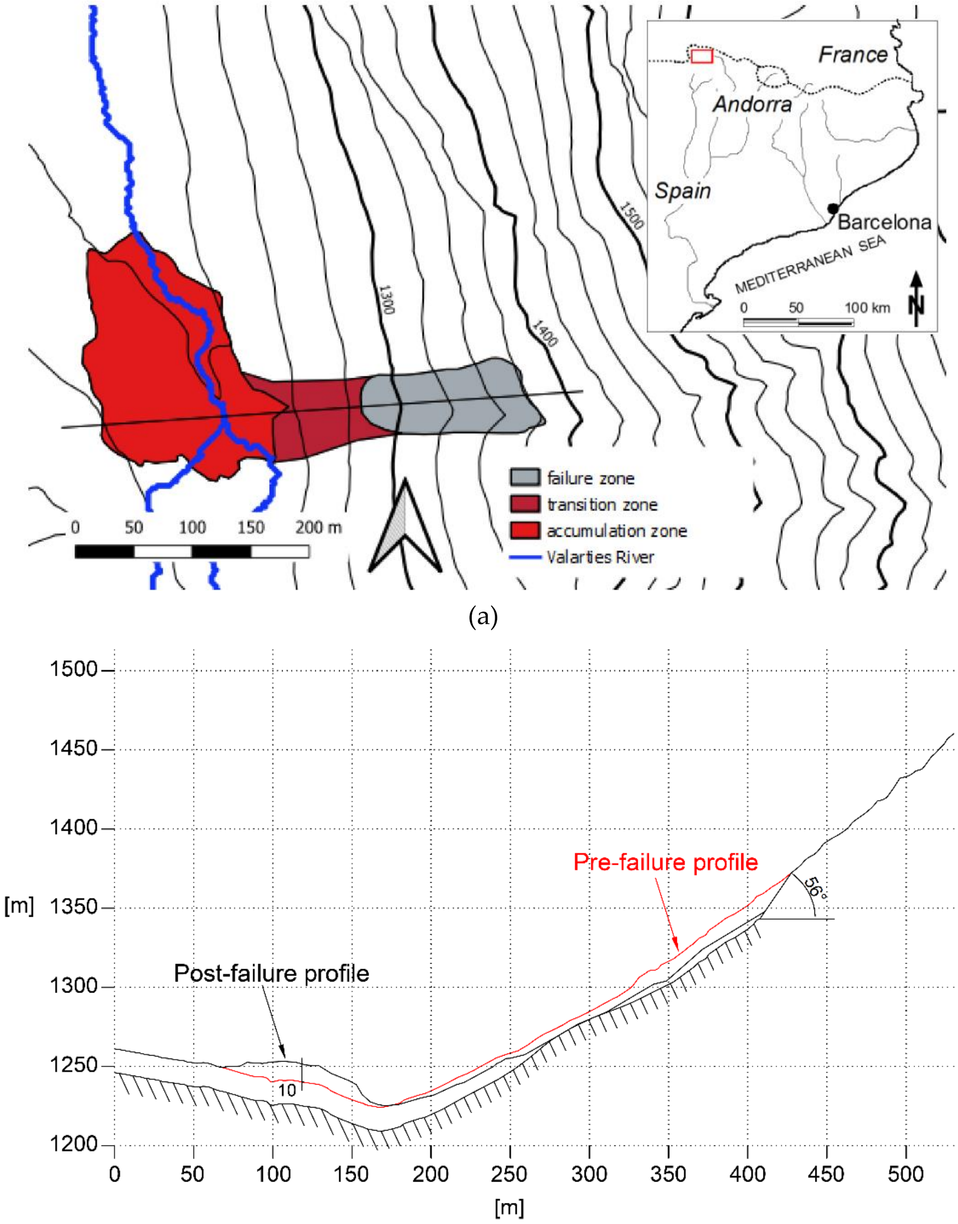

(a)

(b)

Figure 7.2. a) Overview map of the Valarties flow-slide illustrating the failure and the transport and accumulation zones. Inset shows the general situation. b) Longitudinal profile including topographic (pre- and post-failure morphology). The profile is drawn along the line indicated in a).

The hydrogeological conditions in the area of the landslide were not investigated in detail, but field observations showed that the slope probably had a high degree of saturation at the moment of failure. In fact, an important water flow out of the marbles located in the head scarp was observed just after the slope failure. This injected water into the superficial deposits from the karstified rock mass probably played a decisive role in triggering the landslide. Many water springs have been observed around the Valarties landslide, which supports the hypothesis of a generalised high saturation of the slopes.

Regarding the dynamics of the landslide, the field observations showed that, initially, the failed material rapidly transformed into a flow-like movement and incorporated some additional sediment during the runout until reaching the Valarties river (herein called transition zone). The accumulation zone mainly covers the valley floor and the opposite slope. The maximum run-up of the flow was about 30m. It covered the road with sediments 10m thick. Following the updated Varnes classification (Hungr *et al.*, 2014), the Valarties landslide can be classified as an earth-flow.

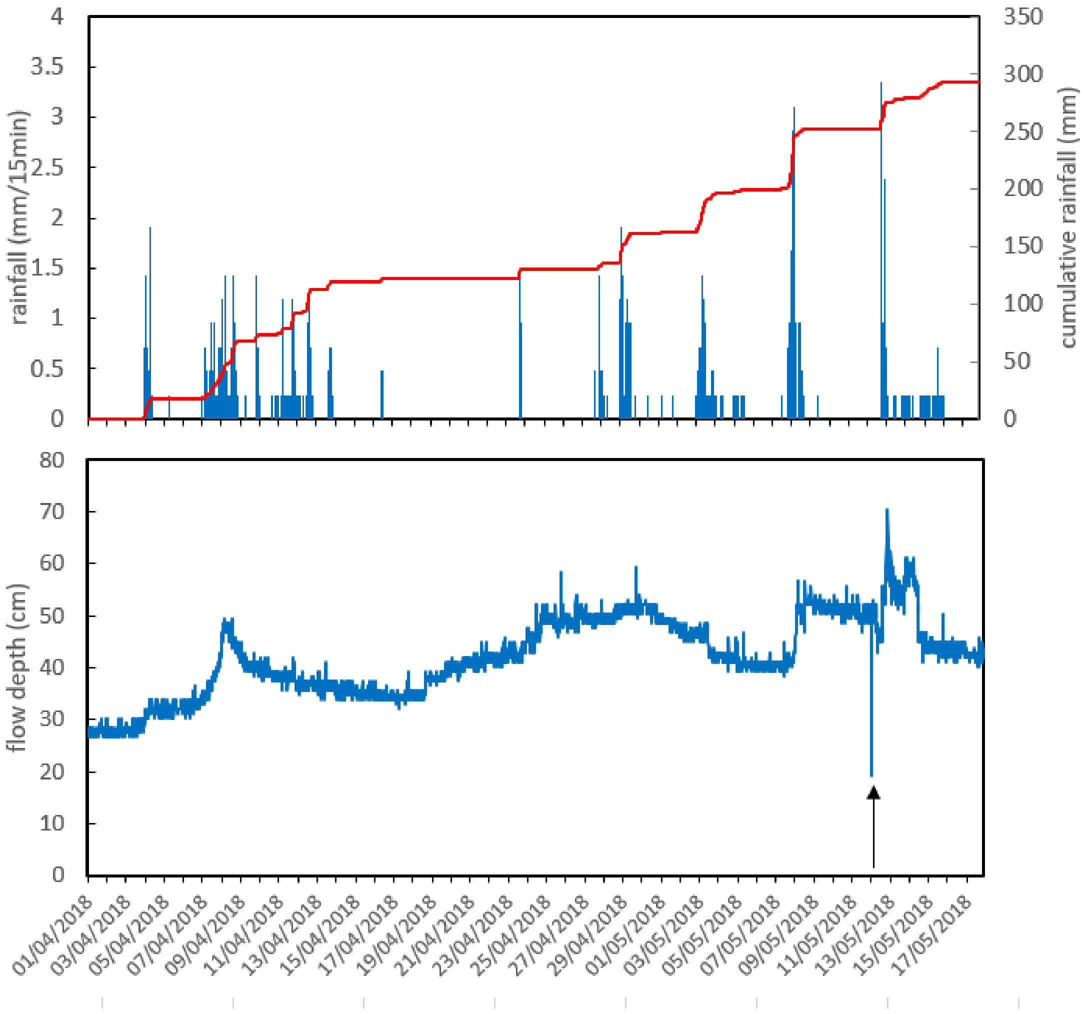

Figure 7.3. Rainfall (top) and flow depth of the Valarties River (bottom) during April and May 2018. The triggering instant of the flow-slide is clearly visible by the sharp reduction of river water depth because of the partial damming of the river (black arrow).

The precipitation previous to the failure was analysed using the data recorded at the rain gage located in the Valarties River valley about 700m downstream of the landslide (Fig. 7.3). The flow depth of the river was measured at the same location. Both time-series had as scan-rate of 15 minutes. The instant of the failure could be determined because of a sharp decrease of the flow depth was observed at 23:45 on May 11th. This observation is related to the partial damming of the Valarties River by the sediment accumulated by the landslide.

Interestingly, no rainfall was measured during the 48 hours previous to the failure. However, winter and spring of 2018 were very humid and precipitation exceeded twice or even three times the average values of Val d'Aran. The accumulated rainfall measured at the Valarties River rain gage during 2018 until the day of the slope failure was 678 mm, while 162 mm were recorded in April and 91 mm between the 1st and 11th of May. All these data confirm that the months previous to the flow-like movement were extraordinarily humid. Our hypothesis is that the superficial formations in the failed slope were highly saturated at the beginning of May 2018 and that the important additional inflow from karstic springs continuously increased pore water pressure in the superficial formations, until eventually provoking the triggering of the landslide.

7.3 MATERIAL PROPERTIES

In situ and laboratory tests were carried out on samples of glacial and colluvial material with the aim of determining the mechanical properties of soil. Field observations indicated that the two soils showed similar properties and it was accepted that the colluvium is representative of the entire superficial formation. Laboratory tests on this material helped to calibrate the Ta-Ger model parameters.

Grain size distribution

Fig. 7.4 shows the grain size distribution of the colluvial material and the different fractions obtained from sieving. Washing the soil did not change much the curve. Based on these results and according to the Unified Soil Classification System (USCS), it can be classified as well graded sand, SW (Tab. 7.1). Atterberg's limits of the fine fraction are summarized in Tab. 7.2.

Table 7.1. Grain size characteristics.

	Coefficient of uniformity Cu	**Fines [%]**	**Soil classification (USCS)**
Without washing	22	5.52	SW
With washing	14.6	3.60	SW

Table 7.2. Atterberg's limits of the fine fraction (Perdices, 2019).

Material	Plastic Limit	Liquid Limit	Plasticity Index
	w_P	w_L	PI
Glacial	13.43%	19.80%	6.37%
Colluvial	20.15%	28.25%	8.10%

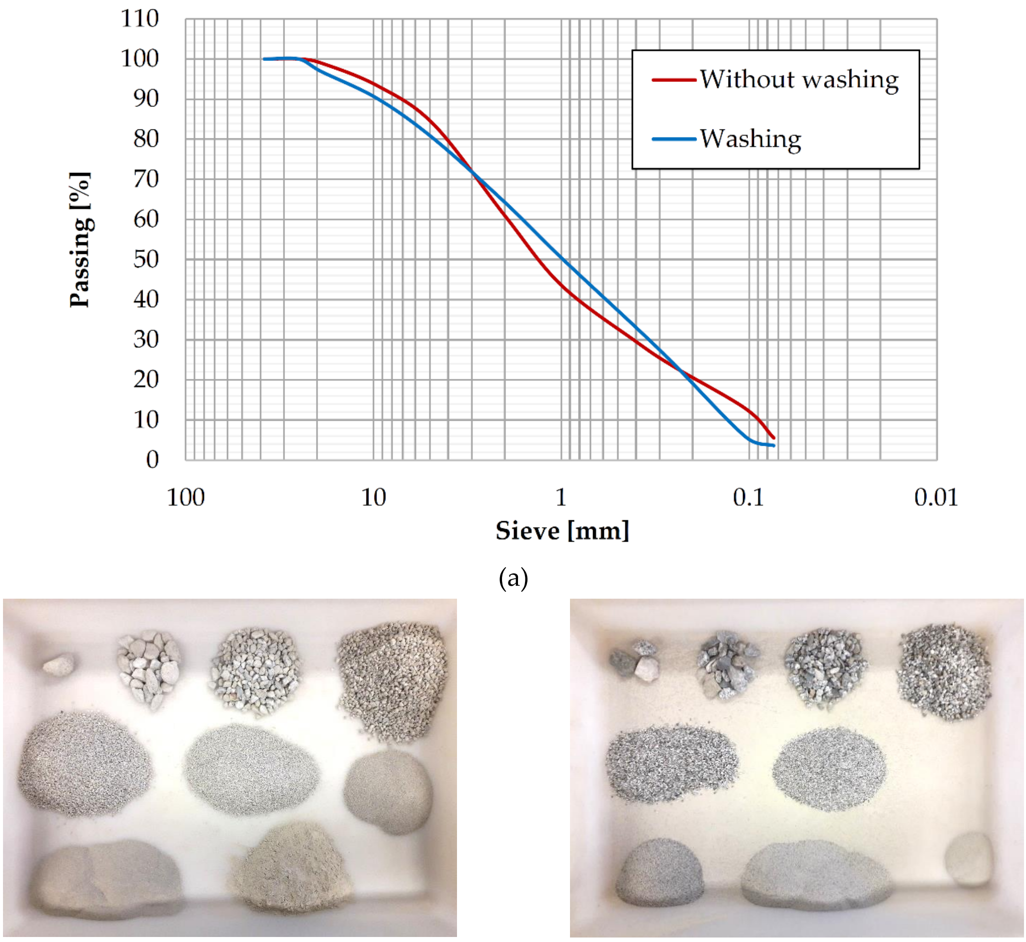

(a)

(b)

(c)

Figure 7.4. (a) Grain size distribution of colluvial material; fractions of colluvial material obtained from sieving: (b) without washing: (c) washing.

In–situ density by sand cone method

Two field tests were carried out to determine the natural density by means of the sand cone method. The tests were performed by adhering a standard plate with a circular opening to the ground under investigation (Fig. 7.5a) in order to dig a hole and collect the material (Fig. 7.5b). Then, through a bottle filled with calibrated sand of known density, the dug hole was filled (Fig. 7.5c, d). From the successive weightings of the residual sand and the extracted material (wet and dry), we obtained both the volume weight of the soil in natural humidity conditions and the dry volume weight.

Tab. 7.3 shows the average values of dry density, natural density and water content. Once the particle density of the soil $\rho_s = 2.69 \frac{g}{cm^3}$ is determined by pycnometer method, two values of porosity $\phi = 0.38 - 0.45$ and void ratios $e = 0.62 - 0.83$ were determined (Eq. 7.1-7.3).

$$\rho_{nat} = \rho_s(1-n)(1+w) \tag{7.1}$$

$$n = 1 - \frac{\rho_{nat}}{\rho_s(1+w)} \tag{7.2}$$

$$e = \frac{n}{1-n} \tag{7.3}$$


(a) (b) (c) (d)

Figure 7.5. Sequence of in situ sand cone method test.

Finally, the maximum and minimum dry unit weight are measured with the standard laboratory tests allowing to obtain the maximum and minimum void index (Tab. 7.3). The estimated average relative density of the soil is:

$$D_r = \frac{e_{max} - e}{e_{max} - e_{min}} = 19.4\% \tag{7.4}$$

Table 7.3. In situ colluvium parameters derived from the sand cone tests (average values) Also given are the maximum and minimum void ratios.

Dry density	Moist density	Water content	Porosity	Void ratio	Maximum void ratio	Minimum void ratio
$\rho_{dry}[\frac{g}{cm^3}]$	$\rho_{nat}[\frac{g}{cm^3}]$	w[%]	ϕ[-]	e[-]	e_{max}[-]	e_{min}[-]
1.56	1.7	8.6	0.42	0.72	0.833	0.250

Ring shear test

Ring shear tests on reconstituted samples indicated a value of residual friction angle around 33-34º for the glacial and colluvial materials (Fig. 7.6). A friction angle of 34º was accepted as a critical state friction for the calibration of consolidated undrained triaxial tests described below.

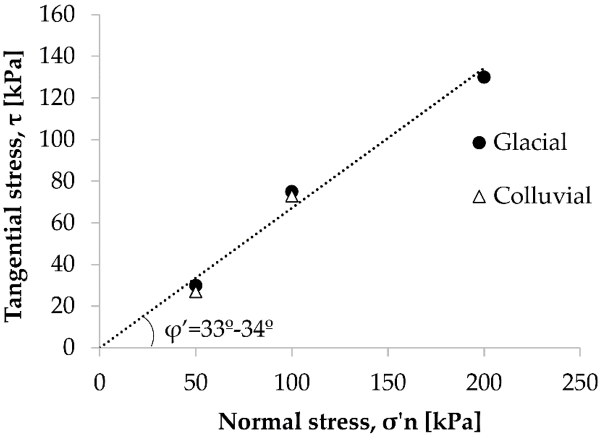

Figure 7.6. Mohr-Coulomb failure envelope from ring shear tests (adapted from Perdices, 2019).

Undrained triaxial tests and constitutive model calibration

Two undrained triaxial compression tests (CIU), carried out on reconstituted samples of colluvial material consolidated at different effective confining pressures and initial void ratios e_0, allowed the calibration of Ta-Ger model parameters.

Due to the difficulty of placing samples of cohesionless material at a desired relative density in the triaxial apparatus, a freezing procedure was used. The material was first placed in the cylindrical mould (length $l = 7.5cm$ and diameter $d = 3.8cm$) shown in Fig. 7.7, at a given relative density and water content and then it was frozen.

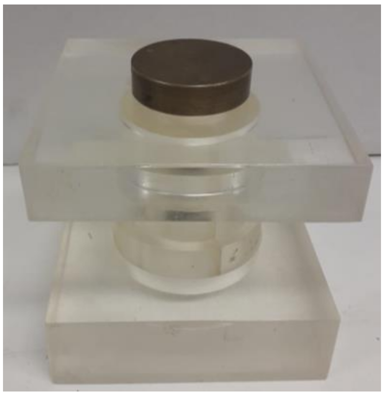

Figure 7.7. Mould used for sample preparation.

At this point the sample can be packed in a cylindrical latex and placed in the triaxial cell. In Fig. 7.8 the setup of a sample in the triaxial apparatus is shown. Once filled the cell with water, a very low confining pressure was applied to the sample, which was allowed to thaw before starting the test. Once saturated and consolidated the sample at a given confining stress a constant axial deformation of 0.1mm/min is applied under undrained conditions. The tests were conducted to around 20% axial strain to ensure that critical-state conditions were reached. The experimental results are shown in Fig. 7.9.

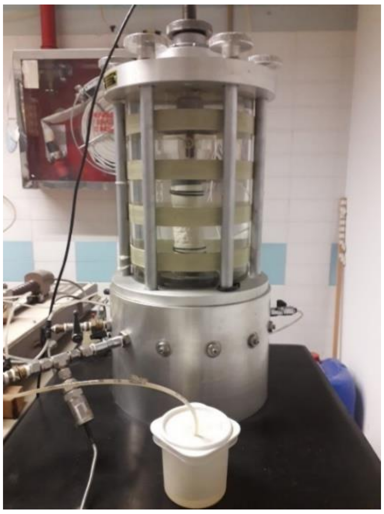

Figure 7.8. Triaxial apparatus.

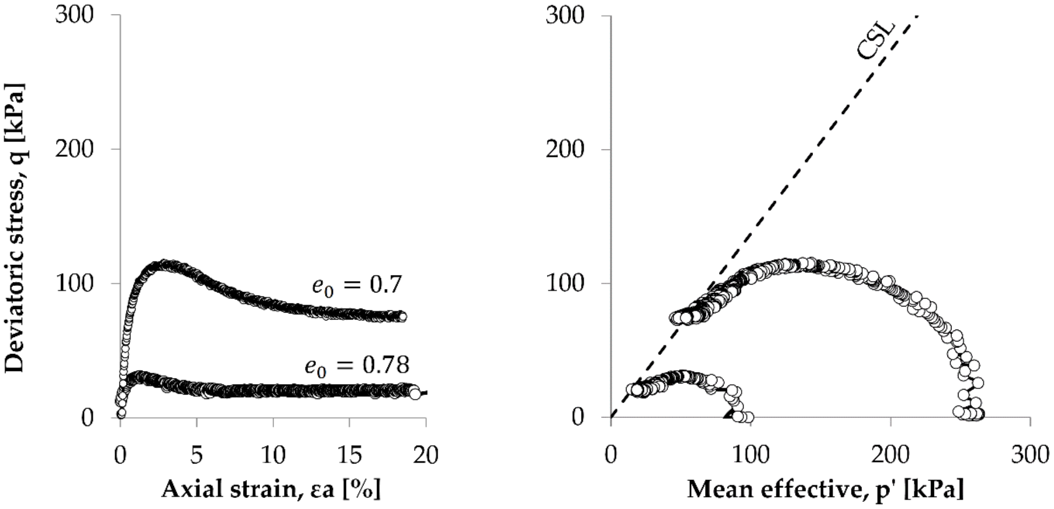

(a) (b)

Figure 7.9. Experimental results of undrained triaxial tests: (a) Deviatoric stress-axial strain relationship; (b) stress path in the triaxial plane.

7.4 CONSTITUTIVE PARAMETERS

Soil Water Retention curve

The soil-water retention curve was predicted from the soil particle-size distribution by using two different physically-based models. In the model proposed by (Arya and Paris, 1981) the particle-size distribution is transformed into a pore-size distribution by estimating an equivalent pore radius for each particle size fraction. The authors assumed that for a given particle size fraction of an ideal soil, the pore volume can be represented by a cylindrical capillary tube, whose length is the sum of the spherical particle diameters presented in the fraction. Based on this assumption, the pore radius is calculated as function of the pore length of the ideal soil which is scaled to that of a natural soil through the scaling factor α_{AP} with an average value of 1.38. The equivalent water pressures are then determined from the pore radii by using the equation of capillarity (Jurin's law).

The pores volume of each size fraction is computed in terms of the corresponding solid mass, the bulk density ($\rho_b = \rho_{dry} = 1.56 \frac{g}{cm^3}$) and the particle density ($\rho_s = 2.69 \frac{g}{cm^3}$). The calculated pore volumes, assumed to be filled with water, are added and divided by the bulk volume ($V_b = 1/\rho_b$) to get the volumetric water contents θ and, finally, the degree of saturation $S_r = {}^{\theta}/_{\phi}$, where ϕ is the porosity. The second model is the modified Kovács method, described by Aubertin *et al.* (1998, 2003), which extended the original model by Kovács (1981) to generalize its application to a variety of porous media.

The degree of saturation is expressed as function of two components acting simultaneously to induce suction. The first component is due to capillary forces (S_c) that mainly contribute to low values of suction. The second component is associated with adhesive forces (S_a) that are dominant at higher values. Both components can be obtained from basic geotechnical properties, including the diameter corresponding to 10% passing on the cumulative grain-size distribution (D_{10} = 0.009 cm), the uniformity coefficient (C_U = 22) and the void ratio (e = 0.724). These properties are used to define model parameters such as the residual suction, the pore size distribution parameter and the equivalent capillary rise, which is the reference parameter to define the relationship between the degree of saturation S_r and matric suction. Fig. 7.10 shows the predicted water retention curves.

Table 7.4. Van Genuchten water retention curve parameters.

Symbol	Unit	Value
S_{rmin}	-	0
S_{rmax}	-	1
p_0	kPa	1
λ	-	0.5

A Van Genuchten water retention curve (Van Genuchten, 1980) whose parameters are listed in Tab. 7.4, is adopted in the calculation. Fig. 7.10 shows the shape of the curve compared with the predictions by (Arya and Paris, 1981) and modified Kovács (Aubertin *et al.*, 1998, 2003) interpretations of the grain size distribution determined in samples.

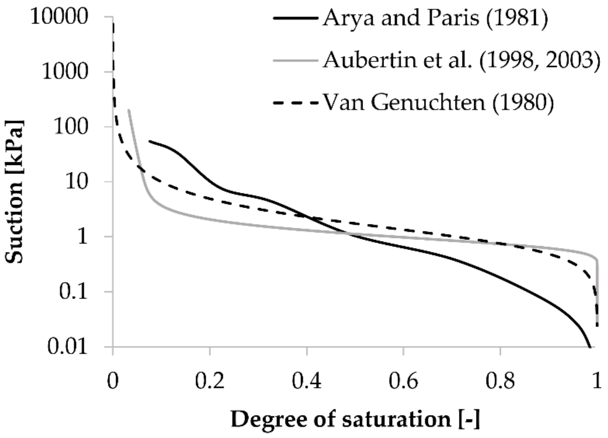

Figure 7.10. Water retention curve predicted by (Arya and Paris, 1981) and modified Kovács models (Aubertin *et al.*, 1998, 2003). Also indicated is the Van Genuchten empirical equation adopted in calculations.

Soil permeability

The intrinsic permeability of soil is assumed constant and equal to 10^{-10}m^2, corresponding to a hydraulic conductivity of 10^{-3} m/s.

Ta-Ger model calibration

The calibrated Ta-Ger model parameters are summarized in Tab. 7.5.

Fig. 7.11 shows the comparison between the experimental data and the prediction of the Ta-Ger model in terms of stress – axial strain ($q - \varepsilon_a$) relationship and the stress path in triaxial plane ($q - p'$). The tests were performed for two values of initial void ratio ($e_0 =$ 0.78 and 0.7) slightly higher and lower respectively than the average value measured in-situ ($e_0 = 0.724$). For isotropic confining stresses of 100kPa and 250kPa, results show a contractive behaviour of the soil and a susceptibility to static liquefaction, which supports the idea that this phenomenon may be responsible for the large run-out observed in Valarties landslide. A third numerical simulation is conducted assuming a lower initial void ratio ($e_0 = 0.55$) in order to check the capability of the model and adopted parameters to interpret the dilative behaviour of a dense sand (Fig. 7.11).

Table 7.5. Ta-Ger model parameters.

Symbol	Unit	Value
G_0	-	1500
m	-	0.33
ν	-	0.15
φ_{cs}	°	34
φ_{s0}	°	$1.1\phi_{cs} + 5I_{r0}$
n	-	$0.4D_{r0} + 0.14$
c	-	$6 + I_{r0}$

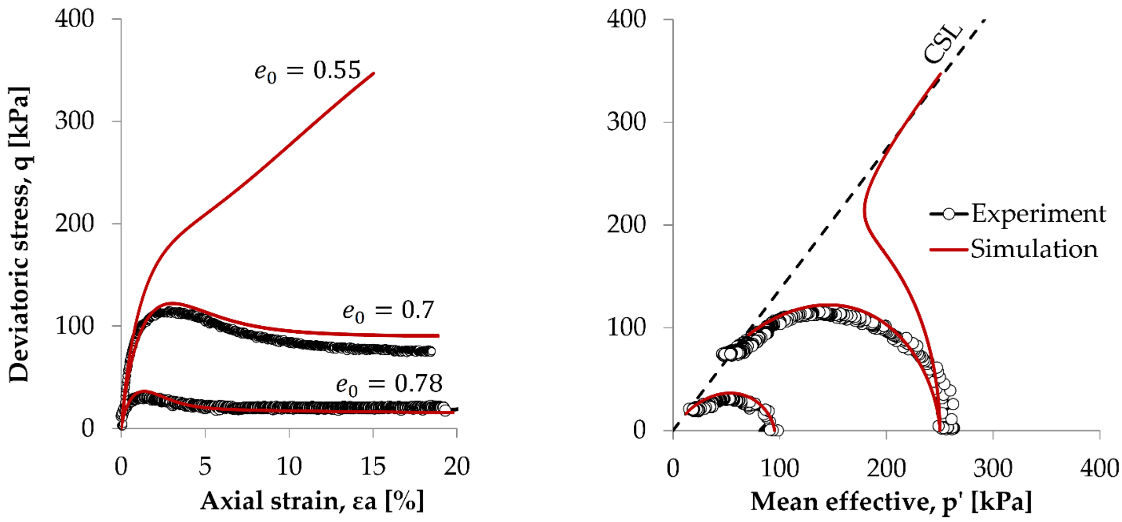

(a) (b)

Figure 7.11. Experimental data versus simulation results of undrained triaxial tests: (a) Deviatoric stress-axial strain relationship; (b) stress path in the triaxial plane.

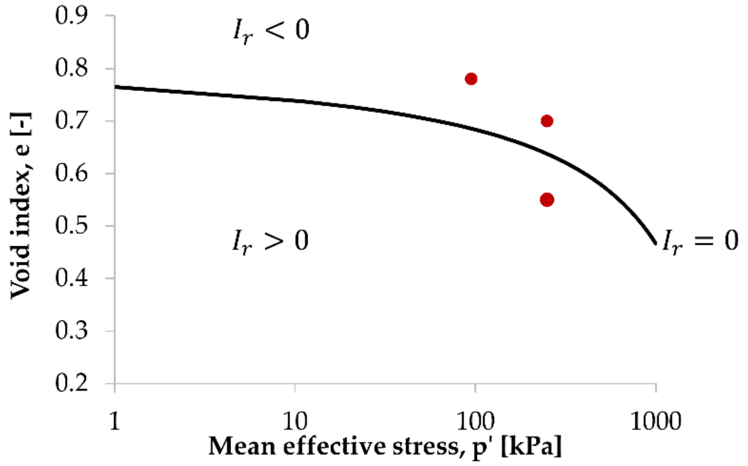

Figure 7.12. Triaxial tests (two carried out and one simulated) and critical state curve in $e - ln(p')$ plane.

The critical state curve derived from the model (Eq. 7.5) is plotted in Fig. 7.12, in a $e - \ln(p')$ plane, together with the position of the void ratios of the triaxial tests mentioned before. The critical void ratio, e_c, is obtained from Eq. 6.16 and Eq. 6.17 by imposing a zero value of relative dilatancy index ($I_r = 0$) and adopting the following fitting parameters $Q = 0.85$ and $R = 1$:

$$e_c = e_{max} - \frac{R}{Q - \ln(p')}(e_{max} - e_{min}) \tag{7.5}$$

Fig. 7.12 shows that the critical state curve, predicted by the calibrated model, explains the transition from contractive to dilative behaviour of soil, and the conditions leading to liquefaction in terms of effective mean stress and void ratio.

7.5 MPM MODEL

7.5.1 Model description

Fig. 7.13 presents the geometry of the problem and the computational mesh (triangular elements with a minimum size of 2.5 m in the colluvial material region). Initially, three material points are distributed within each element in the position of Gauss points. Boundary conditions for solid and liquid phases are applied on the left and right sides of the model to constrain the horizontal displacement, at the top of the mesh to constrain the vertical displacement and at the bottom where both vertical and horizontal displacements are prevented. The bedrock substratum is located at a depth of about 15 m. It is modelled as a linear elastic solid, not involved in the failure.

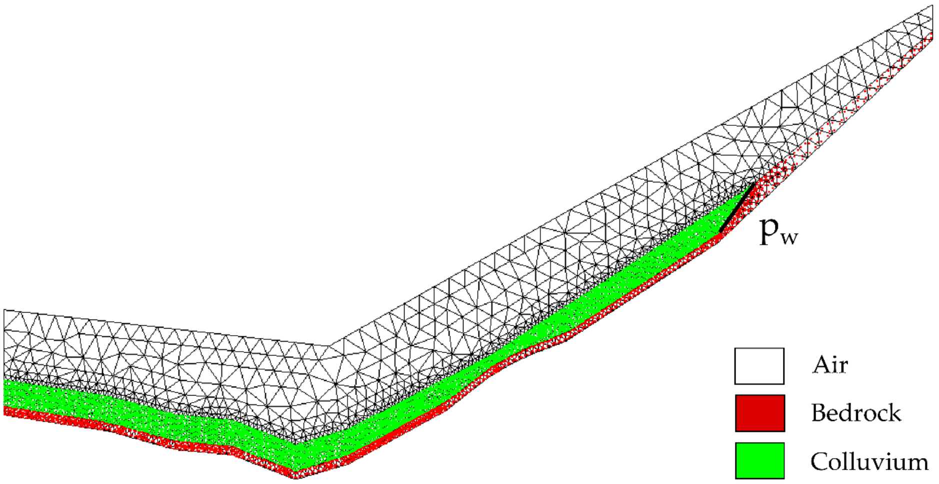

Figure 7.13. Computational mesh, initial distribution of material points and hydraulic boundary condition applied to simulate the inflow from karstic springs (p_w).

7.5.2 Stages of analysis

It is assumed that the slide was at strict equilibrium (safety factor equal to 1) when the karstic spring triggered the failure. The position of the phreatic level imposed is then defined according to the limit equilibrium analysis performed with the commercial code SLIDE (Rocscience, 2018) (Fig. 7.14) for a friction angle of 34º, nil cohesion (the value used in the simulation of the triaxial CU tests performed). The depth of the phreatic level resulting from this calculation is 11.5m. The initial distribution of pore water pressure is set as hydrostatic, below the groundwater level. Suction above the phreatic surface also varies linearly following the same hydrostatic gradient (Fig. 7.15).

In terms of hydraulic boundary conditions, the pore water pressure is imposed on the lower boundary according to the initial phreatic level. On the ground surface, the corresponding suction is also applied (115kPa). Since the default value of pore pressure on boundaries is zero, this condition prevents water infiltration.

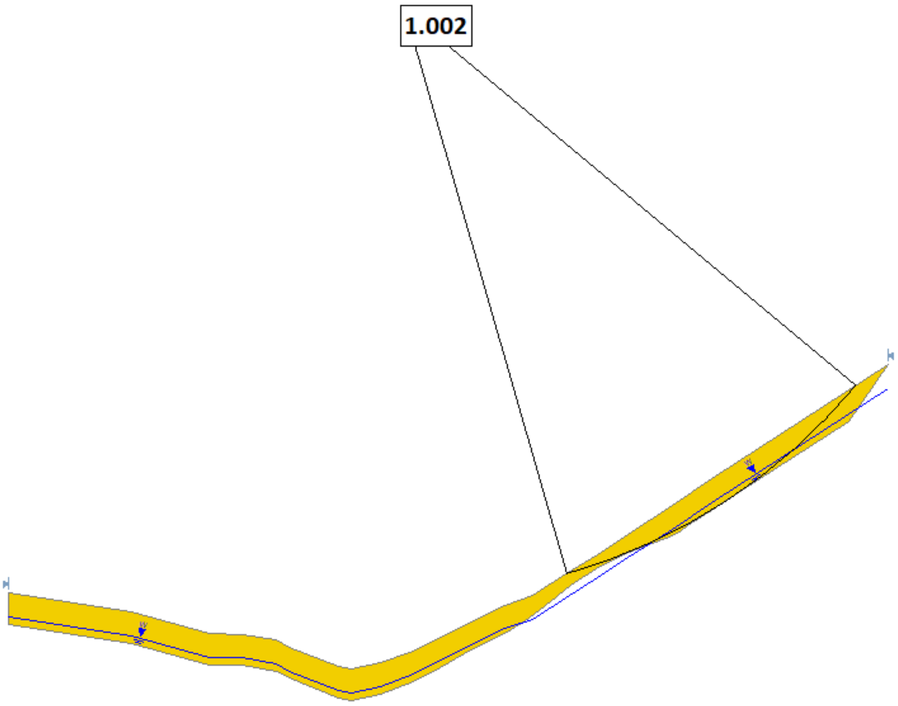

Figure 7.14. Results of limit equilibrium analysis. Critical surface calculated for phreatic level at 11.5m of depth.

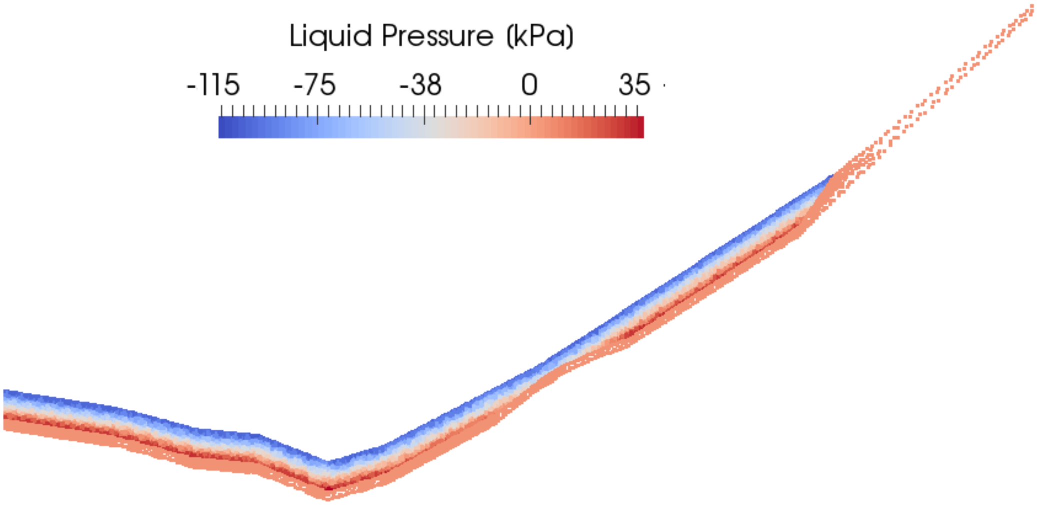

Figure 7.15. Initial distribution of pore water pressure.

The initial stress distribution results from a quasi-static calculation (Fig. 7.16). This calculation starts from a trial stress distribution calculated by K_0 procedure, assuming a value for the coefficient of earth pressure at rest of 0.5. A local damping factor $\alpha = 0.75$ is imposed in this stage.

In the second stage calculation to simulate the triggering, an excess pore water pressure of 100kPa is applied in the upper part of the slope (Fig. 7.13) to simulate the inflow from karstic springs. The local damping factor is reduced to $\alpha = 0.05$ in this dynamic stage to simulate the natural energy dissipation of the material. Also the strain smoothing technique (see §3.3.2) is applied.

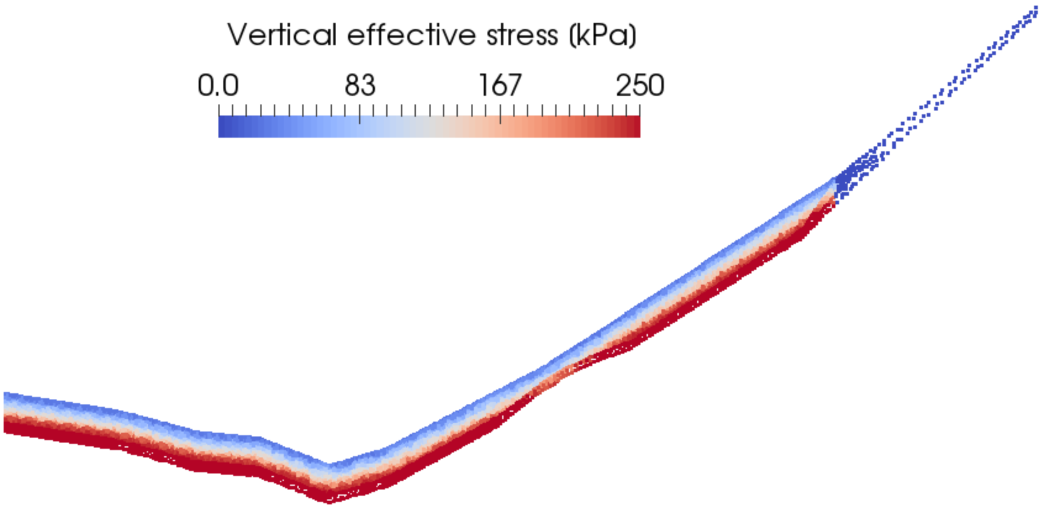

Figure 7.16. Initial distribution of vertical effective stresses.

7.6 NUMERICAL RESULTS

Consider first the results of simulations for three values of initial relative density corresponding to the two measurements by the sand cone method and their average value. Fig. 7.17 shows the initial distribution of the relative dilatancy index and the results in terms of total displacements once stability is achieved. A large run-out explained by the liquefaction of the soil can only occur if the initial void ratio is smaller than the critical value ($I_{r0} < 0$). Results may be explained considering that the larger is the contractive tendency of the soil under shearing, the larger is the transient localized pore water pressure which can be developed during the failure mechanism motion of the earth flow-slide. The maximum run-out is obtained for the case of $e_0 = 0.83$. The black continuous line in the figure represents the observed final configuration of the slope.

Fig. 7.18a shows the evolution of the movement with time for the case of $e_0 = 0.83$. First, the inflow from karstic springs induces a local increment of pore water pressure that triggers the failure in the upper part of the slope at the bedrock-soil contact. A “slab” of unstable soil is visible at *t*=4s. This slab rides over the central - lower part of the slope as shearing strains increase in intensity and extends throughout the moving mass (*t*=8–12s). Shearing the contractive soil increases pore pressures and the soil liquefies. The fast reduction of resisting shear strength leads to an accelerated motion. The kinetic energy of the initial slide increases rapidly and drags the soil layer, which covers the lower part of the valley (*t*=12–16s). Shear straining generalizes in the moving mass, which eventually comes to rest when the flow slide impacts against the valley slope on the opposite margin of the river.

This mechanism can be followed in more detail if the position of material points is tracked during the failure. This is shown in Fig. 7.18b. The initial position of the involved soil mass is divided in a collection of vertical slices of different colours. The position of the initial set of particles can easily be followed in time by observing the distribution of colours as the flow slide develops. The unstable soil mantle covering the bedrock in the middle-upper part of the slope covers the lower part at *t*=12–14s, entrains the soil closer to the valley bottom and pushes the, by now, thicker deposit which covers the river and climbs upward the left margin of the river.

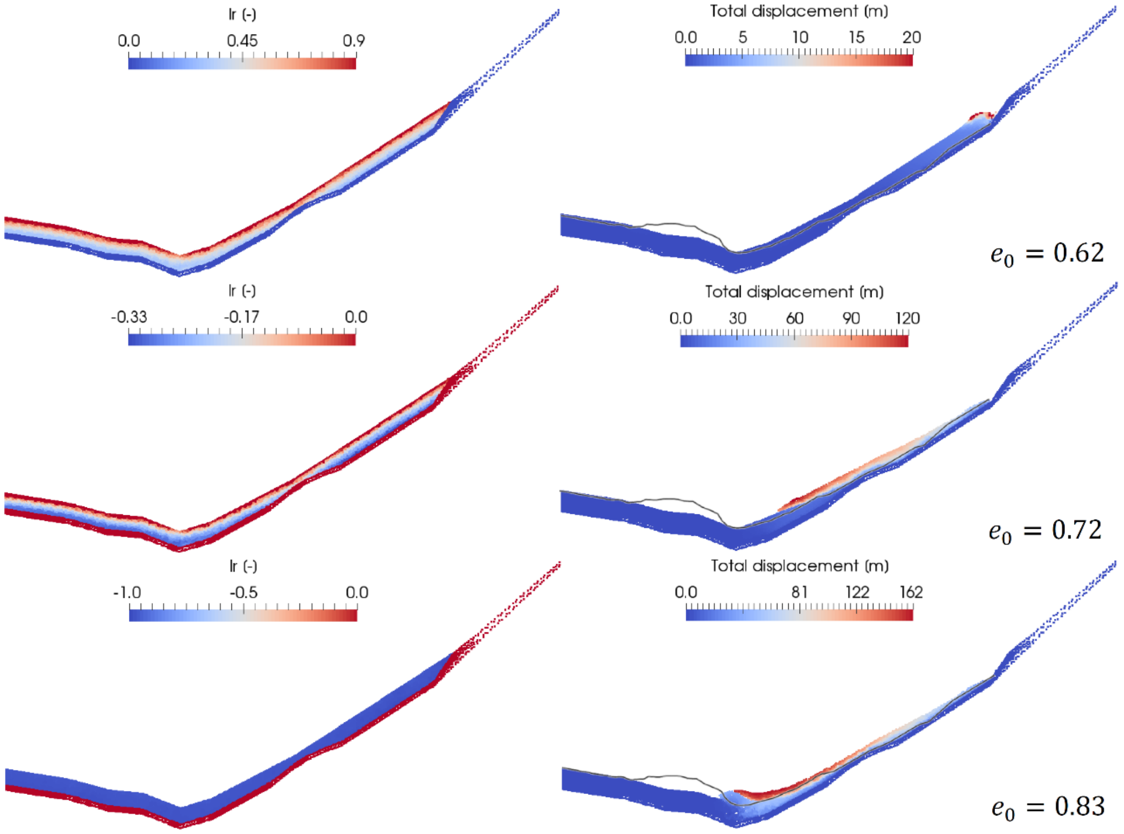

(a) (b)

Figure 7.17. (a) Initial distribution of the relative dilatancy index; (b) total displacement at the end of the simulation for three values of the initial porosity.

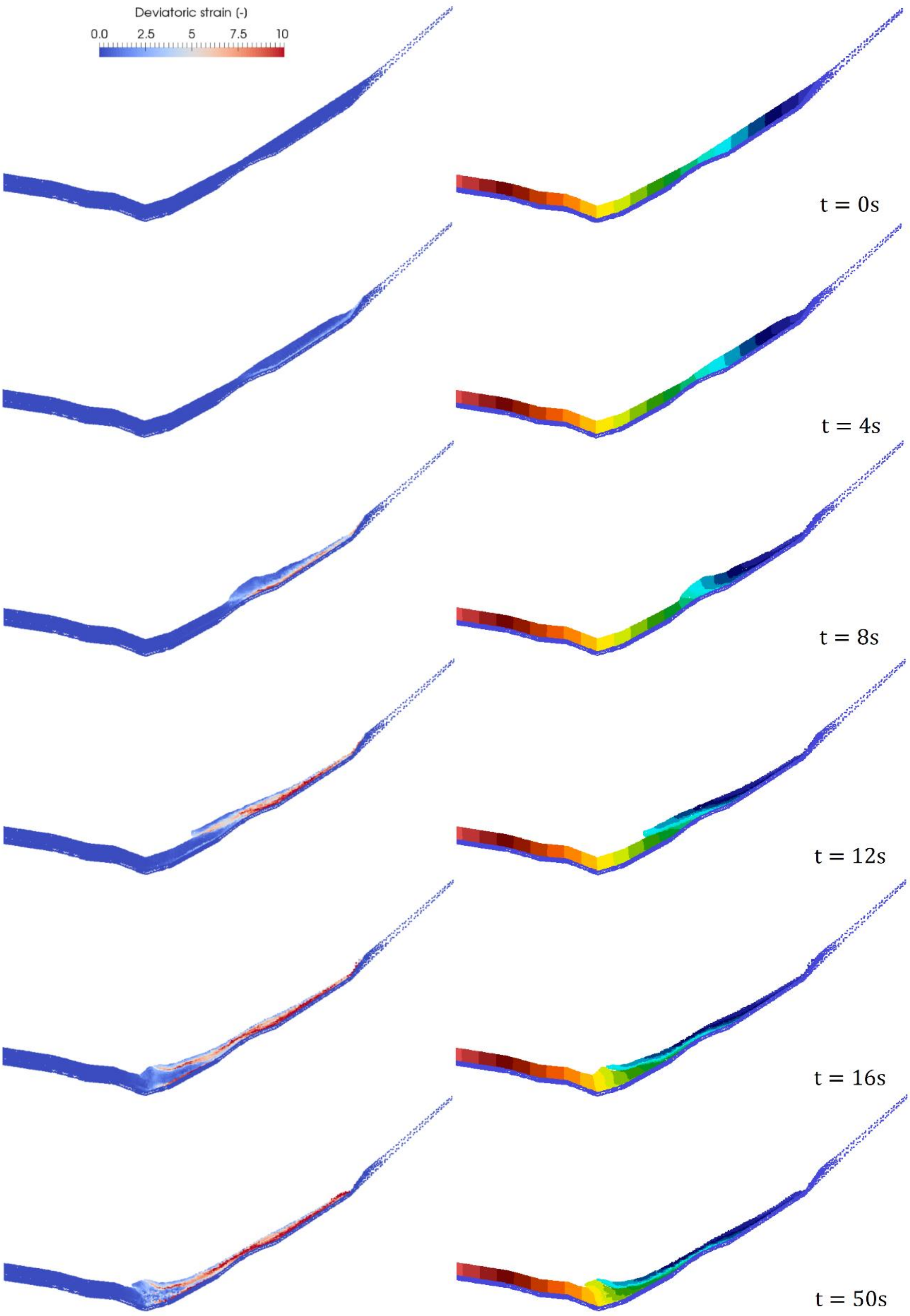

(a)

(b)

Figure 7.18. Evolution of the movement with time ($e_0 = 0.83$). (a) Deviatoric strain increments; (b) Illustration of the evolving position of material points located, before the failure, in vertical slices covering the entire soil mass affected by the flowslide.

A further insight into the physical phenomena developing in the flowing mass is obtained by examining the development of pore water pressures, mean effective stress and the dynamics (run-out, velocity) of particular "points" within the moving soil mass (Fig. 7.19). P1 is initially under unsaturated conditions while P2 is below the phreatic level. P3 and P4, located in the valley floor, will receive the impact of the unstable soil mass coming from higher elevations.

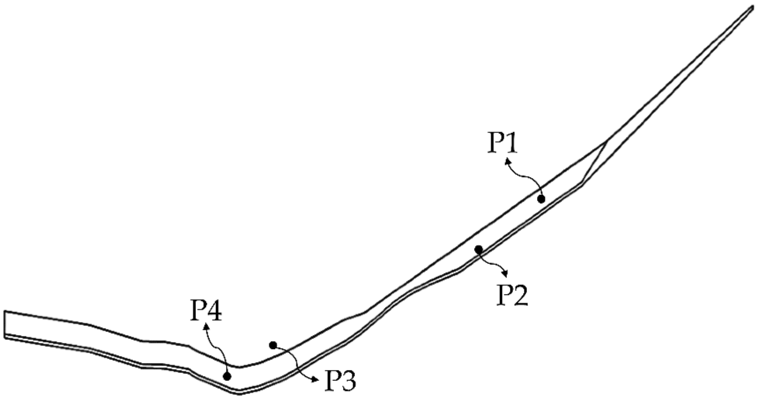

Figure 7.19. Position of material points selected to examine in detail their stress paths, velocity and displacement.

Fig. 7.20 to Fig. 7.23 illustrate the calculated rapid variations of stresses and velocity and a more continuous time averaged values for a "window" interval of 50s. P1, Fig. 7.20, located initially at a higher elevation, experiences first a saturation when pore water pressures increase. The transient water pressure oscillation is shorter for this point, which reaches a high peak velocity (8.5m/s) at t=6.5s. This point belongs to the soil "slab" mentioned before which slid above a slower mass of soil, close to the substratum. This is indicated also by the large run-out (60m) computed for P1.

A similar description, in qualitative terms, may be made for the remaining points selected to interpret the phenomenon. Results for P2 (Fig. 7.21) indicate that, once the instability is triggered, pore-water pressure increases until it reaches maximum values 10s after the initiation of failure. At this time the point reaches its maximum velocity (2m/s) and it has travelled 10m down the slope. The mean effective stress reaches very small values for times in the time interval 7–12s. As pore water pressures dissipate beyond t = 10s, effective mean stress increases and the P2 stops (v = 0) at time t=16s. At this time this material point reached a displacement of 15.2m. Note that changes in average mean stress are a consequence of changes in total stress and pore water pressure. The stress path in (q, p'') space indicates the initial reduction of shear stress to very low values and the subsequent recover when excess water pressures reduce and total mean stress experiences changes due to the evolving slope geometry.

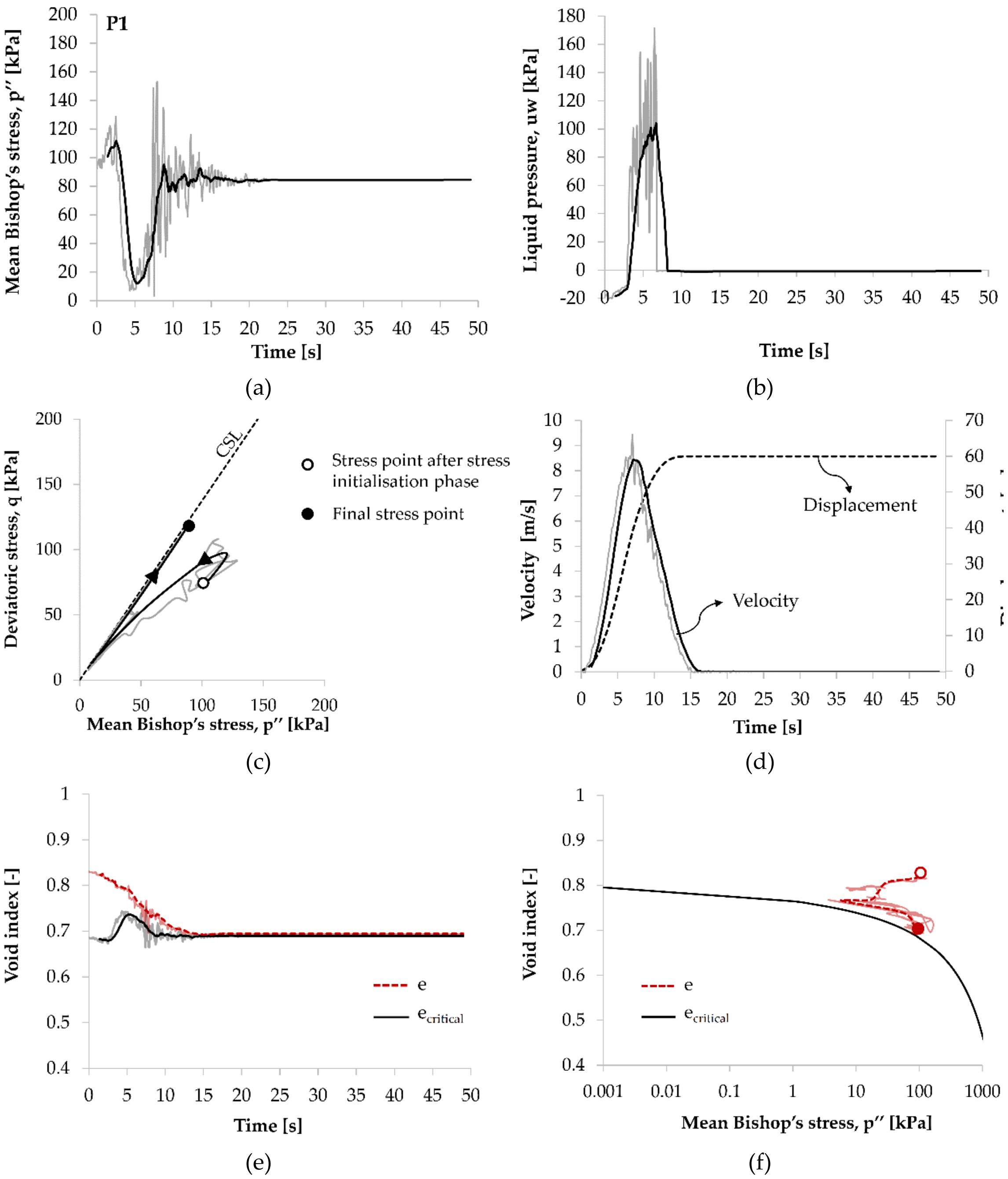

Figure. 7.20. Histories of (a) effective stress; (b) water pressure; (c) stress path; (d) velocity and displacement; and (e) void ratios of Point 1.

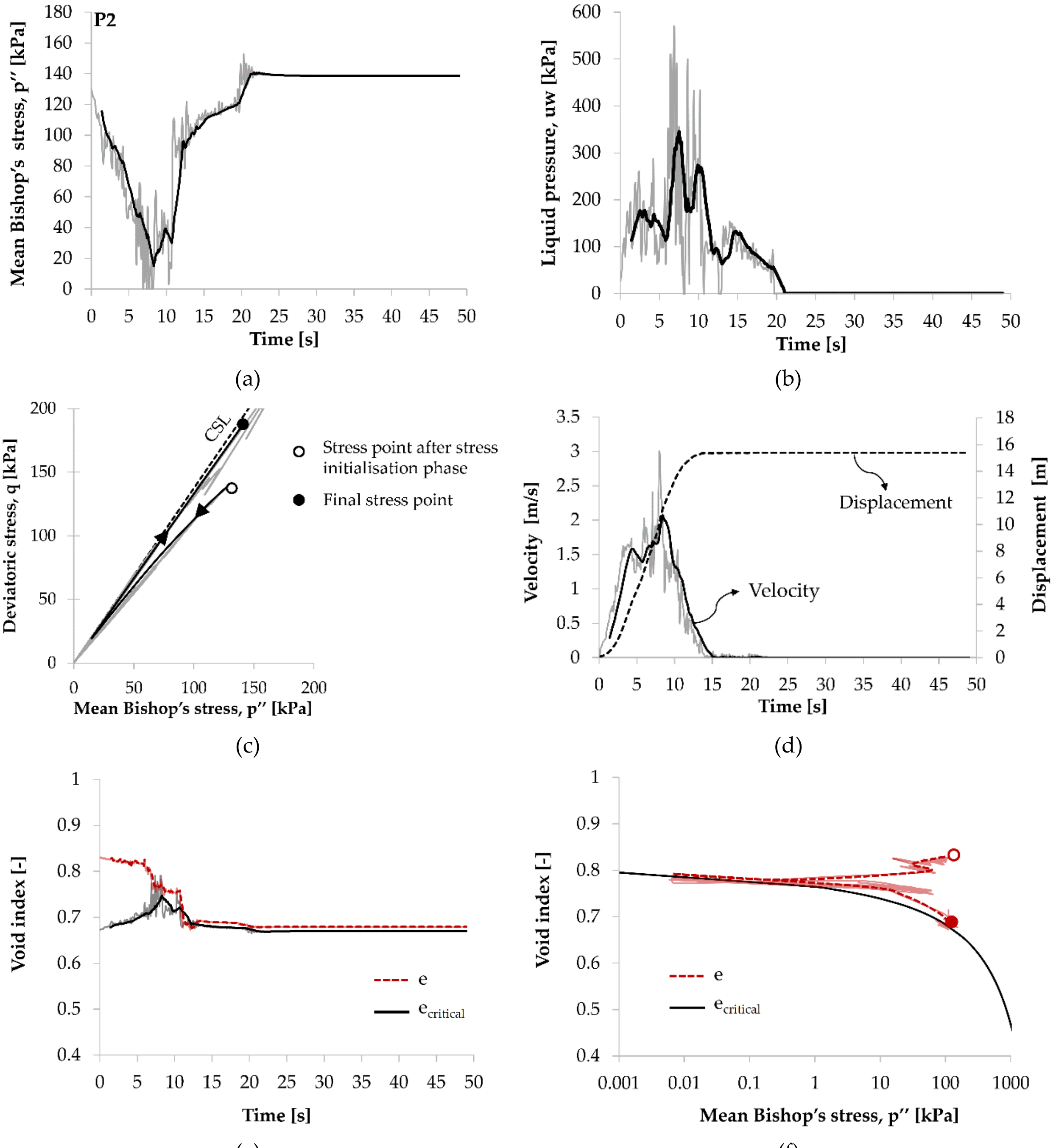

Figure 7.21. Histories of (a) effective stress; (b) water pressure; (c) stress path; (d) velocity and displacement; and (e) void ratios of Point 2.

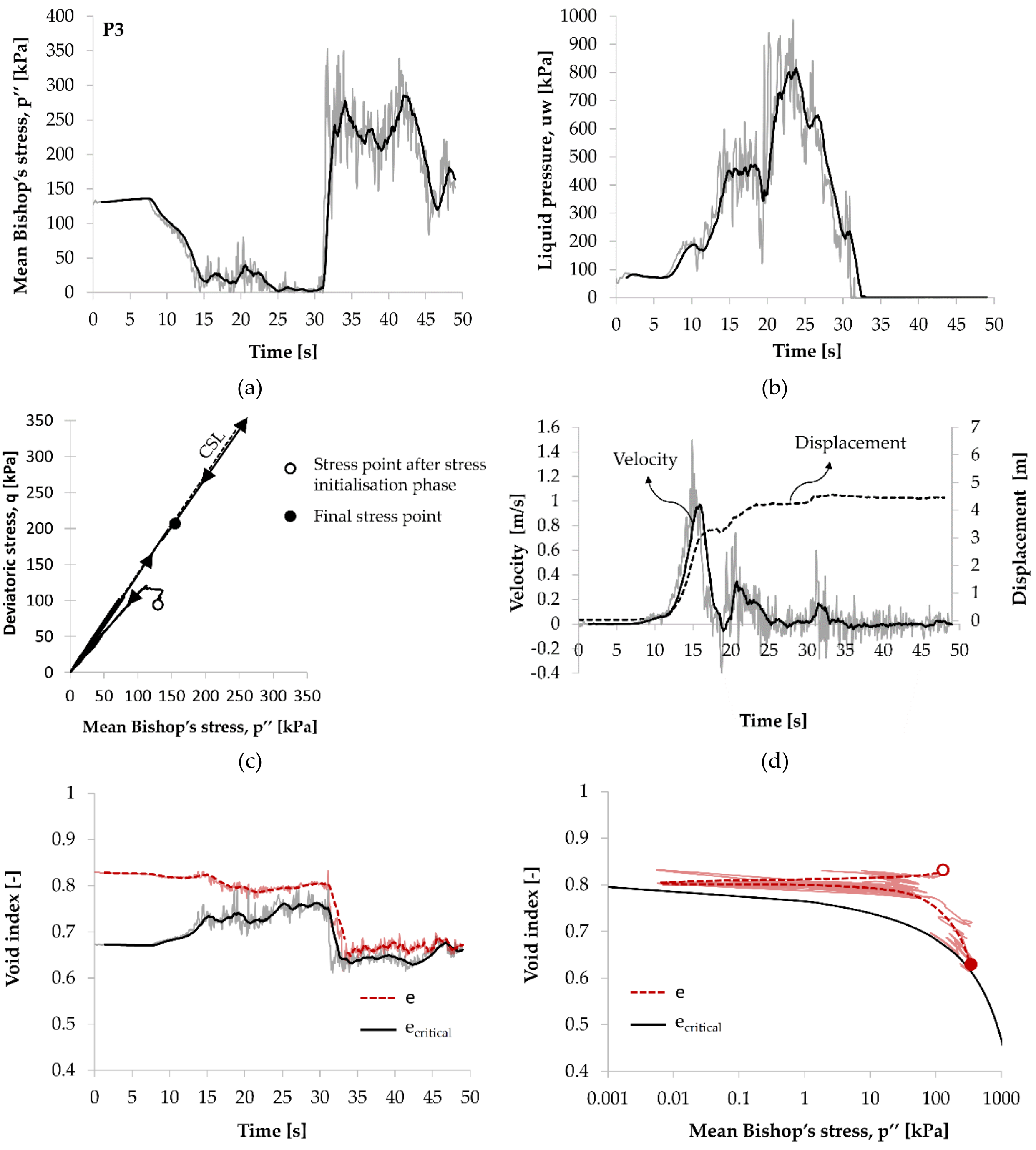

(a) (b) (c) (d) (e) (f)

Figure 7.22. Histories of (a) effective stress; (b) water pressure; (c) stress path; (d) velocity and displacement; and (e) void ratios of Point 3.

P3 (Fig. 7.22), located initially in the vicinity of the river remained undisturbed for 7–8s after the failure triggering. Then, it received the dynamic load of the unstable soil mass coming from a higher elevation. The pore pressure increased fast, it reached high values (700–800kPa) and decreased afterwards until *t*=32s. The effective mean stress reduced to very small values for more than 15s. However, P3 is in a constrained position because of the proximity of the opposite slope of the Valarties valley. Therefore, the calculated maximum displacement is small as well as the maximum velocity (v= 1m/s).

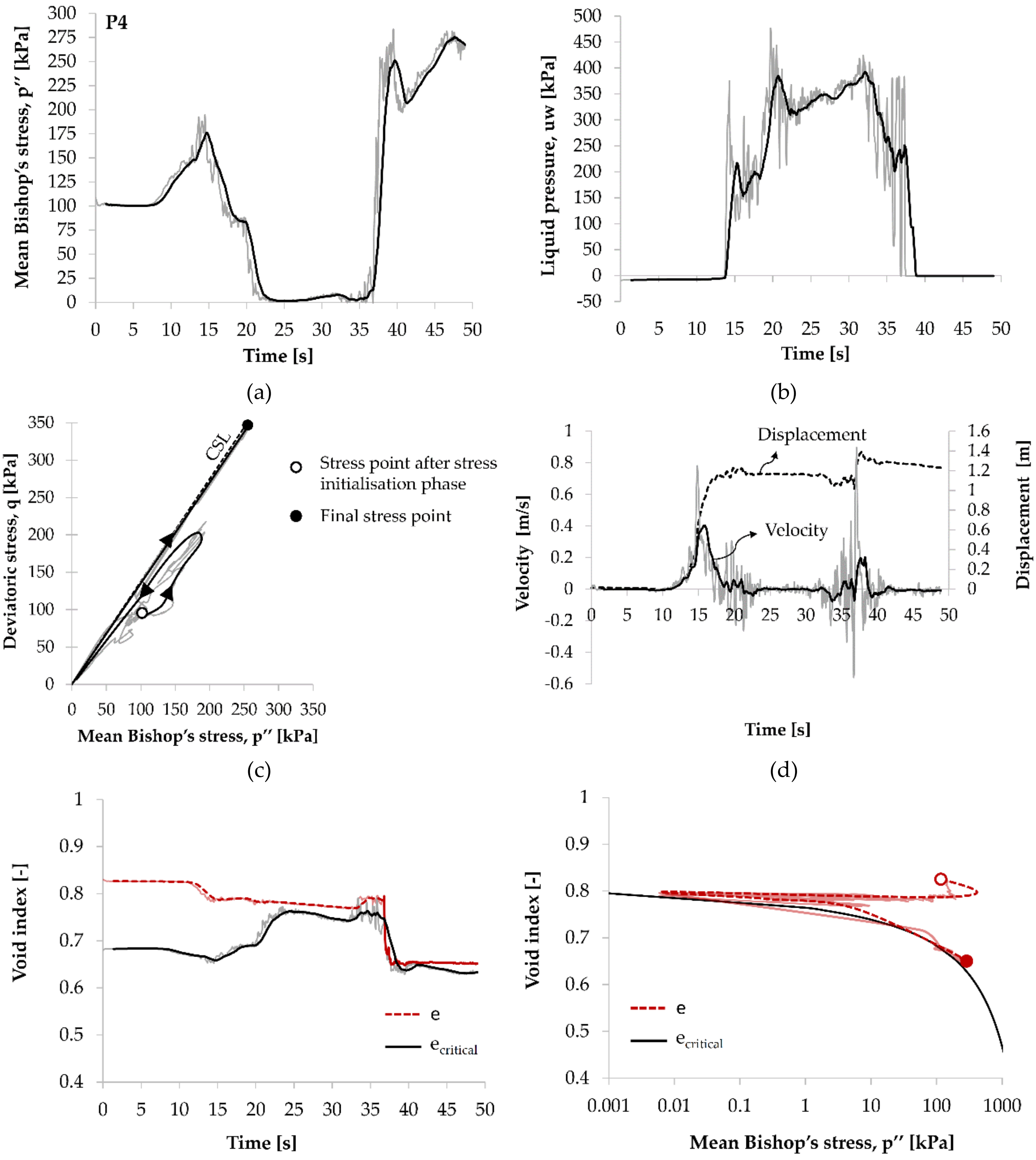

(a) (b) (c) (d) (e) (f)

Figure 7.23. Histories of (a) effective stress; (b) water pressure; (c) stress path; (d) velocity and displacement; and (e) void ratios of Point 4.

P4 (Fig 7.23), located on the opposite side of the valley, unlike P3, receives the impact of the moving mass. Its mean stress increases significantly before shear strains accumulate and the collapse of the soil micro-structure leads to a rapid generation of positive pore pressure and the liquefaction of this point in the period *t*=23 to 35s. Further loading from the landslide leads to a small increase in velocity and P4 only moves 1.35m upslope.

There was an interest to confirm the significance of liquefaction to explain the run-out of the flowslide. The idea was to check the effect of a strain softening soil behaviour leading to a progressive failure and the acceleration of a critical mass of the slope.

In order to evaluate this behaviour, a strain softening Mohr-Coulomb, MPM simulation was performed. Since an average residual friction of 34º was measured in ring shear tests of the colluvium, a peak friction angle of 37º, which could be accepted as a maximum peak friction for the undisturbed colluvium, was selected to perform this exercise. The softening is simulated by reducing the effective strength parameters with the accumulated equivalent plastic strain. Yerro *et al.* (2015) provide details of the procedure.

Following the same hypothesis assumed previously, the position of the phreatic level was imposed in order to simulate a limit equilibrium state before the triggering stage. For the peak angle of 37º, the critical phreatic level was found at a depth of 10m.

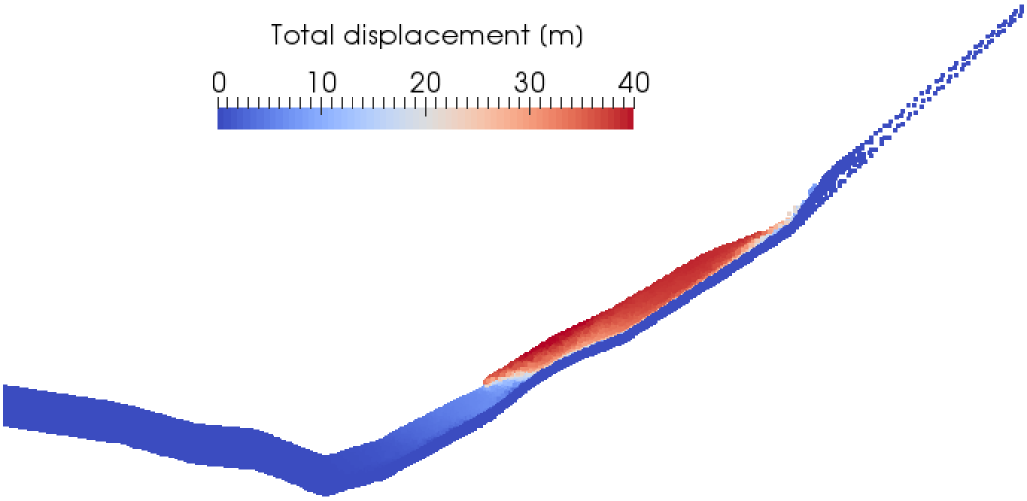

Figure 7.24. Total displacement results at the end of the simulation by using the strain-softening Mohr-Coulomb model.

The results (Fig. 7.24) show that introducing the softening behaviour of the soil the large run-out observed and the flow-like mechanism cannot be reproduced with a Mohr-Coulomb model. The unstable mass remains in the steep slope after a moderate run-out.

7.7 DISCUSSION

The Valarties flowslide provided an opportunity to investigate the role of liquefaction to explain the mobility of a landslide in a glacial deposit of low plasticity. The work started by gathering field information after the failure. The observed karstic flow at the head of the scar left by the slide was a key information to identify the triggering of the slide. Field and laboratory experiments, including undrained triaxial tests, exhibit the liquefaction potential of the soil involved in the failure, a glacial origin low-dense silty sand. The tests also provided basic data to calibrate Ta-Ger model parameters. Realizing that a shallow thickness of the glacial colluvium could be initially unsaturated the Ta-

Ger model was extended in a straightforward manner to deal with unsaturated conditions because collapse or expansion upon saturation of the glacial deposit was not expected in this case.

The available information to validate the computational procedure was the stabilized geometry of the flowslide and its comparison with the initial topography. It was also investigated if a strain-softening (Mohr-coulomb) behaviour of the glacial colluvium could explain the observed mobility of the slide. When this model was subjected to the assumed triggering section (a local injection of water) the calculated run-out was limited (around 40 m) and the unstable mass remained on the mid slope, far from the river.

The model offers the opportunity to follow in some particular locations the deformation of the unstable mass during the short time (45s according to the model) that elapsed from the triggering of the slide to its arrest.

Unlike tests in laboratory (flume tests), the bedrock profile in Valarties is quite irregular. This feature, the present of varying suction and the inertia forces, leads to a complex development of the flowslide. In Valarties, according to the model, an initially unstable shallow surface slab overruns and erodes the underlying soil deposit. This phenomenon is attributed to a protuberance of the rock substrate in the middle part of the slope.

It was also interesting to analyse the stress paths, velocities and displacements of a few distributed point along the initial position of the unstable soil mass. The analysis reveals again the variability of situations. Velocities and run-outs vary widely in the slope. It is observed that, after imposing the triggering failure, a water inflow, the soil located in the upper part of the slope became unstable, fails and liquefy. This involve the mobilization of a relatively small volume. The landslide evolves larger because the impact of the mobilized soil mass coming from higher elevations lead to liquefy the lower and stable soil mass located in the lower part of the slope (near to the river).

The model could not reproduce the relatively long run-out (around 50m) of the flowslide on the opposite slope of the valley. This discrepancy could be attributed to the lateral influx of unstable soil but also to the rapid dissipation of excess pore pressures after liquefaction, which results in a parallel increase in mean effective stress and the gain in strength along the critical state line. This is shown in the stress paths calculated for a few points. This calculated behaviour may be a consequence of the greater than real soil permeability or other formulation details of the constitutive model.

CHAPTER 8 - CONCLUSIONS AND FUTURE WORK

This final chapter aims to summarize the presented research and outline some conclusions. Finally, the on-going work status and the future research lines are defined.

8.1 FINAL CONCLUSIONS

This thesis deals with the numerical modelling of large deformations in geomechanics also accounting for liquefaction phenomenon in saturated and partially saturated soils. The main motivation of this study, the objectives and the followed methodology were described in the introductory chapter (Ch. 1).

The first challenge lied in choosing a proper constitutive model able to reproduce complex aspects of soil behaviour under different initial states, loading and drainage conditions and a computational method to simulate large deformations. A description of the existing constitutive models and computational methods used to simulate liquefaction phenomenon at different levels of accuracy and applicability was introduced in Ch. 2. Ta-Ger model showed promising performance and was selected to be implemented. Among the various numerical techniques used in geomechanics, the Material Point Method (MPM) was considered suitable for the objective of the thesis since it is a powerful tool to model large deformations and multiphase materials.

The MPM code used was presented in Ch. 3 with an overview of the available formulations for multi-phases materials. The 1-phase 1-point formulation can be applied for soil in drained and undrained conditions, when the pore pressure generation and dissipation are negligible, while the 2-phase formulation should be used when the soil is in in partially drained conditions. Unsaturated materials can be modelled with the fully coupled 3-phase 1-point formulation or with a simplified formulation (2-phase 1-point with suction effect). Some numerical features used in the calculations were introduced and the main contributions of this thesis to the code development were highlighted.

MPM was first applied to simulate geotechnical instabilities induced by soil excavation (Ch. 4). A set of undrained total stresses analyses were performed to study the stability of strutted excavations in clay. The aim was to compare with analytical solutions the results in terms of bearing capacity as well as shape and location of failure surface. It was concluded that a proper comparison is possible if an implicit hypothesis of classical solutions, which consists in continuously removing soil as it rises inside the excavation, is accounted for. For a given initial geometry and decreasing values of strength, failure could be detected when an increasing soils displacement rate was observed. In the second example, the well-documented Corte de Pallás landslide due to the toe excavation was simulated. The accumulated displacements and the subsequent new stable configuration are well reproduced. These results contributed to the validation of the excavation feature implemented in Anura3D.

A first attempt to study under seismic loading the complex landslide of Yesa was included in Ch. 5. First, a slope stability analysis with FEM was performed for different scenarios representing the landslide history and futures stabilizations measures. MPM was then used to carry out a motion back analysis to estimate displacements and deformations associated with an unstable scenario that FEM calculation could not provide. The implemented improvement of initial hydraulic conditions were included in the simulation allowing to assign specific water surfaces to the materials for the calculation of the initial stress distribution. Knowing that Yesa is a case of creeping slide motion, an analytical calculation in which it is simplified to a planar landslide was presented to explore the relationship between safety factor and creeping velocity and justify the displacements observed. Finally, the landslide response under earthquake excitation was performed with MPM with a focus on the interaction between the two superimposed sliding surfaces. The seismic action is assigned by prescribing to the MPs of an elastic material located at the model base a velocity-time function. Lateral absorbing boundaries that virtually extend the numerical model were also applied. Results were compared with the well-known Newmark's method in its classical form and by introducing the strain-rate dependence on the residual friction angle. The results obtained provided a deeper understanding of Yesa landslide.

A significant part of the thesis was dedicated to study the liquefaction phenomenon. The advanced constitutive model Ta-Ger, able to simulate liquefaction under monotonic and cyclic loading, was implemented in Anura3D. The algorithm validation and verification was carried out in the MPM code, when possible, or externally through the simulation of conventional monotonic and cyclic laboratory tests (Ch. 6).

The constitutive model could be finally applied for the simulation of a flow-like landslide induced by static liquefaction (Ch. 7). The aim was to provide a methodology, in the MPM framework, to reproduce the failure triggering and the subsequent slide-to-flow transition. The material involved in Valarties landslide was characterized by in situ and laboratory tests. In particular, data from undrained triaxial tests confirmed its liquefaction potential and allowed to calibrate Ta-Ger model parameters. Due to the lack of information about the groundwater level and stress distribution, hypothetical initial conditions of the slope were assumed in the calculation. The model could reproduce the failure initiation caused by a water inflow and the large displacements, in the post-failure stage, due to liquefaction of the unstable mass. Stress paths, velocities and displacements of selected MPs were also analysed to deeper understand the slope motion. The final run-out was found to be affected by the relative dilatancy index I_r that, in Ta-Ger model, accounts for liquefaction susceptibility. However, the maximum run-out obtained was lower than the observed one. This discrepancy was attributed to the lateral influx of unstable soil, not accounted in the plane strain simulations, but also to the rapid dissipation of excess pore pressures after liquefaction. This calculated behaviour may be a consequence of the greater than real soil permeability. To the author's knowledge, this is the first application of Ta-Ger constitutive model in the study of a real case of landslide.

8.2 ON-GOING WORK AND FUTURE RESEARCH

The seismic assessment of Yesa landslide with MPM was performed with a simplified analysis that should be improved to account for important aspects of dynamic calculations. A proper constitutive model to reproduce damping increase and shear modulus reduction with shear strains needs to be included in the MPM model. More adequate boundary conditions should be also implemented to prevent waves reflection. Absorbing boundaries were not developed to deal with problems in which the dynamic source is applied as a boundary condition (e.g. earthquake motions) but, on the contrary, if the dynamic source is inside the mesh.

Regarding the methodology proposed in the thesis to simulate flow-like landslides, it is developed in the framework of the 2-phase 1-point MPM formulation, thus, the slide-to-flow transition is treated at constitutive level by modelling the strength loss due to the excess of pore water pressure development. Future research could be directed to explore different approaches to model this kind of landslide like the 2-phase 2-point formulation that enables the simulation of liquid flow through porous media.

More general numerical issues of the used MPM code are finally highlighted. First, in the explicit integration scheme too low value of soil permeability results in very restrictive time steps and large computational time. This issue leads to use permeability values greater than real ones although it may significantly affect the results. This is the case of Valarties where rapid dissipation of excess pore pressures did not allow to calculate the observed final run-out. To solve such limitation it could be interesting to develop a numerical procedure to pass from the fully coupled to the undrained formulation. Lastly, additional stabilization techniques to avoid oscillations of stresses and pore water pressures in the dynamic MPM formulation should be investigated.

ACRONYMS

AGAUR Agency for Management of University and Research Grants
ALE Arbitrary Lagrangian Eulerian
CIMNE International Centre for Numerical Methods in Engineering
DEM Discrete Element Method
FDM Finite Difference Method
FEM Finite Element Method
LEM Limit Equilibrium Method
MPM Material Point Method
MPM-MIXED Mixed integration
MPM-MP Standard Material Point integration
NMD Nodal Mixed Discretization
SPH Smoothed Particle Hydrodynamics
UL-FEM Updated Lagrangian Finite Element Methods

BIBLIOGRAPHY

Al-Kafaji, I. K. J. (2013) *Formulation of a Dynamic Material Point Method (MPM) for Geomechanical Problems*. Universität Stuttgart.

Alonso-Marroquín, F. and Herrmann, H. J. (2004) 'Ratcheting of Granular Materials', *Physical Review Letters*, 92(5). doi: 10.1103/PhysRevLett.92.0543011.

Alonso, E. E., Gens, A. and Lloret, A. (1993) 'The landslide of Cortes de Pallas, Spain', *Géotechnique*, 43(4), pp. 507–521. doi: 10.1680/geot.1993.43.4.507.

Alonso, E. E., Sondon, M. and Alvarado, M. (2021) 'Landslide and hydraulic structures', *Engineering Geology. Under revision*.

Alsardi, A., Copana, J. and Yerro, A. (2021) 'Modelling earthquake-triggered landslide runout with the Material Point Method', *Proceedings of the Institution of Civil Engineers*.

Alsardi, A. and Yerro, A. (2021) 'Runout modeling of earthquake-triggered landslides with the Material Point Method', in *International Foundations Congress and Equipment Expo 2021*. Dallas, Texas: ASCE, pp. 1–10.

Alvarado, M., Pinyol, N. M. and Alonso, E. E. (2019) 'Landslide motion assessment including rate effects and thermal interactions: revisiting the Canelles landslid', *Canadian Geotechnical Journal*, 56(9), pp. 1338–1350.

Ambraseys, N. N. *et al.* (2002) *Internet-Site for European Strong-Motion Data*.

Ambraseys, N. N. *et al.* (2004) *Dissemination of European Strong-Motion Data, vol. 2*.

Andrianopoulos, K. I., Papadimitriou, A. G. and Bouckovalas, G. D. (2010) 'Bounding surface plasticity model for the seismic liquefaction analysis of geostructures', *Soil*

Dynamics and Earthquake Engineering, 30(10), pp. 895–911. doi: 10.1016/j.soildyn.2010.04.001.

Andrianopoulos, K. I., Papadimitriou, A. G. and Bouckovalas, G. D. (2011) 'Applications of the NTUA-SAND model for the seismic liquefaction analysis of geostructures', in *2nd International FLAC/DEM Symposium on Numerical Modeling*.

Antoinet, E., Buffiere, H. and Kovalcikova, K. (2017) 'Time dependent earthquake modeling of an earth dam', in *1st International Conference on the Material Point Method*. Available at: www.elsevier.com/locate/procedia.

Arya, L. M. and Paris, J. F. (1981) 'A physicoempirical model to predict the soil moisture characteristic from particle-size distribution and bulk density data', *Soil Science Society of America Journal*, 45(6), pp. 1023–1030.

Aubertin, M., Mbonimpa, M. and Chapuis, R. P. (2003) 'A physically-based model to predict the water retention curve from basic geotechnical properties', *Canadian Geotechnical Journal*, 40(6), pp. 1104–1122.

Aubertin, M., Ricard, J. F. and Chapuis, R. P. (1998) 'A predictive model for the water retention curve: Application to tailings from hard-rock mines', *Canadian Geotechnical Journal*, 35(1), pp. 55–69.

Aubry, R., Idelsohn, S. R. and Oñate, E. (2005) 'Particle finite element method in fluid mechanics including thermal convection diffusion', *Computers & Structures*, 83(17–18), pp. 1459–1475.

Bandara, S., Ferrari, A. and Laloui, L. (2016) 'Modelling landslides in unsaturated slopes subjected to rainfall infiltration using material point method', *International Journal for Numerical and Analytical Methods in Geomechanics*, 40(9). doi: 10.1002/nag.

Bardet, J. P. (1990) 'Hypoplastic model for sands', *Journal of Engineering Mechanics*, 116(9), pp. 1973–1994. doi: 10.1061/(ASCE)0733-9399(1990)116:9(1973).

Barrero, A. R. and Taiebat, M. (2015) 'Application of an advanced constitutive model in nonlinear dynamic analysis of tailings dam', in *GEOQuébec*.

Bauer, E. (1996) 'Calibration of a comprehensive hypoplastic model for granular materials', *Soils and Foundations*, 36(1), pp. 13–26.

Beaty, M. and Byrne, P. M. (1998) 'An effective stress model for predicting liquefacion behaviour of sand', in *Geotechnical Earthquake Engineering and Soil Dynamics III, ASCE Geotechnical Special Publication*. ASCE, pp. 766–777.

Been, K. and Jefferies, M. G. (1985) 'A state parameter for sands', *Géotechnique*, 35(2), pp. 99–112.

Vanden Berghe, J. F. (2011) *Sand Strength Degradation within the Framework of Vibratory*

Pile Driving. Université catholique de Louvain.

Beuth, L. *et al.* (2007) 'Formulation and validation of a quasi-static material point method', in *10th International Symposium in Numerical Methods in GeoMechanics*. Rhodes, Greece, pp. 189–195.

Bhandari, T. *et al.* (2016) 'Numerical modelling of seismic slope failure using MPM', *Computers and Geotechnics*, 75, pp. 126–134. doi: 10.1016/j.compgeo.2016.01.017.

Bienen, B. *et al.* (2014) *Interface enabling constitutive models coded as user materials to be employed in explicit analysis*.

Bishop, A. W. (1959) 'The principle of effective stress', *Teknisk Ukeblad*, 106(39), pp. 859–863.

Bjerrum, L. and Eide, O. (1956) 'Stability of strutted excavation in clay', *Geotechnique*, 6(1), pp. 32–47.

Bolton, M. D. (1986) 'The strength and dilatancy of sands', *Gèotechnique*, 36(1), pp. 65–78.

Bouc, R. (1971) 'Modele mathematique d' hysteresis', *Acustica*, 24(1), pp. 16–25.

Boulanger, R. W. and Ziotopoulou, K. (2015) *PM4Sand (Version 3): A Sand Plasticity Model for Earthquake Engineering Applications*.

Brinkgreve, R. B. J. and Bakker, H. L. (1991) 'Nonlinear finite-element analysis of safety factors', in *7th Int. Conf. on Comp. Methods and Advances in Geomechanics*. Cairns, pp. 1117–1122.

Bui, H. H. and Nguyen, G. D. (2021) 'Computers and Geotechnics Smoothed particle hydrodynamics (SPH) and its applications in geomechanics : From solid fracture to granular behaviour and multiphase flows in porous media', *Computers and Geotechnics*. Elsevier Ltd, 138. doi: 10.1016/j.compgeo.2021.104315.

Buscarnera, G. A. and Prisco, C. D. I. (2013) 'Soil stability and flow slides in unsaturated shallow slopes : can saturation events trigger liquefaction processes ?', *Géotechnique*, 63(10), pp. 801–817.

Bv, P. (2021) 'PLAXIS 2D Version 2021'. Delft, The Netherlands.

Calvello, M. *et al.* (2018) 'Optimizing the MPM model of a reduced scale granular flow by inverse analysis', in Cardoso, A. S. et al. (eds) *Numerical methods in geotechnical engineering IX*. Taylor & Francis, pp. 569–574.

Calvetti, F. and di Prisco, C. (2010) 'Discrete numerical investigation of the ratcheting phenomenon in granular materials', *Comptes Rendus Mecanique*, 338(10–11), pp. 604–614.

Cascini, L. *et al.* (2010) 'Modeling of Rainfall-Induced Shallow Landslides of the Flow-Type', *Journal of Geotechnical and Geoenvironmental Engineering*, 136(1), pp. 85–98.

Cascini, L. *et al.* (2014) 'SPH run-out modelling of channelised landslides of the fl ow type', *Geomorphology*, 214, pp. 502–513. doi: 10.1016/j.geomorph.2014.02.031.

Castro, G. (1969) *Liquefaction of Sands*. Harvard University.

Castro, G. and Poulos, S. (1977) 'Factors Affecting Liquefaction and Cyclic Mobility', *Journal of Geotechnical Engineering, ASCE*, 103, pp. 501–516.

Ceccato, F. *et al.* (2018) 'Impact forces of granular flows on rigid structures: Comparison between discontinuous (DEM) and continuous (MPM) numerical approaches', *Computers and Geotechnics*, 103, pp. 201–217.

Ceccato, F. *et al.* (2019) 'Evaluation of Dynamic Explicit MPM Formulations for Unsaturated Soils', in *VI International Conference on Particle-based Methods – Fundamentals and Applications (PARTICLES 2019)*.

Ceccato, F. *et al.* (2021) 'Two-phase dynamic MPM formulation for unsaturated soil', *Computers and Geotechnics*. Elsevier Ltd, 129.

Ceccato, F. and Simonini, P. (2016) 'Granular flow impact forces on protection structures: MPM numerical simulations with different constitutive models', *Procedia Engineering*, 158, pp. 164–169.

Cheng, Z., Dafalias, Y. F. and Manzari, M. T. (2013) 'Application of SANISAND Dafalias-Manzari model in FLAC-3D', in *Continuum and Distinct Element Numerical Modeling in Geomechanics - 3rd International FLAC/DEM Symposium*.

Conte, E., Pugliese, L. and Troncone, A. (2019) 'Post-failure stage simulation of a landslide using the material point method', *Engineering Geology*. Elsevier, 253(March), pp. 149–159. doi: 10.1016/j.enggeo.2019.03.006.

Corominas, J. (2013) *Modelo Geológico e Identificación del mecanismo de inestabilidad que afecta la ladera de la margen derecha de la presa de Yesa*. Available at: http://www.chebro.es/che/informes/Yesa/Informe%2520Ladera%2520Derecha%2520Yesa%2520UNIV%252%0A0POLITECNICA%2520CATALUNA.pdf.

Cremonesi, M. *et al.* (2020) 'A State of the Art Review of the Particle Finite Element Method (PFEM)', *Archives of Computational Methods in Engineering*. Springer Netherlands, 27(5), pp. 1709–1735. doi: 10.1007/s11831-020-09468-4.

Cremonesi, M., Franci, A. and Perego, U. A. (2011) 'A lagrangian finite element approach for the simulation of waterwaves induced by landslides', *Computers & Structures*, 89(11), pp. 1086–1093.

Cundall, P. A. (1987) 'Distinct element models of rock and soil structure', *Analytical and Computational Methods in Engineering Rock Mechanics*, 4, pp. 129–163.

Cundall, P. A. and Strack, O. D. L. (1979) 'A discrete numerical model for granular assemblies', *Géotechnique*, 29(1), pp. 47–65.

Cuomo, S. *et al.* (2019) 'Simulation of Liquefaction and Retrogressive Slope Failure in Loose Coarse-Grained Material', *International Journal of Geomechanics*, 19(10), pp. 1–15. doi: 10.1061/(ASCE)GM.1943-5622.0001500.

Cuomo, S., Di Perna, A. and Martinelli, M. (2021) 'MPM hydro-mechanical modelling of flows impacting rigid walls', *Canadian Geotechnical Journal*.

Department of Natural Resources [DNR] (2015) *Significant Deep-seated Landslides in Washington State — 1984 to 2014*.

Detournay, C. and Dzik, E. (2006) 'Nodal mixed discretization for tetrahedral elements', in *4th international FLAC symposium, numerical modeling in geomechanics. Minnesota Itasca Consulting Group, Inc. Paper, Number 07-02.*

Donea, J. *et al.* (2004) 'Arbitrary Lagrangian-Eulerian methods', in E. Stein, R. de Borst, and T. J. R. H. (ed.) *Encyclopedia of Computational Mechanics*. Jhon Wiley & Sons, Ltd.

Donea, J., Fasoli-Stella, P. and Giuliani, S. (1977) 'Lagrangian and Eulerian Finite element techniques for transient fluid- structure interaction problems', in *Transactions of the 4th International Conference on Structural Mechanics in Reactor Technology, volume B*. San Francisco, pp. 1–12.

Elgamal, A. *et al.* (2003) 'Modeling of cyclic mobility in saturated cohesionless soils', *International Journal of Plasticity*, 19, pp. 883–905.

Elgamal, A. *et al.* (2008) 'Three-Dimensional Seismic Response of Humboldt Bay Bridge-Foundation-Ground System', *Journal of Structural Engineering*. doi: 10.1061/ASCE0733-94452008134:71165.

Elgamal, A., Yang, Z. and Parra, E. (2003) 'Computational modeling of cyclic mobility and post-liquefaction site response', *Soil Dynamics and Earthquake Engineering*, 22, pp. 259–271. doi: 10.1016/S0267-7261(02)00022-2.

Ellen, S. and Fleming, R. W. (1987) 'Mobilization of debris flows from soil slips, San Francisco Bay region, California', *Reviews in Engineering Geology*, 7, pp. 31–40.

EPRI (1993) *Guidelines for determining design basis ground motions. Final Report, No. TR-102293*. Palo Alto, California.

Ering, P. and Sivakumar Babu, G. L. (2020) 'Effect of spatial variability of earthquake ground motions on the reliability of road system', *Soil Dynamics and Earthquake Engineering*, 136.

Faheem, H. *et al.* (2003) 'Two-dimensional base stability of excavations in soft soils using FEM', *Computers and Geotechnics*, 30(2), pp. 141–163. doi: 10.1016/S0266-352X(02)00061-7.

Fern, E. J., Robert, D. J. and Soga, K. (2016) 'Modeling the Stress-Dilatancy Relationship of Unsaturated Silica Sand in Triaxial Compression Tests Modeling the Stress-Dilatancy Relationship of Unsaturated Silica Sand in Triaxial Compression Tests', *Geotechnical and Geoenvironmental Engineering ·*, 142(11). doi: 10.1061/(ASCE)GT.1943-5606.0001546.

Fern, J. *et al.* (2019) *The Material Point Method for Geotechnical Engineering : a Practical Guide*. CRC Press.

Fontboté, J. (1911) 'Reflexions sobre la tectònica dels Pirineus', 889, I, pp. 307–352.

Gabet, E. J. and Mudd, S. (2006) 'The mobilization of debris flows from shallow landslides', *Geomorphology*, 74(1), pp. 207–218.

Galavi, V., Petalas, A. and Brinkgreve, R. B. J. (2013) 'Finite element modelling of seismic liquefaction in soils', *Geotechnical Engineering Journal of SEAGS & AGSSEA*, 44(3).

Gens, A. and Potts, D. (1988) 'Critical state models in computational geomechanics', 5(3), pp. 178–197. doi: 10.1108/eb023736.

Van Genuchten, M. (1980) 'A Closed-form Equation for Predicting the Hydraulic Conductivity of Unsaturated Soils', *Soil Science Society of America*, 44(5), pp. 892–898.

Gerolymos, N. and Gazetas, G. (2005) 'Constitutive model for 1-D cyclic behavior applied to seismic analysis of layered deposits', *Soils and Foundations*, 45(3), pp. 147–159.

Giannakou, A., Travasarou, T. and Chacko, J. (2012) 'Numerical modeling of liquefaction-induced slope movements', in ASCE (ed.) *GeoCongress*.

Gingold, R. A. and Monaghan, J. J. (1977) 'Smoothed particle hydrodynamics: theory and application to non-spherical stars', *Monthly Notices of the Royal Astronomical Society*, 181, pp. 375–389.

Gómez, R. (2018) 'La Presa de Yesa', *XVI Jornada Técnica Annual: casos singulares en mecánica de rocas*. Sociedad Española De Mecánica De Rocas (SEMR).

Gong, G. *et al.* (2012) 'DEM SIMULATION OF Liquefaction for granular media under undrained axisymmetric compression and plane strain conditions', *Acta Mechanica Solida Sinica*. The Chinese Society of Theoretical and Applied Mechanics, 25(6), pp. 562–570. doi: 10.1016/S0894-9166(12)60051-2.

Griffiths, D. V and Lane, P. A. (1999) 'Slope stability analysis by finite elements', *Géotechnique*, 49(3), pp. 287–403.

De Groot, M. B. *et al.* (2018) 'Liquefaction flow slides in large flumes', *International Journal of Physical Modelling in Geotechnics*, pp. 1–17.

Gudehus, G. (1996) 'A comprehensive constitutive equation for granular materials', *Soils* *and Foundation*, 36(1), pp. 13–26.

Gutiérrez, F., Lucha, P. and Galve, J. P. (2010) 'Reconstructing the geochronological evolution of large landslides by means of the trenching technique in the Yesa Reservoir (Spanish Pyrenees)', *Geomorphology*, 124, pp. 124–136.

Harbaugh, A. W. (2005) *MODFLOW-2005, the U.S. Geologica Survey Modular ground-water model. The ground-water flow process*. Available at: https://pubs.usgs.gov/tm/2005/tm6A16/#PDF.

Harlow, F. H., Ellison, M. A. and Reid, J. H. (1964) 'The particle-in-cell computing method for fluid dynamics', *Methods in computational physics*, 3(3), pp. 319–343.

He, M. *et al.* (2019) 'Numerical and safety considerations about 349 the Daguangbao landslide induced by the 2008 Wenchuan earthquake', *Journal of Rock Mechanics and Geotechnical Engineering*, 11(5), pp. 1019–1035.

Hiraoka, N. *et al.* (2013) 'Seismic slope failure modelling using the Mesh-free SPH method', *Internationa Journal GEOMATE*, 5.

Huang, Y. *et al.* (2011) 'Flow analysis of liquefied soils based on smoothed particle hydrodynamics', *Natural Hazards*, 59(3), pp. 1547–1560. doi: 10.1007/s11069-011-9851-3.

Huang, Y., Zhang, W. and Dai, Z. (2013) 'Numerical simulation of flow processes in liquefied soils using a soil – water- coupled smoothed particle hydrodynamics method', *Natural Hazards*, 69, pp. 809–827. doi: 10.1007/s11069-013-0736-5.

Hungr, O., Leroueil, S. and Picarelli, L. (2014) 'The Varnes classification of landslide types , an update', *Landslides*, 11, pp. 167–194. doi: 10.1007/s10346-013-0436-y.

Idriss, I. M. (1990) 'Response of soft soil sites during earthquakes', in *Proceedings of Memorial Symposium to Honor Professor H. Bolton Seed*. Berkeley, California.

Ishihara, K. (1985) 'Stability of natural deposits during earthquakes', in *11th International Conference on Soil Mechanics and Foundation Engineering*.

Ishihara, K., Tatsuoka, F. and Yasuda, S. (1975) 'Undrained deformation and liquefaction of sand under cyclic stresses', *Soils and Foundation*, 15(1), pp. 29–44.

Itasca (2012) 'FLAC – Fast Lagrangian Analysis of Continua in 3 Dimensions'. Minneapolis, Minnesota: Itasca Consult-ing Group, Inc.

Itasca (2016) 'FLAC – Fast Lagrangian Analysis of Continua'.

Iverson, R. M. (1997) 'The physics of debris flows', *Reviews of Geophysics*, 35, pp. 245–296.

Iverson, R. M. *et al.* (2015) 'Landslide mobility and hazards: Implications of the 2014 Oso disaster.', *Earth and Planetary Science Letters. Elsevier B.V.*, 412, pp. 197–208.

Iverson, R. M. and George, D. L. (2016) ʻModelling landslide liquefaction, mobility bifurcation and the dynamics of the 2014 Oso disasterʼ, *Géotechnique*, 66(3), pp. 175–187.

Jefferies, M. and Been, K. (2006) *Soil Liquefaction: a critical state approach*. Taylor & Francis.

Jefferies, M. G. (1993) ʻNor-Sand: a simple critical state model for sandʼ, *Géotechnique*, 43(1), pp. 91–103.

Jefferies, M. G. and Shuttle, D. A. (2005) *NorSand: features, calibration and use*. GSP 128, *Soil Constitutive Models: Evaluation, Selection, and Calibration*. GSP 128. Edited by A. Jerry, P. E. Yamamuro, and V. N. Kaliakin. ASCE.

Jibson, R. W. (1993) ʻPredicting Earthquake-Induced Landslide Displacements Using Newmarkʼs Sliding Block Analysisʼ, *Transportation Research Record*, 1411, pp. 9–17.

Johnson, A. M. and Rodine, J. R. (1984) ʻDebris flowʼ, in Brunsden, D. and Prior, D. B. (eds) *Slope instability*. John Wiley & Sons, Inc., pp. 257–361.

Kato, K. and Nagao, K. (2020) ʻNumerical Evaluation of Liquefaction Resistance for Desaturated Sandsʼ, *Journal of Geotechnical and Geoenvironmental Engineering*, 146(6). doi: 10.1061/(ASCE)GT.1943-5606.0002234.

Keaton, J. R. *et al.* (2014) *The 22 March 2014 Oso Landslide, Snohomish County, Washington. Turning Disaster into Knowledge*.

Kenney, T. C. (1967) ʻThe influence of mineral composition on the residual strength of natural soilsʼ, in *Geotechnical conference on the shear strength properties of natural soils and rocks, vol. 1*, pp. 123–129.

Kovács, C. (1981) *Seepage hydraulics*. Amsterdam, Netherlands: Elsevier Science.

Li, J. and Leao, T. F. (2018) ʻApplication of Nor Sand constitutive model in a highway fill embankment slope stability failure studyʼ, *Civil Engineering Journal*, 4(10), pp. 2252–2262.

Liu, S., Tang, X. and Li, J. (2021) ʻExtension of ALE method in large deformation analysis of saturated soil under earthquake loadingʼ, *Computers and Geotechnics*. Elsevier Ltd, 133. doi: 10.1016/j.compgeo.2021.104056.

Lucy, L. B. (1977) ʻA numerical approach to the testing of the fission hypothesisʼ, *Monthly Notices of the Royal Astronomical Society*, 82, pp. 1013–1024.

Lupini, J. F., Skinner, A. E. and Vaughan, P. R. (1981) ʻThe drained residual strength of cohesive soilsʼ, *Géotechnique*, 31(2), p. 181.213.

Lysmer, J. and Kuhlemeyer, R. L. (1969) ʻFinite dynamic model for infinite mediaʼ, in *Proceeding of ASCE*, pp. 859–877.

Mahardim, H., Bahsan, E. and Marthanty, R. R. D. R. (2021) ʻDevelopment of smoothed particle hydrodynamics (SPH) method to model the interaction of sand and water during liquefaction with bingham fluid model adaptation Development of smoothed particle hydrodynamics (SPH) method to model the interaction of sand', in *IOP Conf. Series: Earth and Environmental Science 622*. doi: 10.1088/1755-1315/622/1/012009.

Manne, A. and Satyam, N. (2015) 'A Review on the Discrete A Review on the Discrete Element Modeling of Dynamic Laboratory Tests for Liquefaction Assessment', *Electronic Journal of Geotechnical Engineering*, 20, pp. 21–46.

Manzanal, D., Fernández-Merodo, J. A. and Pastor, M. (2011) 'Generalized plasticity state parameter-based model for saturated and unsaturated soils. Part1: Saturated state', *International Journal for Numerical and Analytical Methods in Geomechanics* , 35, pp. 1347–1362.

Manzari, M. T. and Dafalias, Y. F. (1997) 'A critical state two-surface plasticity model for sands', *Géotechnique*, 47(2), pp. 255–272.

Martin, E. L., Thornton, C. and Utili, S. (2020) 'Micromechanical investigation of liquefaction of granular media by cyclic 3D DEM tests', *Géotechnique*, 70(10), pp. 906–915.

Martinelli, M. *et al.* (2021) 'Rainfall Boundary Condition in a Multiphase Material Point Method', in *Understanding and Reducing Landslide Disaster Risk*, pp. 303–309.

Mast, C. M. *et al.* (2014) 'Avalanche and landslide simulation using the material point method: flow dynamics and force interaction with structures', *Computational Geosciences*, 18, pp. 817–830.

McNamara, S., Garcia Rojo, R. and Herrmann, H. J. (2008) 'Microscopic origin of granular ratcheting', *Physical Review E*, 72(3).

Mesri, G. and Cepeda-Diaz, A. F. (1986) 'Residual shear strength of clays and shales', *Géotechnique*, 36(2), pp. 269–274.

Milne, F. *et al.* (2012) 'Centrifuge modelling of hillslope debris flow initiation', *Catena*, 92, pp. 162–171.

Newmark, N. M. (1965) 'Effects of earthquakes on dams and embankments', *Géotechnique*, 15(2), pp. 139–160.

Ng, C. W. W. *et al.* (2020) 'Effects of barrier deformability on load reduction and energy dissipation of granular flow impact', *Computers and Geotechnics*, 121. doi: 10.1016/j.compgeo.2020.103445.

O'Sullivan, C. and Cui, L. (2009) 'Micromechanics of granular material response during load reversals: combined DEM and experimental study', *Powder Technology*, 193(3), pp. 289–302.

Okura, Y., Kitahara, H. and Ochiai, H. (2002) 'Landslide fluidization process by flume experiments', *Engineering Geology*, 66, pp. 65–78.

Olivares, L. *et al.* (2009) 'An Instrumented Flume to Investigate the Mechanics of Rainfall-Induced An Instrumented Flume to Investigate the Mechanics of Rainfall-Induced Landslides in Unsaturated Granular Soils', *Geotechnical Testing Journal*, 32(2). doi: 10.1520/GTJ101366.

Oñate, E. *et al.* (2011) 'Possibilities of the particle finite element method for fluid-soil-structure interaction problems', *Computational Mechanics*, 48(3), pp. 307–318.

Pallàs, R. *et al.* (2006) 'Late Pleistocene and Holocene glaciation in the Pyrenees: a critical review and new evidence from 10Be exposure ages, south-central Pyrenees', *Quaternary Science Reviews*, 25, pp. 2937–2963.

Papadimitriou, A. G. and Bouckovalas, G. D. (2002) 'Plasticity model for sand under small and large cyclic strains: A multiaxial formulation', *Soil Dynamics and Earthquake Engineering*, 22, pp. 191–204. doi: 10.1016/S0267-7261(02)00009-X.

Parra, E. (1996) *Numerical Modeling of Liquefaction and Lateral Ground Deformation Including Cyclic Mobility and Dilation Response in Soil System*. Dept. of Civil Engineering, Rensselaer Polytechnic Institute, Troy, NY.

Pastor, M. *et al.* (1999) 'Modelización del comportamiento sísmico de geoestructuras', *Física de la Tierra*, 11, pp. 175–201.

Pastor, M. *et al.* (2009) 'A depth-integrated , coupled SPH model for flow-like landslides and related phenomena', *International Journal for Numerical and Analytical Methods in Geomechanics*, 33, pp. 143–172. doi: 10.1002/nag.

Pastor, M., Zienkiewicz, O. C. and Chan, A. H. C. (1990) 'Generalized plasticity and the modelling of soil behaviour', *International Journal for Numerical and Analytical Methods in Geomechanics*, 14, pp. 151–190.

Perdices, P. (2019) *Análisis de un deslizamiento en el Valle de Arán y simulación mediante el método del punto*. Polytechnic University of Catalonia.

Petalas, A. and Galavi, V. (2013) 'PLAXIS Liquefaction Model UBC3D-PLM'.

Pinyol, N. M. *et al.* (2012) 'Canelles Landslide: Modelling Rapid Drawdown and Fast Potential Sliding', *Landslides*, 9(1), pp. 33–51.

Pinyol, N. M. *et al.* (2018) 'Thermal effects in landslide mobility', *Géotechnique*, 68(6), pp. 528–545.

Pinyol, N. M., Di Carluccio, G. and Alonso, E. E. (2021) 'A slow and complex landslide under static and seismic action', *Engineering Geology. Under revision*.

Prevost, J. H. (1977) 'Mathematical modelling of monotonic and cyclic undrained clay behavior', *International Journal for Numerical and Analytical Methods in Geomechanics*. doi: 10.1002/nag.1610010206.

Prevost, J. H. (1978) 'Anisotropic undrained stress–strain behavior of clays', *Journal of the Geotechnical Engineering Division, ASCE*, 104(8), pp. 1075–1090.

Prevost, J. H. (1985) 'A simple plasticity theory for frictional cohesionless soils', *Soil Dynamics And Earthquake Engineering*, 4(1), pp. 9–17.

Qiao, L. *et al.* (2008) 'Shake-Table Testing and FLAC Modeling of Liquefaction-Induced Slope Failure and Damage to Buried Pipelines', *Geotechnical Earthquake Engineering and soil Dynamics*.

Ravichandran, N., Meguro, K. and Ravicbsodran, N. (2001) '3-D Modeling of Liquefaction Phenomenon Using Distinct Element Method', in *Fourth International Conference on Recent Advances Geotechnical Earthquake Engineering and Soil Dynamics*. Available at: http://scholarsmine.mst.edu/icrageesd.

Robertson, P. K. and Fear, C. E. (1995) 'Liquefaction of Sands and its Evaluation', *Proceedings of the First International*, pp. 1253–1287.

Rocscience (2018) 'SLIDE 2D'.

Rowe, P. W. (1962) 'The stress-dilatancy relation for static equilibrium of an assembly of particles in contact', *Proceedings of the Royal Society A: Mathematical, Physical and Engineering Sciences*, 269(1339), pp. 500–527.

Salazar, F. *et al.* (2015) 'Numerical modelling of landslide-generated waves with the particle finite element method (PFEM) and a non-Newtonian flow model', *International Journal for Numerical and Analytical Methods in Geomechanics*.

Scaringi, G., Hu, W. and Xu, Q. (2018) 'Discussion on: 'Experimental Study of Residual Strength and the Index of Shear Strength Characteristics of Clay Soil', *Engineering Geology*, 242, pp. 218–221. Available at: https://doi.org/10.1016/j.enggeo.2018.06.021.

Schulz, W. H. and Wang, G. (2014) 'Residual Shear Strength Variability as a Primary Control on Movement of Landslides Reactivated by Earthquake-Induced Ground Motion: Implications for Coastal Oregon, U.S.', *Journal of Geophysical Research: Earth Surface Reserach*, 119, pp. 1617–1635.

Schuster, R. L. (2006) *Interaction of Dams and Landslides - Case Studies and Mitigation, Professional paper, 1723, US Geologycal Survey*.

Seed, H. B. and Idriss, I. M. (1970) *Soil moduli and damping factors for dynamic response analysis. Report No. EERC 70-10*. Berkeley, California.

Shamy, U. El *et al.* (2010) 'DEM Simulation of Liquefaction-Induced Lateral Spreading', in *Fifth International Conference on Recent Advances Geotechnical Earthquake Engineering* *and Soil Dynamics*. Available at: http://scholarsmine.mst.edu/icrageesd.

Shi, D. *et al.* (2010) 'A Micro-Mechanical Simulation of Sand Liquefaction Behavior by DEM', in ASCE (ed.) *GeoShanghai 2010 International Conference*.

Skempton, A. W. (1951) 'The bearing capacity of clays.', in *Bluilding Research Congress, London*, pp. 180–189.

Sloan, S. W., Abbo, A. J. and Sheng, D. (2001) 'Refined explicit integration of elastoplastic models with automatic error control models', *Engineering Computations*, 18(1–2), pp. 121–154.

Sriskandakumar, S. (2004) *Cyclic loading response of Fraser River sand for validation of numerical models simulating centrifuge tests*. University of British Columbia.

Sternik, K. (2014) 'Prediction of static liquefaction by Nor Sand constitutive model', *Studia Geotechnica et Mechanica*, XXXVI(3). doi: 10.2478/sgem-2014-0029.

Sulsky, D., Chen, Z. and Schreyer, H. L. (1994) 'A particle method for history-dependent materials', *Computer Methods in Applied Mechanics and Engineering*, 118(1–2), pp. 179–196. doi: 10.1016/0045-7825(94)90112-0.

Sulsky, D., Zhou, S. and Schreyer, H. L. (1995) 'Application of a particle-in-cell method to solid mechanics', *Computer Physics Communications*, 87, pp. 236–252.

Taiebat, M. and Dafalias, Y. F. (2008) 'SANISAND: Simple anisotropic sand plasticity model', *International Journal for Numerical and Analytical Methods in Geomechanics*, 32, pp. 915–948. doi: 10.1002/nag.651.

Tasiopoulou, P. *et al.* (2019) '3D and 2D simulations of liquefaction-induced settlements of shallow foundations using Ta-Ger model', in *7th International Conference on Geotechnical Earthquake Engineering*.

Tasiopoulou, P. *et al.* (2021) 'Cyclic lateral response of OWT bucket foundations in sand : 3D coupled effective stress analysis with Ta-Ger model', *Soils and Foundations*. Japanese Geotechnical Society, 61(2), pp. 371–385. doi: 10.1016/j.sandf.2020.12.002.

Tasiopoulou, P. and Gerolymos, N. (2016a) 'Constitutive modelling of sand: a progressive calibration procedure accounting for intrinsic and stress-induced anisotropy', *Géotechnique*, 66(9), pp. 754–770.

Tasiopoulou, P. and Gerolymos, N. (2016b) 'Constitutive modelling of sand: Formulation of a new plasticity approach', *Soil Dynamics and Earthquake Engineering*, 82, pp. 205–221. doi: 10.1016/j.soildyn.2015.12.014.

Terzaghi, K. (1943) *Theoretical Soil Mechanics, Géotechnique*. John Wiley and Sons, INC., New York. doi: 10.1680/geot.1964.14.1.1.

Tika, T. E., Vaughan, P. R. and Lemos, L. (1996) 'Fast shearing of pre-existing shear zones in soil', *Géotechnique*, 46(2), pp. 197–233.

Tsegaye, A. B. (2010) *PLAXIS Liquefaction Model*. Available at: www.plaxis.nl.

Ukritchon, B., Whittle, A. J. and Sloan, S. W. (2003) 'Undrained Stability of Braced Excavations in Clay', *Journal of Geotechnical and Geoenvironmental Engineering*, 129(8), pp. 738–755. doi: 10.1061/(ASCE)1090-0241(2003)129:8(738).

Della Vecchia, G., Cremonesi, M. and Pisanò, F. (2019) 'On the rheological characterisation of liquefied sands through the dam-breaking test', *International Journal for Numerical and Analytical Methods in Geomechanics*, 43(4). doi: 10.1002/nag.2905.

Veermer, P. A. (1993) 'PLAXIS 2D Reference Manual Version 5'. Balkema, Rotterdam / Brookfield.

Verdugo, R. (1992) *Characterization of sandy soil behavior under large deformation*. University of Tokyo.

Verdugo, R. and Ishihara, K. (1996) 'The steady state of sandy soils', *Soils and Foundations*, 36(2), pp. 81–91.

Wang, B. *et al.* (2016) 'Development of an implicit material point method for geotechnical applications', *Computers and Geotechnics*, 71, pp. 159–167.

Wang, B., Vardon, P. J. and Hicks, M. A. (2018) 'Rainfall-induced slope collapse with coupled material point method', *Engineering Geology*. Elsevier, 239, pp. 1–12. doi: 10.1016/j.enggeo.2018.02.007.

Wang, G. and Sassa, K. (2001) 'Factors affecting rainfall-induced flowslides in laboratory flume tests', *Géotechnique*, 51(7), pp. 587–599.

Wang, G., Suemine, A. and Schulz, W. H. (2010) 'Shear-rate-dependent strength control on the dynamics of rainfall-triggered landslides, Tokushima Prefecture, Japan', *Earth Surface Processes and Landforms*, 35(4), pp. 407–416.

Wang, Z. *et al.* (2019) 'SPH-Based Analysis on the Lateral Response of Pipe Culverts in the Flowing Process of Liquefied Sand', *Mathematical Problems in Engineering*, (11), pp. 1–12.

Wartman, J. *et al.* (2016) 'The 22 March 2014 Oso landslide,Washington, USA', *Geomorphology*, 253, pp. 275–288.

Wedage, A., Morgenstern, N. R. and Chan, D. H. (1998) 'A strain rate dependent constitutive model for clays at residual strength', *Canadian Geotechnical Journal*, 35(2), pp. 364–373.

Wen, Y. K. (1976) 'Method for random vibration of hysteretic systems', *Journal of the Engineering Mechanics Division*, 102(2), pp. 249–263.

Wobbes, E. *et al.* (2016) 'Modeling of liquefaction using two-phase FEM with UBC3D-PLM model', in *1st International Conference on the Material Point Method, MPM 2017*. Available at: www.elsevier.com/locate/procedia.

Von Wolffersdorff, P. A. (1996) 'A hypoplastic relation for granular materials with a predefined limit state surface', *Mechanics of Cohesive-frictional Materials*, 1(3), pp. 251–271.

Yang, Z. (2000) *Numerical Modeling of Earthquake Site Response Including Dilation and Liquefaction*. Dept. of Civil Engineering and Engineering Mechanics, Columbia University, NY, New York.

Yang, Z. and Elgamal, A. (2008) 'Multi-surface Cyclic Plasticity Sand Model with Lode Angle Effect', *Geotechnical and Geological Engineering*, 26(3), pp. 335–348.

Yerro, A. (2015) *MPM modelling of landslides in brittle and unsaturated soils*. Universitat Politècnica de Catalunya.

Yerro, A., Alonso, E. E. and Pinyol, N. M. (2015) 'The material point method for unsaturated soils', *Géotechnique*, 65(3), pp. 201–217.

Yerro, A., Alonso, E. E. and Pinyol, N. M. (2016) 'Run-out of landslides in brittle soils', *Computers and Geotechnics*, 80, pp. 427–439.

Yerro, A., Pinyol, N. M. and Alonso, E. E. (2016) 'Internal progressive failure in deep-seated landslides', *Rock Mechanics and Rock Engineering*, 49, pp. 2317–2332.

Yerro, A., Soga, K. and Bray, J. (2019) 'Runout evaluation of Oso landslide with material point method', *Canadian Geotechnical Journal*, 56, pp. 1304–1317.

Yin, Y. *et al.* (2016) 'Reservoir-Induced Landslides and Risk Control in Three Gorges Project on Yangtze River, China', *Journal of Rock Mechanics and Geotechnical Engineering*, 8(5), pp. 577–595.

Zabala, F. and Alonso, E. E. (2011) 'Progressive failure of Aznalcóllar dam using the material point method', *Géotechnique*, 61(9), pp. 795–808.

Zhang, W., Yuan, W. and Dai, B. (2018) 'Smoothed particle finite-element method for large-deformation problems in geomechanics', *International Journal of Geomechanics*, 18(4).

Zhang, X. *et al.* (2013) 'Computers and Geotechnics Particle finite element analysis of large deformation and granular flow problems', *Computers and Geotechnics*. Elsevier Ltd, 54, pp. 133–142. doi: 10.1016/j.compgeo.2013.07.001.

Zhang, X. *et al.* (2015) 'Numerical simulation of a flow-like landslide using the particle finite element method', *Computational Mechanics*, 55(1), pp. 167–177.

Zhang, X. *et al.* (2019) 'A unified Lagrangian formulation for solid and fluid dynamics and its possibility for modelling submarine landslides and their consequences', *Computer Methods in Applied Mechanics and Engineering*, 343, pp. 314–338.

Zhang, X., Krabbenhoft, K. and Sheng, D. (2014) 'Particle finite element analysis of the granular column collapse problem', *Granular Matter*, 16(4), pp. 609–619.

Zienkiewicz, O. C. *et al.* (1999) *Computational Geomechanics*. Edited by Wiley.

LIST OF PUBLICATION

Book chapter

Excavation-induced instabilities (2019)
Authors: Pinyol, N.M.; **Di Carluccio**, G.
In: The Material Point Method for geotechnical engineering: a practical guide. CRC Press. 2019. pp: 271 - 286. ISBN: 9781138323315.

At conferences

Liquefaction-induced large displacements of caisson quay wall: Barcelona Harbor, Spain (2019)
Authors: **Di Carluccio**, G.; Pinyol, N.M.; Alonso, E.E.
In: MPM 2019 - 2nd International Conference on The Material Point Method for Modelling Large Deformation and Soil–Water–Structure Interaction. University of Cambridge, UK

Numerical modelling of Val d'Arán landslide with Material Point Method (2019)
Authors: **Di Carluccio**, G.; Pinyol, N.M. Perdices, P.; Hürlimann, M.
In: PARTICLES 2019 - VI International Conference on Particle-Based Methods: Fundamentals and Applications. Centro Internacional de Métodos Numéricos en Ingeniería (CIMNE). pp. 534 ~ 542. ISBN/ISSN: 978-84-121101-1-1.

Submitted at indexed journals

Liquefaction-induced flow-like landslides. The case of Valarties (Spain) (2021)
Authors: **Di Carluccio**, G.; Pinyol, N.M.; Alonso, E.E.; Hürlimann, M.

Journal: Géotechnique

A slow and complex landslide under static and seismic action (2021)
Authors: Pinyol, N.M.; **Di Carluccio**, G.; Alonso, E.E.
Journal: Engineering Geology

APPENDIX

A.1 External soil model (ESM) Anura3D interface

```fortran
      SUBROUTINE ESM(NPT,NOEL,IDSET,STRESS,EUNLOADING,
     .PLASTICMULTIPLIER,DSTRAN,NSTATEV,STATEV,NADDVAR,ADDITIONALVAR,
     .CMNAME,NPROPS,PROPS,NUMBEROFPHASES,NTENS)

      !DEC$ ATTRIBUTES DLLEXPORT, ALIAS:"ESM" :: ESM
      implicit double precision (a-h, o-z)
      CHARACTER*80 CMNAME,MATTYPE
      DIMENSION NPT(1),NOEL(1),IDSET(1),STRESS(NTENS),EUNLOADING(1),
     .PLASTICMULTIPLIER(1),DSTRAN(NTENS),STATEV(NSTATEV),
     .ADDITIONALVAR(NADDVAR),PROPS(NPROPS),NUMBEROFPHASES(1)

!---Local variables required in standard UMAT
        integer :: IStep, TimeStep
        double precision, dimension(:), allocatable :: ddsddt ! only for fully
        !coupled thermal analysis: variation of stress increment due to
        !temperature
        double precision, dimension(:), allocatable :: drplde ! only for fully
        !coupled thermal analysis: variation of volumetric heat generation due to
        !strain increment
        double precision, dimension(:), allocatable :: stran
        double precision, dimension(:), allocatable :: time
        double precision, dimension(:), allocatable :: predef
        double precision, dimension(:), allocatable :: dpred

        double precision, dimension(:), allocatable :: coords
        double precision, dimension(:,:), allocatable :: ddsdde ! Jacobian matrix
        !of the constitutive model (tangent stiffness matrix in case of MC)
        double precision, dimension(:,:), allocatable :: drot
        double precision, dimension(:,:), allocatable :: dfgrd0
        double precision, dimension(:,:), allocatable :: dfgrd1
```

```
        double precision :: sse, spd, scd ! specific elastic strain energy,
        !plastic dissipation, creep dissipation
        double precision :: rpl ! only for fully coupled thermal analysis:
        !volumetric heat generation
        double precision :: drpldt ! only for fully coupled thermal analysis:
        !variation of volumetric heat generation due to temperature
        double precision :: pnewdt, dtime, temp, dtemp, celent
        double precision :: Value ! auxiliary variable holding any real valued
        !number
        double precision :: Porosity
        double precision :: WaterPressure, WaterPressure0
        double precision :: GasPressure, GasPressure0, DegreeSaturation


        integer :: ndi, nshr, layer, kspt, kstep, kinc

        allocate( ddsddt(ntens), drplde(ntens), stran(ntens), time(2),
   &            predef(6), dpred(6), coords(3), ddsdde(ntens,ntens),
   &            drot(3,3), dfgrd0(3,3), dfgrd1(3,3) )

        ! initialization
        Eunloading = 0.0
        PlasticMultiplier = 0.0

        ! rename additional variables
        Predef(1) = AdditionalVar(1)      !Porosity
        Predef(2) = AdditionalVar(2)      !WaterPressure
        Predef(3) = AdditionalVar(3)      !WaterPressure0
        Predef(4) = AdditionalVar(4)      !GasPressure
        Predef(5) = AdditionalVar(5)      !GasPressure0
        Predef(6) = AdditionalVar(6)      !DegreeSaturation
        time(1) = AdditionalVar(7)        !TotalRealTime
        time(2) = AdditionalVar(8)        !OverallTotalTime
        dtime = AdditionalVar(9)          !TimeIncrement
        IStep = AdditionalVar(10)
        Timestep = AdditionalVar(11)      !Note: Very first time and load step:
                                          !Istep=1 and TimeStep=1

        if ((IStep == 1) .and. (TimeStep == 1))then !Initial mean effective stress
          p  = (stress(1) + stress(2) + stress(3))/3.
          statev(1) = -p
        end if

          call umat(stress, statev, ddsdde, sse, spd, scd, rpl, ddsddt,
   &        drplde, drpldt, stran, dstran, time, dtime, temp, dtemp,
   &        predef, dpred, cmname, ndi, nshr, ntens, nstatv, props,
   &        nprops, coords, drot, pnewdt, celent, dfgrd0, dfgrd1, noel,
   &        npt, layer, kspt, kstep, kinc)

!---Definition of Eunloading -> required to define the max time step
        Eunloading = max(ddsdde(1,1),ddsdde(2,2),ddsdde(3,3))

        return
      end subroutine ESM
```

A.2 UMAT SUBROUTINE FOR TA-GER MODEL

```
*USER SUBROUTINES
      SUBROUTINE UMAT(STRESS,STATEV,DDSDDE,SSE,SPD,SCD,
     1 RPL,DDSDDT,DRPLDE,DRPLDT,
     2 STRAN,DSTRAN,TIME,DTIME,TEMP,DTEMP,PREDEF,DPRED,CMNAME,
     3 NDI,NSHR,NTENS,NSTATEV,PROPS,NPROPS,COORDS,DROT,PNEWDT,
     4 CELENT,DFGRD0,DFGRD1,NOEL,NPT,LAYER,KSPT,KSTEP,KINC)
!
      !DEC$ ATTRIBUTES DLLEXPORT, ALIAS:"UMAT" :: UMAT
      INCLUDE 'ABA_PARAM.INC'
!
      CHARACTER*80 CMNAME
      DIMENSION STRESS(NTENS),STATEV(NSTATEV),
     1 DDSDDE(NTENS,NTENS),DDSDDT(NTENS),DRPLDE(NTENS),
     2 STRAN(NTENS),DSTRAN(NTENS),TIME(2),PREDEF(6),DPRED(6),
     3 PROPS(NPROPS),COORDS(3),DROT(3,3),DFGRD0(3,3),DFGRD1(3,3)


!***********************************************************************
!*            TA-GER model (Tasiopoulou & Gerolymos, 2016)             *
!***********************************************************************

      call TaGer(STRESS,DSTRAN,NTENS,PROPS,STATEV,DDSDDE)

*
* ... end UMAT routine
*
      Return
      End

!***********************************************************************
!*                             SUBROUTINES                             *
!***********************************************************************
      subroutine TaGer(Sig0,dEps,ntens,Props,Statev,Ddsdde)
      implicit none

      integer :: ICOUNT
      integer :: i,j
      real :: rad, PI

      ! Input variables
      integer, intent(in) :: ntens
      double precision, dimension(16),intent(in) :: Props
      double precision, dimension(ntens), intent(in) :: dEps

      ! Inout variables
      double precision, dimension(ntens), intent(inout) :: Sig0
      double precision, dimension(50), intent(inout) :: Statev
       double precision, intent(inout), dimension(ntens,ntens) :: Ddsdde

      ! Properties
      double precision :: G0,m,ni ! Elasticity
      double precision :: Q_bolton,R_bolton ! Bounding surface and dilatancy
```

```
double precision :: e0,emin,emax ! Void ratios
double precision :: phics ! Critical friction angle
double precision :: delta,kappa ! Calibration coefficients

! State variables
double precision :: p0,e,dW_old,rp(ntens),EpsD

! Constants
double precision :: Dr0,Ir0 ! Initial value of relative density and
! relative dilatancy index
double precision :: n,c,phi0 ! Parameters depending on initial state
double precision :: Ms0 ! Initial value of bounding stress ratio
double precision :: Mcs ! Critical state
double precision :: phimax,gab ! Peak friction angle

! Substepping variables
double precisión :: Rn ! Relative error
double precisión :: STOL ! Tolerance relative error
double precisión :: T,T1,DT,beta,DTmin ! Pseudo times
double precision, dimension(ntens) :: Sig2,dSig1,dSig2,SigP,SigC
double precision, dimension(ntens) :: Stress
double precision, dimension(ntens) :: SUBdEps ! Trial strain increment
double precisión :: SUBdEpsV,SUBdEpsD ! Volumetric and deviatoric
! component of trial strain increment
double precision, dimension(ntens) :: SUMEps ! Trial accumulated strains
double precisión :: SUMEpsD ! Deviatoric component of trial accumulated
! strains
double precisión :: p2,q2 ! Mean and deviatoric component of second order
! estimate of stress

! Local variables
double precision, dimension(ntens)  :: Sig ! Stress
double precisión :: p,q ! Mean and deviatoric stress
double precision, dimension(ntens)  :: n_,s,r,rc ! Stress tensors
double precisión :: np,qp,dW,nr
double precisión :: I1,I2,I3,J2,J3 ! Stress invariants
double precisión :: Lode,Msteta,chi ! Lode angle dependency
double precision, dimension(ntens)  :: GRADf,GRADg ! Bounding surface and
! plastic potential gradient
double precision, dimension(ntens,ntens):: De,Dp,Dep ! Stiffness matrix

double precision :: G,K ! Elastic moduli
double precision :: Dr,Ir ! Current value relative density and relative
! dilatancy index
double precision :: Ms,Mspeak,Msp ! Bounding surface parameters
double precision :: d ! Dilatancy
double precision :: zeta ! Hardening parameter
double precision :: Mpt0,Mpt ! Phase transformation parameters
double precision :: Porosity,BulkW

G0          = Props(1)
m           = Props(2)
ni          = Props(3)
Q_bolton    = Props(4)
```

```
      R_bolton    = Props(5)
      e0          = Props(6)
      emin        = Props(7)
      emax        = Props(8)
      phics       = Props(9)
      delta       = Props(10)
      kappa       = Props(11)

      PI = 3.14159265358979323846264338327950288419716939 9d0
      rad = 180.0d0/PI


!***************************************************************************
!                              Initialization                             *
!***************************************************************************

      Sig = Sig0

      ! State variables
      p0 = statev(1) ! This value is not updated in the subroutine despite
                     ! it is defined as state variable
      e  = statev(2)
      dW_old = statev(3)
      do i = 1,ntens
          rp(i) = statev(3+i)
      end do
      EpsD = statev(10)
      BulkW = statev(11)

      ! Parameters depending on initial state
      Dr0 = (emax - e)/(emax - emin)
      Ir0 = Dr0 * (Q_bolton - log(p0)) - R_bolton

      n = 0.4*Dr0 +0.14
      phi0 = kappa * phics + 5 * Ir0
      c = 6 + delta * Ir0

      if (phi0 < phics) then ! Initial value of bounding stress ratio
          Ms0 = 6.*sin(phi0/rad) / (3.-sin(phi0/rad))
      else
          Ms0 = 6.*sin(0.99*phics/rad) / (3.-sin(0.99*phics/rad))
      end if

      ! Critical value of bounding stress ratio
      Mcs = 6.*sin(phics/rad) / (3.-sin(phics/rad))

      ! Peak friction angle coefficient
      gab = 5.    ! 5 for plain strain, 3 for triaxial

!***************************************************************************
!                              Substepping                                *
!***************************************************************************

      ! Tolerances
      STOL   = 0.001d0
```

```
      DTmin = 0.0001d0

      T  = 0.0d0
      DT = 1.0d0

      do while (T < 1)
      Rn = 100
      ICOUNT = 0

          do while (Rn > STOL .and. ICOUNT < 1000)

            SUBdEps = DT * dEps

            call getDevVolStrain (SUBdEps,SUBdEpsV,SUBdEpsD,ntens)
            SUMEpsD = EpsD + SUBdEpsD

            call getPQ(Sig,p,q,ntens)

            Dr = (emax - e)/(emax - emin)
            Ir = Dr * (Q_bolton - log(p)) - R_bolton

            call getStressInvariants(Sig,I1,I2,I3,J2,J3,Lode,ntens)

            call getMs(SUMEpsD,phics,Mcs,Ms0,c,Mspeak,Msp,Ir,Ms,gab)
            call getMsteta(Ms,Lode,chi,Msteta)
            call getStressTensor(p,zeta,Sig,SUBdEps,rp,n_,r,np,qp,nr,
     *                           dW_old,dW,ntens)
            call getHardeningParameter(Ms,qp,p,np,chi,zeta)
            call getMpt(SUMEpsD,zeta,chi,Mcs,
     *                  Mspeak,c,Ir,Mpt0,n,Mpt)
            d = sqrt(2./3.)*Mpt*chi - nr

            call getGRAD (d,n_,nr,GRADg,GRADf,ntens)

            call getElasticMatrix (p,G0,m,ni,G,K,De,ntens)
            call getPlasticMatrix (zeta,n,GRADg,GRADf,De,Dp,ntens)

            Dep = De - Dp

                    select case(ntens)
                case(4)
                                  do i = 1,4
                           dSig1(i) = Dep(i,1) * SUBdEps(1) + Dep(i,2) *
     *                SUBdEps(2) + Dep(i,3) * SUBdEps(3) + Dep(i,4) *
     *                SUBdEps(4)
                    end do
                           case(6)
                    do i = 1,6
                           dSig1(i) = Dep(i,1) * SUBdEps(1) + Dep(i,2) *
     *                SUBdEps(2) + Dep(i,3) * SUBdEps(3) + Dep(i,4) *
     *                SUBdEps(4) + Dep(i,5) * SUBdEps(5) + Dep(i,6) *
     *                SUBdEps(6)
                    end do
                    end select
```

```
            ! Calculate a second order estimate of stress
            Sig2 = Sig + dSig1


            call getPQ(Sig2,p2,q2,ntens)

            Dr = (emax - e)/(emax - emin)
            Ir = Dr * (Q_bolton - log(p2)) - R_bolton

            call getStressInvariants(Sig2,I1,I2,I3,J2,J3,Lode,ntens)

            call getMs(SUMEpsD,phics,Mcs,Ms0, c,Mspeak,Msp,Ir,Ms,gab)
            call getMsteta(Ms,Lode,chi,Msteta)
            call getStressTensor(p2,zeta,Sig2,SUBdEps,rp,n_,r,np,qp,nr,
     *                          dW_old,dW,ntens)
            call getHardeningParameter(Ms,qp,p2,np,chi,zeta)
            call getMpt(SUMEpsD,zeta,chi,Mcs,
     *                 Mspeak,c,Ir,Mpt0,n,Mpt)

            d = sqrt(2./3.)*Mpt*chi - nr

            call getGRAD (d,n_,nr,GRADg,GRADf,ntens)

            call getElasticMatrix (p2,G0,m,n,G,K,De,ntens)
            call getPlasticMatrix (zeta,n,GRADg,GRADf,De,Dp,ntens)

            Dep = De - Dp

            select case(ntens)
                case(4)
                    do i = 1,4
                        dSig2(i) = Dep(i,1) * SUBdEps(1) + Dep(i,2) *
     *                  SUBdEps(2) + Dep(i,3) * SUBdEps(3) + Dep(i,4) *
     *                  SUBdEps(4)
                    end do
                case(6)
                    do i = 1,6
                        dSig2(i) = Dep(i,1) * SUBdEps(1) + Dep(i,2) *
     *                  SUBdEps(2) + Dep(i,3) * SUBdEps(3) + Dep(i,4) *
     *                  SUBdEps(4) + Dep(i,5) * SUBdEps(5) + Dep(i,6) *
     *                  SUBdEps(6)
                    end do
            end select

            SigP = Sig + (dSig1 + dSig2)/2.

            ! Estimating error
                    select case(ntens)
                           case(4)
                           Rn = 0.5 * sqrt(((dSig2(1) - dSig1(1))**2. + (dSig2(2)
-
     *              dSig1(2))**2. + (dSig2(3) - dSig1(3))**2. + (dSig2(4) -
     *              dSig1(4))**2.)/(SigP(1)**2. + SigP(2)**2. +
     *              SigP(3)**2. * SigP(4)**2.))
```

```
                           case(6)
                           Rn = 0.5 * sqrt(((dSig2(1) - dSig1(1))**2. + (dSig2(2)
-
     *              dSig1(2))**2. + (dSig2(3) - dSig1(3))**2. +
     *              (dSig2(4) - dSig1(4))**2. + (dSig2(5) - dSig1(5))**2.
     *              + (dSig2(6) - dSig1(6))**2.)/(SigP(1)**2. +
     *              SigP(2)**2. + SigP(3)**2. + SigP(4)**2. + SigP(5)**2.
     *              + SigP(6)**2.))
                    end select

            if (DT == DTmin) then
            exit
            end if

            ! If Rn>STOL, the loop is not finished and the substep is
            !recalculated smaller
            if (Rn > STOL) then
                beta = max (0.9d0*(sqrt(STOL/Rn)), 0.1d0)
                DT = max (DT*beta, DTmin)
                ICOUNT = ICOUNT + 1   ! Update counter
            end if

! ************* Check that stresses are inside the bounding surface *************

          call getPQ(SigP,p,q,ntens)

          Dr = (emax - e)/(emax - emin)
          Ir = Dr * (Q_bolton - log(p)) - R_bolton

          call getStressInvariants(SigP,I1,I2,I3,J2,J3,Lode,ntens)

          call getMs(SUMEpsD,phics,Mcs,Ms0,c,Mspeak,Msp,Ir,Ms,gab)
          call getMsteta(Ms,Lode,chi,Msteta)
          call getStressTensor(p,zeta,SigP,SUBdEps,rp,n_,r,np,qp,nr,
     *                         dW_old,dW,ntens)
          call getHardeningParameter(Ms,qp,p,np,chi,zeta)

          do while (zeta > 1.001)
          Stress = SigP
          call getPQ(Stress,p,q,ntens)
          call getStressTensor(p,zeta,Stress,SUBdEps,rp,n_,r,np,qp,nr,
     *                         dW_old,dW,ntens)
          call getHardeningParameter(Ms,qp,p,np,chi,zeta)
          rc = r/zeta

          SigC(1) = - rc(1)*p - p
          SigC(2) = - rc(2)*p - p
          SigC(3) = - rc(3)*p - p
          SigC(4) = - rc(4)*p

          call getPQ(SigC,p,q,ntens)
          call getStressTensor(p,zeta,SigC,SUBdEps,rp,n_,r,np,qp,nr,
     *                         dW_old,dW,ntens)
          call getHardeningParameter(Ms,qp,p,np,chi,zeta)
```

```
    SigP = SigC
    end do

    ! *********************************************************************

    SigC = SigP

    end do

! Update stress and strain
Sig = SigC
EpsD = SUMEpsD

call getPQ(Sig,p,q,ntens)

Dr = (emax - e)/(emax - emin)
Ir = Dr * (Q_bolton - log(p)) - R_bolton

call getStressInvariants(Sig,I1,I2,I3,J2,J3,Lode,ntens)

call getMs(EpsD,phics,Mcs,Ms0, c,Mspeak,Msp,Ir,Ms,gab)
call getMsteta(Ms,Lode,chi,Msteta)
call getStressTensor(p,zeta,Sig,SUBdEps,rp,n_,r,np,qp,nr,dW_old,
*                dW,ntens) ! Update stress ratio tensor at reversal point
call getHardeningParameter(Ms,qp,p,np,chi,zeta)
call getMpt(EpsD,zeta,chi,Mcs,Mspeak,c,Ir,
*           Mpt0,n,Mpt)

d = sqrt(2./3.)*Mpt*chi - nr

call getElasticMatrix (p,G0,m,ni,G,K,De,ntens)

! Tangent stiffness matrix to be returned (done by elastic stiffness)
Ddsdde(1,1) = De(1,1)
Ddsdde(2,2) = De(2,2)
Ddsdde(3,3) = De(3,3)
Ddsdde(4,4) = De(4,4)/2
if (ntens == 6)then
Ddsdde(5,5) = De(5,5)/2
Ddsdde(6,6) = De(6,6)/2
end if

e = SUBdEpsV * (1+e) + e
Porosity = e /(1 + e)

! To be defined for undrained calculations
BulkW = Porosity * (2.*G/3. * (((1.+0.49)/(1.-2.*0.49)) -
*       (1.+ni)/(1.-2.*ni)))

T1 = T + DT
if (T1 >= 1d0) then

  do i = 1,ntens
```

```
          Sig0(i) = Sig(i)
        end do

        ! Update state variables
        statev(1) = p0
        statev(2) = e
        statev(3) = dW_old
        do i = 1,ntens
            statev(3+i) = rp(i)
        end do
        statev(10) = EpsD
        statev(11) = BulkW

      return
      end if

      beta = min(0.9d0*sqrt(STOL/Rn), 1.1d0)  ! If T1<1, calculation of
                                              ! the next substep DT

      if (ICOUNT > 1) then    ! The previous step failed
         beta = min (beta, 1.0d0)
      end if

      DT = beta * DT
      DT = max (beta * DT, DTmin)
      DT = min (DT, 1.0d0-T1)
      T = T1

      end do

      end subroutine TaGer

!***************************************************************************

      subroutine getDevVolStrain(Eps,EpsV,EpsD,ntens)
      implicit none
      integer, intent(in)  :: ntens
      double precision, intent(in)   :: Eps(ntens)
      double precision, intent(out)  :: EpsV, EpsD

      EpsV = Eps(1) + Eps(2) + Eps(3)

      select case(ntens)
      case(4)
          EpsD = sqrt(2./3.) * sqrt( (Eps(1)-EpsV/2.)**2. +
     *           (Eps(2)-EpsV/2.)**2. + (Eps(3)-EpsV/2.)**2. +
     *           (Eps(4)**2.)/2.)
      case(6)
          EpsD = sqrt(2./3.) * sqrt( (Eps(1)-EpsV/3.)**2. +
     *           (Eps(2)-EpsV/3.)**2. + (Eps(3)-EpsV/3.)**2. +
     *           (Eps(4)**2.)/2. + (Eps(5)**2.)/2. + (Eps(6)**2.)/2.)
      end select

      end subroutine getDevVolStrain
```

```
!********************************************

      subroutine getStressInvariants(Sig,I1,I2,I3,J2,J3,Lode,ntens)
      implicit none
      integer, intent(in)  :: ntens
      double precision, dimension(ntens), intent (in) :: Sig
      double precision, intent (inout)            :: I1,I2,I3,J2,J3
      double precision, intent (out)              :: Lode
      double precision, dimension(6)              :: Stress

      Stress = - Sig

      select case(ntens)
        case(4)
            I1 = Stress(1) + Stress(2) + Stress(3)
            I2 = Stress(1)*Stress(2) + Stress(2)*Stress(3) +
     *           Stress(3)*Stress(1) - Stress(4)**2.
            I3 = Stress(1)*Stress(2)*Stress(3) -
     *           Stress(3)*(Stress(4))**2.
            J2 = (1./6.) * ((Stress(1)-Stress(2))**2. +
     *           (Stress(2)-Stress(3))**2. + (Stress(3)-Stress(1))**2. +
     *           6*Stress(4)**2.)
        case(6)
            I1 = Stress(1) + Stress(2) + Stress(3)
            I2 = Stress(1)*Stress(2) + Stress(2)*Stress(3) +
     *           Stress(3)*Stress(1) - Stress(4)**2. - Stress(5)**2. -
     *           Stress(6)**2.
            I3 = Stress(1)*Stress(2)*Stress(3) +
     *           2.*Stress(4)*Stress(5)*Stress(6) -
     *           Stress(1)*(Stress(5))**2. -
     *           Stress(1)*(Stress(5))**2. -
     *           Stress(2)*(Stress(6))**2. -
     *           Stress(3)*(Stress(4))**2.
            J2 = (1./6.) * ((Stress(1)-Stress(2))**2. +
     *           (Stress(2)-Stress(3))**2. + (Stress(3)-Stress(1))**2. +
     *           6.*Stress(4)**2. + 6.*Stress(5)**2. + 6*Stress(6)**2.)
      end select

      J3 = (2./27.) * I1**3. - (1./3.)*I1*I2 + I3

      if (J2 /= 0.0)then
          Lode = 3.*sqrt(3.)*J3/(2. * (J2)**(3./2.))
      else
          Lode = 1.0 ! Isotropic compression
      end if

      end subroutine getStressInvariants

!*************************************************************************

      subroutine getPQ(Sig,p,q,ntens)
      implicit none
      integer, intent(in) :: ntens
```

```
      double precision, dimension(ntens), intent (inout) :: Sig
      double precision, intent (out) :: p,q
      double precision :: tiny,Stress(6)

      Stress = - Sig
      tiny = 0.005

      q = 0.
      do while (q < tiny)
      if (Stress(1) < tiny)  Stress(1) = tiny ! tension cut-off in x-direction
      if (Stress(2) < tiny)  Stress(2) = tiny ! tension cut-off in y-direction
      if (Stress(3) < tiny)  Stress(3) = tiny ! tension cut-off in z-direction

      p  = (stress(1) + stress(2) + stress(3))/3. ! mean effective stress

      ! deviatoric stress
      select case(ntens)
      case(4)
          q  = sqrt(0.5*  ( (stress(1)-stress(2))**2. +
     *         (stress(2)-stress(3))**2. + (stress(3)-stress(1))**2. +
     *         6.*( stress(4)**2.)))
      case(6)
          q  = sqrt(0.5*  ( (stress(1)-stress(2))**2. +
     *         (stress(2)-stress(3))**2. + (stress(3)-stress(1))**2. +
     *         6.*( stress(4)**2. + stress(5)**2. + stress(6)**2.)))
      end select

      if (q < tiny) stress(1) = stress(1) + tiny/3.
      end do

      Sig = - Stress

      end subroutine getPQ

!********************************************

      subroutine getMs (EpsD,phics,Mcs,Ms0,c,Mspeak,Msp,Ir,Ms,gab)
      implicit none

      double precision                :: rad,PI
      double precision                :: Dd,Dd1
      double precision, intent(in)    :: EpsD
      double precision, intent(in)    :: phics,Mcs
      double precision, intent(in)    :: Ms0,c
      double precision, intent(out)   :: Mspeak,Msp
      double precision, intent(in)    :: Ir
      double precision, intent(in)    :: gab
      double precision, intent(out)   :: Ms

      PI = 3.141592653589793238462643383279502884197169399d0
      rad = 180.0d0/PI

      if ((phics + gab*Ir) >= phics) then
          Mspeak = 6*sin((phics + gab*Ir)/rad)/(3-sin((phics + gab*Ir)
```

```
     *             /rad))
      else
          Mspeak = 6.*sin((phics)/rad)/(3.-sin((phics)/rad))
      end if

      Dd1 = (2.*Mcs-4.*Mspeak)**2. - 16.*Ms0*(Mspeak-Mcs) - 4.*Mcs**2.

      if (Dd1 > 0.0)then
          Dd = Dd1
      else
          Dd = 0.0
      end if

      Msp = 2.*Mspeak - Mcs + 0.5*sqrt(Dd)
      Ms = Mcs + (Msp + ( Ms0-Msp ) * exp(-c*EpsD) - Mcs) * exp(-c*EpsD)

      end subroutine getMs

!*********************************************


      subroutine getMpt (EpsD,zeta,chi,
     *                   Mcs,Mspeak,c,Ir,Mpt0,n,Mpt)
      implicit none
      double precision, intent(in)    :: EpsD,zeta,chi
      double precision, intent(in)    :: Mcs ! Critical state ratio
      double precision, intent(in)    :: Mspeak,c ! Ultimate strength line
                                                  ! parameters
      double precision, intent(in)    :: Ir ! Relative dilatancy index
      double precision, intent(inout) :: Mpt0,n ! Phase transformation line
                                                ! parameters
      double precision, intent(out)   :: Mpt

      if (Ir > 0.0d0)then
      Mpt0 = Mspeak * zeta**n - (3.*0.3*Ir)/((3.+0.3*Ir)*chi)
      else
      Mpt0 = Mspeak * zeta**n
      end if

      Mpt = Mcs + (Mpt0 - Mcs) * exp(-0.5*c * EpsD)

      end subroutine getMpt

!*********************************************

      subroutine getMsteta(Ms,Lode,chi,Msteta)
      implicit none
      double precision, intent(in)    :: Ms,Lode
      double precision                :: Mc,Me,Mss
      double precision                :: rad,PI,phi
      double precision, intent(out)   :: chi,Msteta

      PI = 3.14159265358979323846264338327950288419716939937510d0
      rad = 180.0d0/PI
```

```
      phi = asin(3.*Ms/(6.+Ms))
      Me = 6.*sin(phi)/(3.+sin(phi))
      Mss = 2.*sin(phi)

      Msteta = ((Ms + Me)/2. - Mss) * (Lode)**2. + (Ms-Me)/2. * Lode +
     *         Mss

      chi = Msteta/Ms

      end subroutine getMsteta

!********************************************

      subroutine getStressTensor(p,zeta,Sig,Eps,rp,n_,r,np,
     *                           qp,nr,dW_old,dW,ntens)
      implicit none
      integer :: i
      integer, intent(in) :: ntens
      double precision, intent(in) :: p,zeta
      double precision, dimension(ntens), intent(in) :: Sig,Eps
      double precision, dimension(ntens), intent(inout) :: rp,n_,r
      double precision, intent(inout) :: dW_old,dW,np,qp,nr
      double precision :: Stress(ntens),s(ntens),np1

      Stress = - Sig

      s(1) = Stress(1)-p
      s(2) = Stress(2)-p
      s(3) = Stress(3)-p
      s(4) = Stress(4)

      if (ntens == 6) then
      s(5) = Stress(5)
      s(6) = Stress(6)
      end if

      if (p <= 0.0)then
          r = 0
      else
          r = s/p
      end if

      select case(ntens)
        case(4)
            dW = (r(1) - rp(1))*Eps(1) + (r(2) - rp(2))*Eps(2) +
     *           (r(3) - rp(3))*Eps(3) + 2.*(r(4) - rp(4))*Eps(4)
        case(6)
            dW = (r(1) - rp(1))*Eps(1) + (r(2) - rp(2))*Eps(2) +
     *           (r(3) - rp(3))*Eps(3) + 2.*(r(4) - rp(4))*Eps(4) +
     *           2.*(r(5) - rp(5))*Eps(5) + 2.*(r(6) - rp(6))*Eps(6)
      end select

      if ((dW * dW_old <= 0.0d0) .and. (dW_old .ne. 0.0d0)
     *   .and. (zeta /= 0.0d0)) then
```

```
         rp = r
      end if
      dW_old = dW

      select case(ntens)
          case(4)
              qp = sqrt((r(1)*p - rp(1)*p)**2. + (r(2)*p - rp(2)*p)**2.
     *             + (r(3)*p - rp(3)*p)**2. + 2.*(r(4)*p - rp(4)*p)**2.)
          case(6)
              qp = sqrt((r(1)*p - rp(1)*p)**2. + (r(2)*p - rp(2)*p)**2.
     *             + (r(3)*p - rp(3)*p)**2. + 2.*(r(4)*p - rp(4)*p)**2.
     *             + 2.*(r(5)*p - rp(5)*p)**2 + 2.*(r(6)*p -
     *             rp(6)*p)**2.)
      end select

      if (qp /= 0)then
            n_ = (s - rp*p)/qp
      else
            n_ = 0.0
      end if

      select case(ntens)
        case(4)
            np1 = n_(1) * rp(1) + n_(2) * rp(2) + n_(3) * rp(3) +
     *            2.*(n_(4) * rp(4))
        case(6)
            np1 = n_(1) * rp(1) + n_(2) * rp(2) + n_(3) * rp(3) +
     *            2.*(n_(4) * rp(4)) + 2.*(n_(5) * rp(5)) + 2.*(n_(6)
     *            * rp(6))
      end select

      if (np1 > 0.0d0)then
           np = 0.0
      else
           np = np1
      end if

      select case(ntens)
        case(4)
            nr = n_(1)*r(1) + n_(2)*r(2) + n_(3)*r(3) + 2.*n_(4)*r(4)
        case(6)
            nr = n_(1)*r(1) + n_(2)*r(2) + n_(3)*r(3) + 2.*n_(4)*r(4)
     *           + 2.*n_(5)*r(5) + 2.*n_(6)*r(6)
      end select

      end subroutine getStressTensor

!********************************************


      subroutine getHardeningParameter(Ms,q,p,np,chi,zeta)
      implicit none
      double precision, intent(in)    :: q,p
      double precision, intent(in)    :: np,chi
      double precision, intent(in)    :: Ms
```

```fortran
      double precision, intent(out)   :: zeta
      double precision                :: zeta1

      if (p <= 0.0)then
          zeta1 = 0.0
      else
          zeta1 = (q/p) / (sqrt(2./3.) * Ms * chi - np)
      end if

      zeta = zeta1

      end subroutine getHardeningParameter

!********************************************

      subroutine getGRAD (d,n_,nr,GRADg,GRADf,ntens)
      implicit none
      integer, intent(in)  :: ntens
      double precision, intent(in) :: d,nr
      double precision, dimension(ntens), intent(inout) :: n_
      double precision, dimension(ntens), intent(out)   :: GRADf,GRADg

      select case(ntens)
        case(4)
            GRADg(1) = n_(1) + (n_(1)**2. + n_(4)**2) * d
            GRADg(2) = n_(2) + (n_(2)**2. + n_(4)**2) * d
            GRADg(3) = n_(3) + (n_(3)**2.) * d
            GRADg(4) = 2.*n_(4) + (n_(1)*n_(4) + n_(2)*n_(4))*d

            GRADf(1) = n_(1) - (1./3.)*nr
            GRADf(2) = n_(2) - (1./3.)*nr
            GRADf(3) = n_(3) - (1./3.)*nr
            GRADf(4) = 2.*n_(4)
        case(6)
            GRADg(1) = n_(1) + (n_(1)**2. + n_(4)**2. + n_(6)**2) * d
            GRADg(2) = n_(2) + (n_(2)**2. + n_(4)**2. + n_(5)**2) * d
            GRADg(3) = n_(3) + (n_(3)**2. + n_(6)**2. + n_(5)**2) * d
            GRADg(4) = 2.*n_(4) + (n_(1)*n_(4) + n_(2)*n_(4) +
     *                 n_(6)*n_(5))*d
            GRADg(5) = 2.*n_(5) + (n_(4)*n_(6) + n_(2)*n_(5) +
     *                 n_(5)*n_(3))*d
            GRADg(6) = 2.*n_(6) + (n_(1)*n_(6) + n_(4)*n_(5) +
     *                 n_(6)*n_(3))*d

            GRADf(1) = n_(1) - (1./3.)*nr
            GRADf(2) = n_(2) - (1./3.)*nr
            GRADf(3) = n_(3) - (1./3.)*nr
            GRADf(4) = 2.*n_(4)
            GRADf(5) = 2.*n_(5)
            GRADf(6) = 2.*n_(6)
      end select

      end subroutine getGRAD
```

```
!********************************************

      subroutine getElasticMatrix (p,G0,m,ni,G,K,De,ntens)

      implicit none
      double precision :: G1
      double precision :: E1,E2

      integer, intent(in) :: ntens
      double precision, intent(in) :: p,G0,m,ni
      double precision, intent(inout) :: G,K
      double precision, dimension(ntens,ntens), intent(out) :: De

      G1 = G0 * (p)** m

      if (G1 < G0/10.)then
          G = G0/10.
      else if (G1 > 10.*G0)then
          G = 10.*G0
      else
          G = G1
      end if

      K = 2.*G*(1.+ni)/(3.*(1.-2.*ni))
      E1 = K + 4.*G/3.
      E2 = K - 2.*G/3.

      select case(ntens)
        case(4)
            De(1,1) = E1
            De(1,2) = E2
            De(1,3) = E2
            De(1,4) = 0.0

            De(2,1) = E2
            De(2,2) = E1
            De(2,3) = E2
            De(2,4) = 0.0

            De(3,1) = E2
            De(3,2) = E2
            De(3,3) = E1
            De(3,4) = 0.0

            De(4,1) = 0.0
            De(4,2) = 0.0
            De(4,3) = 0.0
            De(4,4) = 2.*G
        case(6)
            De(1,1) = E1
            De(1,2) = E2
            De(1,3) = E2
            De(1,4) = 0.0
            De(1,5) = 0.0
```

```
            De(1,6) = 0.0

            De(2,1) = E2
            De(2,2) = E1
            De(2,3) = E2
            De(2,4) = 0.0
            De(2,5) = 0.0
            De(2,6) = 0.0

            De(3,1) = E2
            De(3,2) = E2
            De(3,3) = E1
            De(3,4) = 0.0
            De(3,5) = 0.0
            De(3,6) = 0.0

            De(4,1) = 0.0
            De(4,2) = 0.0
            De(4,3) = 0.0
            De(4,4) = 2.*G
            De(4,5) = 0.0
            De(4,6) = 0.0

            De(5,1) = 0.0
            De(5,2) = 0.0
            De(5,3) = 0.0
            De(5,4) = 0.0
            De(5,5) = 2.*G
            De(5,6) = 0.0

            De(6,1) = 0.0
            De(6,2) = 0.0
            De(6,3) = 0.0
            De(6,4) = 0.0
            De(6,5) = 0.0
            De(6,6) = 2.*G
      end select

      end subroutine getElasticMatrix

!********************************************


      subroutine getPlasticMatrix (zeta,n,GRADg,GRADf,De,Dp,ntens)
      implicit none
      integer :: i
      double precision :: S
      integer, intent(in) :: ntens
      double precision,dimension(ntens) :: F,G
      double precision, intent(in) :: zeta,n
      double precision, dimension(ntens), intent(in) :: GRADg,GRADf
      double precision, dimension(ntens,ntens), intent(in) :: De
      double precision, dimension(ntens,ntens), intent(out) :: Dp

      select case(ntens)
```

```
        case(4)
            do i = 1,4
            F(i) = GRADf(1)*De(i,1) + GRADf(2)*De(i,2) +
     *             GRADf(3)*De(i,3) + GRADf(4)*De(i,4)
            G(i) = GRADg(1)*De(i,1) + GRADg(2)*De(i,2) +
     *             GRADg(3)*De(i,3) + GRADg(4)*De(i,4)
            end do

            S = GRADg(1) * F(1) + GRADg(2) * F(2) +  GRADg(3) * F(3) +
     *          GRADg(4) * F(4)

        if (S /= 0.0)then
            do i = 1,4
            Dp(1,i) = zeta**n/S * F(i) * G(1)
            Dp(2,i) = zeta**n/S * F(i) * G(2)
            Dp(3,i) = zeta**n/S * F(i) * G(3)
            Dp(4,i) = zeta**n/S * F(i) * G(4)
          end do
        else
          Dp = 0.0
        end if
        case(6)
            do i = 1,6
            F(i) = GRADf(1)*De(i,1) + GRADf(2)*De(i,2) +
     *             GRADf(3)*De(i,3) + GRADf(4)*De(i,4) +
     *             GRADf(5)*De(i,5) + GRADf(6)*De(i,6)
            G(i) = GRADg(1)*De(i,1) + GRADg(2)*De(i,2) +
     *             GRADg(3)*De(i,3) + GRADg(4)*De(i,4) +
     *             GRADg(5)*De(i,5) + GRADg(6)*De(i,6)
            end do

        S = GRADg(1) * F(1) + GRADg(2) * F(2) +  GRADg(3) * F(3) +
     *      GRADg(4) * F(4) + GRADg(5) * F(5) +  GRADg(6) * F(6)

        if (S /= 0.0)then
          do i = 1,6
              Dp(1,i) = zeta**n/S * F(i) * G(1)
              Dp(2,i) = zeta**n/S * F(i) * G(2)
              Dp(3,i) = zeta**n/S * F(i) * G(3)
              Dp(4,i) = zeta**n/S * F(i) * G(4)
              Dp(5,i) = zeta**n/S * F(i) * G(5)
              Dp(6,i) = zeta**n/S * F(i) * G(6)
          end do
        else
          Dp = 0.0
        end if
      end select

      end subroutine getPlasticMatrix

!********************************************
```